Probing the nuclear structure in the vicinity of 78Ni via beta decay spectroscopy of 84Ga

Karolina Kolos

UNIVERSITE PARIS-SUD

ÉCOLE DOCTORALE : *École Doctoral Particules, Noyaux, Cosmos*
Laboratoire de *Institut de Physique Nucléaire d'Orsay*

DISCIPLINE Physique Nucléaire

THÈSE DE DOCTORAT

soutenue le 24/09/2012

par

Karolina KOLOS

Probing the nuclear structure in the vicinity of ^{78}Ni

via beta decay spectroscopy of ^{84}Ga

Directeur de thèse :	Fadi IBRAHIM	Directeur de Recherche, CNRS, IPN Orsay
Co-directeur de thèse :	David VERNEY	Charge de Recherche, CNRS, IPN Orsay

Composition du jury :

Président du jury :	Elias KHAN	Professeur, Universite Paris Sud
Rapporteurs :	Bertram BLANK	Directeur de Recherche,CNRS, CENBG Bordeaux
	Volker WERNER	Associate Professor, Yale University
Examinateurs :	Jaen-Charles THOMAS	Charge de Recherche,CNRS, GANIL
	Fadi IBRAHIM	Directeur de Recherche, CNRS, IPN Orsay
	David VERNEY	Charge de Recherche, CNRS, IPN Orsay

Abstract

Thanks to advances in production of radioactive nuclear beams in the last two decades, we are able to study nuclear systems very far from stability. The region of the nuclear landscape in the vicinity of ^{78}Ni remains still unexplored. This region, with very neutron-rich ^{78}Ni hypothetically considered as a doubly magic core, is interesting in terms of nuclear structures. The experimental information is equally important to guide the emerging shell-model effective interactions in this region. We have studied β-decay of a neutron rich ^{84}Ga isotope at the ALTO facility in IPN Orsay (France). The fission fragments were produced with photo-fission reaction induced by 50 MeV electron beam in a thick UCx target. For the first time the maximum electron driver beam intensity at ALTO - 10μA - was used. The gallium atoms were selectively ionized with a newly developed laser ion source. With this ion source the ionization of the gallium was more than ten times higher compared to the surface ion source previously used by our group. The ions were separated with the PARRNe mass separator and implanted on a movable mylar tape. Two germanium detectors in close geometry were used for the detection of γ-rays and γ-γ coincidence measurement, and a plastic $4\pi\beta$ for beta tagging. We present the results of our experiment: the improved level schemes of the neutron-rich ^{83,84}Ge and ^{84}As isotopes. We discuss their structure and compare the experimental results with the shell model calculations made with the new effective interaction $ni78 - jj4b$ with ^{78}Ni core, constructed in the framework of this thesis.

Keywords: ISOL technique, photofission. uranium carbide target, radioactivity, laser ion source, magic numbers, shell model, nuclear structure.

Résumé

Grâce aux progrés de la production de faisceaux radioactifs au cours des deux dernières décennies, nous sommes à présent capables d'étudier les systèmes nucléaires très loin de la vallée de stabilité. La région de ^{78}Ni, noyau encore inconnu supposé doublement magique, reste encore inexplorée. Cette région est très intéressante en termes de structure nucléaire. En effet, les informations expérimentales obtenues sur l'espace de valence ouvert au dessus de ^{78}Ni, nous permettront de construire des intéractions effectives pour cette région. Nous avons étudié la désintégration de l'isotope ^{84}Ga riche en neutrons auprès de l'installation ALTO à l'IPN d'Orsay. Les fragments de fission ont été produites par photo-fission induite par l'interaction d'un faisceau d'électron de 50 MeV avec une cible épaisse de carbure d'uranium. Pour la première fois, ALTO a été utilisé dans ses conditions optimales, tant du point de vue de l'intensité du faisceau primaire (10μA d'électrons à 50 MeV) que de la méthode d'ionisation. En effet, les atomes de gallium ont été sélectivement ionisés à l'aide d'une source d'ions laser. Grâce à cette nouvelle source l'ionisation du gallium était plus de dix fois supérieur à celui de la source à ionisation de surface utilisée précédemment par notre groupe. Les ions séparés par le séparateur de masse PARRNe ont été implantés sur une bande de mylar mobile, entourée de deux détecteurs germanium placés en géométrie rapprochés d'un détecteur plastique pour le marquage des désintégrations béta. Dans cette thèse je présente les résultats de notre expérience obtenus pour les noyaux riches en neutrons ^{83,84}Ge et ^{84}As. Nous discuterons de leur structure et les comparerons aux résultats obtenus avec des calculs modèle en couches effectués avec la nouvelle interaction $ni78 - jj4b$ construite dans le cadre de cette thèse.

Mot-clès: technique d'ISOL, photo-fission. carbure d'uranium, radioactivité, source d'ionisation laser, numberes magiques, modèle en couches, structure nucléaire.

Remerciements

Tout d'abord, je remercie l'ancienne directrice de l'IPN Mme Dominique Guillemaud-Mueller et le nouveau directeur M. Faiçal Azaiez de m'avoir permis de mener ma thèse dans l'Institut de Physique Nucléaire.

Je souhaite remercier les membres de mon jury : mes deux rapporteurs Bertam Blank et Volker Werner pour leurs commentaires et questions et pour avoir apporteé leur contribution à ce manuscrit avec attention et gentillesse, Elias Khan pour avoir accepté la présidence et Jean-Charles Thomas pour l'étude scrupuleuse mon manuscrit et aussi pour les discussions scientifiques.

Je tiens à remercier sincèrement mes deux directeurs de thèse : Fadi Ibrahim et David Verney. Je les remercie pour l'environnement exceptionel de travail qu'ils m'ont apporté grace à leur enthousiasme et leur bonne humeur. Je remercie Fadi pour la confiance qu'il m'a accordée pendent ce travail de thèse et pour m'avoir guidée et orientée au moment des choix difficiles au cours de ma thèse. Merci également à David pour sa disponibilité, pour ses conseils très enchichissants, ses encouragements, pour la qualité de son encadrement scientifique et pour sa super lettre de recommendation :p

Je remercie Brigitte Roussière pour son encadrement pendent la premiére année de ma thèse et de m'avoir donné l'opportinuté de participer à des mesures de radioactivité de la cible de carbure d'uranium. Je voudrais remercier également à Christophe Lau pour le temps qu'il a consacré à examiner le partie de mon manuscrit concernant le travail sur la cible.

Je remercie le groupe NESTER dans son ensemble qui m'a accueilli. Merci à Megumi Niikura et Iulian Stefan pour leur conseils et nos discussions. Je voudrais remercier aux theésard : Benoit Tastet, Adrien Matta, Baptist Mouginot, Sandra Giron, Dmitri Testov et Mathieu Ferraton (MERCI Mathieu!). Je ne peux pas oublier l'incroyable équipe du Tandem-ALTO qui a permis le déroulement de l'expérience de cette theèse. L'équipe du laser: Franqis LeBlanc, Serge Franchoo et Celine Bonnin pour le développement d'une source d'ionisation laser. Merci à Sebastien Ancelin et Gauillame Mavilla pour leur remarquable travail. Merci aussi à Kane vrai ami de travail qui m'a sauvé la vie plusieurs fois :)

Je veux aussi remercier chaleureusement Kamila Sieja et Fredèric Nowacki, experts du Modèle en Couches, pour l'opportunité de travailler ensemble sur des intéractions effectives, nos discussions, leur disponibilité et pour notre excellent collaboration. Dziękuję,

że mnie "zaadoptowaliscie" :) oraz za wasze niesamowite wsparcie szczególnie w czasie ostatnich miesięcy mojego doktoratu. Niezaprzeczalnie ogromna część mojego doktoratu to Wasza zasługa!

Merci à ma famille : mojej Mamie, Tacie i siostrze za ich ogromne wsparcie w ciągu tyh ostatnich kilku lat które spędziłam wiele kilometrów od nich. Ich miłość, dobre rady i optymizm które zawsze dodają mi otuchy i siły. Chciałabym im podziékować za ich przeogromne zaufanie jakim mnie darzą i poparcie w decyzjach jakie podejmuje nawet jeśli oznacza to trochę wiécej kilometrów jakie nas dzielą. Dziękuję mojej siostrze Michasi za dojrzałość i wyrozumialość i za nasze wszystkie prześmiane rozmowy telefoniczne. Dziękuję Danielowi za ogromne wsparcie w czasie mojej obrony, za jego obecność i pomoc w przygotowywaniach a w szczególności za opiekę nad moją siostrą :)

Daavid, kiitos siitä, että saimme kasvaa yhdessä joka päivä. Kiitos jokaisesta yhdessä vietetystḧetkestä ja yhteisistä seikkailuista Ranskassa :) Kiitos kärsivällisyydestäsi kun olin kaikkein kärsimattömin, ymmärtäväisyydestäsi kun minulla oli vaikea päivä, kannustuksestasi, rakkaudestasi. Nämä kolme vuotta olivat sen arvoiset, koska vietin ne sinun kanssasi.

Karolina

Contents

List of Figures

List of Tables

Introduction

Contents

1.1 Evolution of the $N = 50$ gap towards ^{78}Ni

Recent advances in the production and purification of radioactive ion beams have made a region of nuclei near ^{78}Ni more accessible for the experimental studies. The very neutron-rich ^{78}Ni ($N/Z \simeq 1.8$) is hypothetically considered as doubly magic nucleus with 28 protons and 50 neutrons. It was synthesized and identified in-flight using the projectile fragmentation method [1] but its excitation modes remain unknown and rely on the extrapolation of the properties of its neighbors. The region around ^{78}Ni is interesting in terms of nuclear structures. Firstly, as this nucleus (in some scenarios) is one of the waiting-points in the r-process, testing the rigidity of its gaps remains of a special interest. Secondly, the experimental information is important to guide the emerging shell-model effective interactions in this region. The knowledge of the single particle energies of ^{78}Ni is crucial for shell model studies which utilize this nucleus as a core [2] and to validate the empirical universal monopole interactions [3, 4, 5].

From the evolution of the effective single-particle energy of the proton in Cu isotopes is was shown that the $1f_{5/2}$ orbital goes down and crosses the $2p_{3/2}$ orbital at $N = 44 - 46$ [6] when approaching the more neutron-rich region. It was interpreted as an indication of the reduction of the $Z = 28$ shell gap due to the tensor part of the nucleon-nucleon interaction [7, 4]. The magic number 50 originates from the spin-orbit part of the nuclear interaction which lowers the energy of $g_{9/2}$ orbit from the $N = 4$ major shell and locates it close to the orbits from $N = 3$ major shell. Its partner, the $g_{7/2}$ orbit, is pushed to the upper edge of the gap, above/below the $d_{5/2}$ orbit. The $^{78}_{28}$Ni$_{50}$ isotope belongs to the same family as other doubly spin-orbit nuclei as $^{20}_{6}$C$_{14}$, $^{42}_{14}$Si$_{28}$ and $^{132}_{50}$Sn$_{82}$. The latter has the major characteristics of a doubly-magic
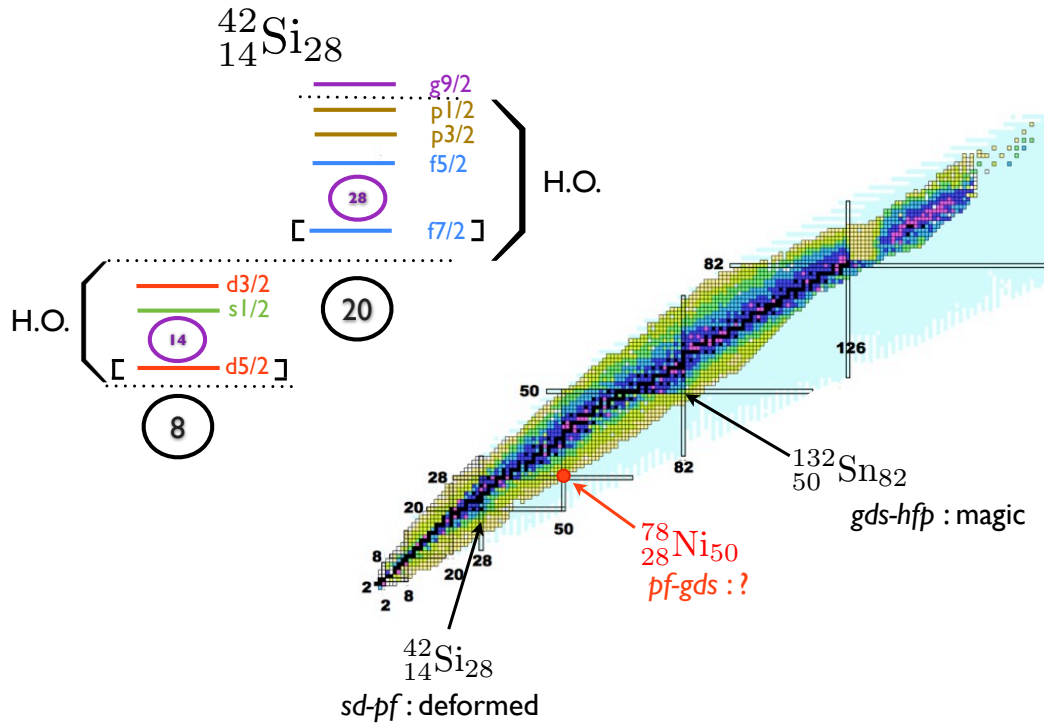
Figure 1.1: Left top: Schematic representation of the orbitals in ^{42}Si. Right: Chart of nuclei. The position of very neutron rich ^{42}Si,^{78}Ni and ^{132}Sn is pointed on the chart.

spherical nucleus [8, 9] while the two others are deformed [10, 11]. The magic numbers 14 and 28 are not a major harmonic oscillator closures but come from the additional spin-orbit interaction (Figure 1.1). In ^{42}Si, the first excited state was measured to be at low energy and explained as an indication of the existence of the erosion of both the $Z = 14$ and $N = 28$ shell closures caused by action of the mutual proton and neutron forces and to the quadrupole correlations between states bounding the two gaps [10]. Such a deformed configuration could be found for the ground state of ^{78}Ni or a low-lying state [12].

The evolution of the size of the $N = 50$ shell gap between $Z = 28$ and $Z = 38$ depends on proton-neutron interactions between the proton $\pi f_{5/2}$, $\pi p_{3/2}$ orbitals and the neutron $\nu g_{9/2}$ and $\nu d_{5/2}$ orbitals [13]. The 2^+ states in the $N = 50$ isotonic chain are expected to be formed by proton excitations within πfp shells. The experimental energies of 2^+ excited states and the ratios of the energies of 4^+ to 2^+ states for $Z = 30 - 38$ ($N = 46 - 54$) are plotted in Figure 1.2. The high energies of the 2^+ states (and low $4^+/2^+$ ratio at $N = 50$) point to the persistence of the $N = 50$ gap .
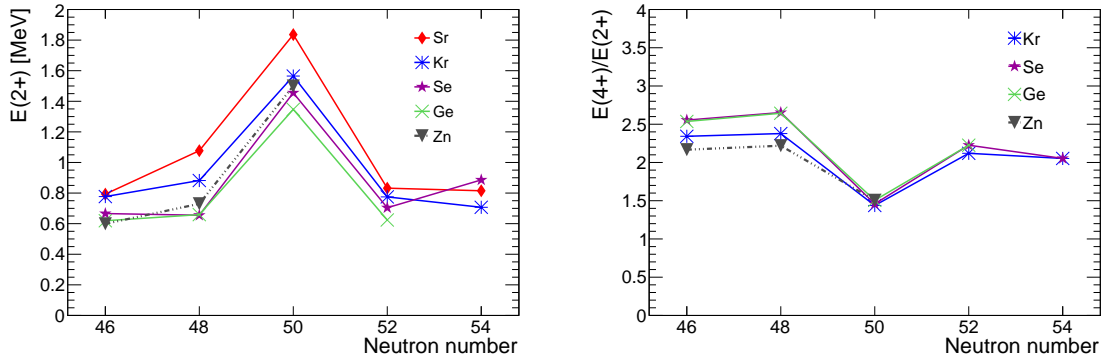
Figure 1.2: (Left:) Experimental $E(2^+)$ and (right:) the ratios of $4^+/2^+$ energies for $Z = 30 - 38$ and $N = 46 - 54$.

The behavior of the two-nucleon separation energies is a widely used indicator of structural evolution as for the emergence of magic numbers. The gap derived from the difference of two-neutron binding energies $(BE_{2n}(N = 52) - BE_{2n}(N = 50))$ is plotted in Figure 1.3. It displays a staggering as a function of the parity of Z and a change of slope at $Z = 32$. Two-neutron separation energies provide evidence for the reduction of the $N = 50$ shell gap energy towards germanium ($Z = 32$, which was not expected from the systematics of the 2^+ energies or the $B(E2)$ values) and a subsequent increase at gallium ($Z = 31$) which was interpreted by Hakala *et al.* [14] as an indication of the persistent rigidity of the shell gap towards nickel ($Z = 28$). The reduction of the spherical gap at $Z = 32$ was described by Bender *et al.* [15] in terms of beyond mean-field dynamic collective quadrupole correlations, and confirmed with the empirical evaluation of one or two-neutron separation energies of ground or isomeric state by Porquet *et al.* [12].

The size of a gap is related to the energy of the states arising from the $1p - 1h$ excitations across it. As the $N = 50$ shell gap is formed between the $g_{9/2}$ and $d_{5/2}$ orbits, the corresponding $1p - 1h$ states have a $(\nu g_{9/2})^{-1}(\nu d_{5/2})^{+1}$ configuration. This gives rise to a multiplet of six states with spin values J ranging from 2 to 7. All the members of this multiplet were successfully identified in $^{90}_{40}$Zr using the neutron pick-up reaction $^{90}_{40}$Zr(^{3}He,α) [16] and in $^{88}_{38}$Sr using the neutron stripping reaction $^{88}_{38}$Sr(d,p) [17]. The high-spin states of $^{86}_{36}$Kr and $^{84}_{34}$Se were studies via ^{82}Se(^{7}Li,$p2n$) reaction[18] and in fusion fission reaction [19]. More recently, the excited states in $^{82}_{32}$Ge were studied by spontaneous fission of ^{248}Cm and two states with spins 5^+ and 6^+ were proposed [20]. The energies of the 5^+, 6^+ and 7^+ states for $N = 50$ isotones as a function of proton number Z are drawn in Figure 1.4. Since the excitation energy is related to the size of
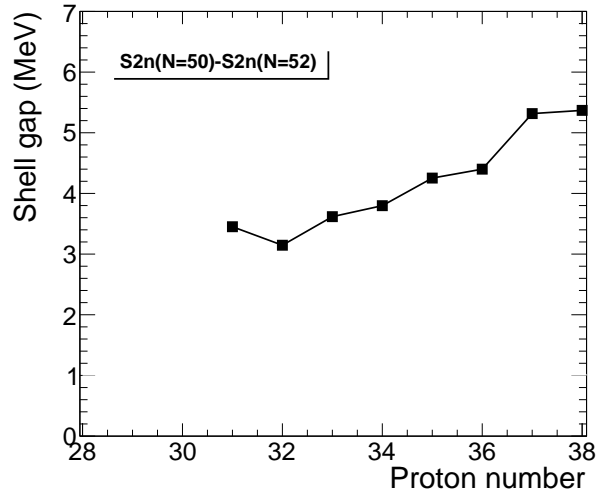
Figure 1.3: Evolution of the $N = 50$ shell gap from the difference in the two neutron binding energies between $N = 50$, 52 isotones.

the $N = 50$ gap their decrease towards smaller Z (here $Z = 32$) could be interpreted as a decrease in the gap, which was the conclusion of Rząca *et al.* [20]. This interpretation argues with the results of the shell model calculation of Zhang *et al.* [21] who reproduced successfully those high spin experimental states assuming the constancy of the shell gap. Recently, the state-of-the art shell model calculations in a large model space (πfp for protons and $\nu fpgd$ for neutrons) which allow to study simultaneously excitations across the $Z = 28$ and $N = 50$ shell gaps were performed [22]. The results for the $1p - 1h$ (5^+ and 6^+) states compared with experimental values are presented in Figure 1.4 (right bottom). There is a minimum of the $N = 50$ gap at $Z = 32$ consistent with experimental data and a further increase towards $Z = 28$, indicating a robustness of the $N = 50$ gap in ^{78}Ni.

The evolution of the $N = 50$ gap has been studied over a wide range of masses also far from the stability. There are evidences that hint to the decrease of this gap, e.g. in some scenarios ($1p - 1h$) the energies of $5^+, 6^+, 7^+$ states, and the results indicating that all the $N = 50$ isotones behave as spherical nuclei, e.g. $E(2^+)$, $4^+/2^+$ ratio or atomic masses. From the last, the minimum of the two neutron separation energy was discovered at $Z = 32$. This minimum, explained by means of theorerical calculations as originating from the extra nuclear correlations (the quadrupole deformations) points at the importance of the collectivity at $Z = 32$. By studying this region of interest one aims to understand the evolution of collectivity and draw conclusions on the magicity of ^{78}Ni.
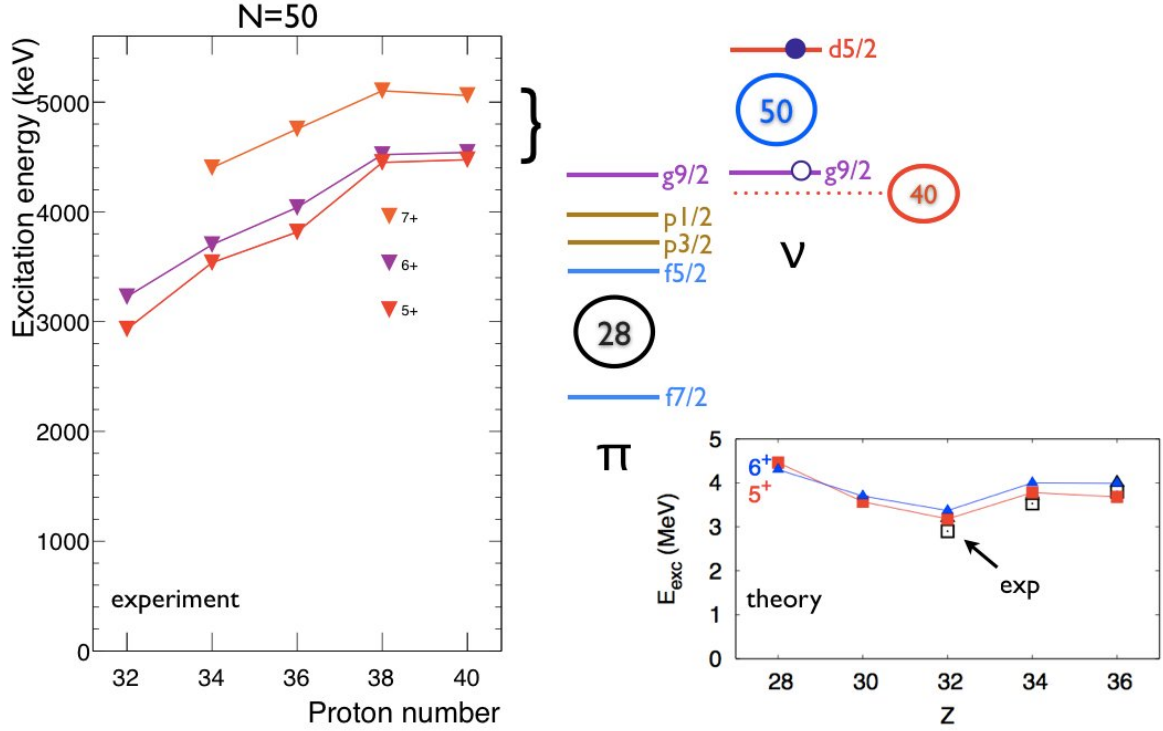
Figure 1.4: The excitation energies of the $5+, 6+7+$ states with $(\nu g_{9/2})^{-1}(\nu d_{5/2})^{+1}$ configuration in the even-even $N = 50$ isotonic chain. Left: Experimental data from [16, 17, 18, 19, 20]. Right: Calculated values from [22] compared with the experimental energies of the 5^+ states.

1.2 Evolution of collectivity in germanium isotopes $(Z = 32)$

The intriguing features of the low-lying states in the even-even neutron-rich germanium isotopes have been discussed in a number of experimental and theoretical papers. The Ge isotopes around $A \simeq 72 - 80$ are well known to exhibit the shape coexistence phenomenon characterized by prolate-oblate and spherical-deformed competition [26, 27, 28, 29, 30, 24, 31]. The systematics of the low-lying positive parity states of $^{72-84}$Ge is presented in Figure 1.5. In neutron-rich Ge isotopes $(A = 72 - 80)$ neutrons occupy the $g_{9/2}$ orbit, which separates the $N = 40$ sub-shell gap and the $N = 50$ shell gap. This unique parity neutron orbit plays a distinctive role in the strength of the shell gap and in the development of collectivity in this mass region. Starting from $N = 40$, the 2^+ state in ^{72}Ge isotope was measured to be lower as compared to ^{70}Ge at $N = 38$. The reduced transition probability was also measured higher indicating an increase in collectivity around $N = 40$. This enhanced collectivity leads to a deformed
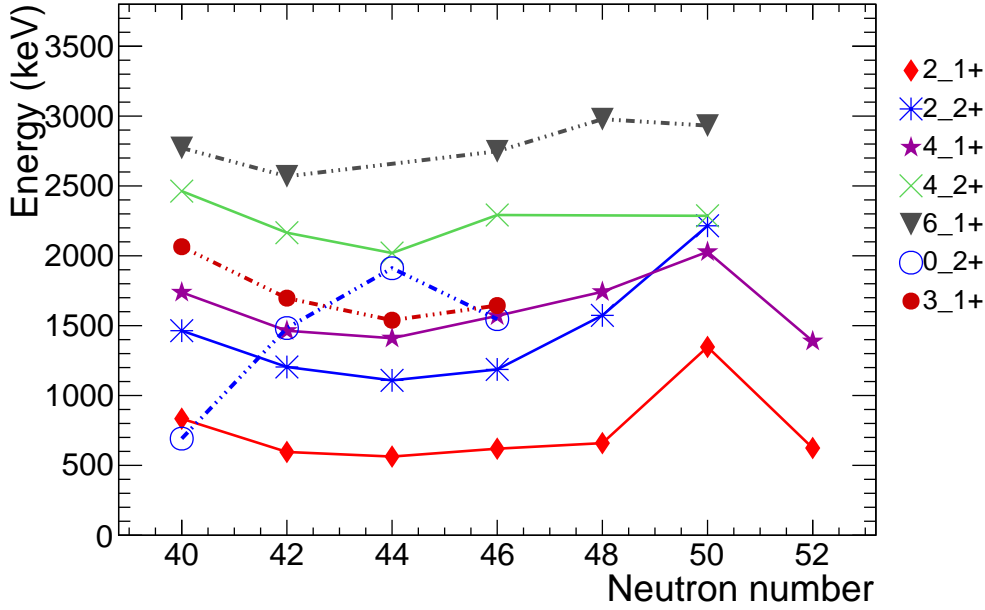
Figure 1.5: Systematics of the low-lying positive parity states of $^{72-84}$Ge.

ground state configuration in ^{72}Ge which was found to be γ-soft [32]. The maximum of deformation is reached at $N = 42$ and then decreases with increasing number of neutrons. Several experiments (two neutron transfer e.g. [33], Coulomb excitation [29]) were performed to study the structure of ^{74}Ge. The first $0^+, 2^+$ and 4^+ states were found to belong to the rotational ground-state band, the 0_2^+ to be an intruder while the 2_2^+ was interpreted as a band-head of the gamma vibration band [29]. The $^{76-78}$Ge isotopes were also found to show the characteristics of an asymmetric rotor with $\gamma \sim 30°$ [27]. The excitation levels in ^{80}Ge located at $N = 48$ (with two holes in the $g_{9/2}$ orbit) were populated with β-decay of ^{80}Ga by Hoff and Fogelberg [34], and recently at ALTO [35, 36]. From the measurement of reduced transition probabilities [31] and comparison with the shell model calculations the 2_1^+ and the 2_2^+ states in the nucleus were shown to have different configurations. The structure of the semi-magic ^{82}Ge isotope ($N = 50$) was studied via β-decay of ^{82}Ga [34, 37]. The $1p - 1h$ states with spins $5^+, 6^+$ were identified with the spontaneous fission of ^{248}Cm [20]. From the recent measurement of the reduced transition probabilities towards $N = 50$ a smooth decrease in the $B(2_1^+ \rightarrow 0_1^+)$ values (Figure 1.6) has been reported [24]. The slope of the reduced transition probabilities is similar to the one in Se or Zn isotopes. The high (1348.17(12) keV) 2^+ energy of ^{82}Ge and low $B(E2)$ value at the $N = 50$ indicate the persistence of the magic 50 for germanium isotopes. When passing the neutron number 50, the first attempt to study the ^{84}Ge isotope was made at ISOLDE-CERN by
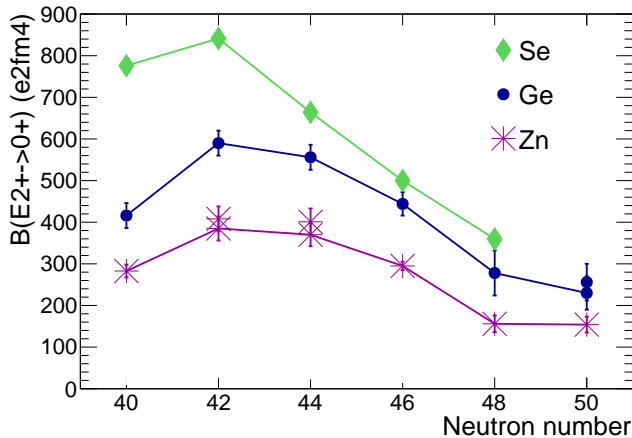
Figure 1.6: Experimental $B(E2)$ values for the Se, Ge and Zn isotopes [23, 24, 25]. A smooth decrease of the $B(2_1^+ \rightarrow 0_1^+)$ values at $N = 50$ indicates a persistence of the magic number $N = 50$ (at $Z = 30, 32$).

Koster *et al.* [38] and at IPN Orsay by Lebois *et al.* [39]. The two γ-rays (624.3(7)keV and 1046.1(7)keV) were attributed as the de-excitation rays from the 2_1^+ and 4_1^+ states. Because of high 4_1^+ to 2_1^+ energy ratio ($R_{4/2} = E(4_1^+)/E(2_1^+) = 2.67$) a sudden increase of collectivity in ^{84}Ge with two neutrons above $N = 50$ was proposed by Lebois. The location of the 4_1^+ state was not confirmed by Winger [37] who proposed the 4_1^+ state at 1389.0(10)keV. This 4_1^+ state was not yet confirmed and more information is needed on the excitation levels of this very neutron-rich isotope. It is extremely interesting to study how the nuclear collectivity evolves in this neutron-rich region while crossing the magic number $N = 50$ and the rigidity of this magic number.

When following the systematics of the germanium isotopes in the $N = 40 - 50$ region one could expect to see a collective behavior in ^{84}Ge. The nature of the collectivity can be probed by measuring the excitation energies of the first $2^+, 4^+, 0^+$ excited states. In the experiment performed in the framework of this thesis we aimed to populate the excited states in ^{84}Ge via β-decay of ^{84}Ga to study the evolution of the collectivity in this neutron-rich nucleus beyond $N = 50$.

1.3 Single-particle energies in $N = 51$ isotonic chain

Systematics of the low-lying positive parity states in the N = 51 isotonic chain is presented in Figure 1.7. The valence space that opens above ^{78}Ni corresponds to the proton $\pi(f_{5/2}, p_{3/2}, p_{1/2}, g_{9/2})$ orbits and the neutron $\nu(g_{7/2}, d_{5/2}, d_{3/2}, s_{1/2}, h_{11/2})$ orbits. The spin of the ground-state of the $N = 51$ odd-even isotones from ^{81}Zn up to ^{101}Sn are well established to be $5/2^+$ originating from the occupation by the valence neutron of the $\nu 2d_{5/2}$ orbital [13, 40]. In the low-lying spectra of odd-even $N = 51$ isotones states correspond to the coupling of the $\nu 2d_{5/2}$ neutron to the first 2^+ excitation of the semi-magic $N = 50$ core which gives rise to a multiplet of states with spins ranging

from $1/2^+$ to $9/2^+$. The second kind of states are the neutron quasi-particle states: $1/2^+$, $3/2^+$, $7/2^+$ and at higher energy $11/2^-$, corresponding to the coupling of the $N = 50$ core 0^+ ground state with the neutron. Those excited states are well identified in ^{89}Sr ($Z = 38, N = 51$) and described in the framework of the core-particle coupling model [41, 42, 43]. An attempt to locate the neutron single-particle centroids by using direct (d, p) reaction with radioactive beams of ^{84}Se and ^{82}Ge has been made [44]. The $\nu 2d_{5/2}$ nature of ground state and the $\nu 3s1/2$ nature of the first excited state in both ^{85}Se and ^{83}Ge were confirmed, but the results remained inconclusive for other low-lying states due to limited statistics.
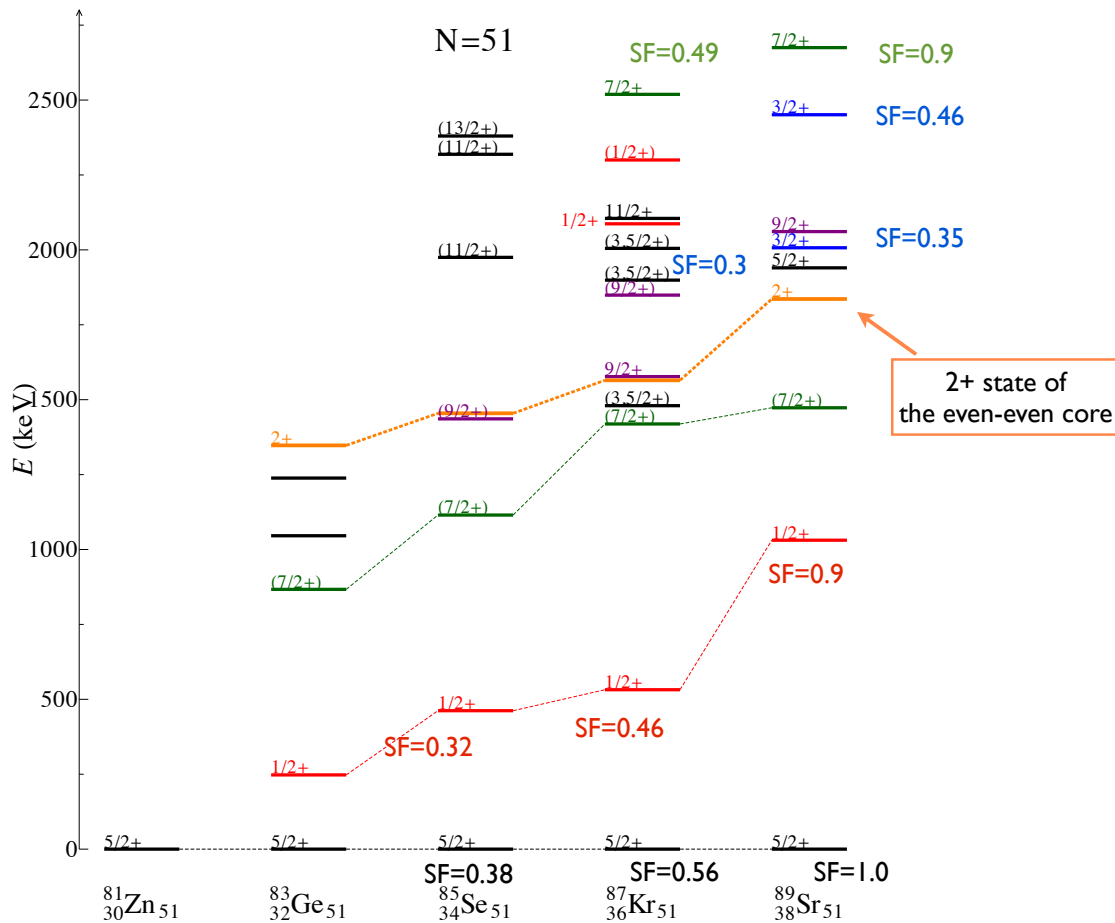
Figure 1.7: Systematics of the low-lying positive parity states in the $N = 51$ isotonic chain. The spectroscopic factors "SF" from [44, 45, 46]

Due to the experimentally hard to reach region our knowledge on the low-lying states

in the $N = 51$ isotonic chain is poor. Up to now, ^{83}Ge is the most exotic $N = 51$ isotone studied in terms of excitation energies but only few transitions were assigned to its level scheme. The low-lying excited states of ^{83}Ge were populated in (d, p) reaction with ^{82}Ge beam at the Holifield Radioactive Ion Beam Facility (HRIBF) at Oak Ridge National Laboratory (ORNL) [44, 47] and with the β-decay of ^{83}Ga performed at IPN Orsay [48, 49] and at HRIBF [37] (β-decay of ^{83}Ga, $\beta - n$ decay of ^{84}Ga). We studied $\beta - n$ decay of ^{84}Ga in order to populate yet unknown excited states of ^{83}Ge. The knowledge on the low-lying excited state in ^{83}Ge would be extremely valuable in order to perform a correct tuning of the monopole part of the residual interactions used in shell model to help us to understand the nuclear structures beyond $N = 50$.

$N = 51$ **odd-odd** ^{84}**As**

From the β-decay study of $^{80-86}$As isotopes the ground state spin assignment (3^-) was proposed by Kratz *et al.* [50]. The first transitions in arsenic were identified first by Omtvedt *et al.* [51] who studied β-decay of $^{84-85}$Ge isotopes. The level scheme was later updated by Winger *et al.* [52] and Lebois *et al.* [49]. The latest updated level scheme of ^{84}As was presented by Tastet [35]. He confirmed already known γ-transitions at 42.7 keV, 100 keV, 242 keV, 386 keV and 608 keV [49, 51, 52], added two γ-lines, one at 346.5 keV the other at 794 keV, both in coincidence with 242 keV, and made an assignement of low-lying spins.

^{84}As is the most exotic odd-odd $N = 51$ isotone of which a few excitation levels and γ-transitions are identified. This nucleus is very interesting to study in terms of proton-neutron interactions of the two valence particles. We populated the excitation levels in ^{84}As in the subsequent β-decay of ^{84}Ge (originating from the decay of ^{84}Ga).

Structure of thesis

In Chapter 2 a brief description of the current understanding of nuclear structure by means of various nuclear models with an accent on the shell model is described. The reader can find the details of the structure of the shell model effective interactions in Chapter 3 where we also present the result of work on the new shell model interaction $ni78 - jj4b$. Chapter 4 is dedicated to the experimental study of the release properties of different uranium carbide targets. This study was performed at IPN Orsay a priori to the β-decay study described later in this work. The ALTO facility and the experimental approach to study β-decay of ^{84}Ga are described in Chapter 5. The experimental details and the detection system are presented in Chapter 6. In the following Chapter 7 the procedure of data analysis is detailed and the results are

presented. In Chapter 8 the experimental results are compared with the shell model calculations. We discuss the structure of the exotic neutron-rich ^{83,84}Ge. In the last Chapter 9 the conclusions and future perspectives are listed.

.

Nuclear theory

Contents

2.1   Nuclear force

Nuclei are formed by composition of neutrons and positively charged protons. There is a repulsive Coulomb force between protons, therefore, in order for nuclei to exist, one can deduce immediately that there must be a strong attractive interaction that can overcome that repulsion and binds nucleons together. This interaction is called the strong interaction and has following properties [53]:

- At distances larger than 0.7 fm the force becomes attractive between spin-aligned nucleons, becoming maximal at a center-center distance of about 0.9 fm. Beyond this distance the force drops exponentially, until about 2.0 fm (beyond 2 to 2.5 fm Coulomb repulsion becomes the only significant force between protons). At that distance the nuclear force is negligibly feeble.

- At short distances it is stronger than the Coulomb force. Although predominantly attractive, it becomes repulsive at nucleon separation of less than ~ 0.7 fm between their centers. It keeps the nucleons at a certain average separation, even if they are of different types. It is to be understood in terms of the Pauli exclusion force for identical nucleons (such as two neutrons or two protons), and also a Pauli exclusion between quarks of the same type within nucleons, when the nucleons are different (proton and neutron).

- It has a noncentral (a *tensor*) component (which does not conserve the orbital angular momentum).

- It depends on whether the spins of the nucleons are parallel or antiparallel (nucleons as fermions have an intrinsic spin of $1/2\hbar$).

- It is nearly independent of whether the nucleons are neutrons or protons (*charge-independence*). Taking into account the correction for a repulsive Coulomb interaction between charged protons it implies that proton-proton and neutron-neutron interactions must have the same strength.

- There is only one bound state of the deuteron, a system with one proton and one neutron, with the angular momentum $J = 1$ (parallel spins) and the total isospin coupling $T = 0$ suggesting that this proton-neutron interaction is the strongest.

The first nuclear model (called *liquid-drop* model) was first proposed by George Gamow in 1928 [54, 55] and later developed by Niels Bohr and John Wheeler [56, 57]. The liquid-drop model was based on the assumption that a nucleus can be described as an incompressible, charged liquid-drop with volume proportional to the number of nucleons A. According to this model, the nucleons move around at random and bump into each other frequently in the nuclear interior. Their mean free path is substantially less than the nuclear radius. The binding energy that keeps nucleons together is expressed by the semi-emphirical Bethe-Weizsäcker mass formula [58]:

$$B(Z, A) = a_v A - a_s A_{2/3} - a_C Z(Z-1)A^{-1/3} - a_A(A - 2A)^2/A \pm \delta a_p A^{-1/2} \quad (2.1)$$

where is a_v a volume, a_s a surface, a_C Coulomb repulsion, a_A asymmetry and a_p pairing constant (they have following values: $a_v = 15.85$ MeV, $a_s = 18.34$ MeV, $a_C = 0.71$ MeV, $a_A = 23.21$ MeV and $a_p = 12$ MeV). For most nuclei the binding energy is about 8 MeV, however, there are exceptions at certain numbers of protons and neutrons, called *magic numbers* $N/Z = 2, 8, 20, 40, 50, 82, 126$. Although the liquid-drop model permits to correlate many facts about nuclear masses and binding energies it does not give an explanation for the higher value of the nuclear binding energy of magic nuclei.

The importance of the magic numbers can be illustrated with the single-particle separation energy, which is defined as an energy required to remove one proton or neutron from the nucleus. The neutron/proton separation energy for doubly magic nuclei is largest (similarly to electrons in nobel gases) implying that paired neutrons/protons result in larger total binding per nucleon. Another proof of this shell effect can be illustrated by the evolution of the energy of the first excited 2+ states in the even-even nuclei. Figure 2.1 highlights the enormous differences in the energy of the 2+ excited states of magic nuclei in comparison with the non-magic ones. The same trend

is represented by the transition probabilities $B(E2)$ which are correlated with the energy of the first 2+ excited states. The occurrence of the magic numbers, from the experimental point of view, was one of the strongest motivations for the formation of the nuclear shell model.
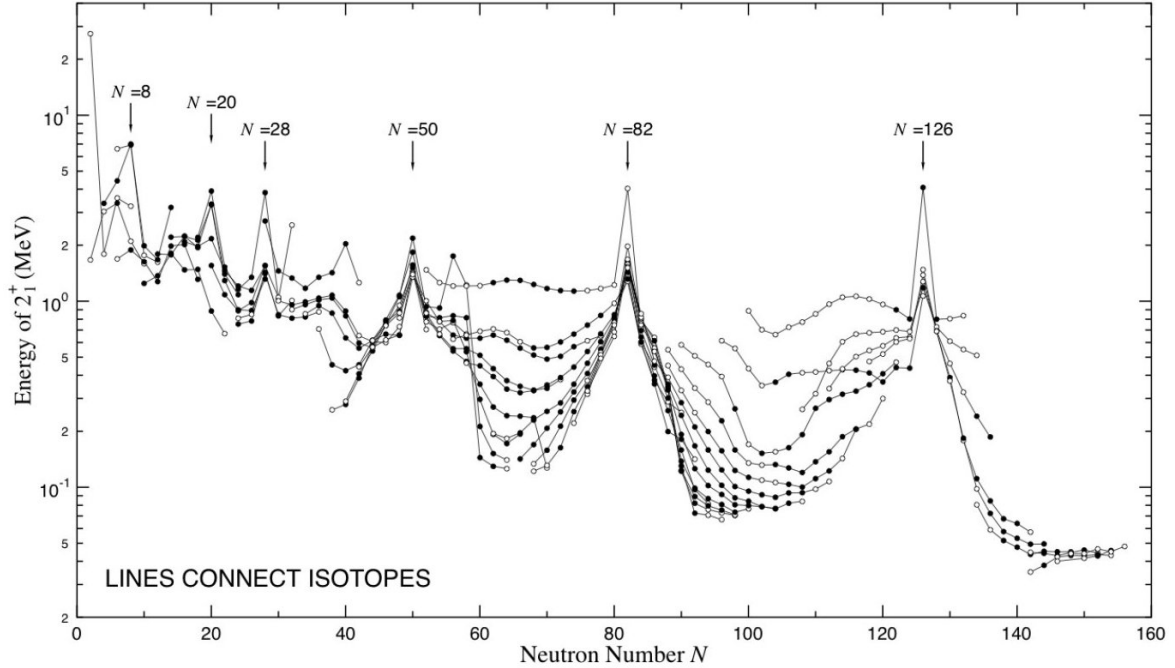
Figure 2.1: The energy of the first 2+ excited state [23].

2.2   Shell model and residual interactions

The nuclear shell model is based on an assumption that nucleons move in orbitals clustered into shells (in analogy with electron shells in atom). The nucleons (proton or neutron) are characterized by their intrinsic spin and isospin. As fermions they are subject to the Pauli principle which excludes two fermions being in the same state at the same time. [53]

2.2.1   Independent particle model

In the simplest approach, the independent particle model, each nucleon is considered as a quasi-independent particle moving in a certain spherically symmetric potential $U(r)$ produced by all the other nucleons. This central potential depends only on the radial distance from the origin to a given point. Then, the angular dependence of a

particle wave function Ψ is independent of the detailed radial behavior of the central potential. The Schrödinger equation for such a potential can be written as:

$$H\Psi = \left(\frac{\mathbf{p}^2}{2m} + U(\mathbf{r})\right)\Psi_{nlm}(\mathbf{r}) = E_{nlm}\Psi_{nlm} \, , \tag{2.2}$$

where $U \to 0$ as $r \to 0$. This equation is separable into radial, $R(r)$, and angular, $Y(\theta\phi)$, part:

$$\Psi_{nlm}(\mathbf{r}) = \Psi_{nlm}(r\theta\phi) = \frac{1}{r}R_{nl}(r)Y_{nl}(\theta\phi) \, . \tag{2.3}$$

Here, n is the radial quantum number, l the orbital angular momentum quantum number and m is the eigenvalue of z-component of the orbital angular momentum, l_z. For a given l, m has the values $l, i-1, l-2, \ldots, 0, -1, -2, \ldots, -(l-1), -l$. Since the nuclear potential is spherically symmetric, l is a good quantum number and each level has a degeneracy of $2(2l+1)$[1]. The number of levels with certain l values is represented by n. There is a centrifugal force associated with each angular momentum L which generates an additional centrifugal part of the nuclear potential:

$$U_{cent} = \int F_{cent}dr = \int \frac{L^2}{mr^3}dr = -\frac{\hbar^2 l(l+1)}{2mr^2} \, . \tag{2.4}$$

Then the radial Schrödinger equation becomes:

$$\frac{\hbar^2}{2m}\frac{d^2 R_{nl}(r)}{dr^2} + \left[E_{nl} - U(r) - \frac{\hbar^2}{2m}\frac{l(l+1)}{r^2}\right]R_{nl}(r) = 0 \, . \tag{2.5}$$

In the first approximation this central potential can be written as a harmonic oscillator potential

$$U(r) = \frac{1}{2}m\omega^2 r^2 \, . \tag{2.6}$$

The eigenvalues are $E_{nl} = (2n + l - \frac{1}{2})\hbar\omega$. The energy levels fall into degenerate multiplets defined by $2n+1$ and a given multiplet contains more than one value of the principle quantum number n and of the orbital angular momentum l. These groupings of degenerate levels appear as a result of the interplay of the harmonic-oscillator and centrifugal potentials. Each energy level has $2(2l+1)$ degenerate m states and, by the Pauli principle, each nl level can contain $2(2l+1)$ particles. The central part of the nuclear potential should have a rather uniform distribution in the interior of the nucleus due to an obvious saturation of the nuclear force. It is possible to otain by adding an attractive term l^2 to the harmonic oscillator potential. The effects of this term increase with the orbital angular momentum of the particle. A stronger attractive interaction between high angular momentum particles lowers their energies.

---

[1] $(2l+1)$ arises from the m degeneracy as there is $(2l+1)$ values of m, the factor of 2 comes from the degeneracy of the intrinsic spin which has two possible values.

Those particles, because of the centrifugal force, spend a larger fraction of their time at larger radii. Therefore, the addition of the l^2 term is equivalent to a more attractive potential at larger radii and comes closer to the desired effect of a more constant interior potential. The consequence of adding the l^2 term to the harmonic oscillator potential on the single particle level is illustrated in the middle panel of Figure 2.2. The degeneracy of the harmonic oscillator levels is broken as high angular momentum levels are brought down in energy.
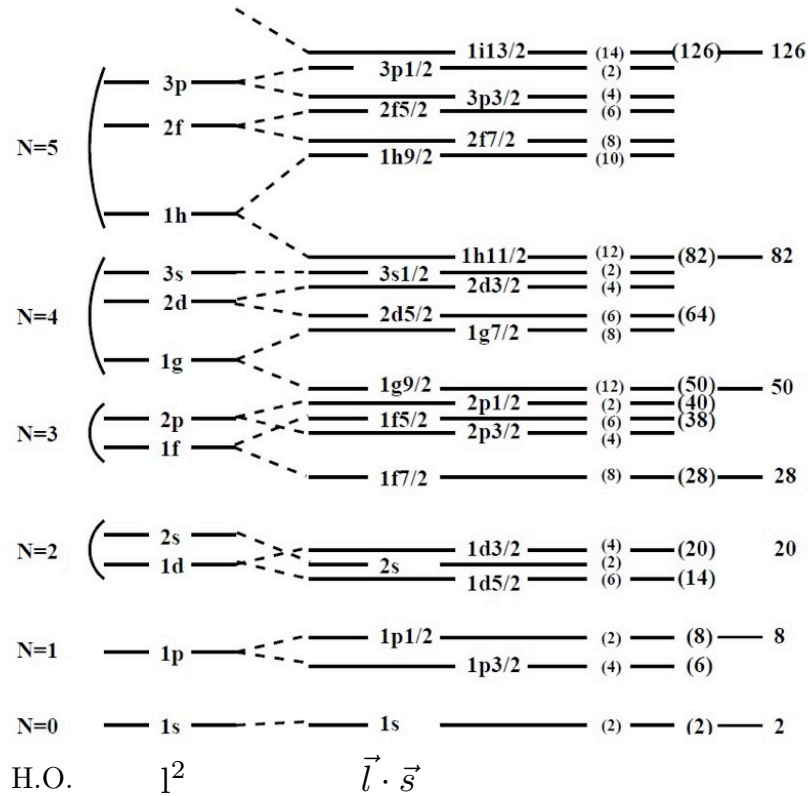
Figure 2.2: The sequence of single-particle energies for the harmonic-oscillator potential, with an additional orbit-orbit l^2 term and with the spin-orbit term [59].

However, it was an empirical modification to the harmonic oscillator potential (an introduction of a spin-orbit interaction term) by Göppert-Mayer [60], and independently, by Haxel [61], Jensen, and Suess, that enabled to reproduce the empirical magic numbers. As protons and neutrons have an intrinsic spin 1/2, the total angular momentum of a nucleon in any orbit is given by the vector coupling of the orbital angular momentum l with a spin angular momentum $s = 1/2$. The force felt by a given particle differs according to whether its spin and orbital angular momenta are aligned parallel or antiparallel. In case of the parallel alignment the spin-orbit terms affects more

higher l values. The spin-orbit term can be written as $U_{\mathbf{l}\cdot\mathbf{s}} = -U_{ls}\frac{1}{r}\frac{\partial U(r)}{\partial r}\mathbf{l}\cdot\mathbf{s}$, where $U(r)$ is a central potential and U_{ls} is a strength constant. Finally, the potential has form:

$$U(r) = \frac{1}{2}m\omega^2 r^2 + C_l \times l^2 - C_{\mathrm{SO}} \times \mathbf{l}\cdot\mathbf{s} \ , \tag{2.7}$$

where C_l and C_{SO} are the angular momentum and spin-orbit coupling constants, respectively. The effects of this potential on the energy splittings are illustrated on the far right in Figure 2.2. The spin-orbit potential can bring down the energy of the $j = l + 1/2$ orbit among the levels of the next lower shell what allows to reproduce the magic numbers. At the same time, it causes that each shell contains a majority of levels of one parity, called normal-parity orbits, and one level of the opposite parity, called unique-parity (intruders) orbits. The unique-parity orbits are situated quite far away from its original multiplets. In case of configuration mixing between different levels, the levels of different parity cannot be mixed (neglecting the very weak parity-nonconserving part of the weak interaction). This is why the unique-parity orbits provide an ideal testing ground for various nuclear models.

For double magic nuclei the sum of all magnetic substates m is coupled to zero, the ground state of any doubly-magic nucleus is always 0^+ (its total wave function is spherically symmetric with no preferred direction in space). In case of nuclei with one particle/hole outside/inside a closed shell, the spin and parity of the ground state is determined by the last filled particle/hole. The independent particle model is however applicable in principle only to nuclei with a single nucleon outside a closed shell. To extend the applicability of the theoretical model one has to refer to nuclei with more than one valence nucleon and that includes residual interactions between these nucleons and allows for the breaking of closed shells.

2.3   Collectivity and deformations

The further from the closed shell and the more valence protons and neutrons are added, the more collective motions appear. It causes a nucleus to collectively vibrate or rotate. Many nuclei, in the midshell, undergo permanent deformations (the quadrupole deformation) even in the ground states. This deviation of the nuclear surface radius from an average value R_0 of the spherical nucleus of the same volume is parameterized by expressing the nuclear radius in the direction $\Omega = (\theta, \phi)$:

$$R = R_0 + \sum_{\lambda=1}^{\infty} \sum_{\mu=-\lambda}^{\lambda} \alpha_{\lambda\mu} Y_{\lambda\mu}(\theta, \phi) \ , \tag{2.8}$$

where $Y_{\lambda\mu}$ are spherical harmonics and α_μ are deformation parameters. The constant term $\lambda = 0$ is incorporated in R_0. The dipole term ($\lambda = 1$), corresponding to a geometrical shift in the center of mass of the nucleus, gives rise to giant dipole resonances from

an oscillation of protons relative to neutrons in the nucleus at considerable energies (8 to 20 MeV). The lowest applicable shape component is the quadrupole deformation ($\lambda = 2$). The corresponding spherical harmonic amplitudes can be expressed in terms of Euler angles and two intrinsic variables α and β:

$$\alpha_{21} = \alpha_{2-1} = 0, \quad \alpha_{20} = \beta \cos \gamma, \quad \alpha_{22} = \alpha_{2-2} = \beta \sin \gamma , \tag{2.9}$$

where β represents the extent of the quadrupole deformation and γ gives the degree of axial asymmetry. The relation between β, γ and the nuclear radius can be seen by representing the quadrupole shape in Cartesian coordinate system with the Z axis chosen as a symmetry axis. Then, $\beta = 0$ represents spherical shape, $\beta > 0$ ($\gamma = 0°$) prolate deformation (an expansion in one and compression in two directions, American baseball) and $\beta < 0$ ($\gamma = 60°, 180°$) oblate deformation (an expansion in two and compression in one directions, a disc), see Figure 2.3. Intermediate values of γ, for instance 30°, correspond to axially asymmetric shapes (in one of the two directions perpendicular to the symmetry axis).

Due to the deformations there is a non-spherical distribution of nuclear matter of the nucleus which leads to a non-sphericity in the distribution of the overall electric charge of the protons. Thus, the deformed nucleus has the electric quadrupole moment [53]:

$$Q_0 = \frac{3}{5\pi} Z R_0^2 \beta (1 + 0.16\beta) , \tag{2.10}$$

where Q_0 is the intrinsic quadrupole moment that would only be observed in the frame of reference in which the nucleus was at rest.

2.3.1 Rotational state in even atomic nuclei

The best known model of fixed asymmetry (triaxiallity) is Davydov and Filippov model [62]. The assignment of nuclear excited state to the so-called γ-vibrations is based on the spin values of these levels and on the large probability of electromagnetic transitions which confirm the collective nature of the levels. Those rotational states do not entail changes of the internal state of the nucleus. The violation of the axial symmetry of the even nuclei only slightly affects the rotational spectrum of the axial nucleus and some new rotational states appear. As the deviations from axial symmetry increase some of those levels become much lower in energy (Figure 2.4). In practical applications of the Davydov model, one can extract the values of γ from the energy ratio $E_{2_2^+}/E_{2_1^+}$. It can be calculated for any γ from the expression:

$$\frac{E_{2_2^+}}{E_{2_1^+}} = \frac{1 + X}{1 - X} , \tag{2.11}$$
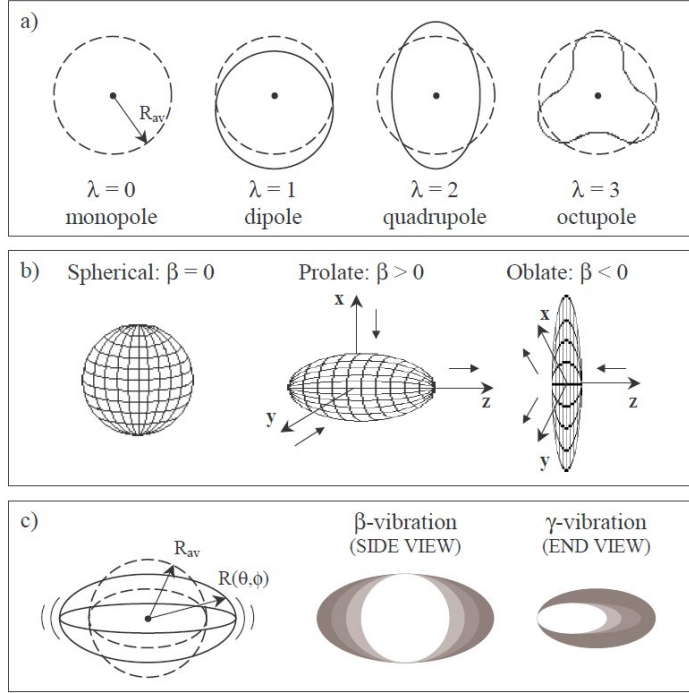
Figure 2.3: a) A potential surfaces for the first four multipole order distortions. b) A schematic illustration of the spherical and the two quadrupole-deformation shapes. c) A scheme of a vibrational motion.

where $X = \sqrt{1 - \frac{8}{9}\sin^2(3\gamma)}$. Thus, $E_{2_2^+}/E_{2_1^+} \to \infty$ for $\gamma \to 0°$ and $E_{2_2^+}/E_{2_1^+} \to 2$ for $\gamma \to 30°$ (as seen in Figure 2.4).

Measurements of the transition probabilities between electric states in nucleus yield important information on the nature of the excited states. One can study the probability of the transition from the second excited 2_2^+ state to the ground state and to the first excited 2_1^+ state. The first 2_1^+ state is referred to as a one-photon state while the second 2_2^+ state is the two-phonon vibration of the nuclear surface. In this case the transition from the second 2_1^+ state to the ground state takes place if the violation of the oscillator approximation occurs. Assuming that one can assign two 2^+ states as the rotational levels, the value of γ can be obtained from the ratio of the transition probabilities [62, 53]

$$\frac{B(E2;\ 2_\gamma^+ \to 2_y^+)}{B(E2;\ 2_\gamma^+ \to 0_y^+)} = \frac{\frac{10}{7}\left(\frac{\sin^2(3\gamma)}{9X^2}\right)}{\frac{1}{2}\left[1 - \frac{3-2\sin^2(3\gamma)}{3X}\right]} \ . \tag{2.12}$$
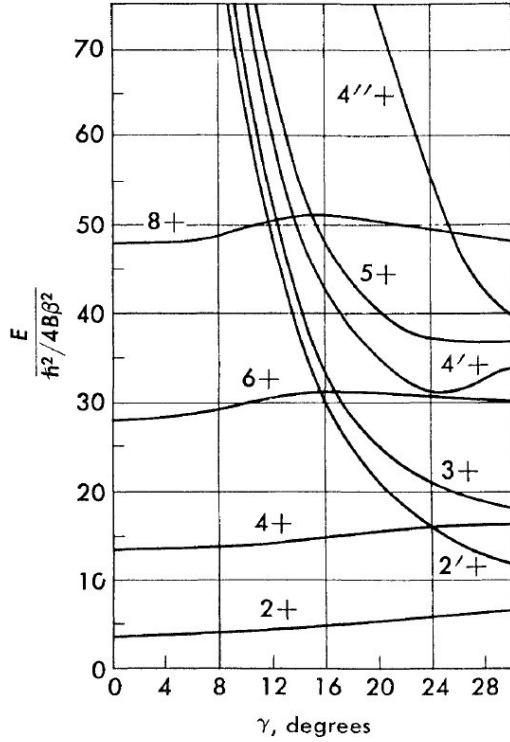
Figure 2.4: Normal and anomalous levels of the triaxial rotor. For $\gamma = 0$ the energy spectrum is identical to that of an axially-symmetric nucleus. The violation of the axial symmetry of the even nuclei leads to the appearance of some new energy levels $(2_2^+, 3_1^+, 4_2^+)$. One can obtain the value of γ from the ratio of energies $E_{2_2^+}/E_{2_1^+}$ [62].

The rotational energy of the nuclei or the transition probability between rotational states do not give us the information whether the nucleus is an elongated or oblate ellipsoid. This information can be obtained from the electric moments in stationary states $(J, M = J)$, the so-called spectroscopic quadrupole moments:

$$Q_{spec} = Q_0 \left(\frac{3K^2 - J(J+1)}{(J+1)(2J+3)} \right) \ , \tag{2.13}$$

here Q_0 represents the intrinsic quadrupole moment. K is the projection of the total angular momentum J along the z axis (symmetry axis). The most common distortion of spherical nuclei is quadrupole in nature. Therefore, the most common low-lying vibrational excitations in deformed nuclei are quadrupole vibrations. They carry two units of angular momentum and can be of two types with $K = 0$ and $K = 2$. The former are known as β vibrations, when $K = 0$ the vibration is aligned along the symmetry axis and therefore preserves axial symmetry. The latter, with $K = 2$, is called γ vibration and represents a dynamic time dependent excursion from axial symmetry. In even nuclei the mean values of the spectroscopic quadrupole moment in the ground state are equal to zero. A state of zero angular momentum can have no preferred direction of the time averaged distribution in space and therefore no quadrupole moment. In the first and the second excited state of spin 2 the mean value of the quadrupole moment has an opposite sign

$$Q_{spec_{2_2}} = -Q_{spec_{2_1}} \ . \tag{2.14}$$

2.3.2 $4_1^+/2_1^+$ ratio

The ratio of $4_1^+/2_1^+$ energies (Figure 2.5) can bring some structural signatures and its absolute value is directly meaningful, especially in the region of heavy nuclei. The ratio can be devided into three parts: below 2.0 near magic nuclei, between 2.0 and 2.4 slightly further away from magic numbers and values very close to 3.33 in midshell regions corresponding to rotational motion.
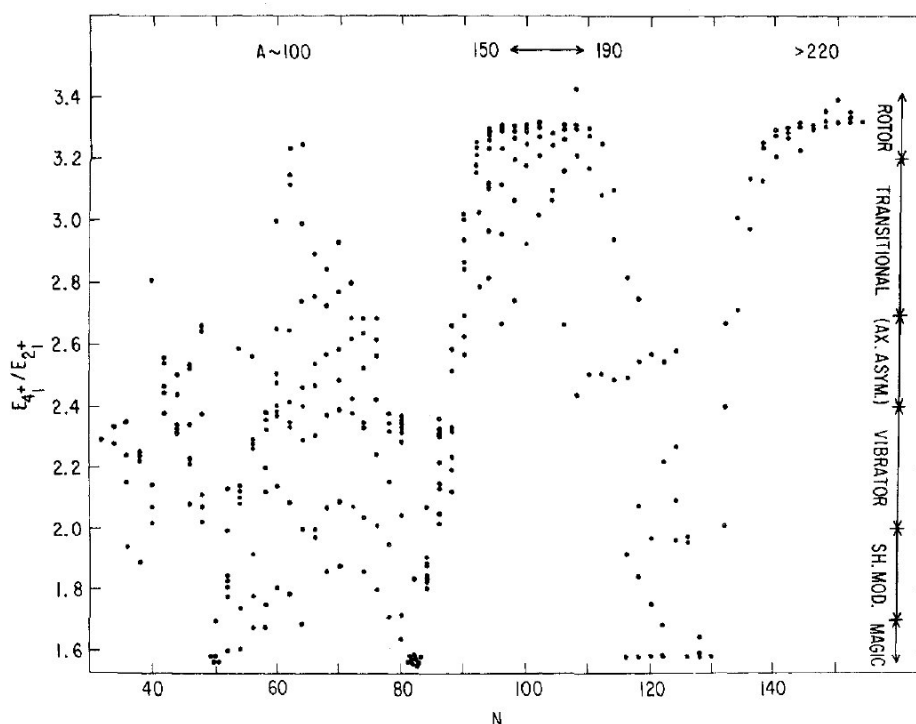
Figure 2.5: The ratios of 4_1^+ to 2_1^+ energies against N for the nuclei with $N \leq 180$. [53]

2.4 Reduced transition probabilities

In the β-decay of nuclei, a given initial nuclear state $^AX_{Z_i}$ is converted into the ground state or an excited state of the final nucleus $^AX_{Z_f}$, where $Z_f = Z_i + 1$. The transition rate for nuclear beta decay is determined by the Q_β value (or energy release) and the structure of the initial and final nuclear states. Beta decays with the fastest rates occur when the leptons carry away $l = 0$ angular momentum and are referred to as *allowed* transitions. Decays with $l > 0$ are referred to as *forbidden* transitions. After the β-decay the final nucleus in an excited state can emit part or all of its excitation energy by electromagnetic radiation. These electromagnetic transitions are classified in terms

of multipole orders of electric and magnetic fields. The electromagnetic transition between them can take place only if the emitted γ-ray carries away an amount of angular momentum $\vec{l}$ such that $\vec{J_f} = \vec{J_i} + \vec{l}$ which means that $|J_i - J_f| \le l \le J_i + J_f$ where $J = \vec{J}$. Since the photon has an intrinsic spin of one, transitions with $l = 0$ are forbidden, and hence gamma transitions with $J_i = 0 \to J_f = 0$ are not allowed. A specific l value determines the multipolarity of the gamma radiation: $l = 1$ is called dipole, $l = 2$ is called quadrupole, *etc.*. In addition, when states can be labeled with a defined parity $\pi_i = \pm 1$ and $\pi_f = \pm 1$, the transitions between them are restricted to the *electric* type of radiation when $\pi_i \pi_f (-1)^l$ is even and the *magnetic* type of radiation when $\pi_i \pi_f (-1)^l$ is odd. The lowest allowed multipolarity in the decay rate dominates over the next higher one (when more than one is allowed) by several orders of magnitude. The most common types of transitions are electric dipole ($E1$), magnetic dipole ($M1$), and electric quadrupole ($E2$). Electromagnetic transition rates provide one of the most unambiguous tests for models of nuclear structure. The interaction of the electromagnetic field with the nucleons can be expressed in terms of a sum of electric, $\mathcal{O}(E\lambda)$, and magnetic, $\mathcal{O}(M\lambda)$, multipole operators with tensor rank λ [63]:

$$\mathcal{O} = \sum_{\lambda\mu} [\mathcal{O}(E\lambda)_\mu + \mathcal{O}(M\lambda)_\mu] \tag{2.15}$$

For a given E or M operator of rank λ the electromagnetic transition rate $W_{M_i,M_f,\mu}$ (the probability for absorption or emission of a photon by a nucleus) can be expressed in terms of the matrix elements of the corresponding multipole operator as

$$W_{M_i,M_f,\mu} = \left(\frac{8\pi(\lambda + 1)}{\lambda[(2\lambda + 1)!!]^2} \right) \left(\frac{k^{2\lambda+1}}{\hbar} \right) |\langle J_f M_f | \mathcal{O}(\lambda)_\mu | J_i M_i \rangle|^2 \ , \tag{2.16}$$

where k is the wave-number for the electromagnetic transition of energy E_γ given by $k = E_\gamma/\hbar c = E_\gamma/(197 \text{ MeVfm})$. The total rate for a specific set of states and a given operator is obtained by averaging over the M_i states and summing over M_f and μ:

$$W_{i,f,\lambda} = \frac{1}{(2J_i + 1)} \sum_{M_i,M_f,\mu} W_{M_i,M_f,\mu} = \left(\frac{8\pi(\lambda + 1)}{\lambda[(2\lambda + 1)!!]^2} \right) \left(\frac{k^{2\lambda+1}}{\hbar} \right) \frac{|\langle J_f || \mathcal{O}(\lambda) || J_i \rangle|^2}{(2J_i + 1)} \ . \tag{2.17}$$

The last factor in this equation is referred to as a *reduced transition probability* B:

$$B = \frac{|\langle J_f || \mathcal{O}(\lambda) || J_i \rangle|^2}{(2J_i + 1)} \ . \tag{2.18}$$

It depends upon the direction of the transition. For electromagnetic transitions the initial state is the higher-energy state. But in Coulomb excitation the initial state is the lower-energy state (let us denote it J_a) while the final state is the higher-energy state (J_b). From the transition from lower to higher state one often uses the notation

$B(\uparrow)$. Then the value used for the electromagnetic transitions is $B(b \to a) = (2J_a + 1)/(2J_b + 1) B(\uparrow a \to b)$. As an example, in case of an $E2$ transition between ground state 0_{gs}^+ and the first excited state 2_1^+ , one obtains $B(0_{gs}^+ \to 2_1^+) = 5 \cdot B(\uparrow 2_1^+ \to 0_{gs}^+)$. Often not only one transition from the initial to the final state is possible and we need to consider mixed transitions of the form ($E1$ and $M1$) or ($M1$ and $E2$), etc.. Each transition is characterized by its partial mean lifetime ($\tau_{M\lambda}$, $\tau_{E\lambda}$). The relation between the mean lifetime of the transition and the reduced transition probability for the first two orders of magnetic transitions can be expressed as:

$$B(M1) = \frac{56.8}{E_\gamma^3 \tau_{M1}} \mu_N^2 \ \mathrm{MeV}^3 \, \mathrm{fs} \ , \tag{2.19}$$

$$B(M2) = \frac{74.1}{E_\gamma^5 \tau_{M2}} \mu_N^2 \ \mathrm{fm}^2 \, \mathrm{MeV}^5 \, \mathrm{ns} \ . \tag{2.20}$$

The values of the magnetic matrix elements are usually taken to be in units $\mu_N \ \mathrm{fm}^{\lambda-1}$, where $\mu_N = e\hbar/(2m_p c) = 0.105 \, \mathrm{e \, fm}$ is the nuclear magneton and m_p is the mass of the proton. For the electric transitions:

$$B(E1) = \frac{0.629}{E_\gamma^3 \tau_{E1}} e^2 \ \mathrm{fm}^2 \, \mathrm{MeV}^3 \, \mathrm{fs} \ , \tag{2.21}$$

$$B(E2) = \frac{816}{E_\gamma^5 \tau_{E2}} e^2 \ \mathrm{fm}^4 \, \mathrm{MeV}^5 \, \mathrm{ps} \ . \tag{2.22}$$

A mean lifetime corresponds to the transition probability of the decaying state, the relation is given by $\tau_{\omega\lambda} = 1/P_{i \to f}$ where ($\omega = M$ or E) [64]. The partial γ-ray transition probability $P_{i \to f}$ can be obtained from

$$P_{i \to f} = \frac{\displaystyle\sum_{\omega,\lambda} \frac{1}{\tau_{i \to f_{\omega\lambda}}}}{\displaystyle\sum_{\omega,\lambda,l} \frac{1}{\tau_{i \to l_{\omega\lambda}}}} \ , \tag{2.23}$$

which is the sum of the inverse of the mean lifetime from the initial level, i, to the final level, f (summing over all possible transitions $\omega\lambda$), divided by the sum over all possible γ transitions from the same initial level to all possible final levels, l (with all possible $\omega\lambda$ transitions).

Modern Shell Model Approach

Contents

3.1 Nuclear Shell Model

The basic assumption of the nuclear shell model is that to a first approximation each nucleon moves independently in a potential that represents the average interaction with the other nucleons in a nucleus. This independent motion can be understood qualitatively from a combination of the weakness of the long-range nuclear attraction and the Pauli exclusion principle [65]. The Hamiltonian for a system of A nucleons can be written as

$$H = T + V = \sum_{i=1}^{A} \frac{\mathbf{p}_i^2}{2m_i} + \sum_{k>i=1}^{A} V(i,k) + \sum_{j>k>i=1}^{A} V(i,k,j) \,, \tag{3.1}$$

where i denotes all the relevant coordinates $\vec{r}_i, \vec{s}_i, \vec{t}_i$ for a given particle ($i = 1, 2, 3....A$). It contains nucleon kinetic energy, a nucleon-nucleon potential generated through the interaction between the $i - th$ and $k - th$ nucleons $V(i,k)$ and the three-body force $V(i,k,j)$. The potential consists of a repulsive core and a strongly attractive part. This simplification is an assumption from the Pauli exclusion principle as the mean free path of a nucleon is large compared to the nucleus size, the probability of interaction between three nucleons is to be neglected (the consequence of this neglect will be discussed later). The nucleon-nucleon potentials can be transformed altogether into a total nuclear potential with a dominant spherically-symmetric part by adding and subtracting a one-body potential $\sum_{i=1}^{A} = U(r_i)$ (e.g., the harmonic oscillator potential, the Woods-Saxon potential or the square-well), which is experienced by all A nucleons

and which approximates the combined effects of all $A(A-1)/2$ two-body interactions:

$$H = \sum_{i=1}^{A} \left[\frac{\mathbf{p}_i^2}{2m_i} + U(\mathbf{r}_i) \right] + \left[\sum_{i>k=1}^{A} V(i,k) - \sum_{i=1}^{A} U(\mathbf{r}_i) \right] = H_0 + H_{residual} . \qquad (3.2)$$

Here, the H_0 Hamiltonian describes the system of nearly independent A nucleons orbiting in a spherically-symmetric mean field potential $U_i(r)$, while $H_{residual}$ is a small perturbation term describing the residual interactions between nucleons. Solving the Schrödinger equation only with the H_0 Hamiltonian gives the eigenfunctions without residual interaction and the eigenenergies are determined by the sum of the energies of individual states of nucleons. It does not describe well the nuclei further from the closed shell. Therefore, it is necessary to consider the residual interaction $H_{residual}$ which introduces configuration mixing and collective effects such as vibration and deformations of the nuclei.

The most fundamental two-nucleon interaction to be exploited in the many-body calculations can be derived from a bare NN potential for free nucleons in a vacuum taking into account in-medium effects, the Pauli principle and truncated model space (called *an effective interaction*). In the shell model approach it is necessary to determine for each mass region the effective interaction that can reproduce many properties of the corresponding nuclei. Starting from the Hilbert space, the problem is simplified to the sub-space and the corresponding effective interaction and effective operators. This sub-space contains a reduced number of "basic states" $\Psi_i^{(0)}$. Effective wave function can be written:

$$\Psi_{eff} = \sum_{i \in M} a_i \Psi_i^{(0)} . \qquad (3.3)$$

Using the effective interaction V_{eff} one can solve the Schrödinger equation for a model wave function and obtain realistic energies E. In the Hilbert space the Schrödinger equation becomes equivalent to the one in the sub-space using an effective force:

$$H\Psi = E\Psi \Rightarrow H_{eff}\Psi_{eff} = (H_0 + V_{eff})\Psi_{eff} = E_{eff}\Psi_{eff} . \qquad (3.4)$$

The traditional way to get the effective shell-model interaction was via calculation of the so-called G-matrix and then computation of the effective interaction between two nucleons in the valence space [65]. This nucleon-nucleon interaction in the atomic medium is calculated starting from the known interaction between two free nucleons. Using this microscopic description of the nuclei one faces certain problems, for instance, the complexity of the numerical calculation for N body problem and the repulsive part of nucleon-nucleon interaction at short distances. The G-matrix of Brückner allows to eliminate the repulsive part at the short distances and describes the diffusion of two free nucleons in the nuclear matter. By definition, it gives a transition amplitude for the two nucleon states which propagate independently in the nuclei before and after

collision. The elements of this matrix are defined as state of two independent nucleons inside the nuclei and represent the effective interaction for nucleons in independent states. A huge problem of this realistic interaction is that it has spectroscopic behavior that degrades as the number of particles in the valence space increases. A modern alternative to the G-matrix is a low-momentum interaction V_{low-k}. Since the efficient low energy degrees of freedom for nuclear structure are not quarks and gluons, but the colorless hadrons of traditional nuclear phenomenology in the low-momentum interaction V_{low-k}, the high-momentum component of the bare NN-interaction is integrated out down to a given cut-off momentum within the renormalization group approach [66]. Shell-model applications were one of the main motivations for developing the low-momentum interactions [67, 68]. Up to now, either microscopic interaction based on the G-matrix, or on V_{low-k}, derived from two-nucleon potential, leads to a reasonable description of nuclei with two or a few valence nucleons beyond a closed shell core in a one-oscillator shell valence space. As soon as the number of valence particles (holes) increases, the agreement with experimental data deteriorates. The plausible reason is the absence of many-body forces, in particular, the lack of a three-body force.

In spite of the progress in recent years, the three-nucleon potentials are still under developement and effective interactions with the three-nucleon forces are not yet available. The Shell Model practitioners account for the missing three-body forces in an empirical manner, i.e. by the adjustement of the effective interaction (based no a realistic NN one) to the experimental data (energy levels). The two-body matrix elements (TBME) of such interaction are obtained either by the monopole corrections[69, 70, 71] (see the next paragraph for more details) or by least square fit [72, 73] of all TBME by minimizing the deviations between SM and experimental energies for nuclei of interest. The latter procedure gives the more accurate results, however, the link with the underlying theory becomes difficult to establish.

3.1.1 Structure of the effective interaction

Dufour and Zuker [74] demonstrated that any effective interaction H_{eff} can be written:

$$H_{eff} = H_{monopole} + H_{Multipole} = H_m + H_M \ . \tag{3.5}$$

This effective Hamiltonian is split into two parts:

- $H_{monopole}$ contains all the terms affected by a spherical Hartree-Fock variation, hence, is responsible for global saturation properties and evolution of the spherical single particle field,

- $H_{Multipole}$ is responsible for correlations beyond the mean field (in the valence space) such as, for instance, pairing, quadrupole and octupole terms.

H_M contains two-body terms which cancel for doubly magic nuclei and for closed shell plus one particle/hole nuclei. The monopole Hamiltonian H_m represents a spherical mean field and is responsible for global saturation properties and spherical single particle energies. This important property can be written as:

$$\langle CS \pm 1|H_{eff}|CS \pm 1\rangle = \langle CS \pm 1|H_m|CS \pm 1\rangle . \tag{3.6}$$

where CS is a closed shell. The single-particle states in this average potential are called effective single particle energies (ESPE's). They can be defined as a nucleon separation energy for an unoccupied orbital or the extra energy necessary to extract a nucleon from a fully occupied orbital (taken with an opposite sign). In the particle-particle formalism it can be written

$$V = \sum_{JT} = V_{ijkl}^{JT}[(a_i^+ a_j^+)^{JT}(\tilde{a}_k \tilde{a}_l)^{JT}]^{00} . \tag{3.7}$$

One can express the number of particles operators $n_i = a_i^+ a_i \propto (a_i^+ \tilde{a}_i)^0$ and write this two-body potential in particle-hole recoupling:

$$V = \sum_{\lambda\tau} = \omega_{ijkl}^{\lambda\tau}[(a_i^+ \tilde{a}_k)^{\lambda\tau}(a_j^+ \tilde{a}_l)^{\lambda\tau}]^{00} , \tag{3.8}$$

where

$$\omega_{ijkl}^{\lambda\tau} \propto \sum_{JT} V_{ijkl}^{JT} \begin{Bmatrix} i & k & \lambda \\ j & l & \lambda \\ J & J & 0 \end{Bmatrix} \begin{Bmatrix} \frac{1}{2} & \frac{1}{2} & \tau \\ \frac{1}{2} & \frac{1}{2} & \tau \\ T & T & 0 \end{Bmatrix} . \tag{3.9}$$

where index represents total angular momentum of particle, $H_{monopole}$ corresponds only to the terms $\lambda\tau = 00$ and 01 ($H_{Multipole}$ corresponds to all other combinations of $\lambda\tau$) which implies that $i = j$ and $k = l$. Using a Racah transformation $H_{monopole}$ can be written as:

$$H_m = E_0 + \varepsilon_i \sum_i n_i + \sum_{i \leq j} V_{ij} \frac{n_i(n_j - \delta_{ij})}{1 + \delta_{ij}} , \tag{3.10}$$

where

$$V_{ij} = \frac{\sum_{JT}(2J+1)(2T+1)V_{ijij}^{JT}}{\sum_{JT}(2J+1)(2T+1)} . \tag{3.11}$$

It is important to note that nuclei with one particle or one hole beyond the closed shell core are the best examples to check the monopole field, since in these cases other particle-particle correlations are often negligible and one can associate single-particle centroids with the eigenstates of the monopole Hamiltonian.

The multipole part H_M of the shell-model Hamiltonian can be defined as the total Hamiltonian minus its monopole part. It contains basically all multipoles of the two-body interaction: isoscalar and isovector pairing, quadrupole-quadrupole interaction, hexadecapole-hexadecapole term, spin-flip term and others [74]. This term is universal for all realistic NN interactions.

3.1.2 The ANTOINE code

The shell model code ANTOINE [75, 76] was used to perform calculations in the framework of this thesis. The coupling scheme in the shell model calculations in ANTOINE code is a $m - scheme$ which means that the basis is formed by all the Slater determinants contained in the valence space. In order to obtain the relevant eigenvalues and eigenvectors the Lanczos method is used. Starting from initial pivot (starting vector) with a given (good) J by repeated action of the Hamiltonian H on this basic state, the final tridiagonal matrix is created. The Lanczos iteration process has variational properties and the convergence for the lowest (and highest) eigenvalues is very efficient [76].

The valence space

The individual space is divided into three parts:

- inert core, the orbits that are always full (the core nucleus),

- valence space, the orbits available to the valence particles, those orbits will be populated according to the effective interaction,

- external space, the orbits above the valence space, not involved in the calculations, that remain always empty.

It is the task of the theory to find the valence spaces that contain the relevant degrees of freedom for a given problem as demanded by the effective interaction. The definition of the core and the valence space is usually defined by the natural boundaries formed by the gaps between shells associated with magic numbers. For isotopes with $Z \geq 28$ and $N \geq 50$ (considered in this thesis) the inert core could be ^{78}Ni considered as a doubly magic nucleus. Thus, the proton valence space includes orbitals $2p_{3/2}, 1f_{5/2}, 2_{p1/2}$ and $1g_{9/2}$. For neutrons, the valence space consists of orbitals $1g_{7/2}, 2d_{5/2}, 2d_{3/2}, 3s_{1/2}, 1h_{11/2}$ (Figure 3.1).
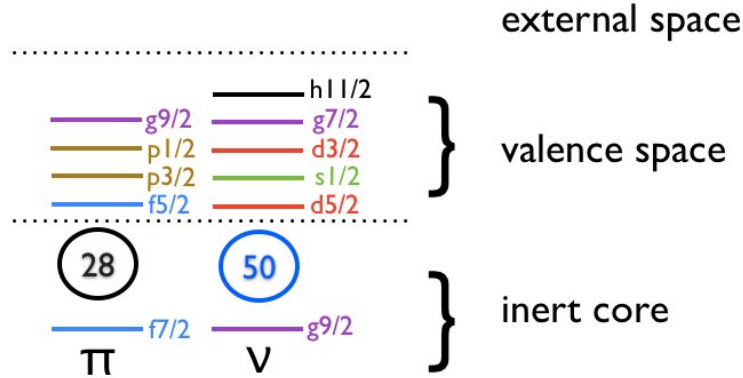
Figure 3.1: Schematic view of the ^{78}Ni core with $N = 50$, $Z = 28$ and the valence orbitals.

3.2 New effective interaction

The emerging shell-model effective interactions can provide us the microscopic description of the structure of the neutron-rich nuclei in the vicinity of the very exotic ^{78}Ni. Although still more experimental information is needed, the first attempts have been already made to create the effective interactions that could describe this region, e.g., the $ni78 - lis$ interaction of Sieja [2]. This interaction (with the ^{78}Ni as an inert core and the proton valence space: $2p_{3/2}, 1f_{5/2}, 2p1/2$ and $1g_{9/2}$, and for neutrons: $1g_{7/2}, 2d_{5/2}, 2d_{3/2}, 3s_{1/2}, 1h_{11/2}$) reproduces very well the low-lying spectra of zirconium isotopes ($Z = 40$) with neutron numbers from $N = 50$ to $N = 58$. However, there are some discrepancies in the energies and spins for the ground and the excited states of $N = 50$ isotones (Figure 3.6). As for the even-even nuclei: 2^+ excited state in ^{84}Se and 0_2^+ in ^{86}Kr are too low, additionally, the 4^+ excited state in ^{82}Ge is too high. In case of even-odd isotopes: spin of the ground state of ^{83}As is $3/2^-$ while the experimental one is $5/2^-$ [77] and the $9/2^-$ state in ^{81}Ga is too high. Those differences come from the proton-proton part of the $ni78 - lis$ interaction and could be ameliorated.

The calculations for the $N = 50$ isotones were also made with another available interaction, $jj4b$ [78], with ^{56}Ni as an inert core and the $2p_{3/2}, 1f_{5/2}, 2p1/2$ and $1g_{9/2}$ as a valence space for protons and neutrons. The $jj4b$ interaction reproduces well the nuclear spectra in this valence space. For $N = 50$ (Figure 3.6) one obtains the energy of the 2^+ state in ^{80}Zn and ^{84}Se very close to the experimental value, a good agreement for 0_2^+, 2_2^+ and 4^+ excited energies for ^{82}Ge, and correct ($5/2^-$) spin of the ground state of ^{83}As. There are no big discrepancies in the spectra for the other $N = 50$ isotones (except 0_2^+ excited state in ^{84}Se) and the proton part of this interaction looks reliable.

Therefore, we decided to try to build a new interaction that could be used for the calculations for this neutron-rich region based on the two interactions introduced above. We replaced the proton-proton part on the $ni78 - lis$ interaction by the one from $jj4b$. The $jj4b$ interaction has a core of ^{56}Ni so the matrix elements were scaled to the core of ^{78}Ni. In the next step it was necessary to adjust the proton-neutron monopoles to obtain good values of the effective single particle energies of $N = 51$ isotones (we account for the "missing" three-body forces). The results on the effectove signle particle energies normalized to the $2d_{5/2}$ orbital are presented in Figure 3.2. As can we seen on the left side of the figure, the ESPE of $3s_{1/2}$ orbital was below $2d_{5/2}$ for ^{89}Sr. As a result, in the calculated spectra for $N = 51$ even-odd isotones for $Z = 28 - 38$ the first $1/2^+$ states were reproduced too low. To find out what are the monopoles that should be corrected I checked the wave function of, at first, ^{89}Sr. In ^{89}Sr in case of the ground state configuration there are two protons in the highest $p_{1/2}$ orbital and one neutron in the $2d_{5/2}$ orbital, Figure 3.3 (resulting in $5/2^+$ ground state spin parity). In case of the first excited state $1/2^+$ the single neutron is located in the $3s_{1/2}$ orbital. Repulsion added to both of those monopoles ($\pi\, p_{1/2} \otimes \nu\, d_{5/2}$ and $\pi\, p_{1/2} \otimes \nu\, s_{1/2}$) improved the energy spectra but only for higher $Z = 38$ element. In order to improve the lower Z, I took another element into consideration ^{87}Kr. In case of ^{87}Kr the thighest proton orbit occupied was $p_{3/2}$, thus the proton-neutron monopole change for $\pi\, p_{3/2} \otimes \nu\, s_{1/2}$ was done. In total, I added a repulsion to three monopoles : $V_{2p_{3/2}-3s_{1/2}}$, $V_{2p_{1/2}-3s_{1/2}}$ and $V_{2p_{1/2}-2d_{5/2}}$ (300 keV, 100 keV and 200 keV, respectively) to obtain satisfactory agreement with experimental spectra. The final ESPE of the new interaction $ni78 - jj4b$ with corrected position of the $s_{1/2}$ neutron orbital are plotted on the right in (Figure 3.2).
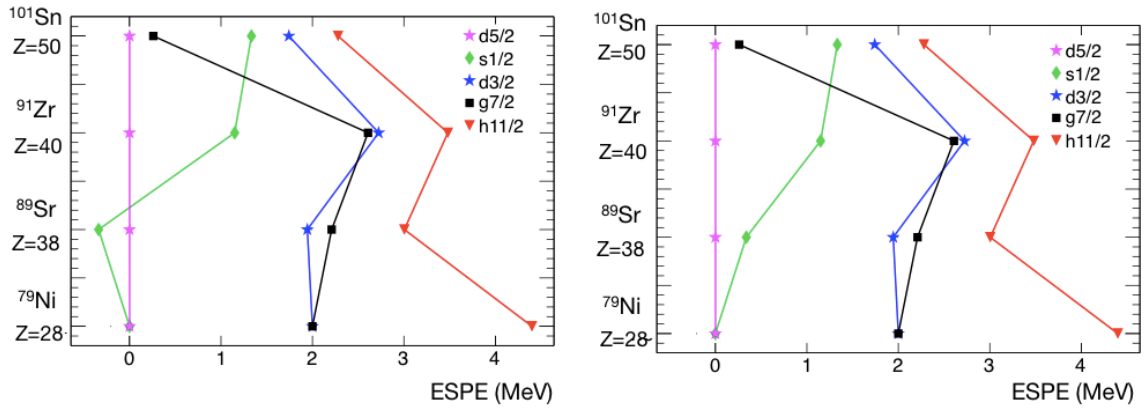
Figure 3.2: Calculated evolution of the $N = 51$ neutron effective single-particle energies between ^{79}Ni and ^{101}Sn. Left: before the monopole changes, right: after the monopole changes.
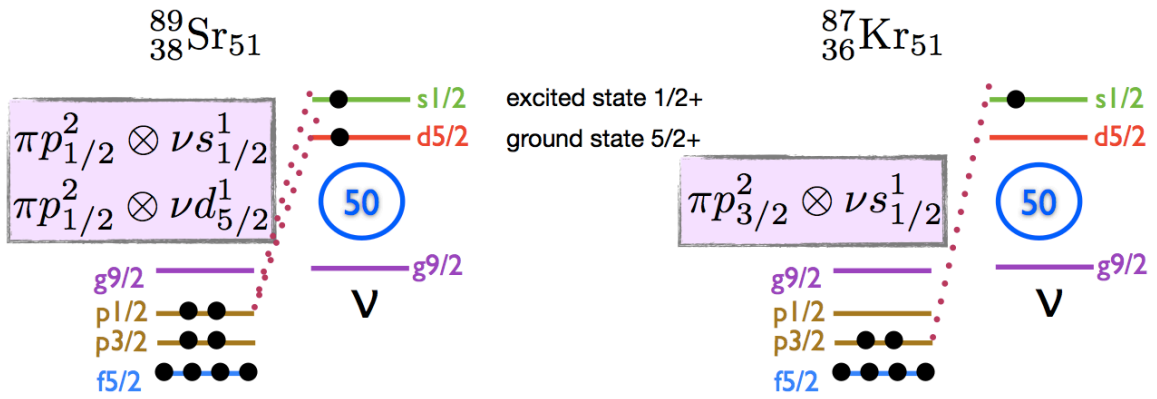
Figure 3.3: Schematic view of the wave function composition and the monopoles responsible for the ground state in ^{89}Sr and the first excited states in ^{87}Kr and ^{89}Sr.

Figure 3.4: Experimental $E(2+)$ (in black) compared to the shell model calculations made with the $ni78 - jj4b$ interaction (in red) and $ni78 - lis$ interaction (in blue).
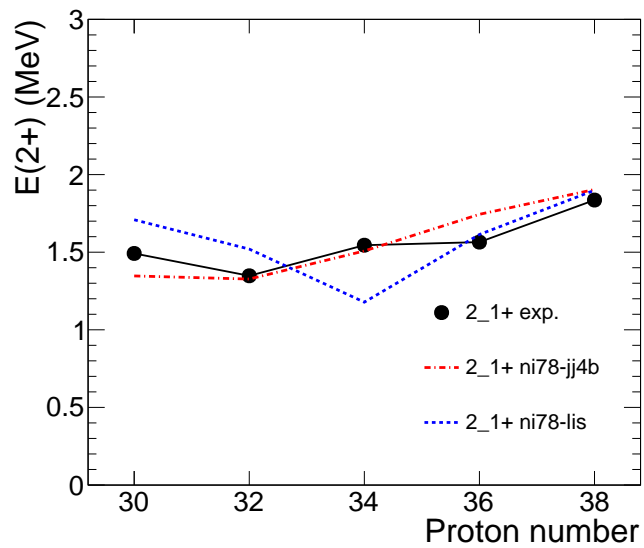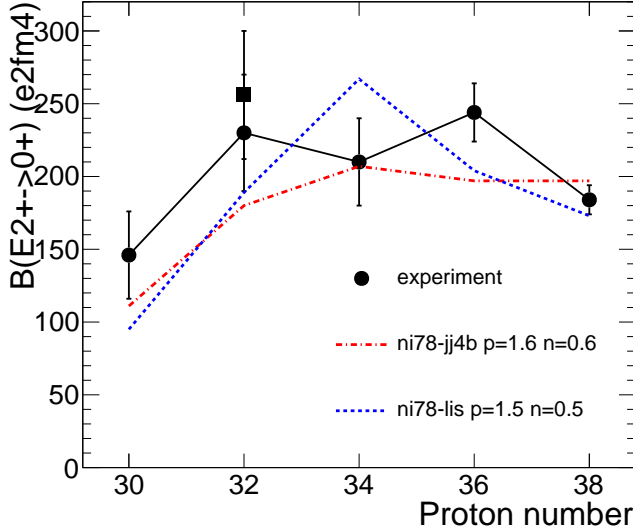
Figure 3.5: The $B(E2; 2+ \rightarrow 0+)$ values in the $N = 50$ isotonic chain compared to the shell model calculations made with the $ni78 - jj4b$ interaction in red and $ni78 - lis$ interaction in blue. To reproduce the experimental results the effective charge of protons in the $ni78 - jj4b$ interaction was set to 1.6.

The spectra for $N = 50$ isotones are presented in Figure 3.4 and Figure 3.6. As expected the spectra obtained with the $ni78 - jj4b$ interaction does not differ a lot from those with the $jj4b$ interaction (as they have the same proton part). The differences come only from the density dependence which is present in the $jj4b$ interaction but not in $ni78 - jj4b$. The new $ni78 - jj4b$ interaction reproduced well the low lying spectra of $N = 50$ even-even and even-odd systematics. It gives also satisfactory results for $N = 52$ isotonic chain (Figure 3.8). It reproduces well the ground state spins and parities for $N = 50, 52$ isotones as well as the low-lying excited states. The performance of the new interaction was also tested with the reduced transition probabilities for $N = 50$ isotonic chain (Figure 3.5). To reproduce well the $B(E2)$ values the effective charges for proton and neutron were set to $\pi_e = 1.6$ $\pi_\nu = 0.6$. Through those effective charges one accounts for the effect of core polarization so the contribution of the protons and neutrons from the core to the excitations of valence quasi-particles.

To conclude, we consider the $ni78 - jj4b$ interaction as a good interaction which will be used in the proceeding chapters to describe the low-lying states in energy spectra of our nuclei of interest.
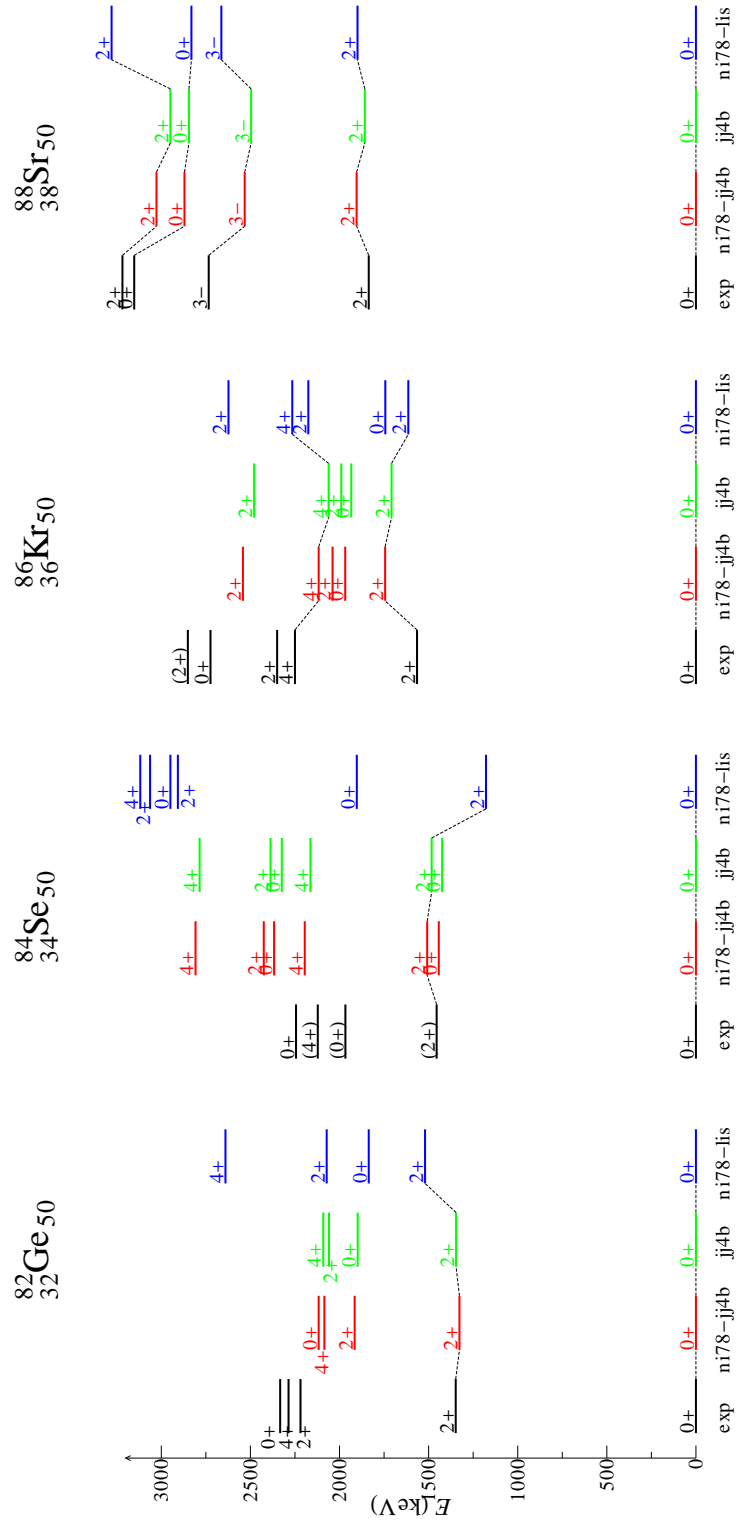
Figure 3.6: The experimental and calculated energy spectra for even-even N=50 isotones.
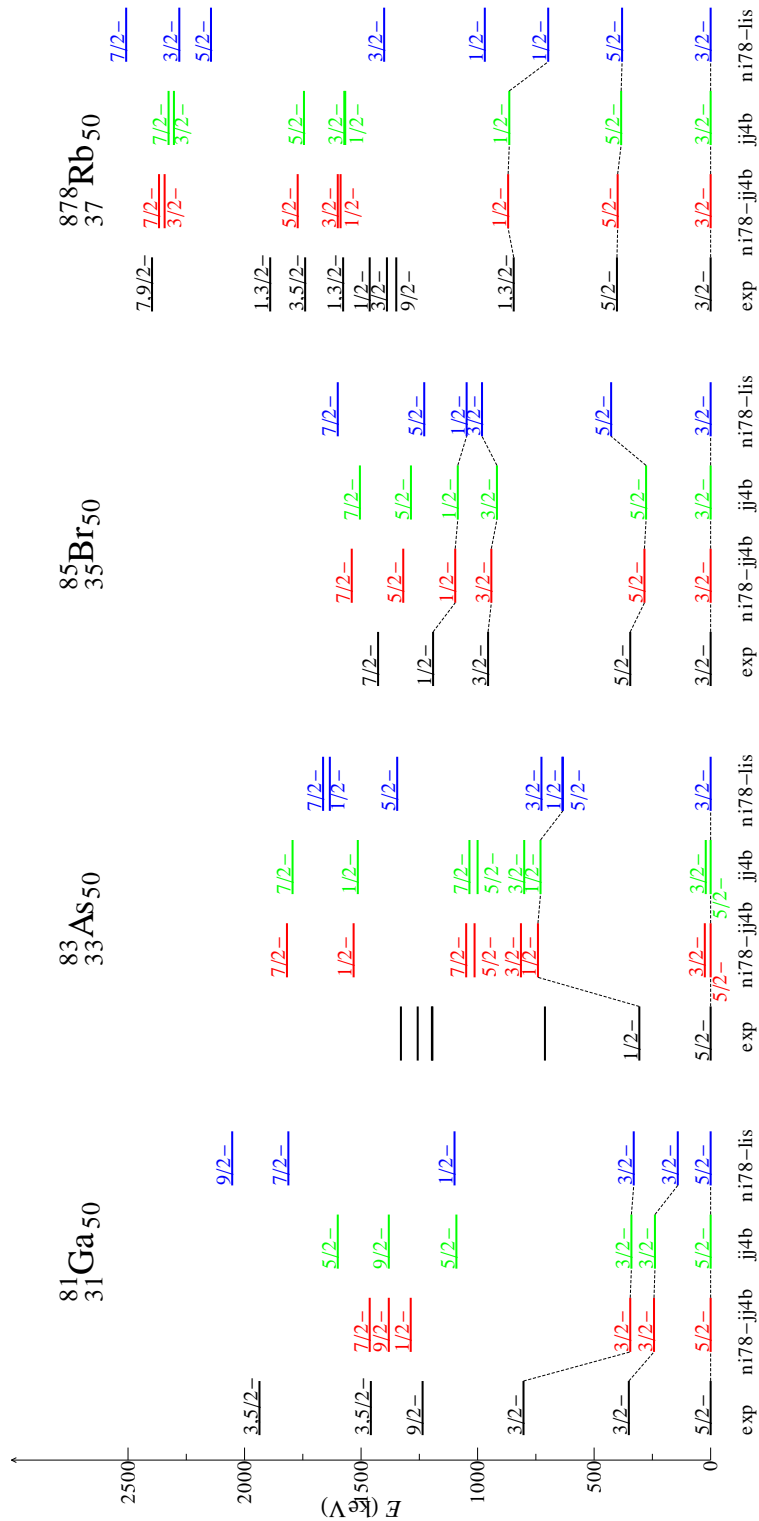
Figure 3.7: The experimental and calculated energy spectra for even-odd N=50 isotones.
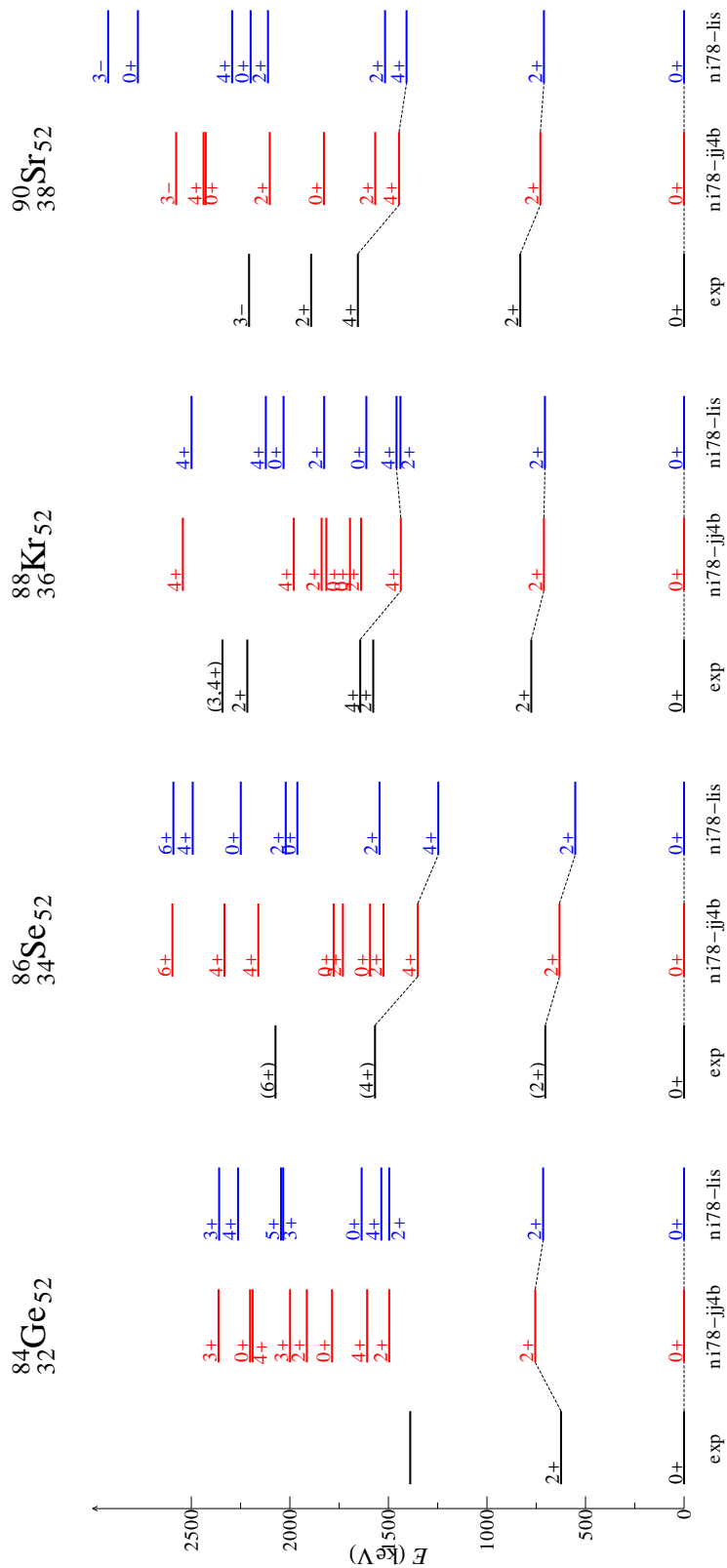
Figure 3.8: The experimental and calculated energy spectra for even-even N=52 isotones. From left: experimental values, calculated with $ni78 - lis$ and $ni78 - jj4b$ interactions.

CHAPTER 4

Development of an experimental setup to characterize the release of UC$_X$ target prototypes

Contents

4.1 Study of the feasibility of the experiment

Over the last two decades, facilities using ISOL (Isotope Separation On-Line) have been developing around the world: ISOLDE (CERN), TRIUMF (Canada), SPIRAL (France), HRIBF (USA) etc. Those facilities have proved their capability to efficiently produce a variety of beams. This is confirmed by today's international projects for the construction of second generation ISOL facilities: SPIRAL2, EURISOL-DS, SPES etc. These projects focus on the development of neutron-rich isotope beams obtained from the irradiation of well-designed fission targets. The target is indeed the element at the heart of an ISOL installation. In 2002, a European project TARGISOL was dedicated to the creation of a general database for the optimization of ISOL targets. Experimental work has been initiated to develop UC targets in the framework of the European projects SPIRAL2 and EURISOL-DS.

The research and development (R&D) programme PARRNe (Production d'Atomes Radioactifs Riches en Neutrons) at the Institute of Nuclear Physics in Orsay (IPNO) is devoted to studying the production of neutron-rich fission fragment beams extracted

from the thick targets [79] produced to an ISOL design (e.g. [80]). The continuous development of the targets is required since all chemically "easy" beams are already in use and the experiments are pursued far from the valley of beta-stability, where often one has to work with extremely short half-lives and low production cross-sections. This development concentrates at present on creating a more solid understanding of the performance of the target in order to reduce the decay losses and make beams of the remaining elements available [81]. Various materials have been tested and used as ISOL targets. The release properties of UC_x and molten U thick targets have been studied at PARRNe [82, 83]. Such developments are fundamental for the next generation of ISOL facilities. The current study carried out at IPNO is in particular supported by the SPIRAL2 project.

At present, the target PARRNe used at ALTO consists of 160 pellets of UC_x (x indicates an excess of graphite), each 1 mm thick. The geometrical density of the pellet is 3.5 g/cm^3 (measured volume includes pores). The design of the standard fission target for SPIRAL2 is based on the pellets used at ALTO. This standard target would be composed of 19 x 80 UC_x pellets. For this target the fission yield is estimated to be in the order of 10^{13} fission/s [84]. One of the goals of the R&D programme at IPN Orsay in collaboration with Laboratory of Chemical Science in Renne, is to produce a material which would allow one to obtain up to 10^{14} fission/s. The amount of uranium and the porosity of the target influence essentially the final flux of the fission products. The higher density of the uranium increases the production rate and at the same time prohibits the radioactive elements from easily leaving the target, while the efficiency of the release of elements depends on the porosity of the material. Thus the best compromise between these two factors will be found to design the target of interest. This compromise requires an investigation of the manufacturing processes. The pellets differ from each other by the amount of uranium and the structure. Those pellets are produced within an internal collaboration between ALTO and the radiochemistry group at IPN Orsay.

We aimed to perform an experiment which would allow us to compare the release properties of differently manufactured UC_x pellets. In order to find out which of the pellets has better release properties and could be used in future experiments with radioactive beams.
The basic procedure is as follows:

1. *Production of radioactive species in the UC_x target.*
   Two identical UC_x pellets are irradiated with fast neutrons to induce fission (see Chapter 5). Those fast neutrons are produced by impinging the 26 MeV deuteron beam delivered by the tandem accelerator on the graphite converter placed in front of the first pellet.

2. *Heating one of the pellets up to high temperature.*
   The radioactive fission product does not leave the target of its own accord. In order for the elements of interest to effuse from the target the pellet should be heated to a high enough temperature. In this step of the experiment one of the pellets is placed in a tubular oven and heated for about 30 min to allow the elements to effuse. The second pellet is placed in a plastic container, thus prepared for the further measurement as a reference.

3. *Measurement of the radioactivities and data analysis.*
   After heating, each pellet is placed in front of a germanium detector and the activities are measured. The pop-tops of the detectors are covered with lead shields in order to avoid background radiation. The pellet which has been heated is expected to be less radioactive than the non-heated one, since due to the heating some elements effused from it. Thus the gamma spectra should not be identical and some differences are expected to be visible. An identification of the isotopes is made through their $\gamma-$lines. From further analysis of the data one should be able to deduce which elements effused during heating and how abundantly. Moreover, since the same experimental procedure is used for the different sets of UC_x pellets, we shall find out which manufacturing method is the most efficient when it comes to production of the target with the best release properties.

The short-lived (ns to s) radioactive species created by fission induced by fast neutrons will decay towards longer-lived isobars emitting β and γ radiations. The experiment was planned to be performed without mass selection, thus, one must be aware of the complexity of the spectra which will contain γ-lines from all the radioactive elements present in the target at the time of measurement. The measurement of the radioactivities is done after heating, that is, when the initial fission products will already have decayed to their daughters.

Several aspects had to be considered before the experiment as many fission products were expected. Will it be possible to find well identified γ-lines with high statistics to identify the elements? After over about half-hour heating will there be enough activity in the pellets? There are also other factors, like the time of irradiation or the time of measurement, that should be planned and optimized:

- t_{irr} ($t_{irradiation}$): the time for which two pellets are irradiated. The irradiation time should be long enough to produce many radioactive elements but not too long for the activity of the pellets to be too high for manipulation and counting. The measurement with germanium detectors will be performed at least half an hour after the irradiation so only the radioactive elements with half-lives of a few minutes and longer will be counted. Taking all these factors into account the time of irradiation was first estimated to be 30 minutes.

- t_{wait}: the total time needed for the manipulation of the pellets after the irradiation and heating one of them in the oven for approximately 30 min. A priori the "waiting" time was foreseen to be 45 minutes.

- t_{meas} ($t_{measurement}$): the time required to measure the pellets using two HPGe detectors. Taking into account the duration of heating we are considering elements with few minutes half-lives. The time of counting should be long enough to have sufficient statistics while the activity of the pellets is still high enough.

- detection system: two HPGe detectors will be used to measured both pellets simultaneously. The acceptance of the detector is about 20000 c/s and too high an activity of the pellets can disable the detector. This factor may be controlled by putting the pellet further from the crystal.

To demonstrate feasibility and plan the experiment, a simulation of the γ-spectrum was made. It played a crucial role before making the measurement. The goal of the simulation was to study the feasibility of the experiment by evaluating the complexity of the spectrum and determining the release of which elements of interest we can expect to study. We needed to predict how the spectrum recorded after heating would look when measured for 1 h if there are enough radioactive elements and if the various peaks would be identifiable, thus, if the identification of certain elements of interest will be possible. Furthermore, the calculations would prove whether an irradiation time of 30 minutes is feasible and whether the counting rate will be below the acceptance of the detector.

4.1.1 Simulation

Production of radioactive species

During the irradiation, radioactive elements are produced at a given rate. This rate R will depend on the number of target atoms N_a, of the flux of incident particle I and on the reaction cross section σ:

$$R = N_a \sigma I \ .$$

After the nuclei are formed they decay according to the exponential law of radioactive decay

$$N(t) = N_0 \cdot e^{\lambda t}$$

where N_0 gives the original number of nuclei present at time $t = 0$ and $\lambda = \frac{ln2}{t_{1/2}}$ where $t_{1/2}$ is the half-live, the time necessary for half of the nuclei to decay.

Let us assume the following situation: we have a target of stable nuclei and we bombard it with the beam of particles. N_A is the number of nuclei that are formed as a

result of reactions. Those nuclei decay with decay constant λ_A to the nuclei denoted by B. The number of nuclei A present increases due to the production rate R and decreases due to the radioactive decay:

$$\frac{dN_A(t)}{dt} = R_A - \lambda_A N_A \ . \tag{4.1}$$

Integration of this equation over the time of irradiation $(0, t_{irr})$ gives the result:

$$N_A(t_{irr}) = \frac{R_A}{\lambda_A} \left(1 - e^{-\lambda_A t_{irr}}\right) \ . \tag{4.2}$$

Since no new activity is formed after irradiation, the radioactive nuclei will decay according to the exponential law

$$N_A(t_{wait}) = \frac{R_A}{\lambda_A} \left(1 - e^{-\lambda_A t_{irr}}\right) e^{-\lambda_A t_{wait}} \ , \tag{4.3}$$

where t_{wait} is the time from the end of irradiation until the beginning of the measurement. Finally, during the period of the measurement the number of nuclei present is given by

$$N_A(t_{meas}) = \frac{R_A}{\lambda_A} \left(1 - e^{-\lambda_A t_{irr}}\right) e^{-\lambda_A t_{wait}} e^{-\lambda_A t_{meas}} \ . \tag{4.4}$$

We are interested in the number of decays of nuclei A during the whole period of measurement (t_0, t_{end}) where t_0 is the end of the waiting time $(t_0 = t_{wait})$ and t_{end} is the time at the end of the measurement. This can be found by integrating Eq. (4.4):

$$N_A(t_0, t_{end}) = \int_{t_0}^{t_{end}} \lambda_A N_A(t) \, dt \ , \tag{4.5}$$

here $t_0 = 0$. Therefore, the total number of disintegrations for nuclei A is:

$$N_A(t_{end}) = \frac{R_A}{\lambda_A} \left(1 - e^{-\lambda_A t_{irr}}\right) e^{-\lambda_A t_{wait}} \left(1 - e^{-\lambda_A t_{end}}\right) \ . \tag{4.6}$$

Let us consider the second generation of nuclei which in this case is also radioactive and has a decay constant λ_B. The number of daughter nuclei N_B present increases as a result of decays of the parent and decreases as a result of its own decay:

$$\frac{dN_B(t)}{dt} = \lambda_A N_A - \lambda_B N_B \ . \tag{4.7}$$

Solving Eq. (4.7) in the same manner as for mother nuclei one obtains the solution for the number of decays of the daughter nucleus during the whole measurement period:

$$\begin{aligned}
N_B(t_{end}) = &\frac{R_A \lambda_B}{\lambda_A (\lambda_B - \lambda_A)} \left(1 - e^{-\lambda_A t_{irr}}\right) e^{-\lambda_A t_{wait}} \left(1 - e^{-\lambda_A t_{end}}\right) \\
&- \frac{R_A \lambda_A}{\lambda_B (\lambda_B - \lambda_A)} \left(1 - e^{-\lambda_B t_{irr}}\right) e^{-\lambda_B t_{wait}} \left(1 - e^{-\lambda_B t_{end}}\right) \ .
\end{aligned} \tag{4.8}$$

The same equations can be solved for the third, fourth and n^{th} generations until one reaches the stable nucleus or, as in our case, the half-live of the nth daughter is long enough to be ignored.
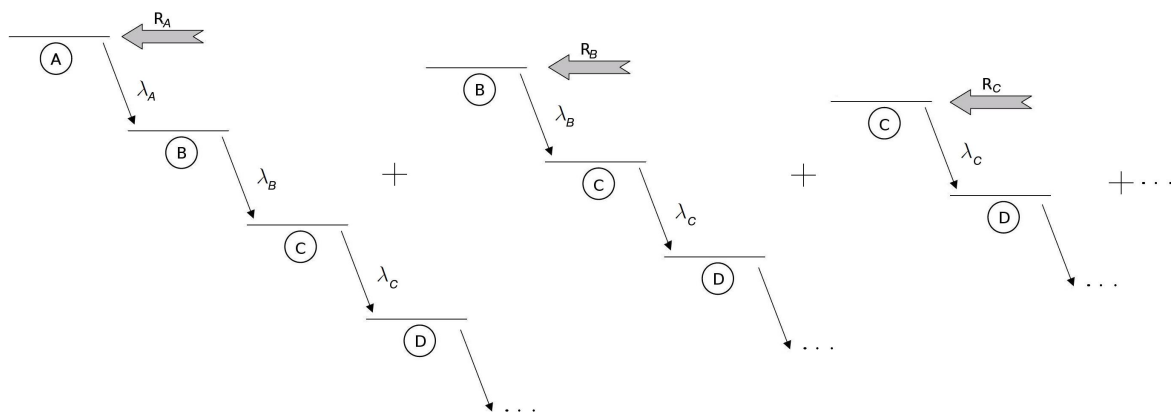
Figure 4.1: Production of radioactive species. Scheme of decay chains.

In our target not only nuclei A are produced but also B, C .. up to a few generations. The direct production of the daughter in the target should also be taken into account for the final number of disintegrations of this element during the measurement. In this case the total number of disintegrations will consists of both : decay of the elements produced by the decay of the parent and decay of the elements which were produced in the target (Figure 4.1). Thus, in the next step B will be the primary nuclei produced in the target with the production rate R_B. One can apply the same procedure for the calculation starting from the equation (4.1) this time for the nuclide B. The same can be done for all the generations of interest and the final number of disintegrations of the elements of interest will be the sum of disintegrations calculated from all the considered chains.

Case of several generations: Bateman equations

If we assume that there are several succeeding generations of radioactive nuclei we can write

$$\frac{dN_i(t)}{dt} = \lambda_{i-1}N_{i-1} - \lambda_i N_i \ . \tag{4.9}$$

We consider the simplified case where at the initial time $t = 0$ only the parent nuclide is present $N_{i=1,0} \neq 0$ and none of the other types. Bateman [85] has given the solution

for a chain of n members with this assumption:

$$N_n(t) = \sum_{i=A}^{n} C_i e^{-\lambda_i t}$$

$$= (C_A e^{-\lambda_A t} + C_B e^{-\lambda_B t} + \ldots C_n e^{-\lambda_n t}) \,, \tag{4.10}$$

where C is a constant having the form

$$C_m = \frac{\displaystyle\prod_{i=A}^{n} \lambda_i}{\displaystyle\prod_{i=A}^{n} (\lambda_i - \lambda_m)} N_{i=1,0} \qquad (i \neq m)$$

$$= \frac{\lambda_A \lambda_B \ldots \lambda_n}{(\lambda_A - \lambda_m)(\lambda_B - \lambda_m) \ldots (\lambda_n - \lambda_m)} N_{i=1,0} \,. \tag{4.11}$$

Let us demonstrate it for the case studied before:

$$N_{i=A,0} = N_A(t_{wait})$$

$$= \frac{R_A}{\lambda_A} \left(1 - e^{-\lambda_A t_{irr}}\right) e^{-\lambda_A t_{wait}} \,. \tag{4.12}$$

$$N_A(t) = N_A(t_{meas}) = \frac{R_A}{\lambda_A} \left(1 - e^{-\lambda_A t_{irr}}\right) e^{-\lambda_A t_{wait}} e^{-\lambda_A t_{meas}} \,. \tag{4.13}$$

Integrating over the period of measurement (t, t_{end}) one recovers Eq. (4.6). The same can be applied for the subsequent generations.

Details of the simulation

The conditions for the simulation were taken as follows: t_{irr}=30 min, t_{wait}=45 min and t_{meas}=60 min. As mentioned before, the fission products are very short-lived and most of them will decay before the detection. What will be measured in the spectrum are γ-lines coming not from the parents but their decay products (daughters and grand-daughters even up to a few generations). The nuclei taken into account for calculation must be γ emitters with half-lives of minutes. The spectrum contains γ-lines from 62 radioactive elements (Tab.4.1). For the calculation of the number of disintegrations of the elements of interest the Bateman equations were used. The γ-lines were simulated as gaussian-shaped peaks. The simulation was made with ROOT in a first approximation of the full energy peak (without Compton, backscattering, Bremsstrahlung). For the simulation the resolution of the detector was assumed to be a linear function of energy $y = a \cdot E_\gamma + b$ where $a = 0.0003$ and $b = 0.6497$. Those coefficients were calculated assuming that the resolution of the germanium detector is 1.6 keV and 2.5 keV at 100 keV and 1.3 MeV γ-rays, respectively.

Table 4.1: Radioactive nuclids used in the simulation. Half-lives are taken from ([86]) and the independent yields from [87].

Element	Half-life	Independent yield [%]	Element	Half-life	Independent yield [%]
^{87}Kr	76.3 m	8.28E-002	^{128}mSb	10.4 m	1.02E-001
^{88}Kr	2.84 h	5.57E-001	^{129}Sb	2.23 m	5.56E-001
^{88}Rb	17.77 m	1.50E-002	^{129}Te	69.6 m	4.19E-003
^{89}Rb	15.15 m	1.11E-001	^{130}Sb	39.5 m	7.43E-001
^{91}Sr	9.34 h	6.95E-002	^{131}Sb	23.3 m	2.49E+000
^{91}mY	49.71 m	0.00E+000	^{131}Te	25 m	9.78E-002
^{92}Sr	2.71h	2.63E-001	^{132}Te	3.204 d	1.46E+000
^{92}Y	3.54 h	0.00E+000	^{132}I	2.29 h	1.86E-001
^{93}Y	10.18 h	3.06E-002	^{133}mTe	55.4 m	2.54E+000
^{94}Y	18.7 m	1.65E-001	^{133}Te	12.4 m	5.58E-001
^{95}Y	10.3 m	5.98E+000	^{133}mI	9 s	0.00E+000
^{97}Zr	16.91 h	3.46E-001	^{133}I	20.8 h	4.68E-001
^{97}mNb	52.7 s	4.34E-004	^{134}Te	41.8 m	3.72E+000
^{97}Nb	72.1 m	3.51E-003	^{134}I	52.5 m	5.97E-001
^{99}Mo	65.04 h	1.13E-003	^{135}I	6.57 h	2.57E+000
^{101}Mo	14.61 m	6.02E-002	^{135}mXe	15.29 m	2.02E-001
^{101}Tc	14. 2m	2.14E-004	^{135}Xe	9.13 h	2.02E-001
^{102}Mo	11.3 m	2.08E-001	^{138}Xe	14.08 m	1.85E+000
^{102}Tc	5.28 s	9.33E-004	^{138}Cs	33.41 m	1.74E-001
^{104}Tc	18.3 m	6.75E-002	^{139}Cs	9.27 m	1.39E+000
^{105}Ru	4.44 h	2.82E-003	^{139}Ba	83.06 m	2.72E-001
^{105}mRh	45 s	1.11E-007	^{141}Ba	18.27 m	5.19E-001
^{107}Rh	21.7 min	1.35E-004	^{141}La	3.92 h	7.98E-003
^{117}Cd	2.49 h	2.62E-004	^{142}Ba	10.6 m	1.11E+000
^{117}mIn	116.2 m	3.46E-006	^{142}La	91.1 m	4.62E-002
^{117}In	43.2 m	3.46E-006	^{143}La	14.2 m	1.88E-001
^{118}In	5 s	4.70E-005	^{143}Ce	33.03 h	1.80E-003
^{123}mSn	40.06 m	1.02E-003	^{146}Ce	13.5 m	2.19E-002
^{125}mSn	9.52 m	2.19E-002	^{146}Pr	22.15 m	3.57E-003
^{127}Sn	2.1 h	5.46E-001	^{147}Pr	13.4 m	2.22E-002
^{128}Sn	59.07 m	1.13E+000	^{149}Nd	1.7 h	6.28E-003

4.1.2 The simulated spectrum and its interpretation

The simulated spectrum corrected for the efficiency of the detector is presented in Figure 4.2. Although the spectrum contains many peaks, there are several that are well separated, pure and of high statistics. The estimated counting rate was 12000 c/s which is high enough to get good statistics during the measurement and at the same time not too high for detection (the acceptance of HPGe detectors 20000 c/s). The irradiation time estimated for the purpose of the simulation is sufficient and there are well separated peaks which can be identified from the measured spectra. Thus one can conclude that these experimental conditions are sufficient to perform successful measurements.

Table 4.2: The γ-lines ([86]) of the elements of interest identified in the spectrum Figure 4.2.

Element	Energy [keV]	$T_{\frac{1}{2}}$ [86]	Element	Energy [keV]	$T_{\frac{1}{2}}$ [86]
^{135}Xe	249.77	9.13 h	^{129}Te	27.81	69.6 m
^{138}Xe	1768.26	15.29 m	^{134}Te	79.45	41.8 m
^{138}Cs	1435.8	33.41 m	^{134}Te	201.24	41.8 m
^{138}Cs	2218	33.41 m	^{134}Te	565.99	41.8 m
^{138}Cs	2639.59	33.41 m	^{133m}Te	334.27	55.4 m
^{134}I	235.47	52.5 m	^{133m}Te	863.96	55.4 m
^{135}I	288.45	6.57 h	^{133m}Te	1683.23	55.4 m
^{134}I	514.4	52.5 m	^{133}Te	1881.52	12.5 m
^{134}I	595.36	52.5 m	^{88}Kr	196.3	2.84 h
^{134}I	847.03	52.5 m	^{87}Kr	402.59	76.3 m
^{134}I	884.09	52.5 m	^{88}Kr	1529.77	76.3 m
^{132}I	954.55	2.29 h	^{88}Kr	2195.84	2.84 h
^{134}I	974.67	52.5 m	^{88}Kr	2392.11	2.84 h
^{134}I	1072.55	52.5 m	^{87}Kr	2554.8	76.3 m
^{135}I	1131.51	6.57 h	^{88}Rb	1836.06	17.77 m
^{134}I	1613.8	52.5 m	^{89}Rb	2570.19	15.15 m
^{135}I	1791.2	6.57 h			
^{135}I	1791.2	6.57 h			
^{134}I	1806.84	52.5 m			

Not all elements can escape from the target in the same way (see Chapter 5). The release of a given element depends on various physico-chemical parameters which are difficult to characterize at high temperature. Nevertheless, at a temperature of 1200 C we expect to observe the release of the most volatile elements such as alkalis and noble gases. Other less volatile elements which are produced in great amounts are also expected. At 1200 C the elements that can evaporate from the target are mostly

alkalies (e.g. Rb, Cs) and noble gases (e.g. Kr, Xe) Figure 5.11. The gamma peaks of identified elements are indicated in the spectrum (Fig. 4.2, Table 4.2) and are potential candidates for identification in the experimental spectra.
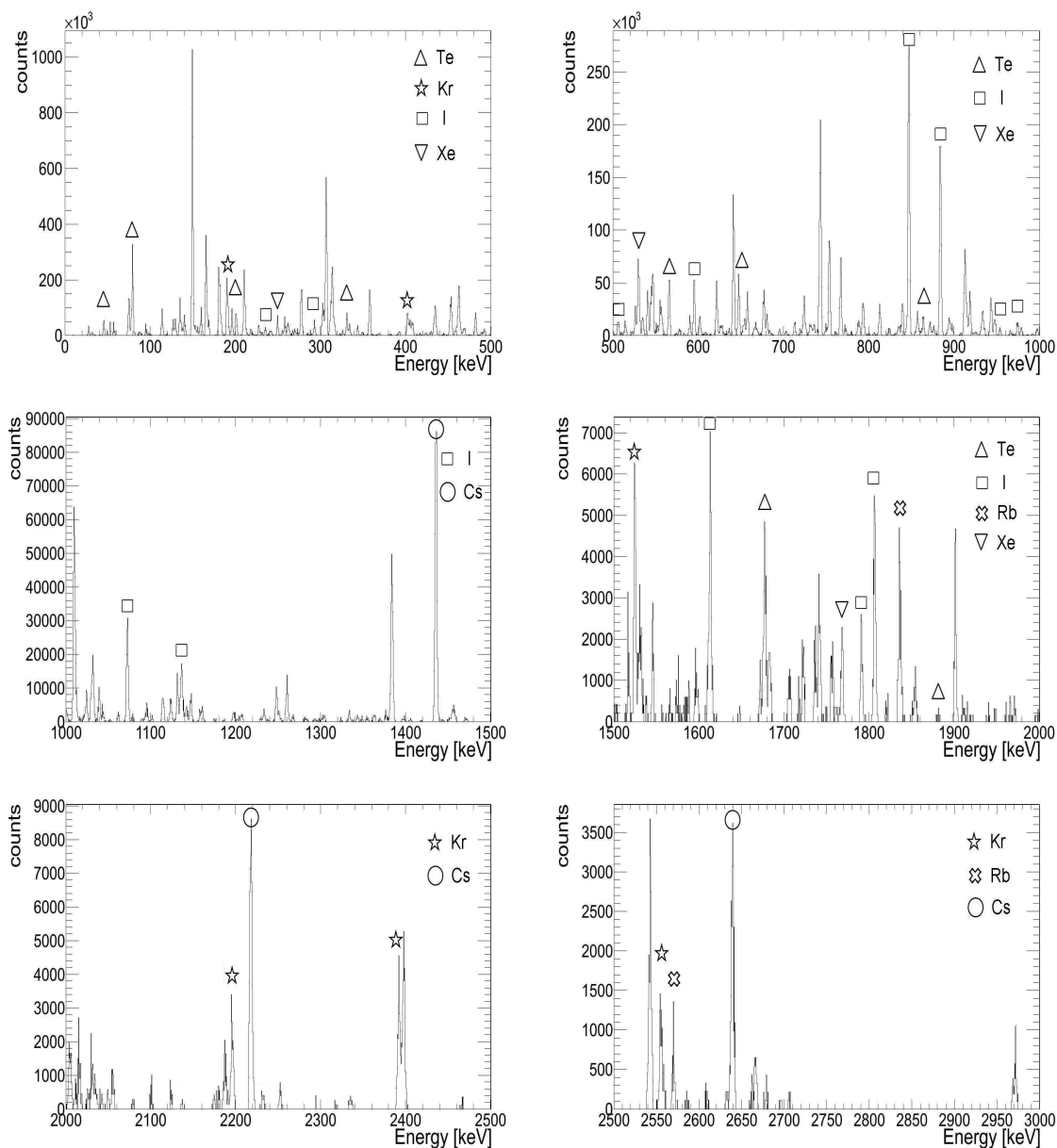
Figure 4.2: The simulated spectrum of the fission products produced in the uranium carbide target. It presents the prediction of the target activity measured 45 min after irradiation. The measurement time is one hour. The spectrum has been corrected for the detector efficiency. γ-lines of Kr ($\star$), Xe ($\bigtriangledown$), Te ($\triangle$), Cs ($\bigcirc$), I ($\square$) and Rb ($\times$) are identified.

4.2 The experiment

4.2.1 Description of the experiment

The deuteron beam of energy 26 MeV and intensity 20 nA was delivered using the 15MV tandem accelerator. The 3 mm graphite (neutron) converter was placed in front of the first UC_x pellet. The pellets were irradiated in pairs placed one behind the other. The scheme of the experimental procedure is presented in Figure 4.3.

Different methods of target synthesis must be investigated. Indeed, the physico-chemical properties of the pellet depends directly on the synthesis process. It was first decided to explore two different synthesis methods:

- UC_x pellets synthesized by the carbo-reduction method

- UC pellets synthesized by the arc melting method

The advantage of the first method is that it is possible to have a large variety of different compositions depending on the chemical components involved. For instance, standard pellets used at ALTO and named PARRNe have been obtained by the carbo-reduction of uranium oxide and carbon. To improve the porous structure of the target a prototype has been developed by inserting a certain amount of carbon fibers. The prototype containing 30% of those fibers has been named COM30. In the second method an electric arc is used to melt a blend of carbon and uranium (ARC melting). The interest of this method is to have a pure UC target in order to reach the highest concentration of uranium in the target. The disadvantage however is, as mentioned before, that the higher the uranium density in the target the more compact the target will be, which is not favorable for release.

Step 1. *The irradiation.*
    In the first step the targets were irradiated in couples (e.g. COM30.P1 and COM30.P2). The first couple of pellets was irradiated as previously planned for 30 min. Unfortunately, the overall activity generated in the setup did not allow us to extract safely the pellets for identification and heating for 1 hour. For safety reasons the extraction was allowed only when the overall dose rate was below 20 mSv/h. In fact, when it became possible to extract the pellets, we found that the strong radioactivity observed was in great part coming from the metallic system used as a fast removable support for the pellets. The decision was made to shorten the irradiation time to 20 min with a beam intensity of 20 nA.

Step 2. *Measurement of the activities.*
    The radioactivities of two pellets were measured for 10 min with HPGe detectors.

This measurement was done in order to study the distribution of neutron flux coming from the converter. As two pellets were irradiated at the same time, one placed behind the other, it was crucial to know if the neutron flux was the same and as a consequence if the number of neutrons interacting, thus the number of fission events, in the first and the second pellet were the same.

Step 3. *The heating.*
In this step one of the two pellets was heated in the oven (see picture 4.3). The heating time was 30 min and the temperature inside the oven was 1200 C.

Step 4. *The radioactivity measurement.*
The radioactivities of both pellets were measured for 1 h with two individual HPGe detectors: DIANE and GUOC11 with resolutions of 2.14 keV and 2.66 keV at 1.3 MeV (measured with ^{60}Co source); respectively. In order to estimate a dead time of the acquisition we have used two pulsers, one for each detector. The detectors were covered with lead cups to suppress background radiation.

4.2.2 Exploitation of the calculations and measured spectra

Because of a few safety issues the irradiation conditions were slightly changed. Even so the experimental spectra were rather comparable to the simulated ones. Figure 4.4 presents the spectrum from the measurement of a pellet prototype named COM30.P1 recorded for 1 hour after heating. The γ -lines predicted by the simulation are visible in the spectrum which made the identification much simpler and faster. As expected, peaks coming from: alkalies (Rb, Cs), noble gases (Kr, Xe) and a few elements like Te and I were identified.

Figure 4.5 presents three spectra: the first measured for COM30 pellets, the second for PARRNe pellets and the third for ARC melting pellets. Two peaks of interest are zoomed: from ^{88}Kr at 2392.11 keV and ^{142}La at 2398 keV. The pellets indicated with number "P1" (red) were measured with DIANE detector and the ones with number "P2" (black) with GUOC11 detector. The data in red are from pellets which were previously heated in the oven. The difference between the "red" and the "black" curves is attributed to the release from the pellet during heating. Since the detectors were different, the spectra were normalized according to the size of the 2398 keV peak in ^{142}La. This peak has been chosen because no release of radioactive lanthanum at 1200 C was expected. The comparison of the "black" spectrum with the "red" one highlights the release of krypton in COM30.P1 and PARRNe.P1 samples which is absent in ARC.P1. This difference is especially visible for sample COM30.P1 where the peak of krypton is significantly lower than from the non-heated pellet COM30.P2. For
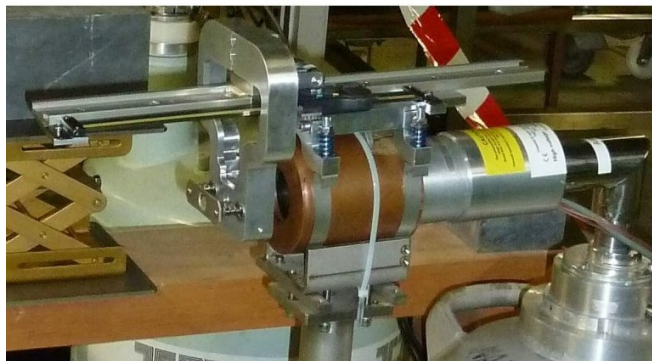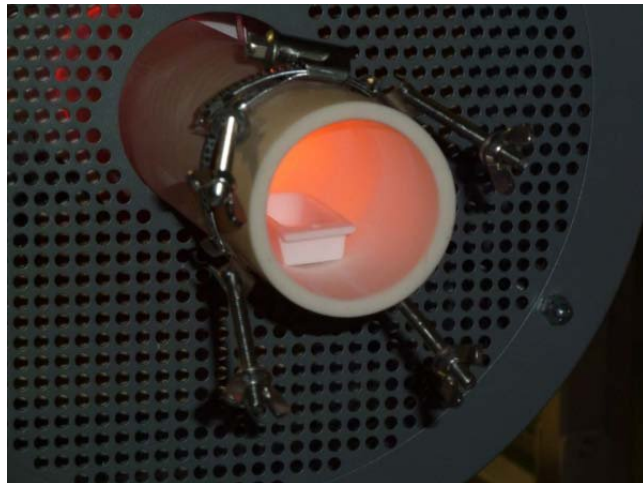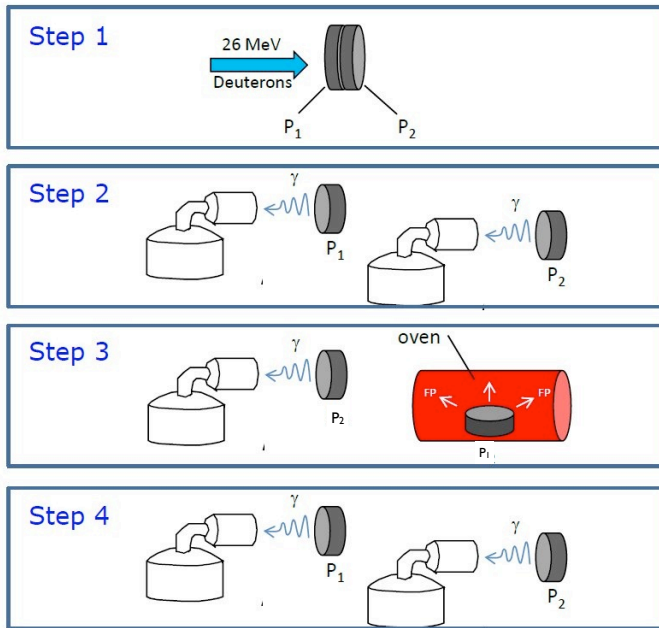
Figure 4.3: Up: Scheme of steps for experimental procedure. Middle: a UC_x pellet in the oven. Bottom: germanium detector with pellet placed on the support system in front of the crystal
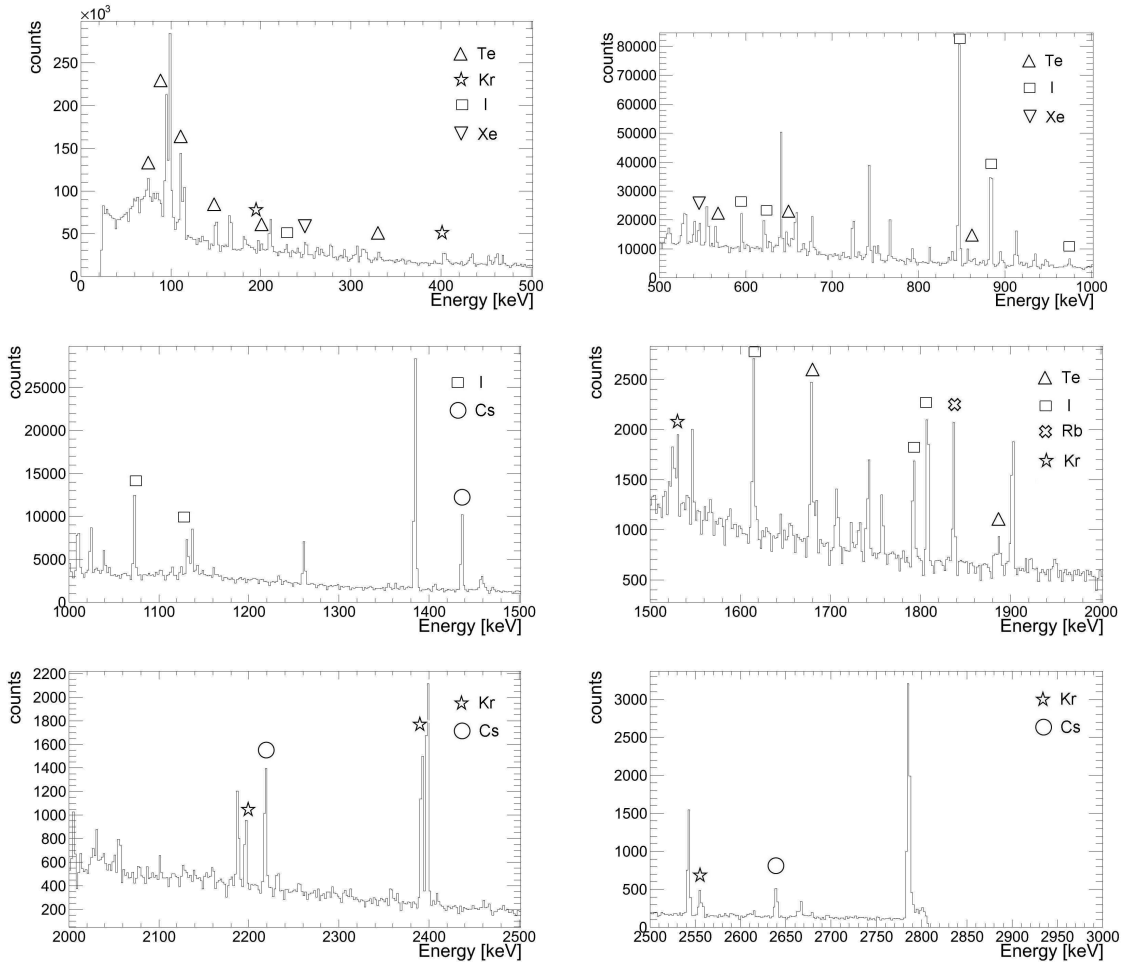
Figure 4.4: Spectrum from COM30.P1 pellet prototype measured with the DIANE detector. The measurement lasted 1 h after the pellet has been heated in the oven. The γ -lines from Kr ($\star$), Xe ($\bigtriangledown$), Te ($\triangle$), Cs ($\bigcirc$), I ($\square$) and Rb ($\times$) can be identified.

the PARRNe target this difference is not so large but is still apparent. While studying the ARC-melting pellets spectrum one essentially sees no effect. Already here, one can learn three major points from this experiment. Firstly, the heating test has showed the release of krypton, one of the nuclei of interest, demonstrating the feasibility of such an experimental setup. Secondly, as expected the amount of radioactive elements that escaped from the targets depends significantly on the composition of the pellets (very visible release from COM30 while no release from ARC). The third point is that the release depends on the chemical nature of the element. For instance, as observed, Kr is released already at 1200 C in proportions depending on the target composition while, as expected, La is not released at all.
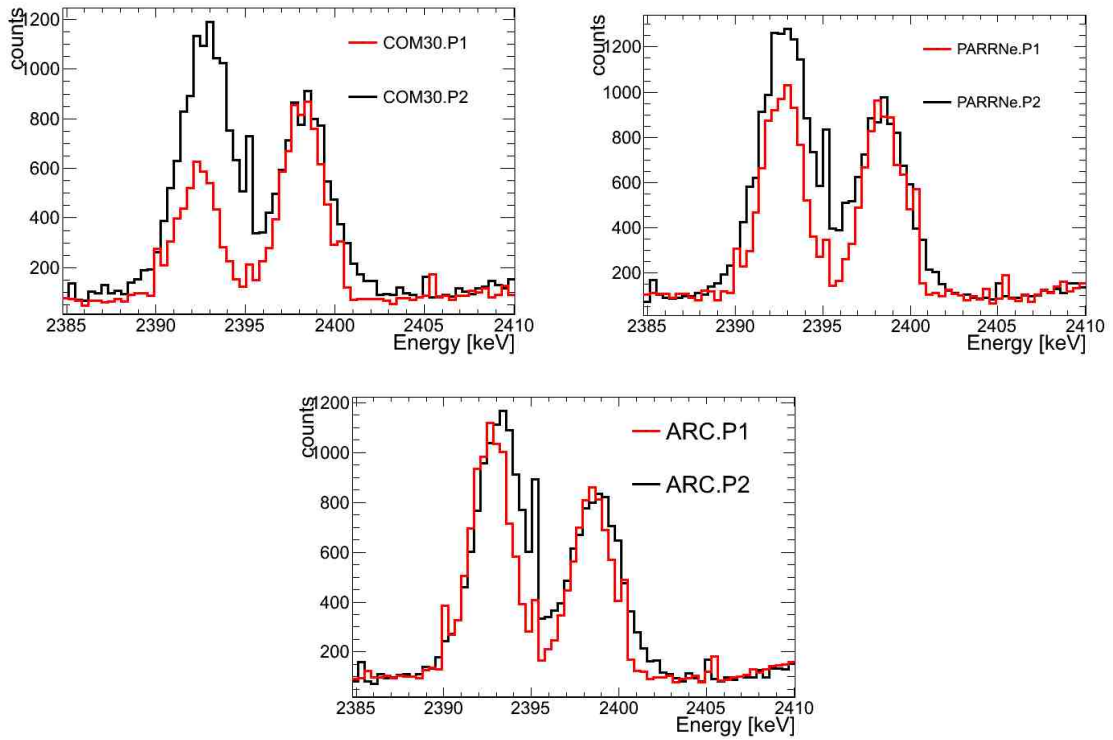
Figure 4.5: Comparison of the release fraction of krypton from pellets: COM30, PAR-RNe and ARC-melting. Left peak ^{88}Kr (2392.11 keV) and right peak ^{142}La (2398 keV). The data from the two detectors were normalized according to the size of the peak of lanthanum.

The feasibility of the experiment studied with the simulation was confirmed and the simulated spectrum was found to be very useful when studying the measured ones.
The second experiment to study the release properties of different prototypes of UC$_x$ targets have been carried out with 1500 C heating temperature. The first results with the detailed release fractions from the first and the second experiment were recently published [88]. The three pellets OXA, COM30 and PARRNe were found to have the highest release fraction but the interpretation of the material properties is still in progress. Most importantly, it was demonstrated that the experimental method to study differently pellets was confirmed.

For the future developement of the target more new prototypes will be developed and the heating temperature should be increased to be as close as possible to the operating temperature at ALTO and SPIRAL2 (2000 C). A big part of any future work will concentrate on the material synthesis for new target prototypes.

Chapter 5

Production of radioactive ion beams

Contents

5.1   Production methods

There are different methods to produce neutron or proton radioactive ion beams: multi-nucleon transfer reactions, induced fission, spallation and fragmentation reactions. The choice of reaction mechanism depends on the region of interest. After their production, the nuclei of interest must be separated from other reaction products. There exist two separation techniques: In-Flight Separation and Isotope Separation On Line.

In-Flight Separation

The In-Flight (IF) separation method can be explained on the fragmentation reaction. The high-energy heavy-ion projectiles bombard a thin target (less than a gram/cm^2) and radioactive isotopes are produced through the fragmentation reaction. The target should be as thin as possible to avoid absorption of the reaction products and to narrow their energy distribution. The nuclei leave the target highly ionized and are separated in-flight by means of magnetic and/or electric fields. This method provides

us with so-called "cocktail" beams and specific nuclides can be selected according to their atomic number and atomic mass. In this method the produced nuclei are available instantly. However, the products are often highly energetic (hundreds of MeV per nucleon) which is suitable for reaction studies but too high for nuclear structure studies. They may have a broad energy distribution, often large angular divergence and their purity is rather poor.

There are a number of facilities worldwide which are based on this technique, like the FRS facility at GSI (Darmstadt, Germany), LISE at GANIL (France), COMBAS at FLNR (Dubna, Russia), the fragmentation facilities at MSU (Michigan, USA) and at RIKEN (Japan).

Isotopic Separation On-Line

In the ISOL method an intermediate- or heavy-mass thick target is bombarded with light beam (neutrons, protons, electrons or γ -rays). Various kinds of reaction can be induced: if the energy of the primary beam is low (a few tens of MeV per nucleon) fusion-evaporation, fission, or multi-nucleon transfer reactions, or in case of a highly energetic projectiles (e.g., a few hundreds of MeV for neutrons or around 1 GeV for protons) fragmentation and spallation. In this technique the radionuclides are stopped in the target from which they are subsequently released by diffusion in the target material and desorption from the material surface while heating the target to sufficiently high temperatures. The radionuclides can diffuse out of the target and effuse eventually through a transfer line to the ion source where they are ionized. Using the ISOL technique one can produce good-quality beams of nuclei of interest. The beam has a very low energy spread, which allows for a possibility of post-acceleration of the beam, and small angular divergence. This method has also some disadvantages, for instance, a relatively long extraction time which makes the study of many short-lived nuclear species almost impossible. The exotic nuclides are produced in limited amounts, thus the release has to be as efficient as possible, i.e. the radio-nuclides must reach the ion source, be ionized, accelerated and mass separated before they decay. The chemical selectivity introduced by the choice of target is limited.

Some of the most known and advanced beam facilities using proton beams are ISOLDE at CERN (Switzerland), IGISOL at Jyväskylä (Finland), HRIBF at ORNL (Oak-Ridge, USA), SPIRAL at GANIL (France), ISAC at TRIUMF (Vancouver, Canada) and ALTO (IPN Orsay, France).

5.2 Production of radioactive nuclei with fission reaction

Nuclear fission is a process in which a heavy nucleus splits into two lighter nuclei emitting several neutrons. The reaction is exothermal since the nuclear binding energy per nucleon for the produced medium mass nuclei is significantly higher than the binding energy of the original nucleus. To be able to fission, the nucleus has to first stretch to a very elongated shape. It requires energy to deform the nucleus to the so-called saddle point, after which the energy is released. The energy may be brought to the nucleus as electromagnetic radiation (photofission) or via a particle (e.g., protons or neutrons). There is a potential barrier against the fission which height for medium heavy nuclei is of the order of 50 MeV, while for actinides (^{233}U, ^{235}U, ^{239}Pu, ^{241}Pu, ^{241}Am, *etc.*), of the order of 5 MeV.

The research and development (R&D) program PARNNe (Production d'Atoms Radioactifs Riches en Neutrons) was initiated at the Institut de Physique Nucléaire d'Orsay (IPN Orsay, France) in 1997. This program was devoted to study the production of neutron-rich fission fragment beams extracted from the thick target produced with ISOL method [79]. In the framework of the PARNNe program different techniques were used to characterize the release properties of the elements of interest from a UC_x target [89, 90]. Together with the R&D program, the physics research of the neutron-rich elements was started [91, 92]. At first, the fission of ^{238}U was induced with the deuteron beam provided by the Tandem accelerator (the Orsay Tandem Van de Graff accelerator with nominal voltage 15 MV). In 2005, the construction of the ALTO (Accélérateur Linéaire auprès du Tandem d'Orsay) facility was completed and the first tests with the electron beam were performed. Today, the ALTO accelerator provides 50 MeV electron beam of $10\mu A$ intensity.

5.2.1 Neutron-induced fission

Various experiments on the thick uranium carbide target (UC_x) bombarded with fast neutrons were performed in IPN Orsay with PARRNe separator [48, 78]. Fast neutrons were produced by impinging the 26 MeV deuteron beam, delivered by Tandem accelerator, on the graphite converter placed 5 mm to 110 mm from the center of the uranium target. As deuteron has a low binding energy it can break on the converter (for the beam energy of 40 MeV, 0.013 neutrons per deuteron are produced [93]). The protons from the break-up are absorbed by the converter while the neutrons can escape and travel to the uranium carbide target (with an energy of about 0.4 times of the incident energy). To optimize the neutron beam energy many studies have been made. The measurements of ^{238}U fission cross section were performed by Lestone and Gavrin [94]. The results of the measurements are shown in Figure 5.1. The cross

section (Figure 5.1 (right)) for the reaction increases slowly up to 40 MeV neutron flux energy. However, there is a saturation in the production with increasing beam energy (Figure 5.1 (left)) [95]). Another important parameter is the selectivity of the fission fragments. The fission of ^{238}U at low excitation energy is very asymmetric (Figure 5.2). This asymmetry decreases with increasing energy. Simulations by Mirea *et al.* [96] show that in order to obtain the most neutron-rich fission fragments in the vicinity of nickel, the energy of the primary neutron beam should not be higher than 20 MeV (even though the rate of the deuteron break up is lower than for higher energy). The Tandem accelerator at IPN Orsay delivers a deuteron beam of energy 26 MeV and intensity of $1\mu A$ (which correspons to 10 MeV neutron beam). It allows the production of 10^9 fissions/s in the target.
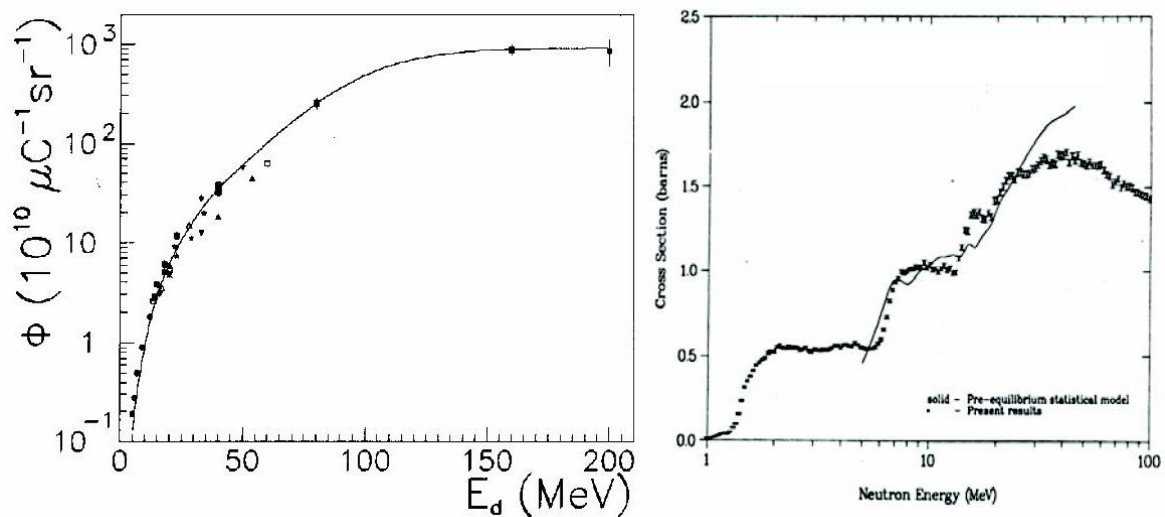
Figure 5.1: (Left) Neutron production at $0°$ as a function of deuteron beam energy [95]. (Right) Fission cross section of ^{238}U as a function of neutron energy [94].

5.2.2 Photo-fission

In the photo-fission process fast electrons interact with the atoms and as a result of their deceleration continuous spectrum of γ-rays (Bremsstrahlung) is produced. Those γ-rays induce fission in the target. It was Diamond *et al.* [98] and Oganessian *et al.* [99] who proposed to use the electrons to induce photo-fission in the uranium target. According to Diamond's calculation with 30 MeV and 100 kW electron beam it is possible of induce more than 10^{13} fissions/s. It was experimentally validated by Oganessian. In his experiment, an 25 MeV and a 0.5 kW electron beam was sent on a tantalum converter to induce fission in a sheet of uranium. The fission rate in the
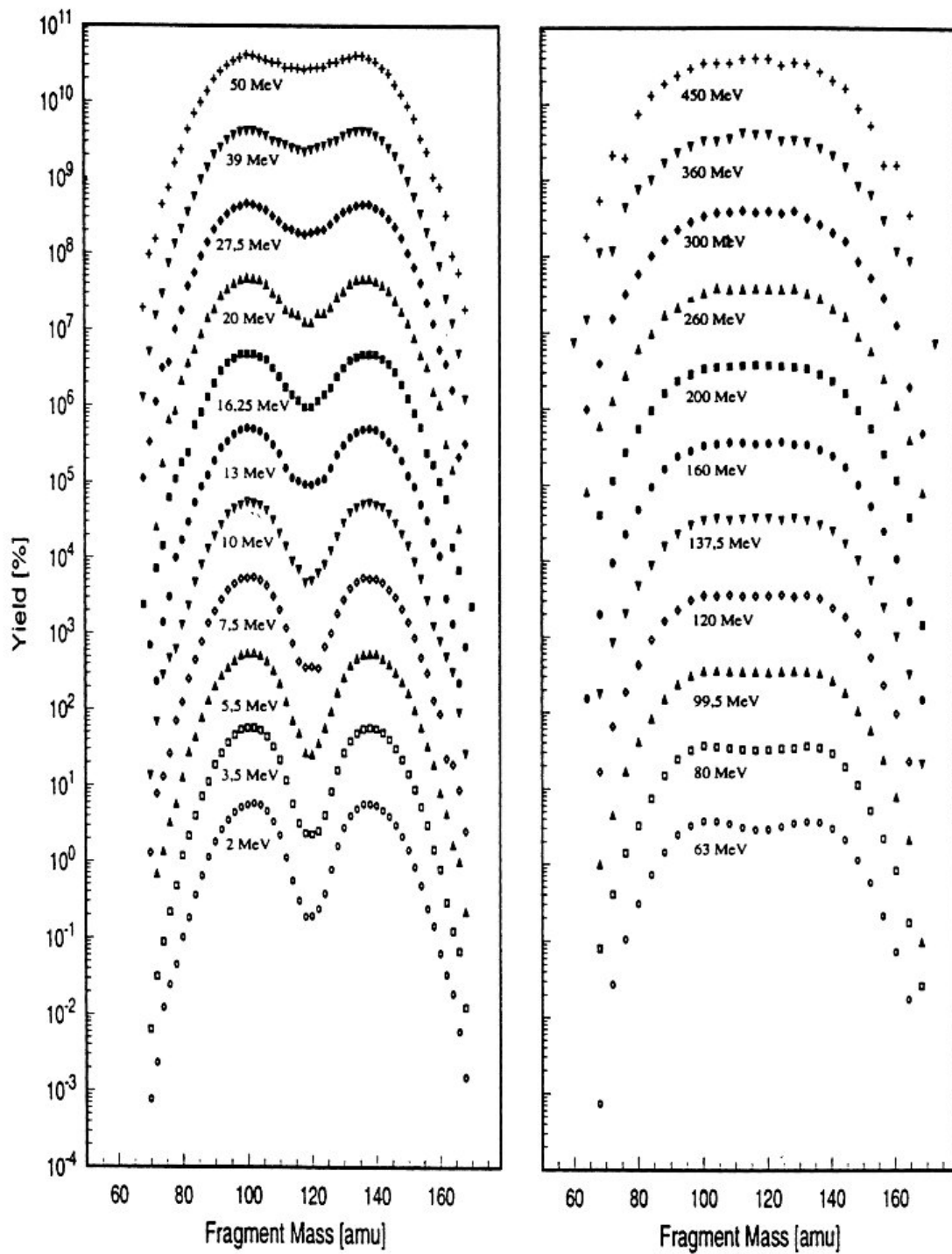
Figure 5.2: Distribution of fission fragments as a function of the excitation energy of ^{238}U [97].

target was measured to be of the order of 10^{11} fissions/s.

The energy spectrum produced by the electron beam is presented in Figure 5.3 (a) (left-hand scale). As can be seen, the energy of γ generated by the Bremsstrahlung varies up to a maximum corresponding to the energy of the incident electron beam. The trend increases gradually with the increase of the electron beam energy. To induce fission the photons energy must be greater than the fission threshold energy of 238 uranium which is 6 MeV. On the right axis the fission cross section is plotted as a function of incident photon energy. The total photon absorption cross section ^{238}U has a giant dipole resonance peak (GDR) between 10 and 17 MeV photon energy. This curve shows that the yield of photo-fission is the convolution between the incidents γ-rays and the cross section for photo-fission. The convolution of the curves is presented in Figure 5.3 (b) where the fission yield increases rapidly with the electron energy up to 30 MeV, and then continues to increase slowly until reaching the saturation at 45 MeV. Thus, 50 MeV seems to be the optimal energy for the electron beam.

The ALTO facility using the old pre-injector CERN LEP can deliver an electron beam of 50 MeV which allows to achieve optimal conditions for the photo-fission reaction.
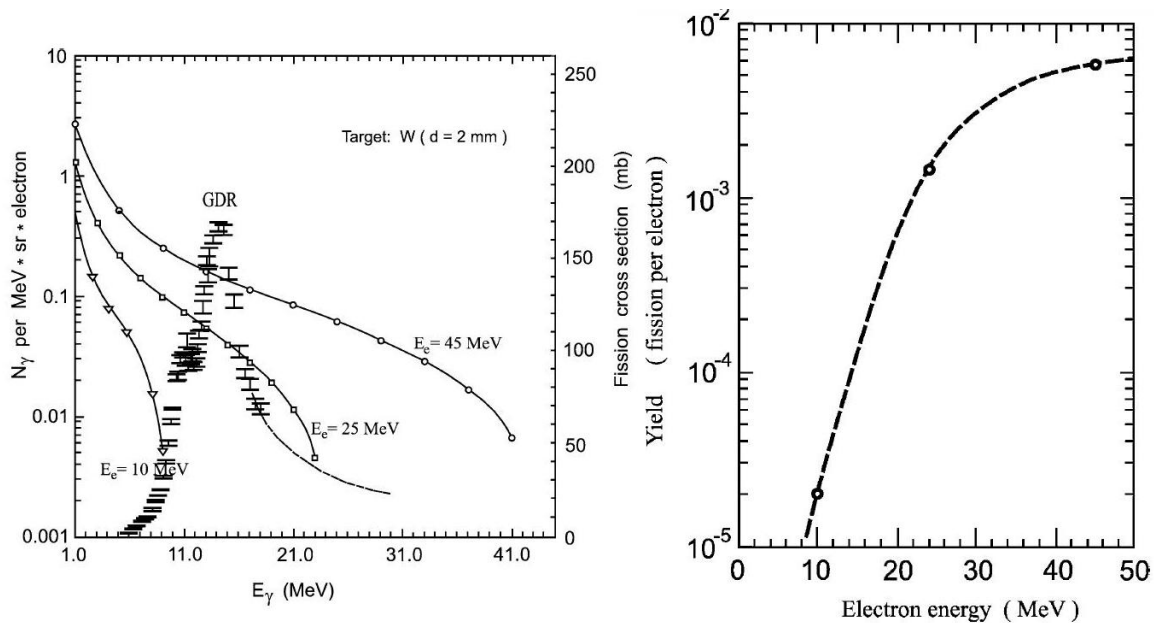
Figure 5.3: (a) The solid lines (the left-hand scale) is the γ-quanta spectrum produced by electrons with various energies (indicated in the figure). The experimental points (the right-hand scale) represent the ^{238}U photo-fission cross section. (b) The fission yield per electron for ^{238}U as a function of electron energy [99].

5.3 Ion sources

After release from the target the radioactive atoms have to be ionized and accelerated for subsequent magnetic mass separation and electrostatic beam guiding. There are three different types of ion sources used at ISOL facilities: surface ionization ion source, plasma ion source and laser ion source.
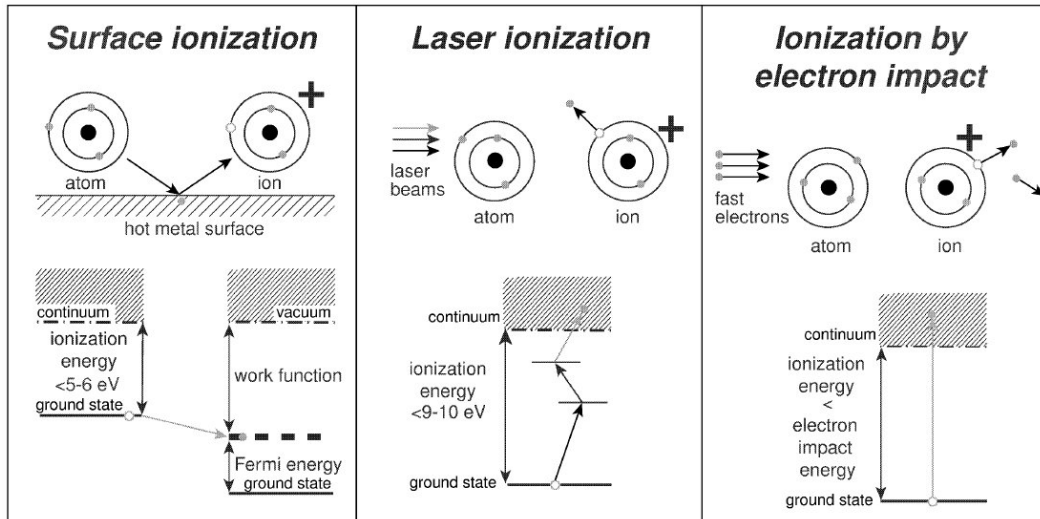
Figure 5.4: Schematic representation of surface ionization, resonant photo ionization and ionization by electron impact [100].

Surface ionization ion source

The concept of surface ionization involves the ionization of an element with low ionization potential (IP < 6eV) on a high work function surface (q). When an atom has a low first ionization potential and the tube surface is hot enough, it desorbs the ion thermally and the valence electron is lost to surface upon desorption. This process is called (positive) surface ionization and the created ion has charge 1+. An analogous process of negative surface ionization exists for elements with high electron affinity A_E which hits a hot surface of a material with low work function (q) and get negatively ionized. Although the surface ionization source cannot produce multi-charged ions the advantage of this kind of ion source is its simplicity and selectivity. Only elements with low ionization potential are ionized Figure 5.5. The ionization tube of the source used at ALTO has diameter of 3 mm and is 3 cm long. Ionization efficiency of this source for alkalis vary between 50% to 100% [101]. For gallium the efficiency of this source (measured at ISOLDE) is 1% [100].
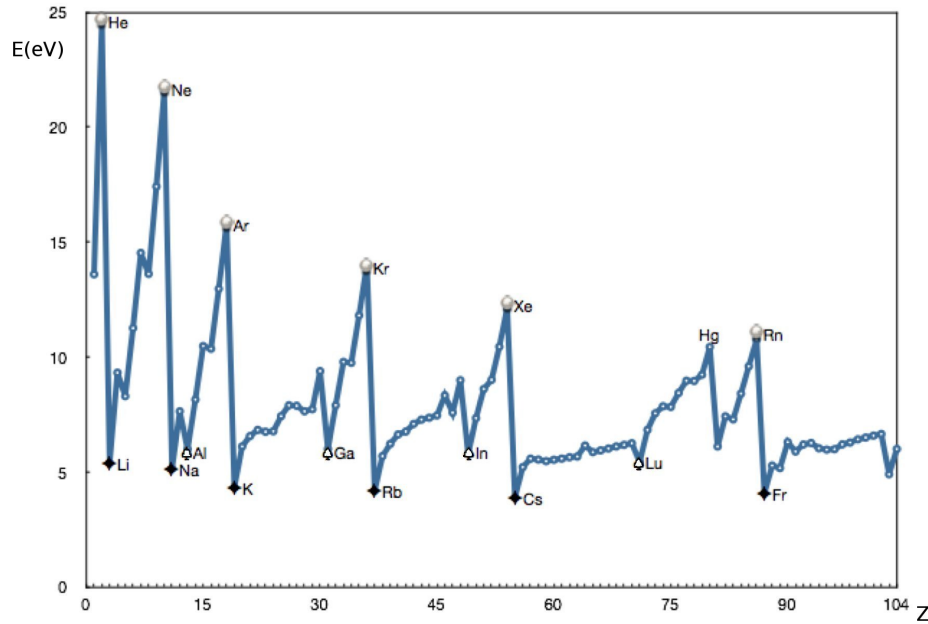
Figure 5.5: The evolution of the first ionization energy as a function of atomic number. The noble gases are indicated by spheres, the alkalies by black diamonds and the white peaks non-alkali elements [35].

Plasma ion source

Plasma ion sources may ionize many different elements even with higher ionization potential. If the plasma temperature T_p is high enough ($kT_p > IP$) practically all atoms entering the plasma can get ionized by electron impact (Figure 5.4) and charge exchange collisions. The plasma ion source used in ALTO facility is MK5-ISOLDE [102]. The principle of its work is based on the Forced Electron Beam Induced Arc Discharge (FEBIAD) source developed by Kirchner and Roeckl for the GSI on-line separator [103]. The FEBIAD source can reach high efficiencies (around 50 % [103]) for elements above argon and runs stably even at low gas pressures (10^{-5} mbar). MK5 is the so-called hot plasma source where the transfer line is maintained around 1900 °C . It permits to ionize also less volatile elements. The entire source is heated by an electric current flowing through the closed circuit composed of a transfer tube, an anode, a cathode and a support of the target. The anode is a cylinder molybdenum connected to a voltage of 100 to 200 V in which a vacuum of 10^{-4} bar is maintained. The end which faces the cathode consists of a graphite grid. The holes in the grid allow electrons to pass through the anode and form the arc discharge. The cathode is a cylinder of tantalum in which the atoms move to reach to the discharge chamber. The distance between the anode and the cathode is a few millimeters. The difference

in potential between the anode and cathode will remove electrons from the elements. At the output of the source the ions are subjected to a potential difference of 30 kV and transported to the mass separator.
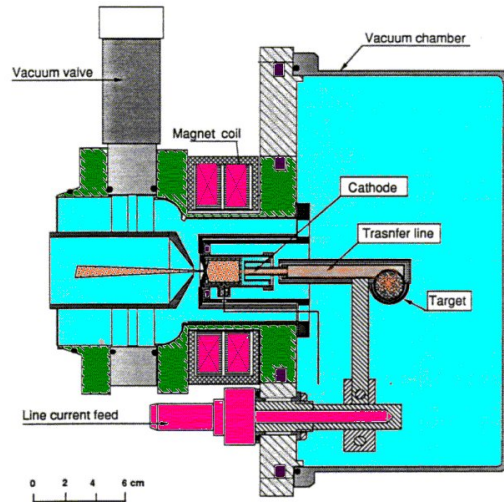
Figure 5.6: Drawing of the MK5 ion source [102].

Laser ion source

The principle of the laser ion source is based on the resonant ionization method which was developed for resonance ionization spectroscopy (RIS) [104, 105]. The RIS method is based on ionization by absorption of one or more photons (photoionzation) coming from laser beams. The absorption by an atom of one or more photon ejects an electron from the electron cloud of the atom. In case of two steps ionization the first light beam is tuned to the frequency of the resonant transition of a given state (usually the electronic ground state) to an intermediate state. The atom is then photoionized from this intermediate state with a second laser pulse. This method has two advantages. First of all, as the levels of the electrons vary for different elements it permits creations of very pure radioactive beam of ions (high selectivity). This selective ionization of atoms is due to the choice of the unique combination frequency laser to ionize the atoms of a selected item which prevents the ionization of other atoms. The second advantage is the ionization efficiency which is maximal if each atom in its ground state exposed to the laser flux is ionized.
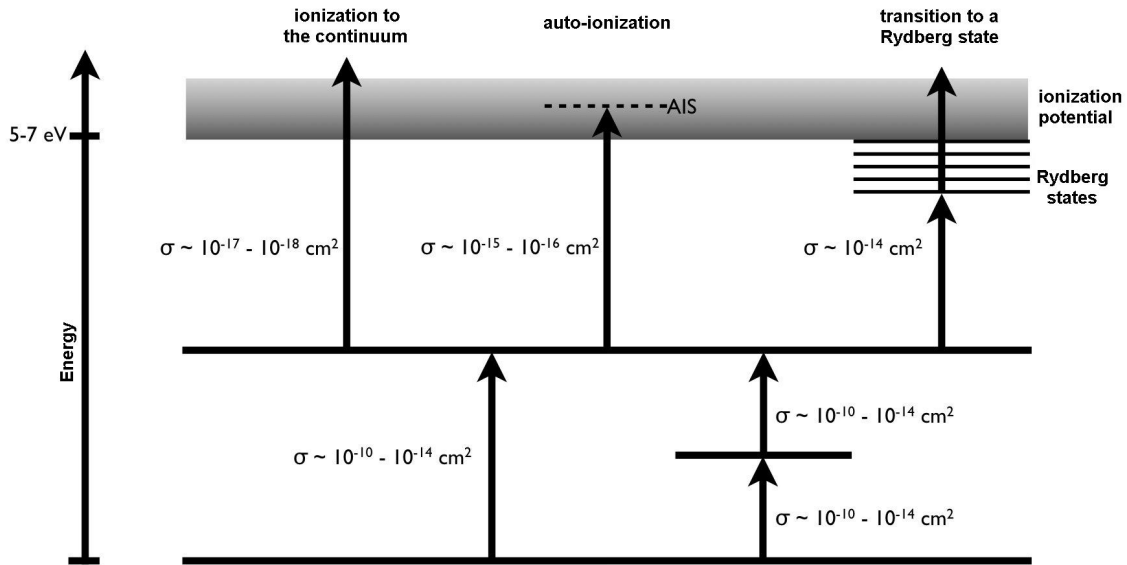
Figure 5.7: Schematic of different methods of ionization and the corresponding cross sections (photo [35]).

Ionization schemes include two, three or more transitions (Figure 5.7) and are classified according to the nature of the last populated level before ionization:

- **Ionization to the continuum:**
  In the case of ionization to the continuum the last step of the ionization is non-resonant. The non-resonant cross-sections into the continuum are relatively small ($\sigma = 10^{-17} - 10^{-18}$ cm^2). The ionization efficiency depends strongly on the laser power for the last transition. A strong non-tunable laser is used for this non-resonant step. The minimum energy of the beam of light required for ionization is of the order of a few mJ/pulse. The ionization to the continuum is used when the autoionizing states are not known or too narrow.

- **An autoionizing state (AIS):**
  In the case of autoionization method, the ionization is resonant and the cross section is higher than for the non-resonant ionization ($\sigma = 10^{-15} - 10^{-16}$ cm^2). An autoionizing state (AIS) is a two electron excitation above the atomic ionization potential W_i which decays in a radiationless transition into an ion and an electron. While one electron is ejected the other drops to the ground state or excited state of the ion. Typical lifetimes of AIS are from $10^{-15} - 10^{-10}$ s. All many-electron atoms have autoionizing states but the knowledge of those states

is limited to few elements. The autoionizing states have very precise frequency and require the use of lasers with high resolution.

- **Transitions to a Rydberg state:**
  The last type of ionization is ionization to Rydberg states [106, 107]. Using this ionization method high cross-sections can also be obtained (of the order of $\sigma = 10^{-14}$ cm^2). However, to allow the ionization of the atom, the application of a static electric field (approx. 10 kV/cm) is required to move by Stark effect the Rydberg levels to the continuum [108, 109]. The necessity of a strong electric field to induce the Stark effect makes this method difficult to implement.

5.4   The ALTO facility

The ALTO facility (Figure 5.8) can be decomposed into three main components: the electron accelerator (LINAC), the target-ion-source unit and the mass separator (PAR-RNe).
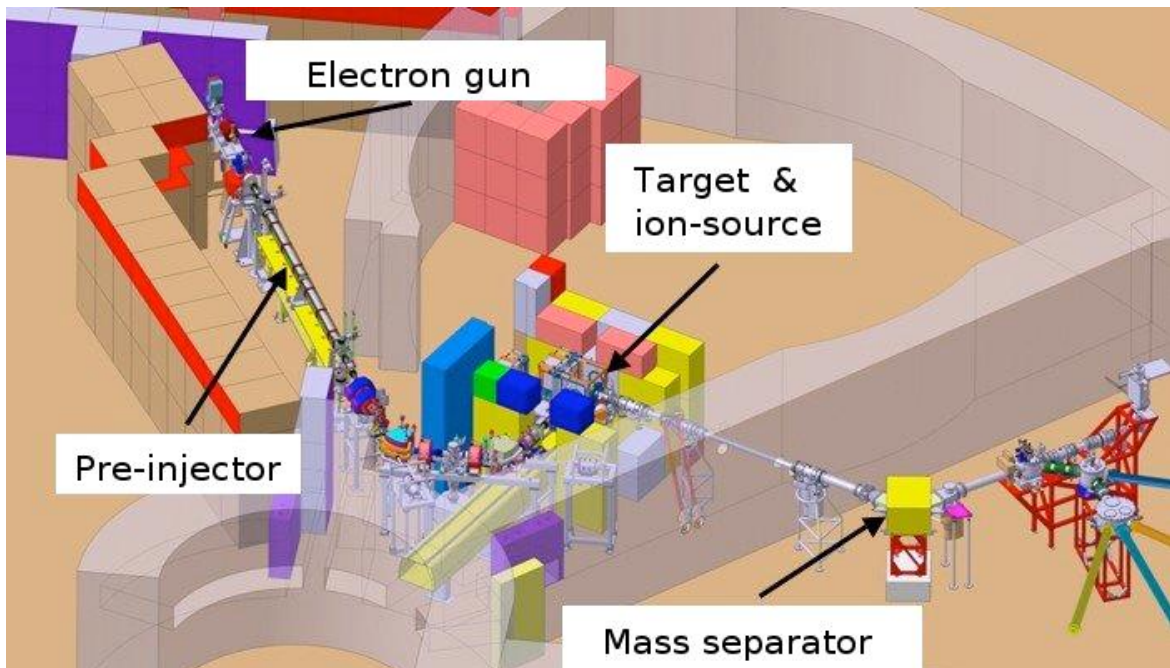
Figure 5.8: The scheme of the ALTO facility.

5.4.1 LINAC

LINAC consists of three parts: an injector, an acceleration section and a transport line. The injector consist of an electron gun which provides a pulsed electron beam of 100 Hz frequency and a length which can be adjusted between $0.2-2$ microseconds. At the exit of the electron gun there are two high-frequency cavities (a pre-buncher and a buncher) to accelerate pulses of electrons to an energy of 3 MeV. After the injector electrons are accelerated in the accelerating section which consists of the former LEP pre-injector and allows electrons to reach an energy of 50 MeV over a 4.5 m distance. Once the beam is formed it is transmitted to the target-ion source through the transfer line. This line is equipped with two magnetic dipoles allowing deflection of the beam at an angle of 130°. It is connected to the existing transmission line to keep the possibility of using a deuteron beam for experiments with fast neutrons. At the exit of LINAC the electron beam has energy of 50 MeV, average current of 10 μA and a width of 15 ps with a repetition period of 333 ps (Figure 5.9).
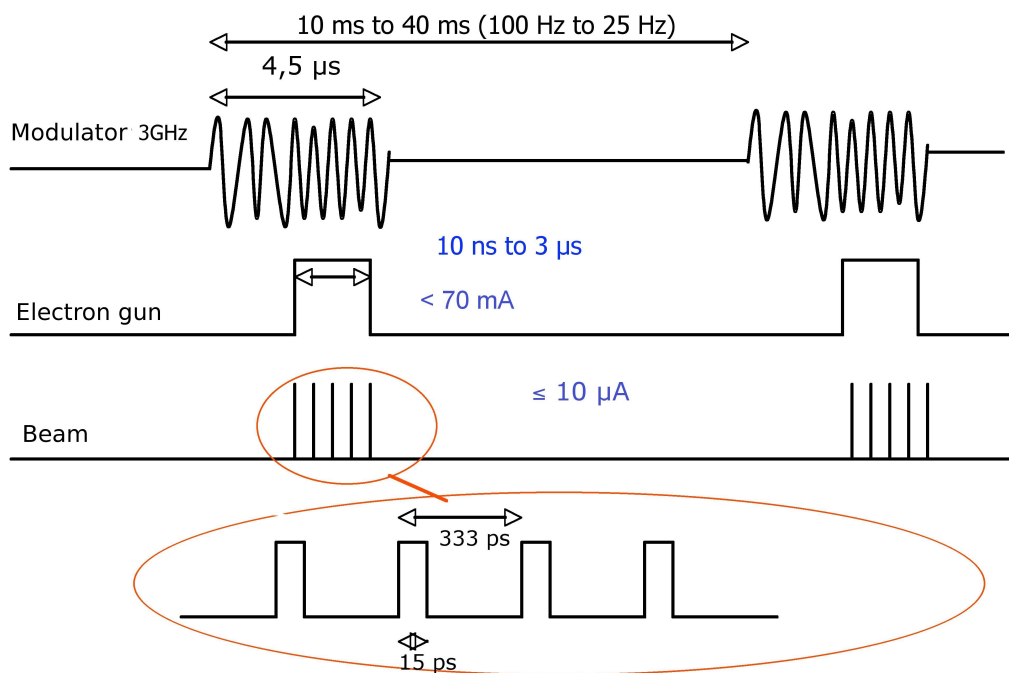
Figure 5.9: Time structure of the electron beam at the entrance of the accelerator [110].

5.4.2 Target and the ion source

Uranium carbide target (UC_x)

After the deflection in the dipoles, the electron beam strikes a uranium carbide target (UC_x). Electrons are converted into photons (Bremsstrahlung) in the first centimeters of the target. The generated electromagnetic cascade initiates the fission process. The uranium carbide target UC_x used in ALTO consist of 143 pellets (Figure 5.10) of 14 mm diameter and density of 3.36 g/cm^3 (in total 70 g) of uranium. The target is placed in cylindrical container made of graphite. This cylinder is mounted inside 20 cm long and few millimeters thick cylindrical tantalum oven. The target is heated up to 2000°C . This implies that the materials has to withstand the intensity 700 A and temperatures ranging up to 2000°C . In the middle of the cylindrical oven there is a 8 mm diameter hole to which the transfer tube is welded. This connection permits the effusion of the elements to the ionization source.
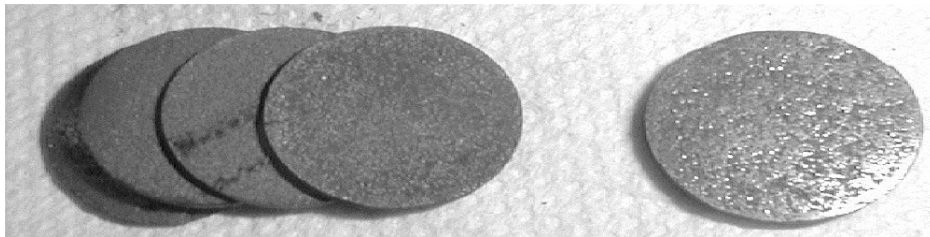
Figure 5.10: Photo of the uranium carbide pellets.

The release of a given element from the target depends on various physico-chemical parameters which are difficult to characterize at high temperature. The most volatile elements are alkalis (Li, Na, K, Rb, Cs, Fr) and noble gases (He, Ar, Kr, Xe ...). Their boiling temperature (the temperature when it changes into gaseous form, Figure 5.11) is relatively low. Although other elements such as metals (Al, Ga, In, Sn, Tl, Pb, Bi) or earth alkaline metals (Be, Mg, Ca, Sr, Ba, Ra) have a high boiling temperature they can still leave the target if the temperature is high enough. The saturation vapor pressure allows some of those elements to diffuse from the target and effuse to the ion source. However, if the melting and boiling points of the elements are too high, the elements remain in solid form and are extremely difficult to extract.
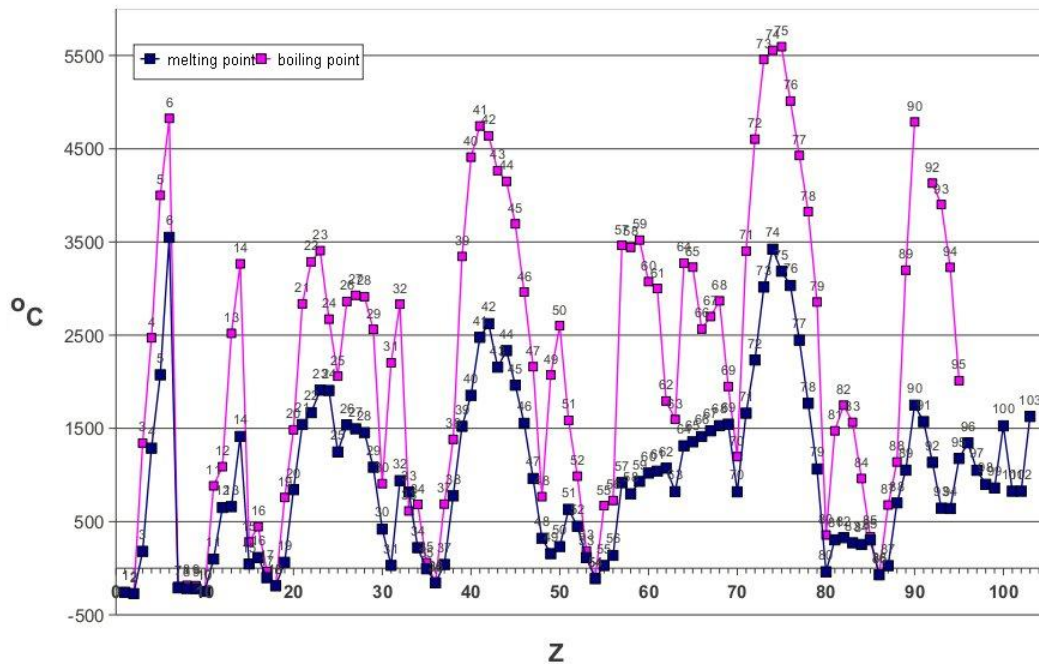
Figure 5.11: The melting and the boiling point for different chemical elements.

5.4.3 The laser ion source at ALTO

Ionization scheme for gallium isotopes

In case of the ionization of gallium atoms one uses ionization to the continuum method where two beams of laser are needed. The ionization scheme for gallium atoms, presented in Figure 5.12, consists of two steps:

- the first transition is an excitation of the electron from the electronic ground state $4s^2 4p^2 P_{1/2}$ to the intermediate excited state $4s^2 4d^2 D_{3/2}$. For this step the UV laser with a wavelength of 287.4 nm is used.

- the second step is the ionization from the $4s^2 4d^2 D_{3/2}$ level to the continuum using a green beam of 532 nm wavelength.

With the laser ion source the efficiency for the ionization of gallium atoms achieved at ISOLDE (CERN) was 21% [100].
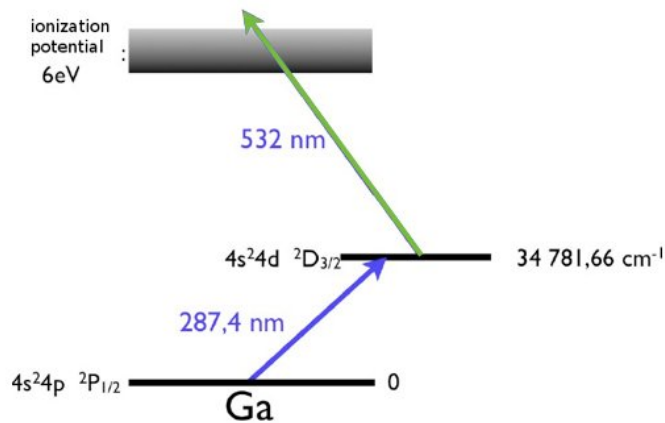
Figure 5.12: Two step ionization scheme for gallium [35]. The maximum efficiency for the ionization of gallium atoms with the laser ion source achieved at ISOLDE (CERN) was 21% [100].

Ionization of gallium atoms at ALTO

In order to insure maximum ionization of the gallium atoms in our experiment the new laser ion source system was built. The schematic view of the system is presented in Figure 5.13. It consisted of two lasers:

- the pump laser Edgewave Nd:Yag (model INNOSLAB IS2011-E). This laser provides vertically polarized 532 nm beam with a pulse repetition rate of 10 kHz and a pulse duration of 10 ns. The maximum rated power of the laser is 100 W.

- the dye laser (commercial-type Lambda Physik model FL3002). The Lambda-Physik dye lasers can deliver wavelengths from 300 nm to 900 nm. To obtain the wavelength of interest (UV light) a Rhodamine 6G dye was used. The dye laser has an oscillator, a preamplifier and two amplifiers. The oscillator and the preamplifier consist of a cell in which the dye flows at a high speed. This unit operates in two steps, the first is the oscillator (pumping the cell) that generates the laser beam required wavelength, and the second, the preamplifier that amplifies the beam.

Two laser beams are obtained in following procedure:

1. Inside the Nd:Yag laser, the cavity produces a light of a wavelength of 1064 nm. The frequency of this beam is doubled inside the laser with a nonlinear BBO (barium borate crystal BaB_2O_4) crystal to obtain at the exit a green laser beam of 532 nm. The beam coming out from the pump laser is split into two with a beam splitter (having 30% and 70% of the initial power for the first and second beam, respectively). The first beam of 532 nm is guided directly to the ionization tube. Since the cross section for this transition is low ($\sigma = 10^{-18} - 10^{-17}$ cm^2) the power of the laser was relatively high (30 W). The transmission of the beam to the ionization tube was 67% , 20 W at the source.
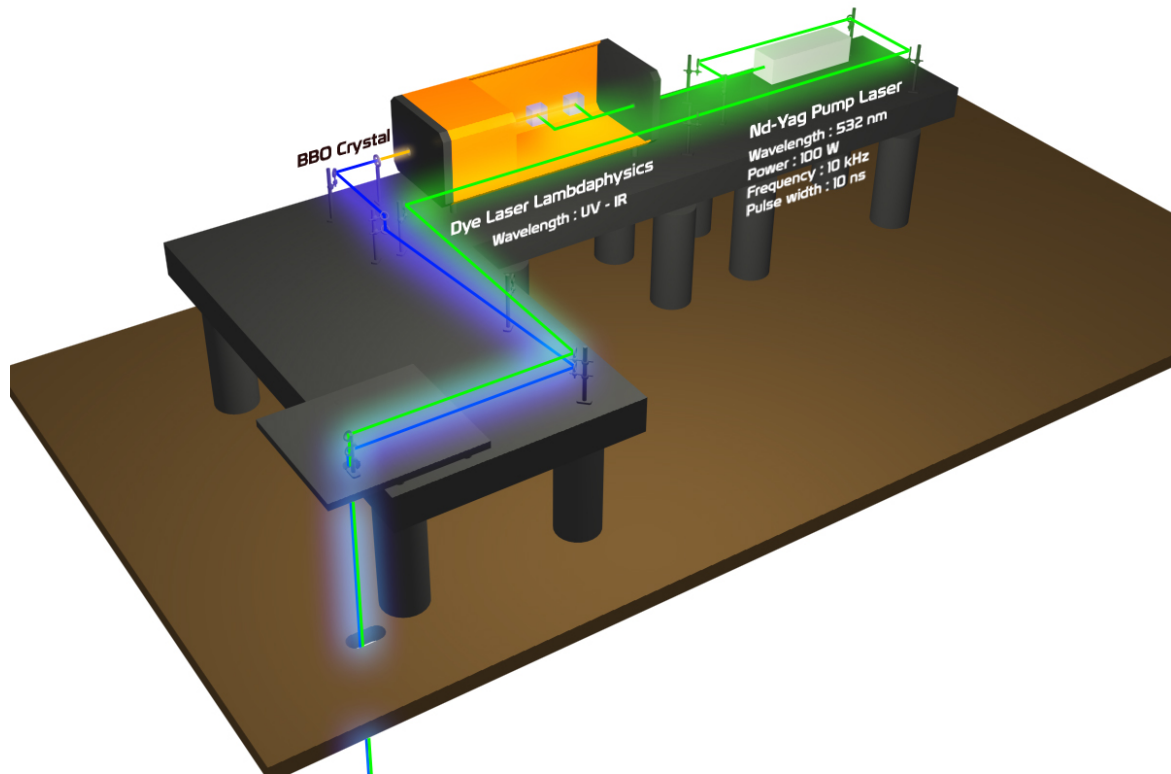
Figure 5.13: The laser ion source at ALTO (photo courtesy of B. Lesellier).

2. The second beam was sent to pump the dye lasers. After the 532 nm laser beam enters the dye laser the beam with the new desired wavelength is generated (in our case 574.8 nm) and the beam is amplified.

3. After the dye laser the beam of 574.8 nm is sent on BBO crystal to obtain the UV beam of 287.4 nm. The power of this laser (500 mW) is much lower than that of the pump laser but sufficient, since the cross section of this transition is high ($\sigma = 10^{-14} - 10^{-12}$ cm^2). This UV light is sent to the ionization tube. The transmission of the UV beam to the ionization tube was 24% , 120 mW at the source.

The wavelength of the beam was monitored with an optical spectrometer, commonly called "lambdameter". The ionization tube of a diameter of 3 mm is placed 8 m from the last optical element (optical prism) which sends beams towards the tube (Figure 5.14). To control the position of the beams in the tube, a partial reflection of the optical prism was monitored on a screen placed 8 m upstream to image of the ionization tube.
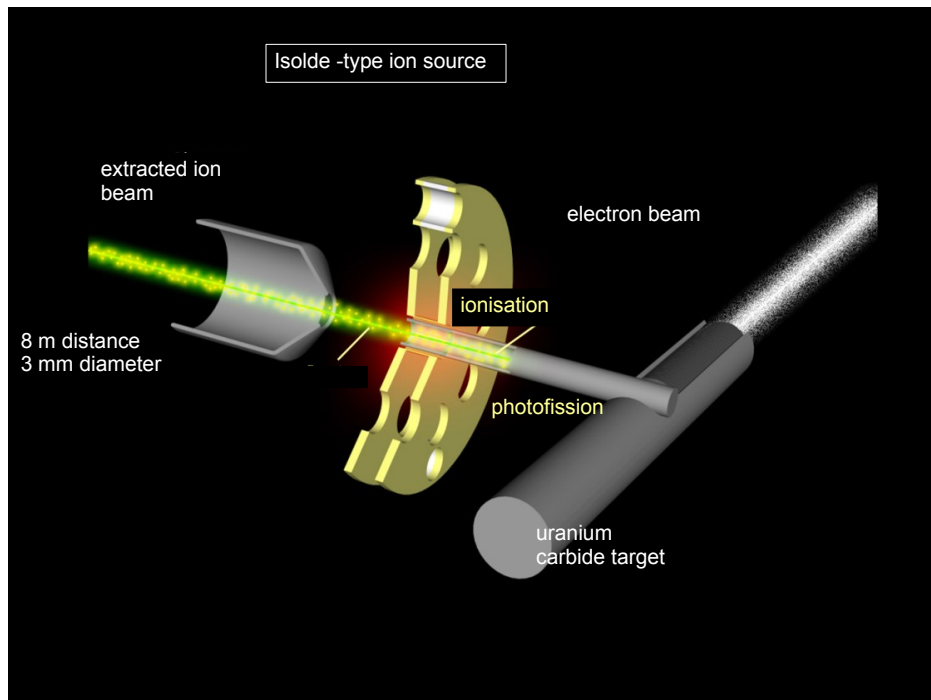
Figure 5.14: Schematic view of the ionization source (photo courtesy of B. Lesellier).

Performance of the laser ion source

The performance of the laser ion source was tested with a stable ^{69}Ga beam during a one week test run performed before the experiment to study ^{84}Ga beta-decay (see Chapter 6). The number of ions was monitored by measuring the current with two Faraday cups, one placed behind the mass separator and the second before the collection point on the tape. The ionization of ^{69}Ga with the laser was a factor of ten higher than with the surface ionization (the measured current was 1 nA and 10 nA without and with the laser, respectively).

Figure 5.15 shows a part of the γ-ray spectrum measured with the surface ionization ion source (blue) compared to the spectrum measured in our experiment with the laser ion source (red) for mass $A = 84$. The spectrum in blue was measured during the experiment performed in 2008 at ALTO [39, 49]. One can instantly notice a great improvement in the statistics and the purity of the spectrum achieved thanks to the laser ion source, higher beam intensity (blue: 1 μA, red: 10 μA) and the lead shielding of the mass separator to prevent the random coincidences of rubidium which was very abundant in the previous experiment.
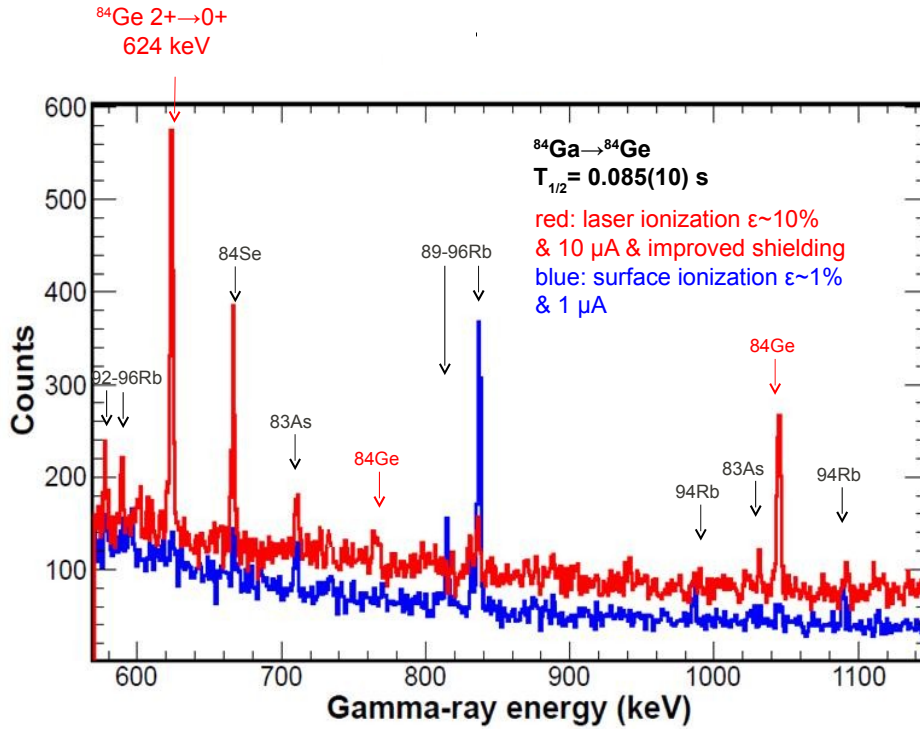
Figure 5.15: Energy spectrum measured for mass 84 with surface ionization ion source and wit the newly developed at ALTO laser ion source.

5.4.4 Mass separator PARRNe

Ions affected by the 30 kV potential at the exit of the ion source travel to the mass separator (PARRNe). The mass separator is isolated from the target-ion source unit with a 1.5 m thick concrete wall and the experimental room with a 20 cm thick concrete wall. It shields from background radiation (γ's) and neutrons coming from the target or accumulated in the magnet. The beam has a good optical quality and is well focused to optimize the transmission and the resolution of the mass separator. The ions are separated in mass with a H-shaped electromagnetic dipole separator [111, 112]. It has a homogeneous magnetic field B which is adjustable, a deflection angle of 65 °and a radius of curvature ρ of 60 cm. The mass selection is proportional to the mass number A of the nuclei and inversely proportional to the charge of the ion q $\cdot$ e ($\rho \cdot B = \frac{\sqrt{2 \cdot E \cdot M}}{q \cdot e}$ where M is the mass of the isotope). As most of the ions are of charge 1+, those are mass separated. The separation between two beams Δx of masses m and m + Δm is expressed by the equality $\Delta x = D \cdot \frac{\Delta m}{m}$ where D = 1370 mm is the dispersion of the magnet. As an example, the resolution of the separation of the masses 100 and 101 is 13.7 mm [89].

Experimental set-up

Contents

6.1   Experimental details

The experiment dedicated to study β-decay of neutron-rich gallium isotopes was performed at ALTO in 2011. It was the test run of the facility dedicated to the safety measurements in the phase of the commissioning of ALTO. The fission fragments were produced with the photo-fission reaction induced by 50-MeV electron beam in a thick UC_x PARRNe type target. It was the first experiment performed at ALTO where electron beam intensity was 10 μA which is the maximum electron intensity provided by the LINAC. The uranium carbide target was heated up to 2000 C to allow the diffusion of fission products. The elements diffused to the transfer tube where the gallium atoms were ionized with the selective laser ion source newly installed at the ALTO facility. Those gallium ions were extracted with the 30 kV electric field and traveled to the mass separator. The field in the PARRNe mass separator was set to pass only the atomic mass 84 (to obtain desirable pure beam of ^{84}Ga). At the last stage, those ions were implanted on aluminum-coated mylar tape.
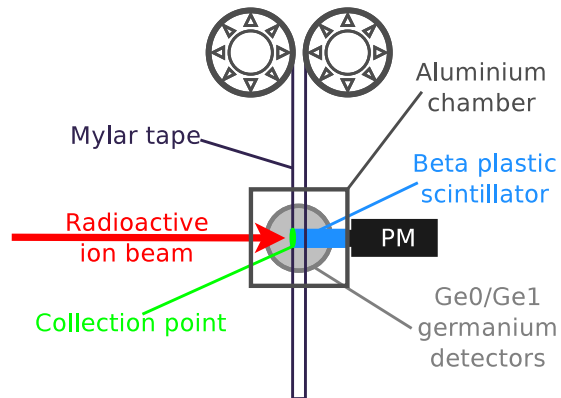
Figure 6.1: Schematic view of the tape station and the detection system. Figure courtesy of G. Germogli.

6.2 Detection system

6.2.1 The tape system

The nuclei of interest were implanted into the aluminum-coated mylar tape. The tape is rolled on two reels above the detection system. As it goes down it intercepts the beam, extends a bit farther down and turns up again ending in the second reel (Figure 6.1). The system is kept under the same vacuum as the beam transport line. The implanted radioactive nuclei and their descendants undergo β-decay. In order to obtain the clean spectrum (meaning not polluted by the γ-rays from the daughter nuclei) the tape has to be moved in cycles so that the implantation position changes and the previous one in far enough ($\sim$ 1.3m) to not to contribute as a background radiation source. The average time required for one tape move is 2 s. The tape movement was set and controlled with an automatic system which sends the signal to the acquisition system ("coding enable") once the tape is stable, to allow for the acquisition.

Choice of the measurement cycles

The choice of the time of the cycle obviously depends on the half-life of the element of interest and the half-lives of the daughters, as well as precision required for the half-life determination. The number of nuclei present on the tape increases owing to the production rate and decreases owing to the radioactive decay (Eq. 4.1). The number of parent nuclei decreases with time and the number of daughter nuclei increases as a result of the decay of the parent and decreases as a result of its own decay (Eq. 4.7). The relative production of ^{84}Ga on the tape (assuming that the neutron emission probability for gallium is 74(14) %[37]) and the descendants as a function of time is schematically presented in Figure 6.2.
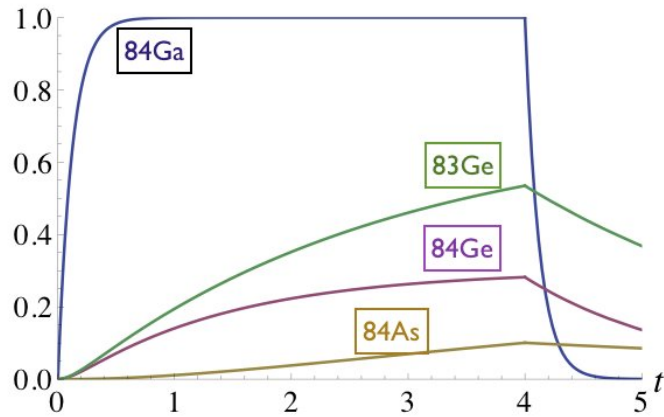
Figure 6.2: Simulation of the activity of ^{84}Ga and its descendants on the tape during the cycle of 4 s of "collection time" and 1 s "decay time".

The collection time was chosen to last three seconds:

- to discriminate the half-lives of the peaks. This information permits us to know the origin of the γ-line. If the half-life of the chosen line is compatible with the half-life of ^{84}Ga (half-live of ^{84}Ga 0.085(10) s [113]) one can believe this line belongs to the β/β n-decay of this element.

- in order to obtain as much as possible $\gamma - \gamma$ coincidences from ^{84}Ga β-decay. As seen in Figure 6.2 the production of gallium saturates already after 1 s of collection. The ^{84}Ga isotope is short lived and will decay during very short time (1 s). The longer the time when collecting ions the more decays and thus, the more $\gamma - \gamma$ coincidence recorded by the detection system.

- to have the least contribution from the descendants possible. The short-lived ^{84}Ga β/β n-decays to ^{83,84}Ge isotopes which then decay to arsenic. The longer the collection time the more descendants are created and the more peaks appear on the spectra recorded with germanium detectors. In order to minimize this contribution on the spectrum the production of the daughter nuclei (production through the decay of the mother) should not be higher than the one of the mother nuclei.

The time required for the decay of gallium (as seen in Figure 6.2) is only one second, and it was set to be the "decay time".

6.2.2 Electronics

The schematic view of the electronic system is drawn in Figure 6.3.

- germanium detectors: The signal from the detector was first connected to the preamplifier placed close to the crystal (to reduce the thermal noise and achieve an optimum charge collection). From the preamplifier the signal was sent to the Linear Amplifier where it was amplified and its shape was formed into semi-Gaussian shape. The decay part of the signal is determined by the feedback circuit of the preamlifier. To avoid so called undershoots (which is the differentiation of exponential tail from the preamplifier), which may cause an amplitude defect in case if the second signal arives just after the first one, the pole-zero cancelation circuit was used. The time signal from the detector was sent first to the Fast Timing Amplifier (FTA). It provided voltage pulses which amplitudes are proportional to the incident amplitudes. This signal was then changed into a logical signal by Constant Fraction Discriminator (CFD). The rising edge of this logic signal was used to trigger the acquisition of the energy channel. Since the Linear Amplifier process is much slower than the FTA or the CFD, in order to fulfill the condition of coincidence, the signal was delayed before entering to the acquisition card.

- BGO detector: Each of 10 crystals was connected to a photomultiplier. The signal from each PMT was sent to the Dual Gate Generator (DGG) where the threshold (the minimum energy of the incident gamma) for each of them was set independently. The signal from BGO shield was recorded as "marker" by acquisition card if there was an event detected in one of the crystals. This event was used to build a coincidence (when two signals, one from BGO and the second from germanium detector occur in short time interval) with the GFOC24 germanium detector.

- plastic detector $4\pi\beta$: The signal from the plastic detector $4\pi\beta$ was sent to the Constant Fraction Discriminator and then directly to acquisition card. This logic signal was used in the analysis process to built the coincidences with the germanium detector.

- Veto: The time signal from the plastic detector Veto was amplified with the TFA and then double with Fan In/OUT module. One of the signals traveled to the Dual Gate Generator and from there to acquisition card (as "marker" for GV1 germanium detector), the second was used as a timing signal to build coincidences with germanium detectors.
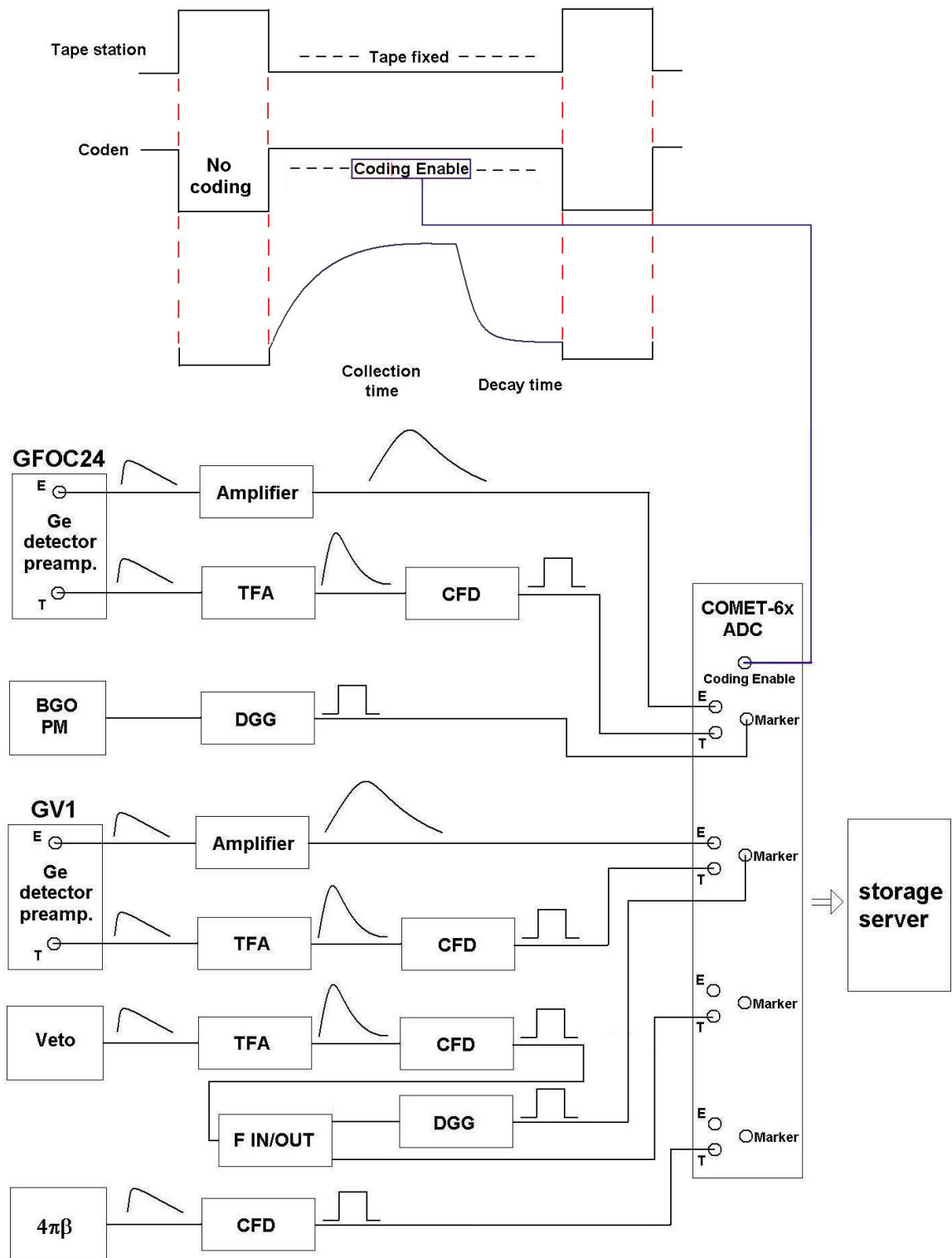
Figure 6.3: Schematic view of the electronic system.

6.2.3 Acquisition system

The analog signals from the electronics were transmitted to the acquisition card COMET-6x (Coding Marked Time) where they were converted into numeric format. The card has 6 channels, each channel has three inputs: one for energy signal, the second for time signal and the third input for the marker. The energy signal is coded in 15 bits, the time 47 bits and the marker is a logic NIM 1-bit signal. The COMET system is a trigger-less system. Each detector (plastic scintillator, germanium detector) is considered as an independent source for which the physical signal associated with an absolute time is coded. The time accuracy is 400 ps. The COMET card can encode up to 20000 events per second per channel (which is well above the count rate usually observed at ALTO when studying very neutron-rich species). During the experiment the CODEN (Coding Enable) signal was used. It is a TTL signal sent by the tape station system which inhibits the coding while the tape is moving (0 V coding inhibited, 5 V coding enable). Each cycle the absolute COMET time is reset to zero. Only the radiation from the cycles sent to the tape station system are measured. The data are transmitted and stored on the server. The data can be monitored on-line during the experiment with the computer program "cvisu". This program creates the energy spectra of 15 bits and time spectra of 47 bits.

6.3 Performance of the detection set-up

The detection system is presented in Figure. 6.4:

- two germanium detectors GV1 and GFOC24 (the energy resolution of 2.6 keV and 2.3 keV at 1 MeV, respectively) cooled down with liquid nitrogen using automatic cooling system,

- cylindrical shape $4\pi\beta$ plastic detector, providing an angular acceptance of 4πsr, was used to detect β particle from $\beta-$decay,

- to reject the background radiation (Compton contiuum), the detector GFOC24 was shielded with BGO shield (which is the prototype for the ORGAM2 project under construction in IPN Orsay). The BGO shield was used for the rejection of the Compton scattered γ-rays.

- plastic detector Veto was placed in front of the second germanium GV1. This detector was used to reject the electron continuum produced in the germanium crystal.
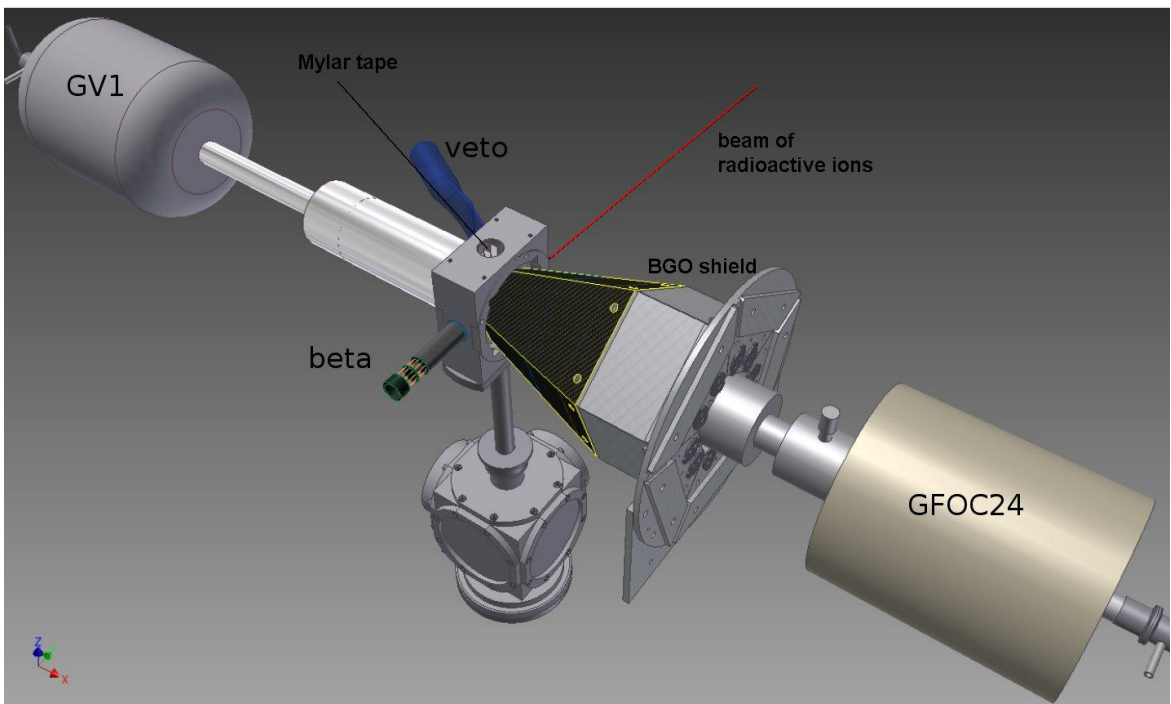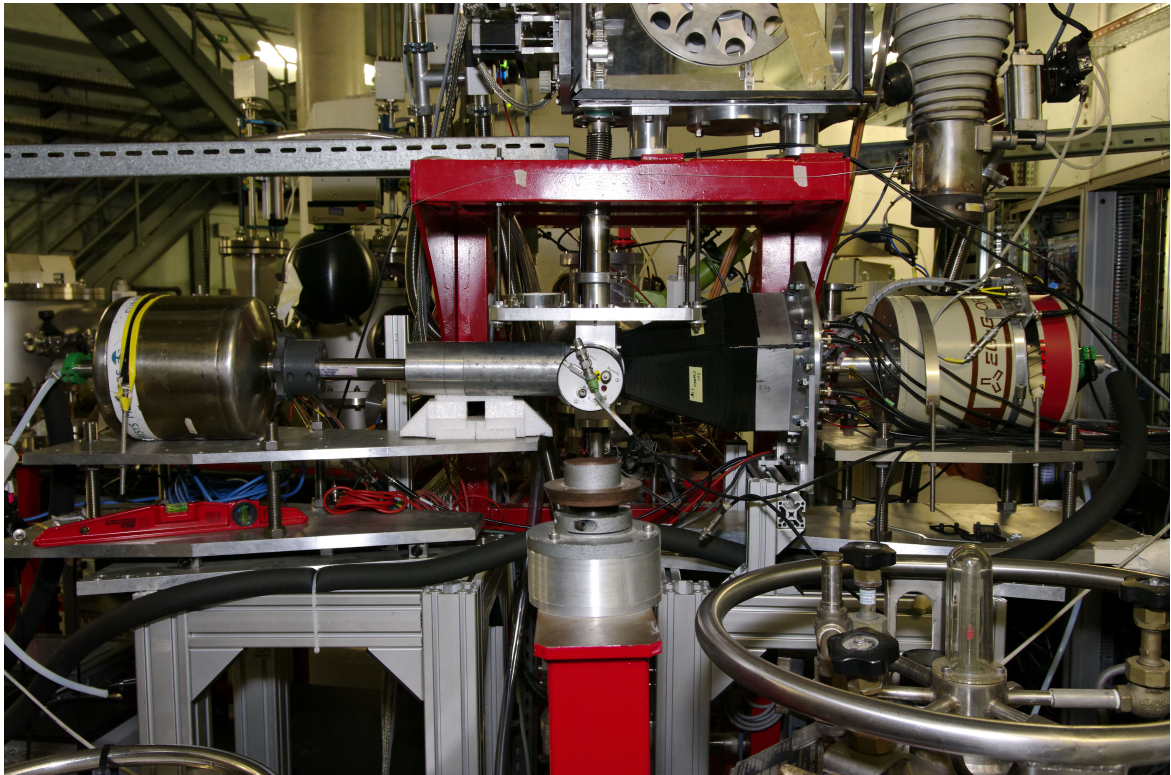
Figure 6.4: Top: Picture of the detection system. Bottom: Schematic view of the detection system.

6.3.1 Germanium detectors

Efficiency

The efficiency of germanium detectors was measured with calibrated ^{152}Eu, ^{137}Cs and ^{60}Co sources placed at the position of the collection point. The total efficiency of our detection system and a fit function with several adjustable parameters are plotted in Figure 6.5. The efficiency of the detection system was 2% at 1 MeV.
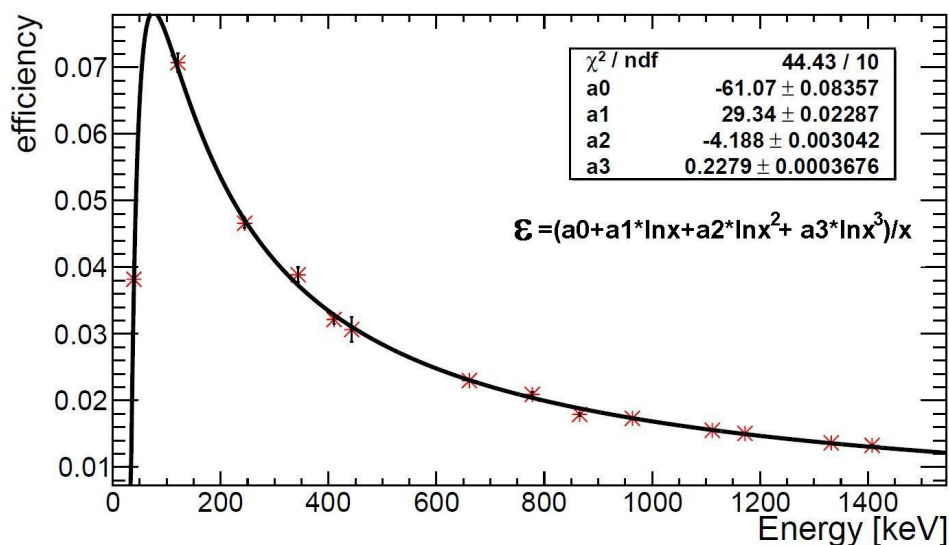
Figure 6.5: Efficiency of the germanium detectors measured with ^{152}Eu, ^{137}Cs and ^{60}Co sources.

Energy calibration and resolution

The energy calibration for germanium detectors was performed using the calibrated ^{152}Eu source and, additionally, for better precision at the higher energy, the tabulated peaks of ^{84}Ge [114] were used. As a fit for the energy calibration, second polynomial was used. The precision of the energy calibration is plotted in Figure 6.6. The resolution of the germanium detectors system as a function of energy is presented in Figure 6.7 for detectors GFOC24 and GV1. The energy resolution of the detection system was 2.8 keV at 1 MeV.

The timing resolution for β-γ coincidences, calculated from the full width at half maximum, was 20 ns and 40 ns for GFOC24 and GV1 at 1 MeV, respectively (for more details see Chapter 7, Figure 7.1).
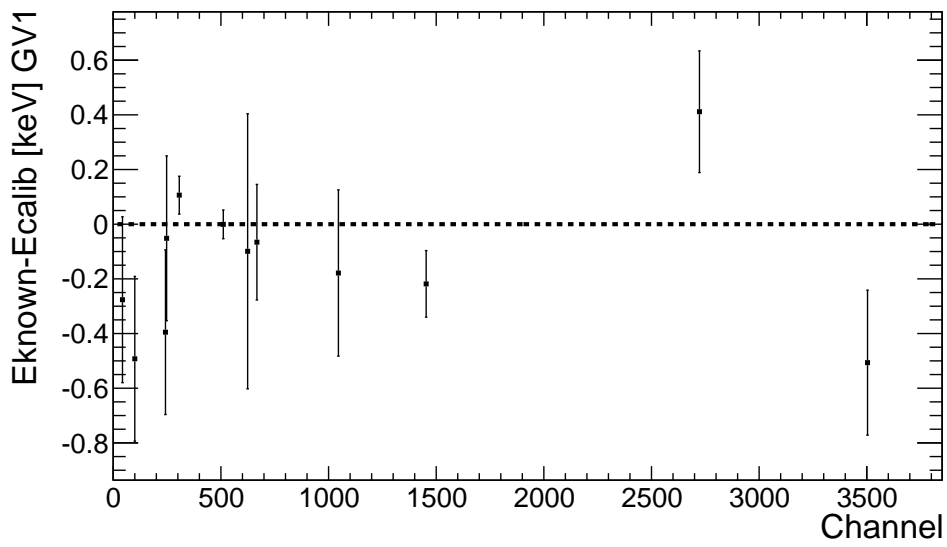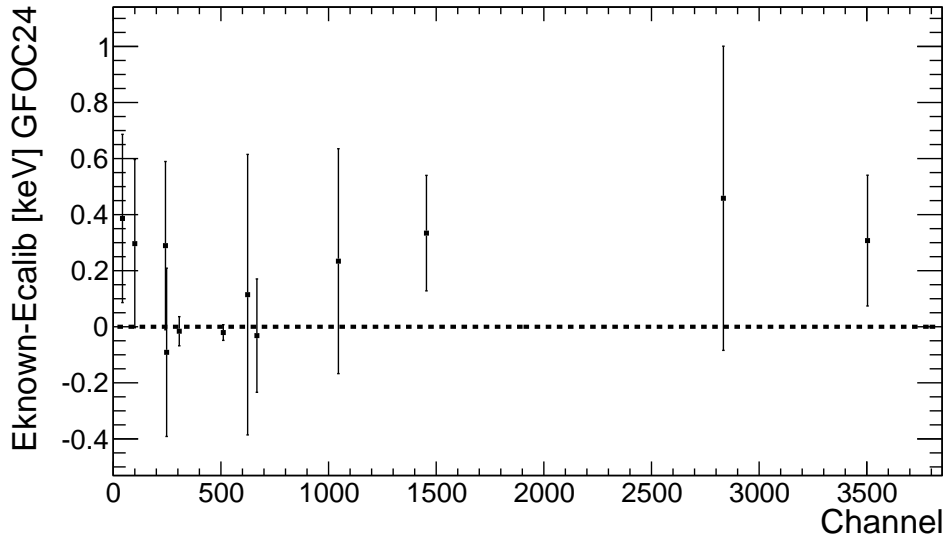
Figure 6.6: The precision plot of the energy calibration for GFOC24, GV1 germanium detectors. The energy precision is 0.4 keV and 0.5 keV for GFOC24 and GV1, respectively.
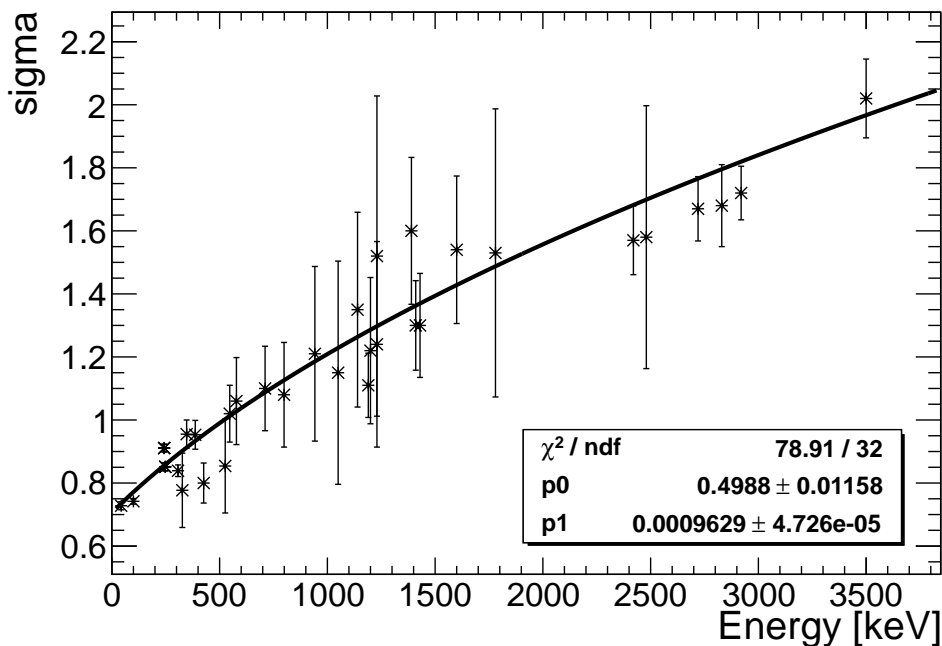
Figure 6.7: Resolution of the germanium detectors as a function of the energy. The resolution is measured with the spectrum from ^{84}Ga β-decay.

6.3.2   BGO shield

Of the various ways γ-rays can interact in matter photoelectric absorption, pair production, and Compton scattering are the most significant. Photoelectric absorption predominates for γ-rays up to several hundred keV, pair production predominates for energy above $5 - 10$ MeV, and Compton scattering is the most probable process over the range of energies between those extremes [115]. Partial absorption of γ-ray energy due to Compton scattering results in continous background (Compton continuum) which extends up to its maximum called Compton edge.

In our experiment bismuth germanate ($B_4G_3O_{12}$) scintillator detector was used as a shielding against Compton scattered γ-radiation. It consisted of five high-efficiency crystals mounted in pentahedral shaped carbon cell (Figure 6.8). Each of the crystals was connected to two photomultipliers. The signal from each photomultiplier was sent to the input of the Constant Fraction Discriminator. The threshold in the Constant Fraction Discriminator was adjusted for each photomultiplier, with ^{60}Co source placed in front of the germanium detector, in order to obtain the same counting rate in each of them.
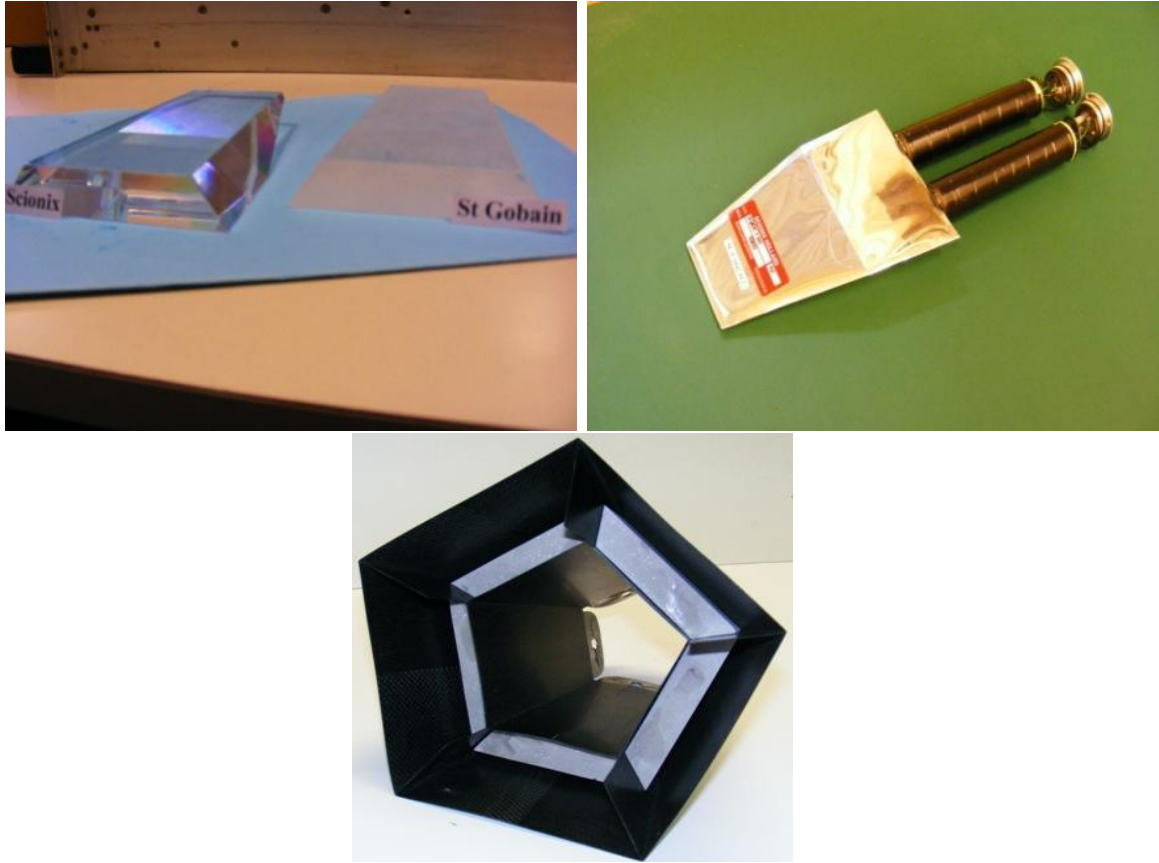
Figure 6.8: Left top: BGO crystals. Right top: two photomultipliers connected to BGO crystal. Bottom: the pentahedral carbon cell. Courtesy of T. Zerguerras.

The performance of the shield (the so-called rejection factor) was tested with the calibrated ^{60}Co source, with the source placed 2 cm in front of detector. The photo-peak to total ratio, the number of counts in the two cobalt peaks compared to the number of counts in the spectrum with and without the Compton rejection give the quantitative factor for the rejection. The results of the measurement is presented in Figure 6.9. Without the Compton rejection the ratio peak/total = 0.269. When we included BGO shield the ratio was 0.414 what indicates that a great part of the background was rejected. The suppression factor of the BGO shield as a function of incident γ energy is plotted in Figure 6.10. The suppression factor is the ratio between counts in the unsuppressed and suppressed spectra. The factor was on average 2, except for the high energy γ-rays going forward. Since the shield was placed around the germanium crystal forward and backward angles were not covered, thus highly energetic γ-rays are not rejected.
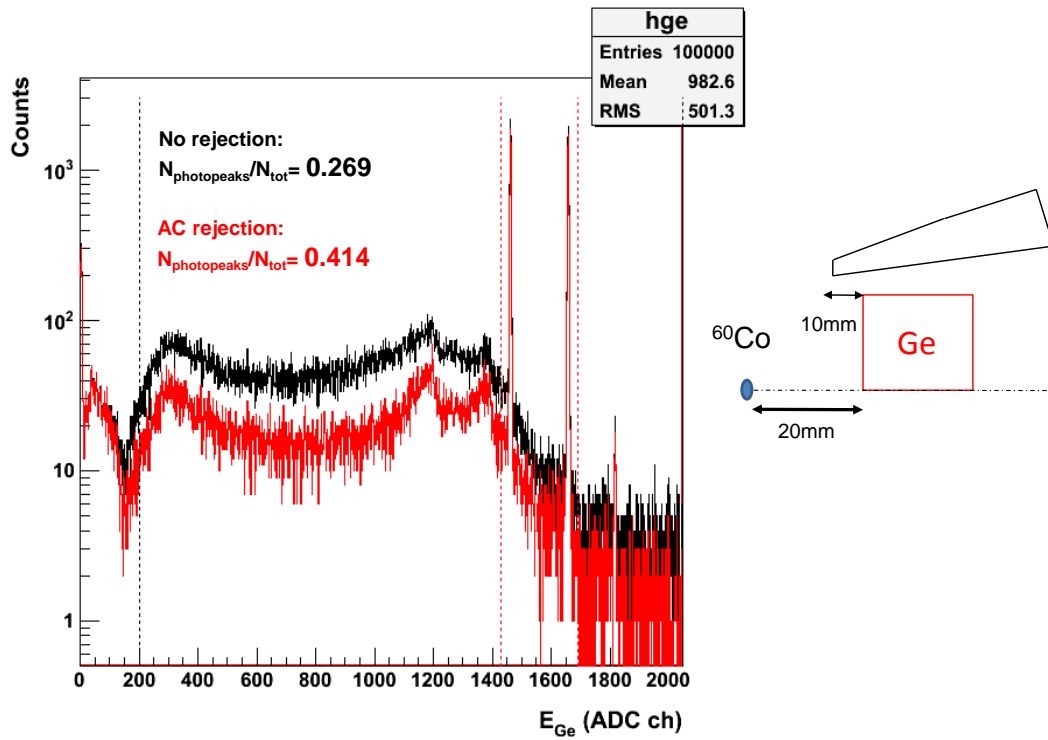
Figure 6.9: Measured γ-ray spectrum of ^{60}Co with and without Compton suppression. Figure courtesy of T. Zerguerras.
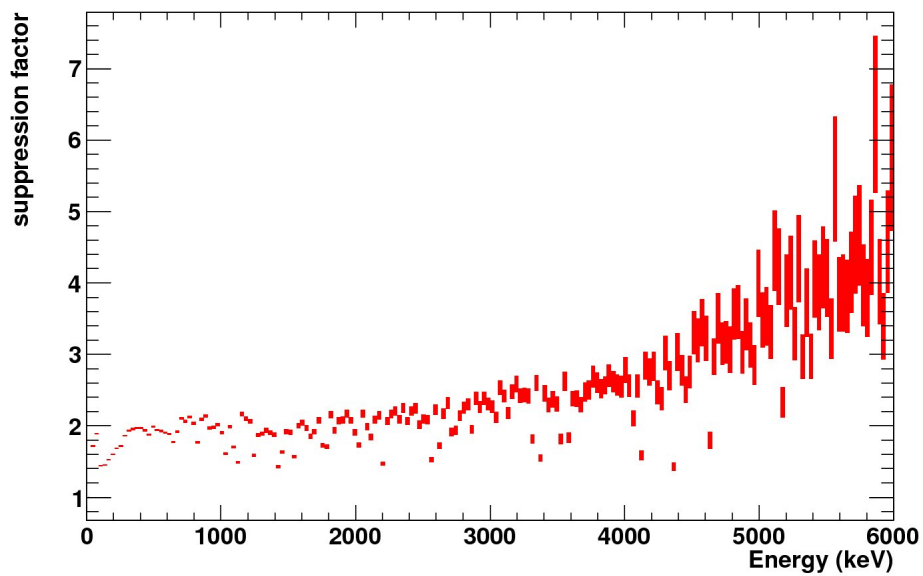
Figure 6.10: The suppression factor of the BGO shield as a function of incident γ-ray energy.

6.3.3 Veto detector

The primary electrons, β^- particles or electrons produced through various mechanisms of interaction of γ-radiation with matter, continuously lose their kinetic energy in the detector absorber material. Large deviation of their path are possible because its mass is equal to that of the orbital electron with which it is interacting and much larger fraction of its energy can be lost in a single encounter [115]. Electrons may lose their energy through radiative processes. The major component of such losses is Bremsstrahlung, which is an electromagnetic radiation produced by the interaction of fast electrons with the Coulomb field of a nucleus in the absorbing material and can be emitted from any position along the electron track. The fraction lost by this process increases sharply with electrons energy and becomes dominant for electrons with energy over few MeV [115]. The electron energy deposition through Bremsstrahlung in the germanium detector may extend to the maximum energy of the β-particle, but significant yields can be seen as a continuous low-energy background. In our experiment, the electrons interacting in the detectors originate from the β-decay of the ions implanted on the tape (in case of ^{84}Ga decay $Q_\beta = 13690$ keV [116]) or from the cosmic radiation in the detector (typically ionization muons). Because of close geometry of the detection system the backscattered electrons can also bring the contribution to the energy spectrum. The Bremsstrahlung contribution cannot be simply substracted as a background and its inclusion may lead to errors in measurements of peak areas. In order to minimize this background the plastic Veto detector (Figure 6.11) was placed in front of germanium detector GV1 to serve as a marker for the events created by the electrons.
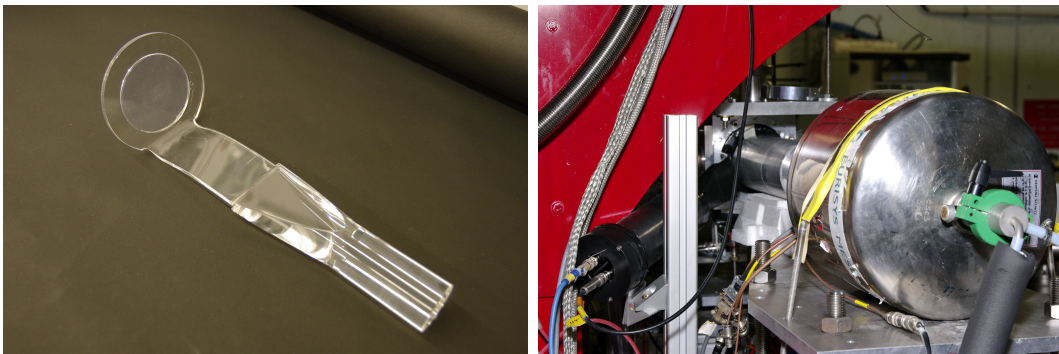
Figure 6.11: Left: Picture of the Veto plastic detector. Right: Veto detector installed in front on the germanium GV1 detector. Courtesy of S. Ancelin.

The result of the background subtraction with the Veto plastic detector in presented in the coincidence spectra in Figure 6.12. The black line is the $\beta - \gamma$ spectrum of the

detector GFOC24 and the $4\pi\beta$ plastic detector. With the $\beta-\gamma$ coincidence one ensures to have in the spectrum the γ-lines which belong to the β-decay. The blue line presents the result of β-γ-BGO anticoincidence where the coincidence with the BGO shield is included (one can clearly see the disappearance of the Compton-scattering part of the spectrum). However, even after Compton rejection the low energy background is still present. It most probably originates from Bremsstrahlung process. In order to find out what is the origin of this background the third spectrum was built with the coincidence with the Veto detector (red line). In this case the accepted events where those that occured in detector GFOC24 in coincidence with $4\pi\beta$ and anticoincidence with BGO shield if at the same time the electron was detected on the other side of the interaction point: in the Veto plastic detector. Obviously, since the Veto detector was placed in front of GV1 detector, the acceptance angle was small and the statistics on the spectrum is low. The optimal position would be to mount it in front of GFOC24 and use in anti-coincidence procedure. Nevertheless, the data analysis described above helped us to understand the origin of this background. The lower-energy continuous background, greatly minimized on the red spectrum, as suspected comes from the electron contribution in the germanium detector.
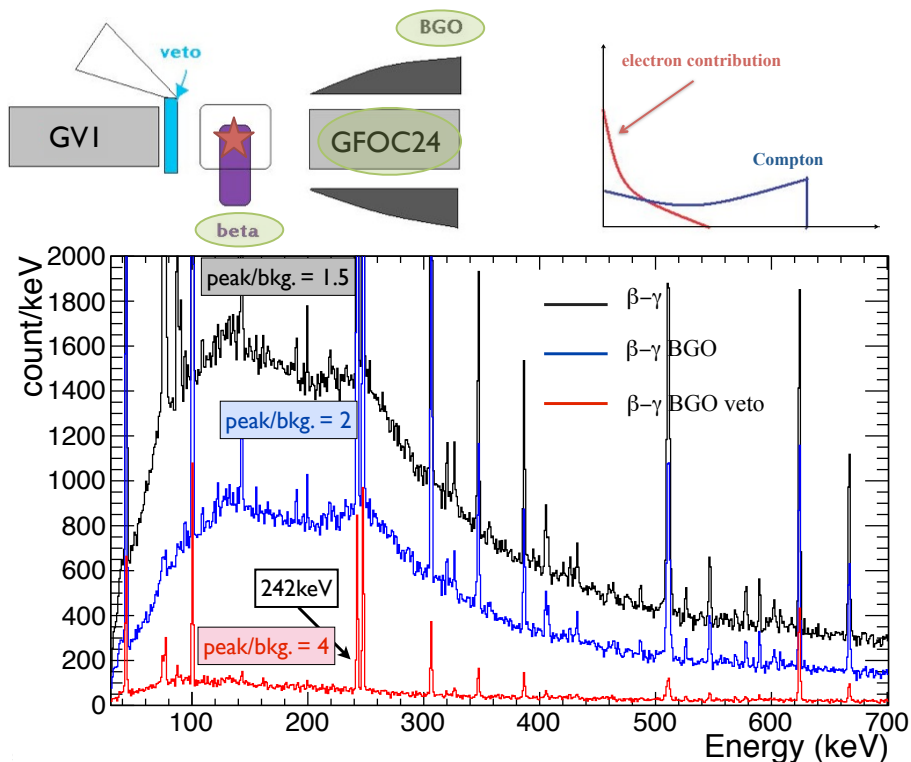
Figure 6.12: The $\beta - \gamma$ coincidence spectra with background rejection. The peak/background ratios at 242 keV: without Compton rejection 1.5, with Compton rejection 2, including the coincidence with the Veto detector 4.

Data analysis and results

Contents

7.1 Analysis procedure

The data generated by COMET-Narval acquisition are registered, event by event, in a format specific for this acquitistion system [117]. Since we decided to perform the analysis with software ROOT, the data generated by the COMET-Narval acquisition were converted with NarvalToRoot "Event Builder" [49] to a format (ROOT) suitable for their further treatment. The events were stored in the ROOT trees (TTree), each divided into several branches containing specific information (e.g. energy, time, marker). The type of each branch was declared depending on the information it contained. To optimize the size of the data each branch was compressed independently, this conversion reduced the volume of the data by at least one third compared to the COMET-Narval format where the data are not compressed. The time required to reread the data is also greatly reduced, especially when one wants to re-read only specific branches. The branches could be read independently from each other, depending on the needs.

Analysis of the data requires the reconstruction of the correlations between different events, e.g. in case of β-decay considered events are β particle and γ-ray. The acquisition in the COMET system is triggerless which means that each detected event is saved on the disk with a time stamp (an integer stored in 47 bits) where "time" (in β-decay experiment with measurement cycles) is relative to the last coded signal and each signal resets the clock. The ROOT tree contains the raw data with the time stamp conversted into double precision float (64 bits) and the events are listed in chronological order. The time of the event is used to build so-called "coincidences" which associate events in time when the time window for those events is less than a time window ("coincidence window") specified by the user.

In the following subsections, the procedure of the data analysis is described. At first, the β-γ coincidences time spectra are presented and the time resolution of the germanium detectors is calculated. In the second part, we describe the procedure for determination of the half-life of γ-lines. Finally, the example of the analysis of γ-γ coincidences is shown.

7.1.1 Time spectra

It is essential to build a β-gated energy spectrum to assure that the γ-lines in the spectrum come from the β-decay. The coincidence of γ-ray detected in germanium detector and β particle seen by plastic detector allow us to built that kind of energy spectra. In order to obtain a proper energy spectrum one needs to investigate the time spectra for the coincidences. The plastic detectors are much faster than the germanium detector, thus in principle, one expects to see the γ events in the germanium after the β particle as a trigger detected in the plastic. The time spectrum is the difference in time between those two events (β and γ), or in other words if the β detector is a trigger and its time is set as a start zero time then the time distribution follows the time of the γ-ray detected after β-particle. To build the coincidence events the "coincidence window" was chosen to be 500 ns. The distribution of β-γ coincidence events, for each energy of γ, in time is presented in Figure 7.1. Once gating on the chosen energy (in Figure 7.1 the gate is set on 1000 keV) one obtains the time distribution (right side of the figure). One can see the steep slope on the left side of the peak and the tail of the right side. This tail is an electronic effect coming most probably from badly set Constant Fraction Discriminator treshold and should not be considered for the further analysis. The time resolution for β-γ coincidence calculated from the full width at half maximum, was 20 ns and 40 ns for GFOC24 and GV1 at 1 MeV, respectively. To build the β-gated γ-spectrum (presented in Figure 7.6) or for β-γ-γ events (Figure 7.4) those time gates were used.
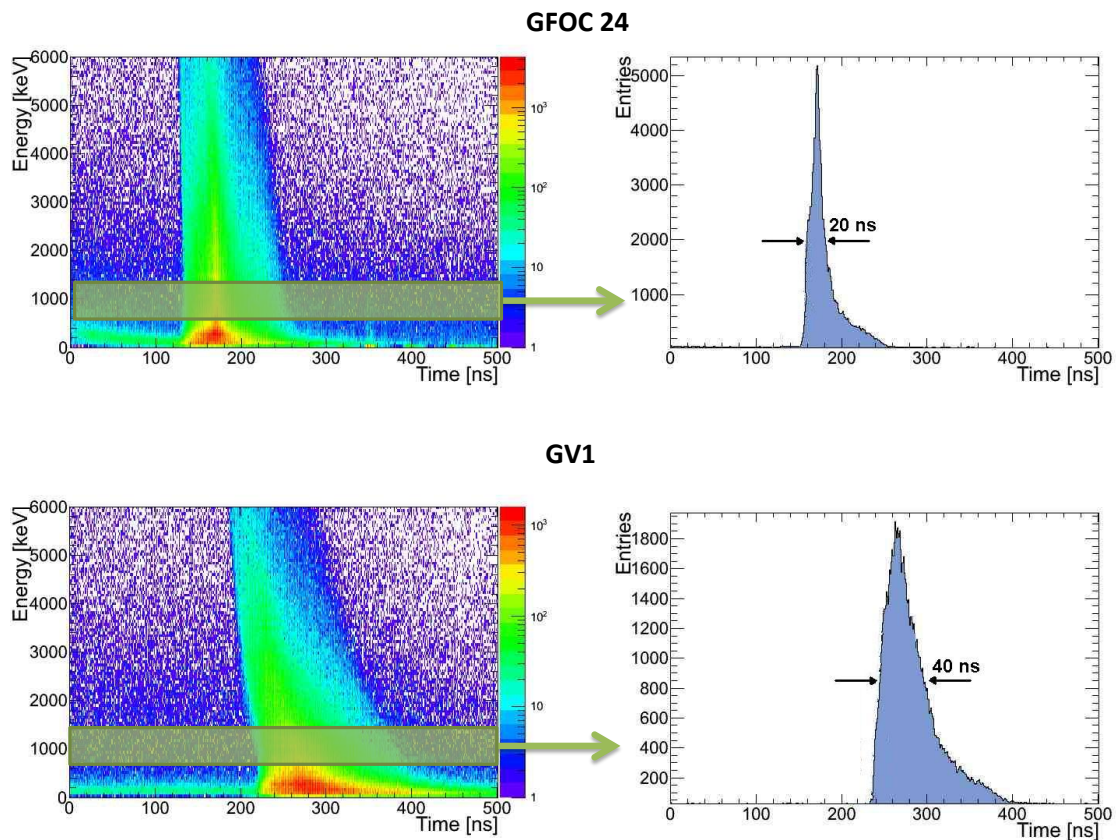
Figure 7.1: Time distributions of $\beta - \gamma$ coincidence events for the GFOC24 detector (upper) and the GV1 detector (lower plot).

7.1.2   Determination of the half-life

The "time-energy" matrix represents the energy as a function of time in the measurement cycle. To build this matrix the contribution of all channels of germanium detectors is summed. The time-energy matrix allows to monitor the activity of γ-lines over a period of time. Using this data one is able to discriminate the half-life of the γ-line of interest and assign it to the proper decaying element.

The example of the determination of half-life for line at 624 keV ($2^+ \rightarrow 0^+$ transition in ^{84}Ge) is presented in Figure 7.3. The time-energy matrix was analyzed in partial time of 20 ns. Each 20 ns the energy spectrum was built, the gaussian peaks and the polynomial functions were used for fitting both to the peak and the background. The result of the integration of the peak was used to built the activity spectrum in time (right top in Figure 7.3). In the final step, the half-life was determined from the fit of the growing and decaying parts of the curve (see Figure 7.2).

Figure 7.2: Example of the determination of the half-life. Two function were fit: one to the growing part and the second to the decaying part.
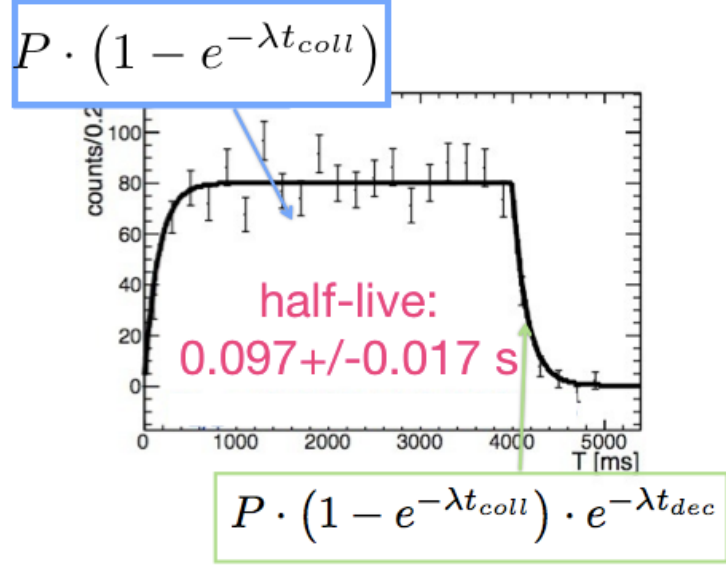
If we consider the decay of the mother to the daughter the following equations hold:

$$A_{coll} = P \cdot (1 - e^{-\lambda t_{coll}}) \,, \tag{7.1}$$

$$A_{dec} = P \cdot (1 - e^{-\lambda t_{coll}}) e^{-\lambda t_{dec}} \,, \tag{7.2}$$

where A_{coll}, A_{dec} are the activities during the collection and the decay time, P is the production of the mother nucleus and $\lambda = ln2/T_{1/2}$ contains the half-life of interest. The times are chosen to be $0 - 4$ s collection and 1 s for the decay.
If one needs to consider the decay of the second generation the half-life will be obtained from:

$$A_{coll} = P \cdot (1 - e^{-\lambda_1 t_{coll}}) + P \cdot \frac{\lambda_2}{\lambda_2 - \lambda_1} (e^{-\lambda_2 t_{coll}} - e^{-\lambda_1 t_{coll}}) \tag{7.3}$$

$$A_{dec} = P \cdot \frac{\lambda_2}{\lambda_2 - \lambda_1} \left[\lambda_2 (1 - e^{-\lambda_1 t_{coll}}) e^{-\lambda_1 t_{dec}} - \lambda_1 (1 - e^{-\lambda_2 t_{coll}}) e^{-\lambda_2 t_{dec}} \right] \tag{7.4}$$

where the index 1 describes the mother and the index 2 the daughter nucleus.

As 624 keV is the γ-line from $(2^+ \rightarrow 0^+)$ transition in ^{84}Ge, Eq. 7.1 and Eq.7.2 were fit to determine properly the half-life. The obtained results $0.097(17)$ s is consistent with the tabulated value $0.085(10)$ s [113], thus, proving that the line comes from the decay of ^{84}Ga.
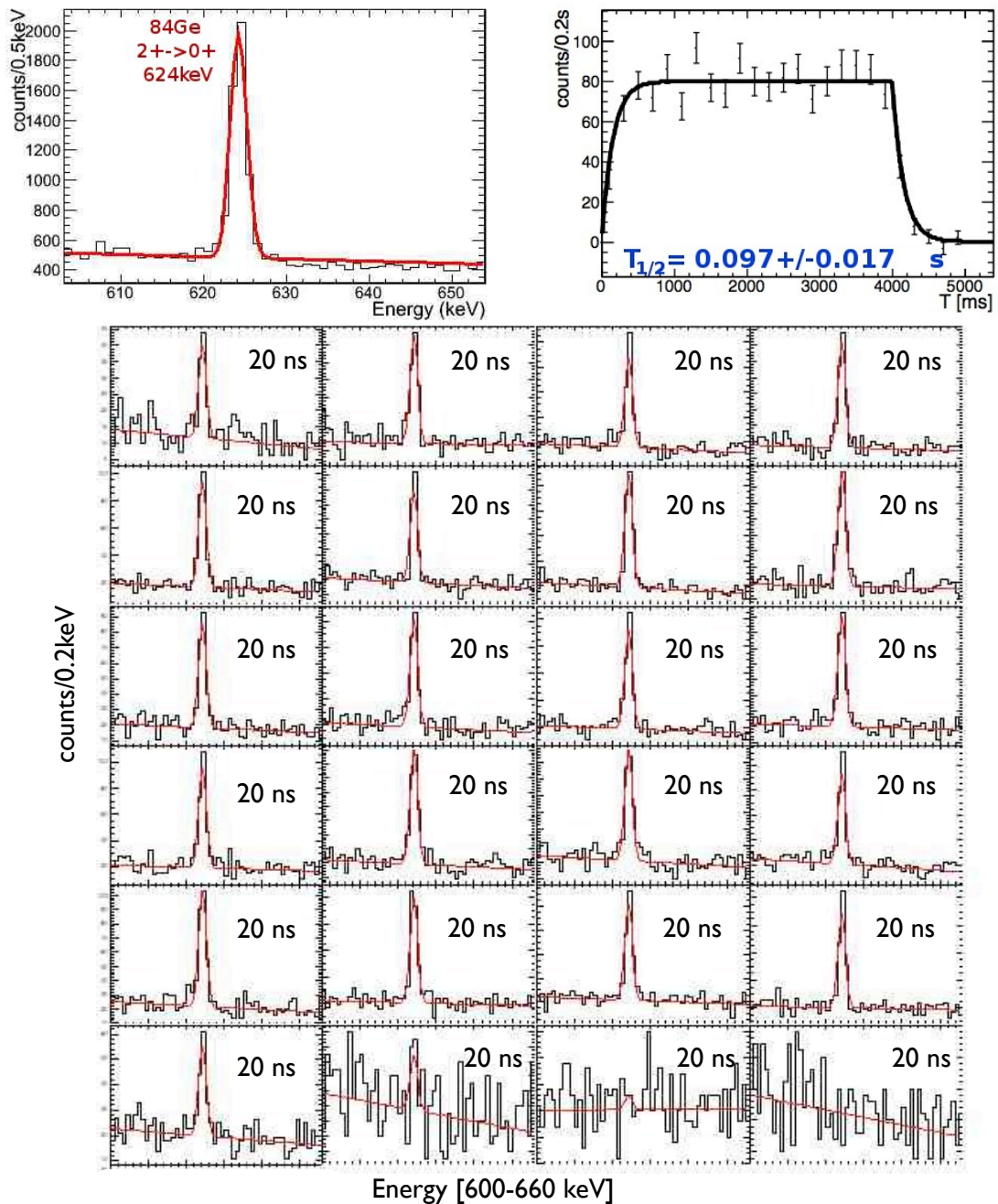
Figure 7.3: Procedure for the determination of the half-life. Left top: gaussian fit on the γ-line of interest, right top: a result of the time distribution from the fitting procedure, bottom: fitting of the peak and the background in different time periods.

7.1.3 The γ-γ coincidences

The "energy-energy" matrix contains the triple coincidence of the β-γ-γ events in the specified "coincidence window". It allows us to seach for the γ-γ coincidences in the β-decay which would correspond to the γ cascade in the excited states of the nucleus of interest. The matrix in presented in Figure 7.4. Except for the clear points from the γ coincidences one can also see oblique line from the backscattered γ-rays (due to a very close detection geometry).
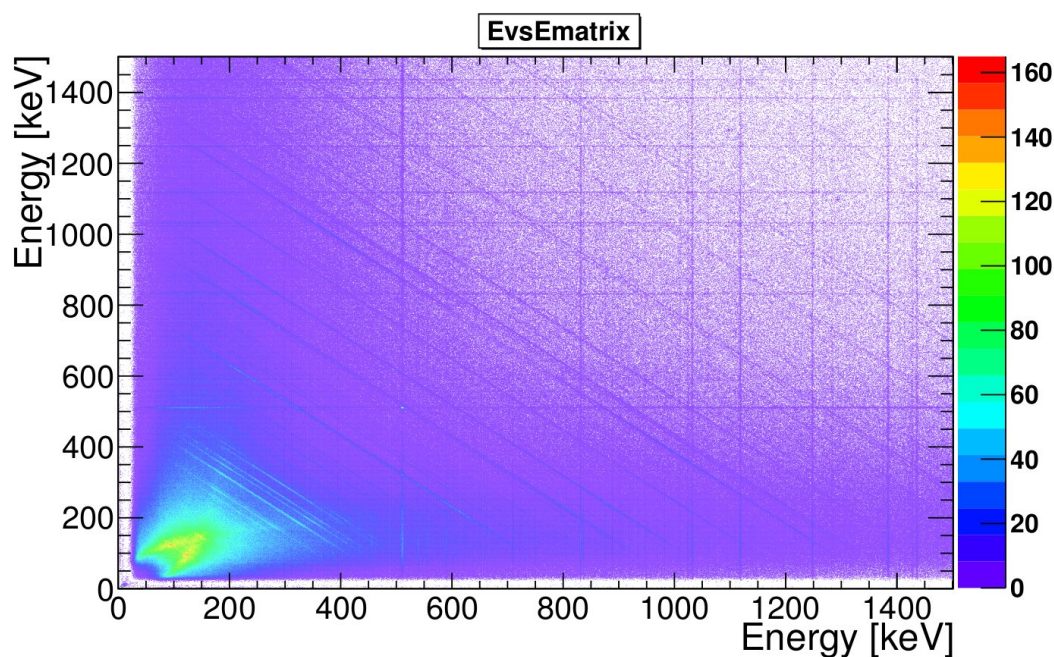
Figure 7.4: The γ-γ coincidence energy matrix.

With the energy-energy matrix one can search for the γ-γ coincidences. The procedure is as follows: after choosing a peak of interest and subtracting the background from the right and left side of the peak and correcting from the factor of the number of channels one obtains the coincidence spectrum. To confirm the coincidence it is important to gate on the γ-line seen in the coincidence to check if the coincidence really exists. The example of the coincidences with line at 624 keV ($2^+ \rightarrow 0^+$ transition in ^{84}Ge) is shown in Figure 7.5. One can clearly see three lines: at 765 keV, 1605 keV and 2878 keV in coincidence with 624 keV. The concidences are confirmed while looking at gate on those three γ-lines: the peak at 624 keV is well visible.
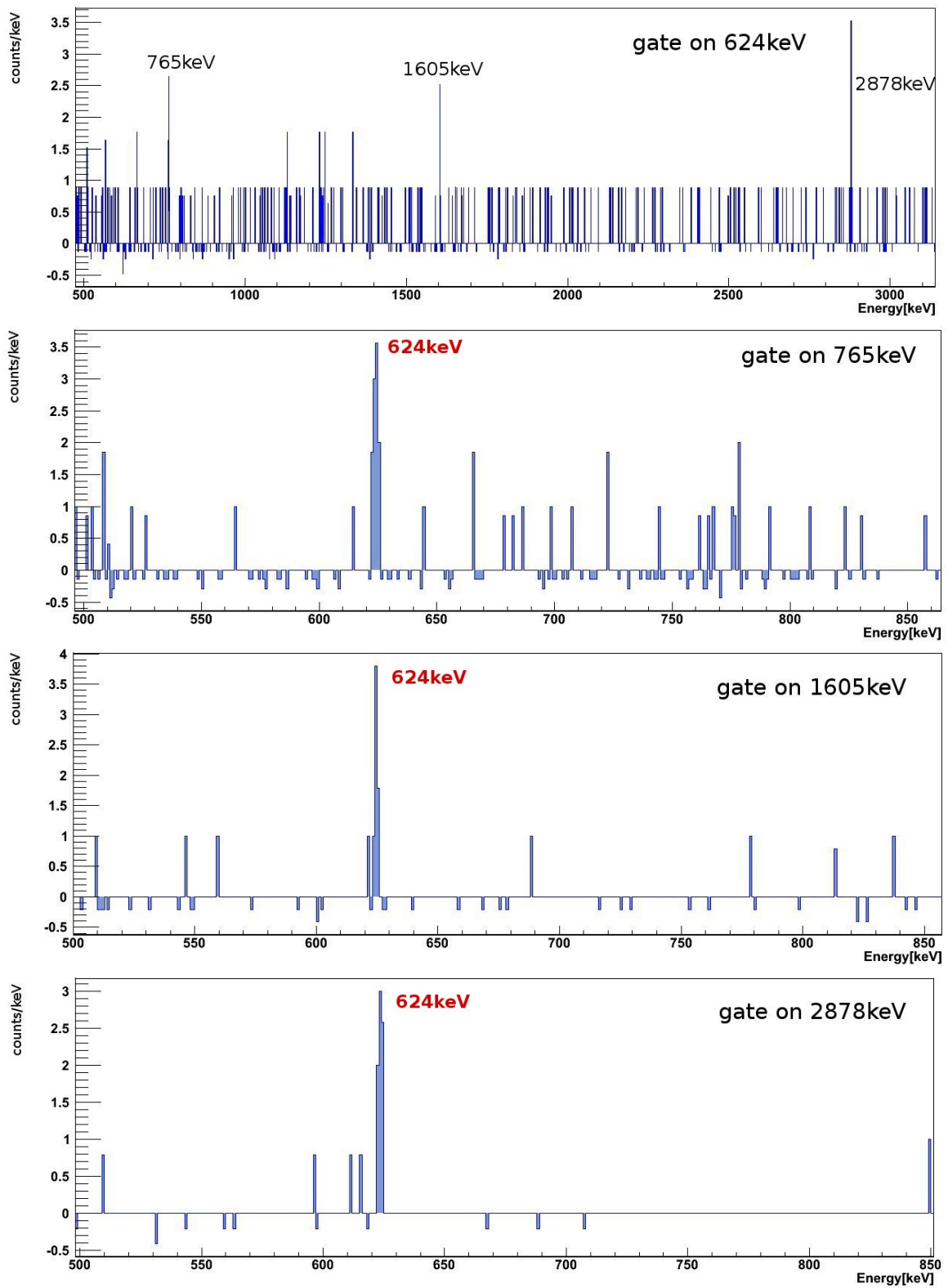
Figure 7.5: The coincidence spectra for line 624 keV. Gating on the lines from the coincidence one can clearly see 624 keV γ-ray, thus confirm that the two transitions belong to the cascade.

7.2 Experimental results

7.2.1 The β-gated energy spectrum

The β-gated γ-spectrum measured during three-day experiment is presented in Figure 7.6. One can see the peaks belonging to ^{83,84}Ge,^{83,84}As and ^{84,83}Se. There are also γ-lines belonging to the neutron-rich Rb isotopes with mass ranging from 89 to 96. The Rb isotopes are strongly favored in both the fission process and the ionization mechanism. For the ionization of gallium atoms the laser ion source was used, however, since the transfer tube is a W ionizer heated up to 2000 C which selectively ionizes alkalies and also elements with particularly low first ionization potentials (see Figure 5.5). The Rb isotopes were stopped within the separator chamber which was additionaly shielded with lead blicks. However, due to their high activity some of the γ-lines appear as random coincidences with β events. Despite this experimental difficulty the γ-lines characterizing the activity of nuclei of interest are clearly visible proving that ^{84}Ga was successfully ionized with the laser ion source and collected on the tape.

7.2.2 Results for ^{84}Ge

Thanks to higher electron beam intensity $(10\mu A)$ and a laser ion source we were able to increase the statistics. A new shielding around the focal plane of the magnet allowed us to have less contaminants from the Rb isotopes. We were able to discriminate the half-lives through γ-lines present in our spectrum and obtain $\gamma - \gamma$ coicidence spectra. The population of the excited states of ^{84}Ge through the β-decay of ^{84}Ga allowed us to improve the level scheme of ^{84}Ge. The first results from the β-decay studies of ^{84}Ga were observed at ISOLDE-CERN. The two short-lived elements with γ-lines: one at 624.3(7) keV and the other at 1046.1(7) keV [38, 39] were seen and assigned as belonging to the level scheme of ^{84}Ge: as 2_1^+ and 4_1^+ excited states. This result, however, was not confirmed by Winger [37] who placed the 4_1^+ state at 1389.0(10) keV and the γ-ray transition of 765.1(8) keV in coincidence with 623.9(6) keV.

The results of the half-life determination for four γ-rays assigned to the β-decay of ^{84}Ga are presented in Figure 7.7. Their determined half-lives: 0.097(17) s, 0.107(93) s, 0.159(100)s, 0.086(29)s are all consistent with the half-life of ^{84}Ga $T_{1/2} = 0.085(10)$ s [113]. From the coincidence spectra (presented in Figure 7.5) we were able to confirm the existence of the state at 1389.1 keV and the coincidence with γ-ray of energy 623.9 keV, as well as improve the level scheme by adding two new coincidences (623.9 keV with 1603.9 keV and 2878 keV) and the transitions to the ground state.

Due to the low statistics in the peaks at 1389 keV and 2878 keV, the determination of
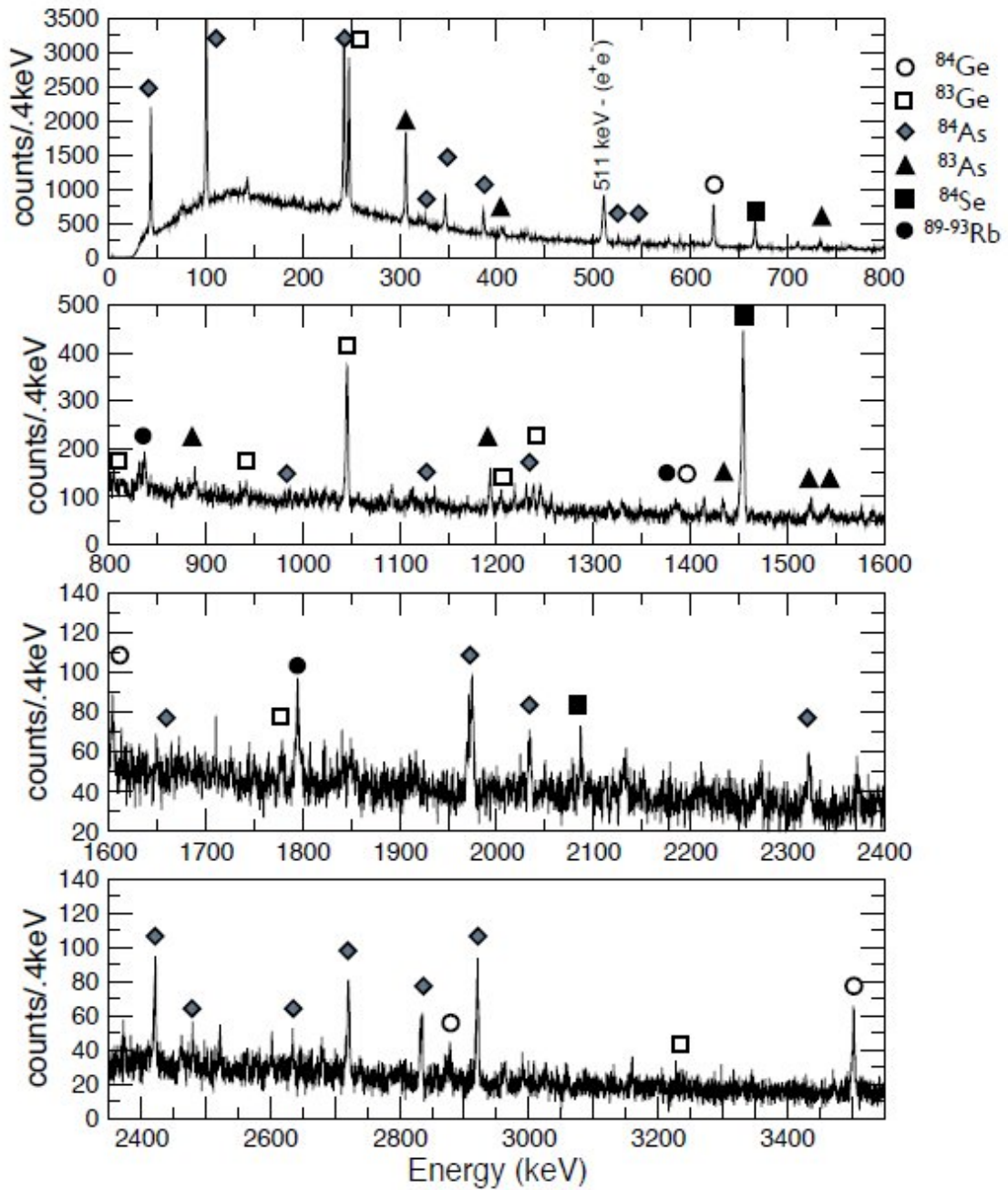
Figure 7.6: Single γ spectrum conditioned with β and BGO detectors.

their half-lives was not possible. However, the coincidence spectrum for the 2878 keV γ-line with 624 keV ($2^+ \rightarrow 0^+$ transition in ^{84}Ge) is already convincing enough to allow us to assign these transition to the level scheme of ^{84}Ge.
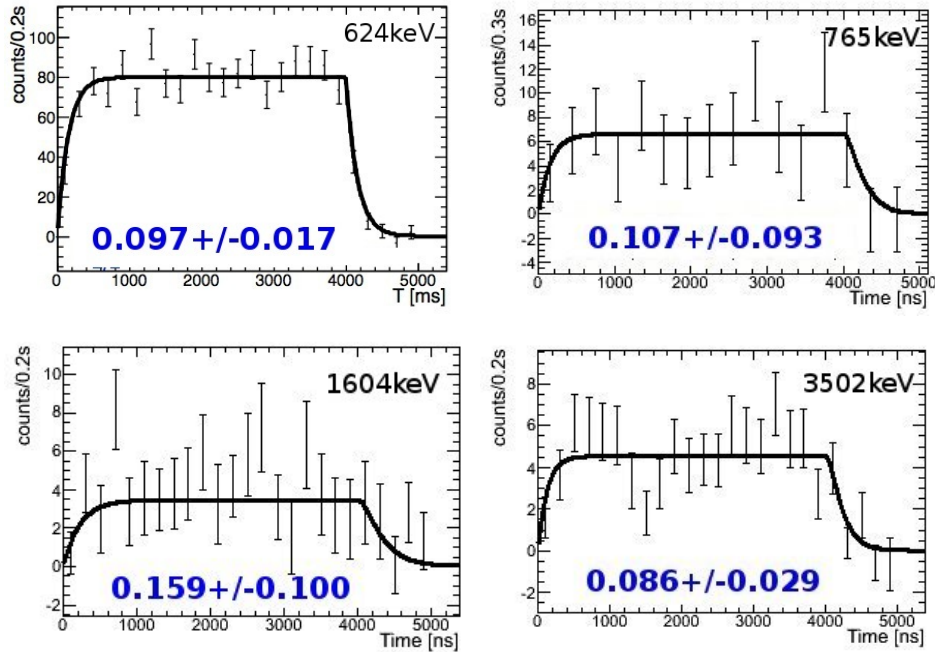
Figure 7.7: The results of the half-life (in seconds) determination for the lines of ^{84}Ge.

Table 7.1: The final list of γ-lines observed in the β-decay of ^{84}Ga assigned to the de-excitation from the excited states of ^{84}Ge. The list contains the energy of the γ-ray, the intensity as relative to the most intense γ-ray, the energy of the excited level and the calculated half-life. The γ-ray with asterix to be confirmed.

Energy [keV]	Relative intensity [%]	Level [keV]	Half-life [s]
624.2(2)	100(5)	624.2(2)	0.097(17)
765.1(3)	15(4)	1389.3(4)	0.107(93)
*1389.3(4)	9(5)	1389.3(4)	
1603.9(2)	16(4)	2228.1(3)	0.159(100)
2878.1(6)	21(7)	3502.3(6)	
3502(1)	50(7)	3502.3(6)	0.086(29)

To ensure the possibility of the transition at 1389 keV in ^{84}Ge we performed carefull analysis of the γ-peak 1389 keV. The zoom on the β-gated energy spectrum in the region of the peak is presented in Figure 7.8. As one can see, the peak of interest is small and located close to another peak at 1385 keV. The number of counts in peaks was estimated: 74(30) counts in the peak at 1385 keV and 28(9) counts in the peak at 1389 keV (see Table 7.2).
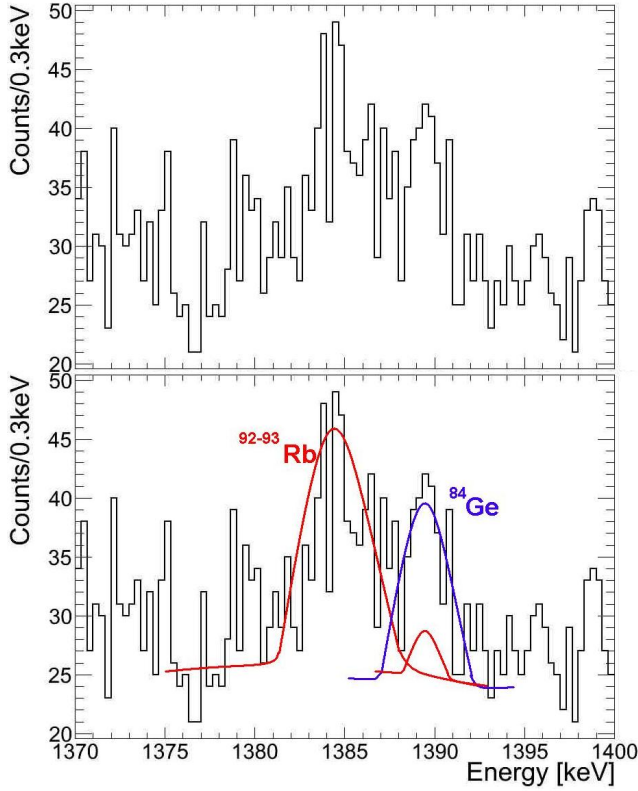
Figure 7.8: Single β gated energy spectrum zoomed to show the region of interest $(1370 - 1400$ keV) and the peak at 1389 keV.

Table 7.2: Contribution of the activities of rubidium isotopes in peaks at 1385 keV and 1389 keV.

Energy$_{peak}$ [keV]	Counts in peak	Element	T$_{1/2}$ s [116]	Energy [keV]	Intensity % [116]	Counts
1385	74(30)	^{92}Rb	4.49(2)	1384.6(3)	3.6(7)	2(1)
		^{93}Rb	5.84(2)	1385.21(8)	6.6(3)	74(32)
1389	28(9)	^{91}Rb	58.5(4)	1388.13(44)	0.22(3)	3(1)
		^{93}Rb	5.84(2)	1388.7(6)	0.26(6)	1(1)

The peak at 1385 keV was identified as random coincidence γ-line from ^{93}Rb isotope with half-life of 5.84(2) s [116]. This isotope has also very weak transition at 1388.7(6) keV (intensity of 0.26(6)%). The estimation of the contribution from rubidium isotopes in those two peaks was done starting from the analysis of the biggest peaks found in the spectrum. ^{93}Rb has the strongest line at 432.61(2) keV (20.2(10)% [116]) and the second strongest at 986.05(6) keV (7.9(4)%). We used those lines to estimate the total activity of this isotope and further the contribution in the two peaks: 1385.21(8) keV and 1388.7(6) keV. This contribution was found to be 74(32) counts and 1(1) counts, in those two peaks respectively (see Table 7.2).

Figure 7.9: The resulting level scheme of ^{84}Ge. In black already known [37, 38, 39], in red newly discovered transitions, the dotted transition: tentative assignmet.
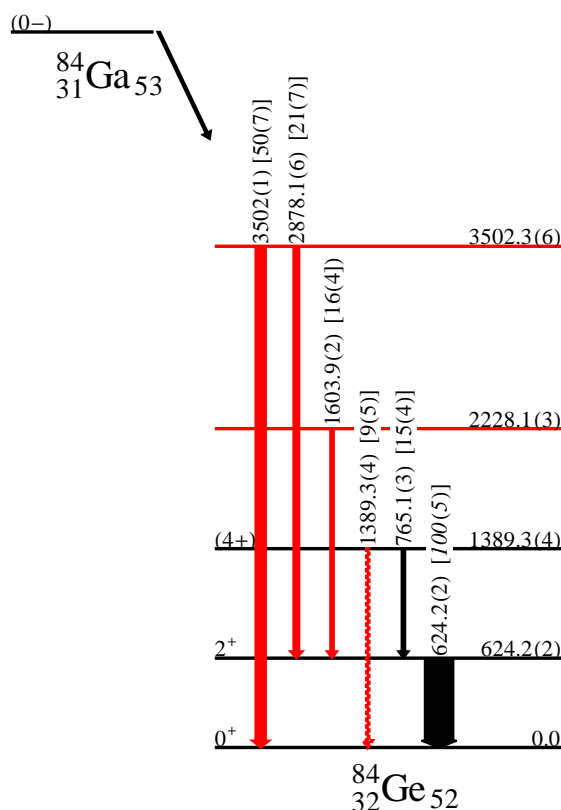
^{92}Rb (half-life of 4.49(2) s [116]) has line at 1384.6(3) keV with intensity of 3.6(7)%. The same procedure was done for this isotope starting from its strongest transitions: γ-lines of energy 814.98(3) keV (33(2)% intensity [116]) and 569.8(1) keV (5.6(3)% intensity [116]) to estimate the total activity. Then the contribution of ^{92}Rb in the peak of interest at 1384.6(3) keV was calculated to be 2(1) counts. Third strongest γ-line of ^{91}Rb was identified at 439.15(3) keV (2.09(10)% intensity [116]), using this line we estimated the number of counts of this isotopes at the energy of 1388.13(24) keV (0.22(3)%) to be 3(1) counts.

The peak at 1385 keV was identified as ^{93}Rb. Even summing the possible maximum activities of ^{91}Rb and ^{93}Rb in the peak at 1389 keV (6 counts) there is still contribution from the other element (22 counts) which we assign as the transition in ^{84}Ge. The final level scheme is presented in Figure 7.9 and the list of γ-lines, their relative intensities and half-lives are listed in Table 7.1.

7.2.3 Results for ^{83}Ge

Up to now, only few transitions were assigned to the level scheme of the neutron-rich ^{83}Ge. The low-lying excited states of ^{83}Ge were populated in (d,p) reaction with ^{82}Ge beam at the Holifield Radioactive Ion Beam Facility (HRIBF) at Oak Ridge National Laboratory (ORNL) [47, 44], and with the β-decay of ^{83}Ga performed at IPN Orsay [48, 49] and at HRIBF [37] (β-decay of ^{83}Ga, β n-decay of ^{84}Ga).

In our experiment we populated the excited states of ^{83}Ge with β n-decay of ^{84}Ga. The results of the discrimination of half-lives of few γ-lines are presented in Figure 7.10.
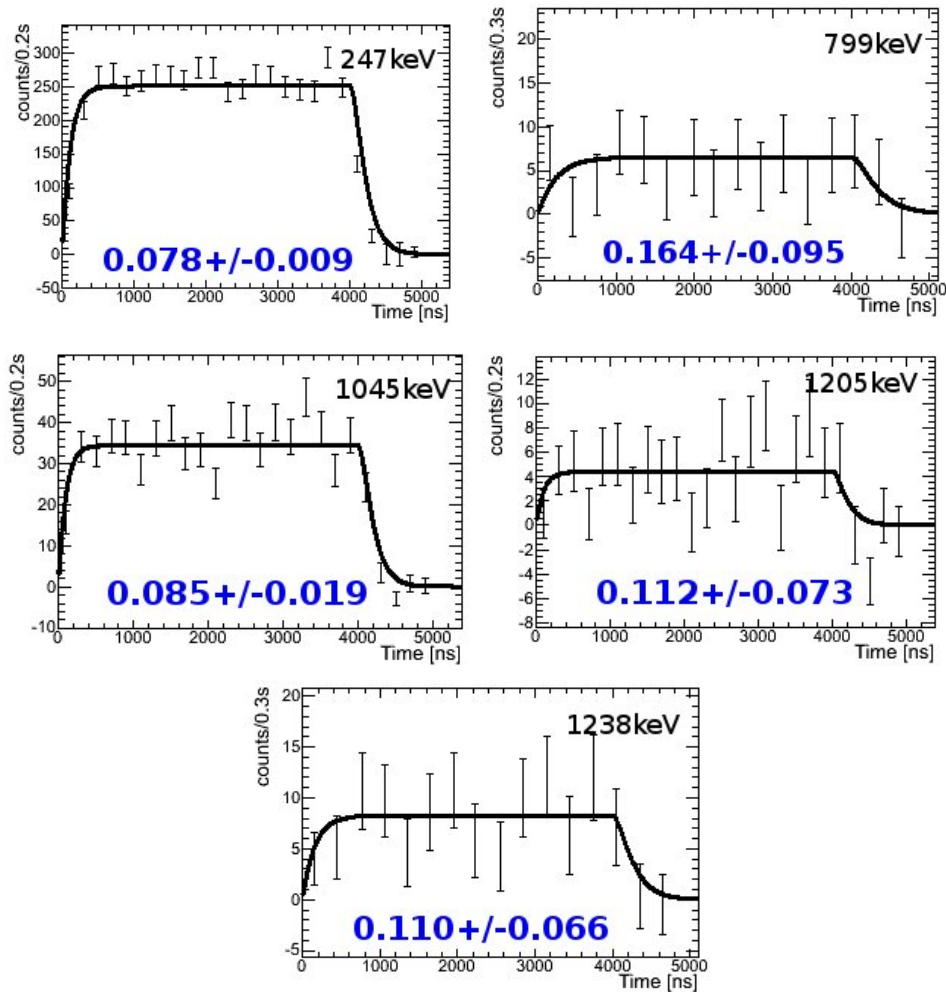
Figure 7.10: The results of the half-life (in seconds) determination for the lines of ^{83}Ge.

From the $\gamma-\gamma$ coincidence analysis three concidences with line at 247.7 keV were found (Figure 7.11): at 798.9 keV, 1204.9 keV and 1778.7 keV, and two weak concidences with line at 1045.9 keV, one at 941 keV and the other at 2193 keV. Having seen the coincidence of 247.7 keV with 798.9 keV we confirm the existance of the excited state at 1045.9 keV (as stated in [37]). The half-life of the line at 1045.9 keV was determined to be short (85(19) ms) and this information permits us to believe it comes from the β or β n-decay of ^{84}Ga. There is no coincidence with other known γ-ray, neither from ^{83}Ge nor ^{84}Ge, however, since there is an excited level at this energy in ^{83}Ge, this γ-ray is assigned to belong to a level scheme of ^{83}Ge (as in [37]). We confirm the γ-line at 1238 keV but no new coincidence for this line was found. There was no visible peak at 867 keV (possible $7/2^+$ from [48], assigned by Winger [37] as transition in ^{82}Ge), however, if this line is really $7/2^+$ in ^{83}Ge, since the spin of this level is high, starting from a low spin (0^- [39]) mother, one would not expect to populate this state with β n-decay.

The level scheme for ^{83}Ge is presented in Figure 7.12. The list of γ-lines, their relative intensities and half-lives are listed in Table 7.3. Six new γ-line were added, two in coincidence with 247 keV, two (however weak, thus presented with dashed lines, tentative assignment) with 1045 keV, and two transitions to the ground state.

Table 7.3: The list of γ-lines observed in the β-decay of ^{84}Ga belonging to the excited states of ^{83}Ge. The list contains the energy of the γ-ray, the intensity as relative to the most intense γ-ray, the energy of the excited level and the half-life. The γ-rays with asterix: tentative assignmet.

Energy [keV]	Relative intensity [%]	Level [keV]	Half-life [s]
247.7(3)	100(3)	247.7(3)	0.078(9)
798.9(3)	5(1)	1045.9(4)	0.164(95)
*941.5(4)	5(1)	1987.4(5)	
1045.9(4)	55(3)	1045.9(4)	0.085(19)
1204.9(6)	7(2)	1452.7(4)	0.112(73)
1238.4(8)	9(3)	1238.4(8)	0.110(66)
1778.7(4)	6(2)	2026.4(5)	
2026(1)	3(1)	2026.4(5)	
*2193(1)		3238(1)	
3238(1)	6(2)	3238(1)	
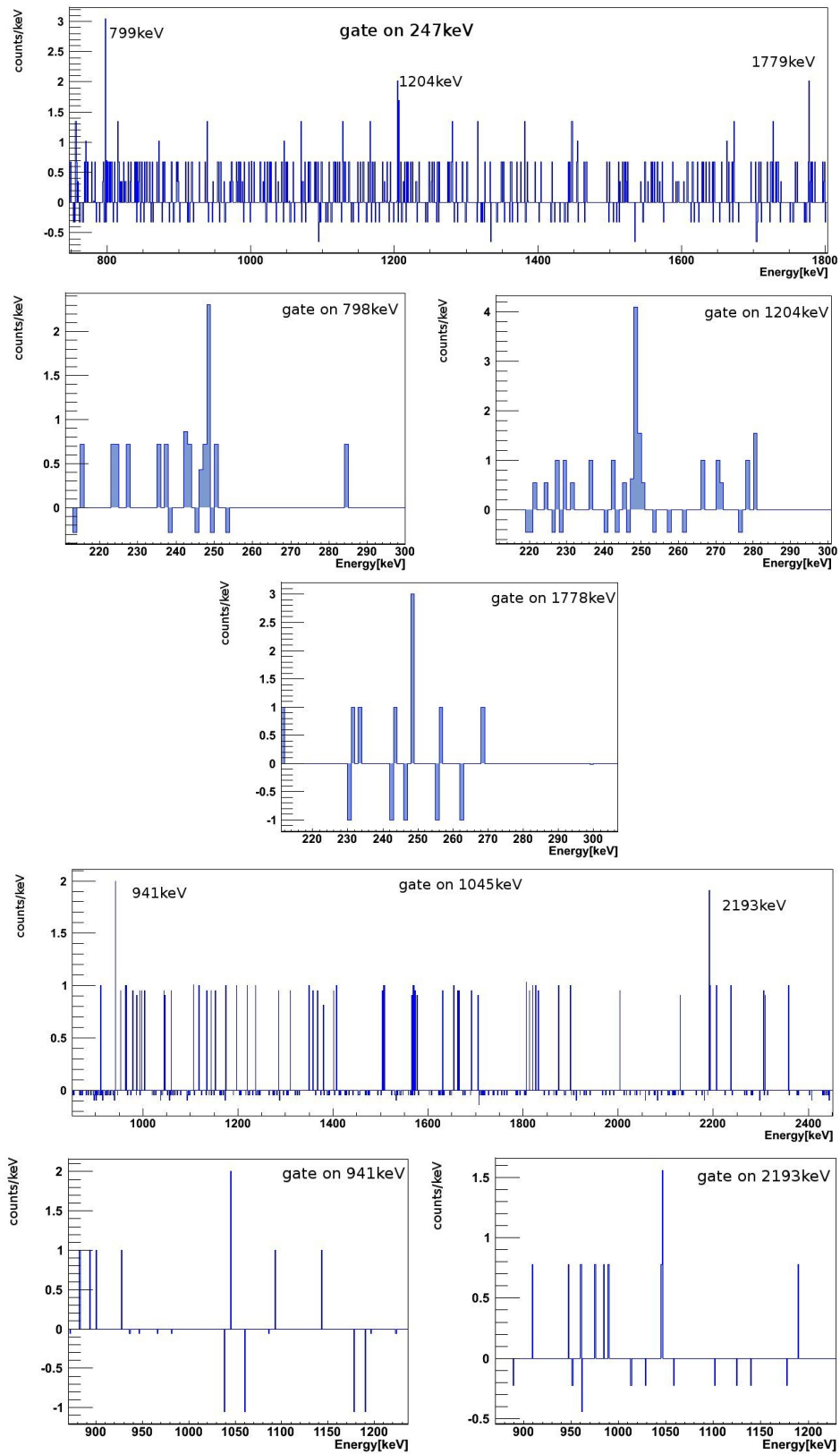
Figure 7.11: Top: The coincidence spectra for γ-line at 247 keV. Gating on the lines from the coincidence one can clearly see 247 keV γ-ray, thus confirm that the three transitions belong to the cascade. Bottom: The coincidence spectra for γ-line at 1045 keV.
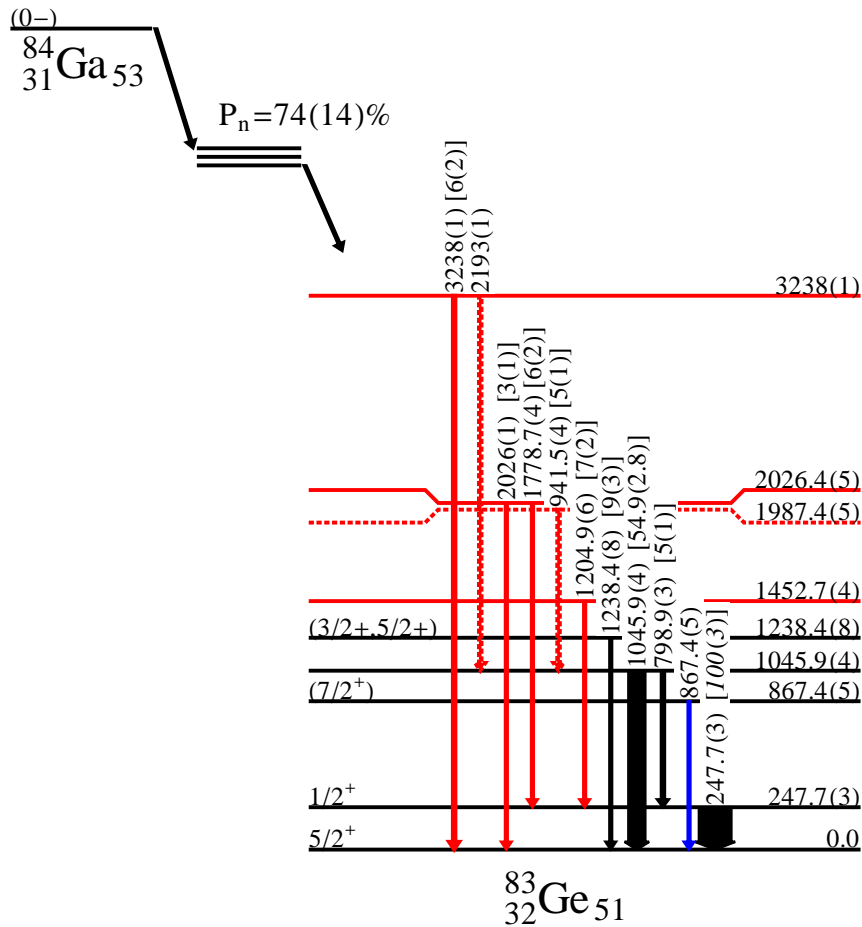
Figure 7.12: The resulting level scheme of ^{83}Ge. In black already known [37, 47, 44, 48], in red newly discovered transitions. The transition in blue was proposed by [48] but not confirmed yet. The level at 867 keV was not populated in this experiment. The two γ-lines drawn with the dotted lines (941 keV and 2193 keV), to be confirmed. The neutron emission probability from [37].

7.2.4   Results for ^{84}As

The latest updated level scheme of ^{84}As was presented by Tastet in thesis [35]. He confirmed already known γ-transitions at 42.7 keV, 100 keV, 242 keV, 386 keV and 608 keV [51, 52, 49], added two γ-lines, one at 346.5 keV the other at 794 keV, both in coincidence with 242 keV, and made spin assignement for low-lying states.

We confirmed the level scheme proposed by Tastet (except the line at 794 keV) and extend the scheme of excitation levels in ^{84}As. The results for the discrimination of the half-life of the γ-lines are presented in Figure 7.13 and Figure 7.14. Many new coincidences of γ-rays at 42.7 keV, 100 keV and 242 keV were found (Figure 7.15).

The final level scheme is presented in Figure 7.16. The list of γ-lines can be found in Table 7.4. Two new transitions to the ground state were assigned at 464.6 keV and 589.9 keV, however, since the statistics for those peaks was poor, both of the were drawn with the dashed lines (tentative assignement).
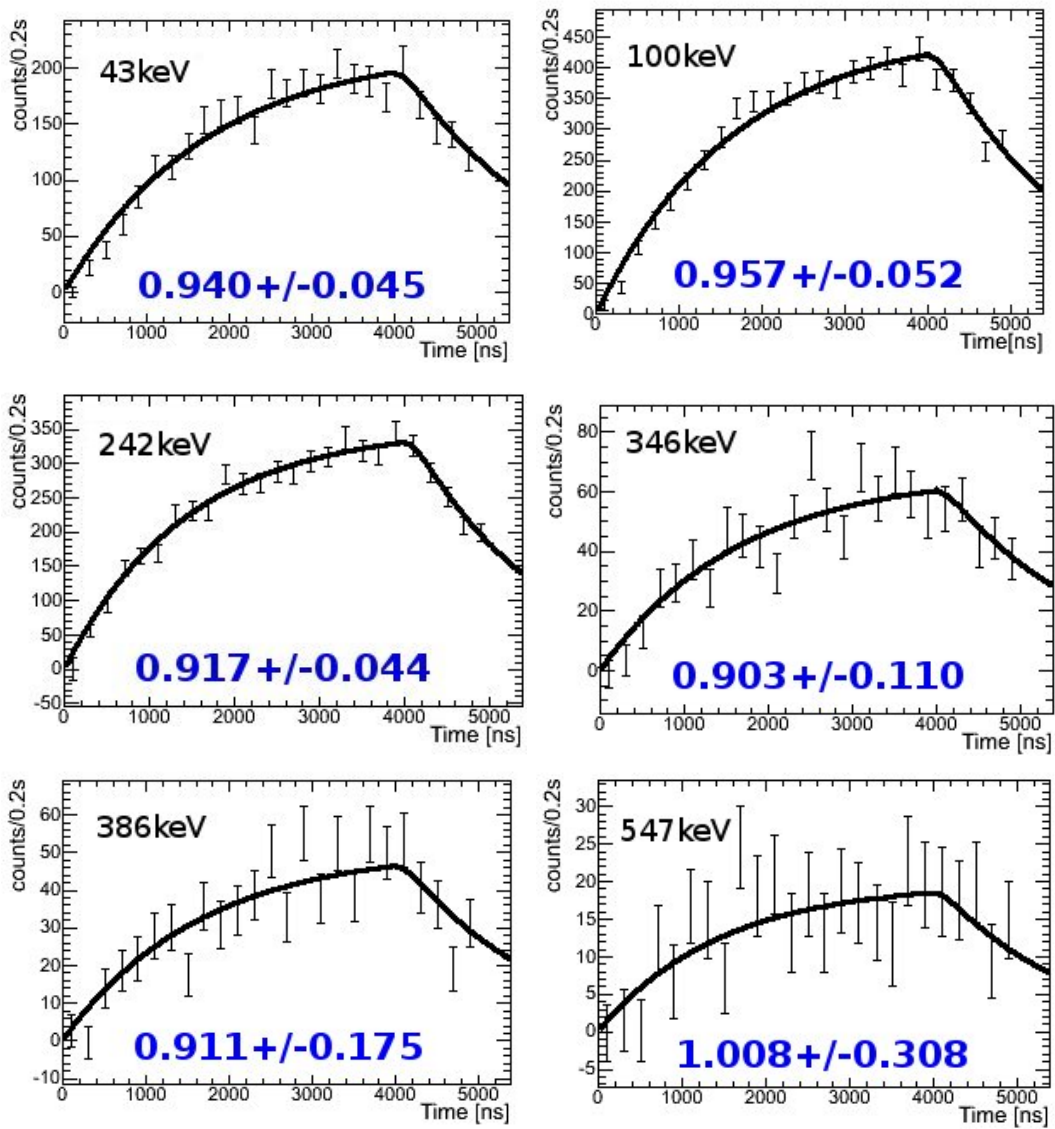
Figure 7.13: The results of the half-life (in seconds) determination for the lines of ^{84}As.
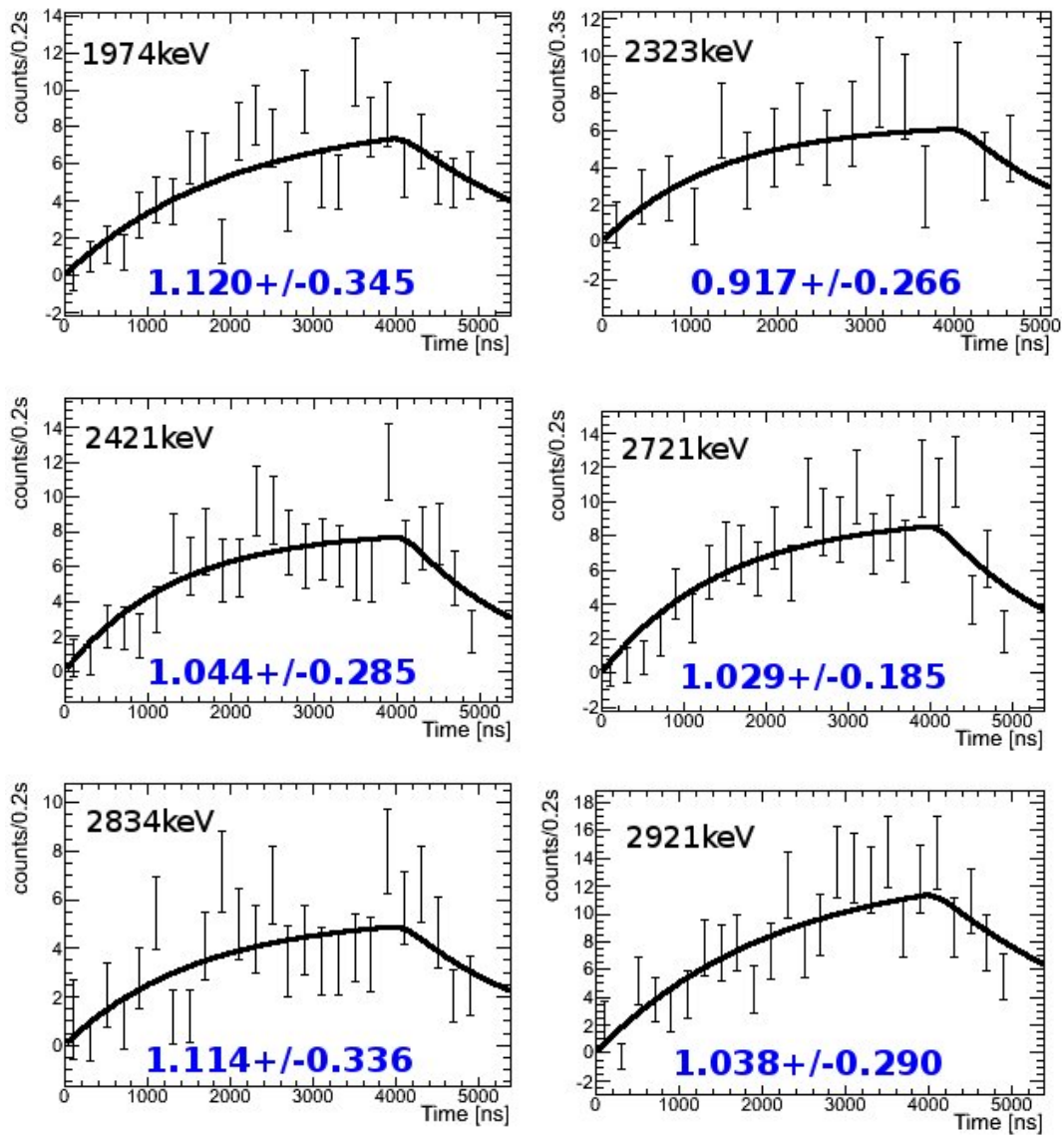
Figure 7.14: The results of the half-life (in seconds) determination for the lines of ^{84}As.
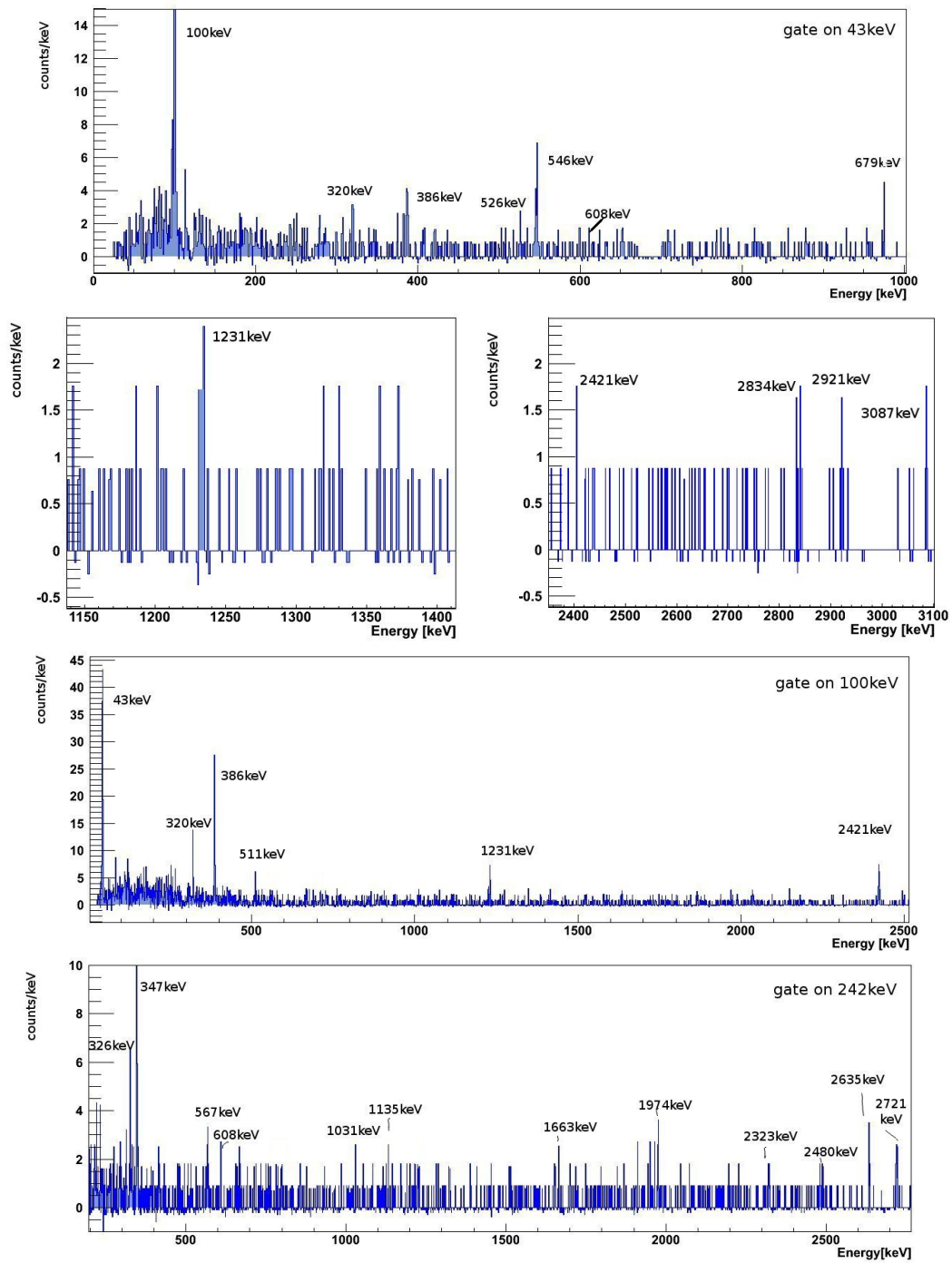
Figure 7.15: Top: the coincidence spectrum for γ-line at 43 keV, middle: the coincidence spectrum for γ-line at 100 keV, bottom: the coincidence spectrum for γ-line at 242 keV.
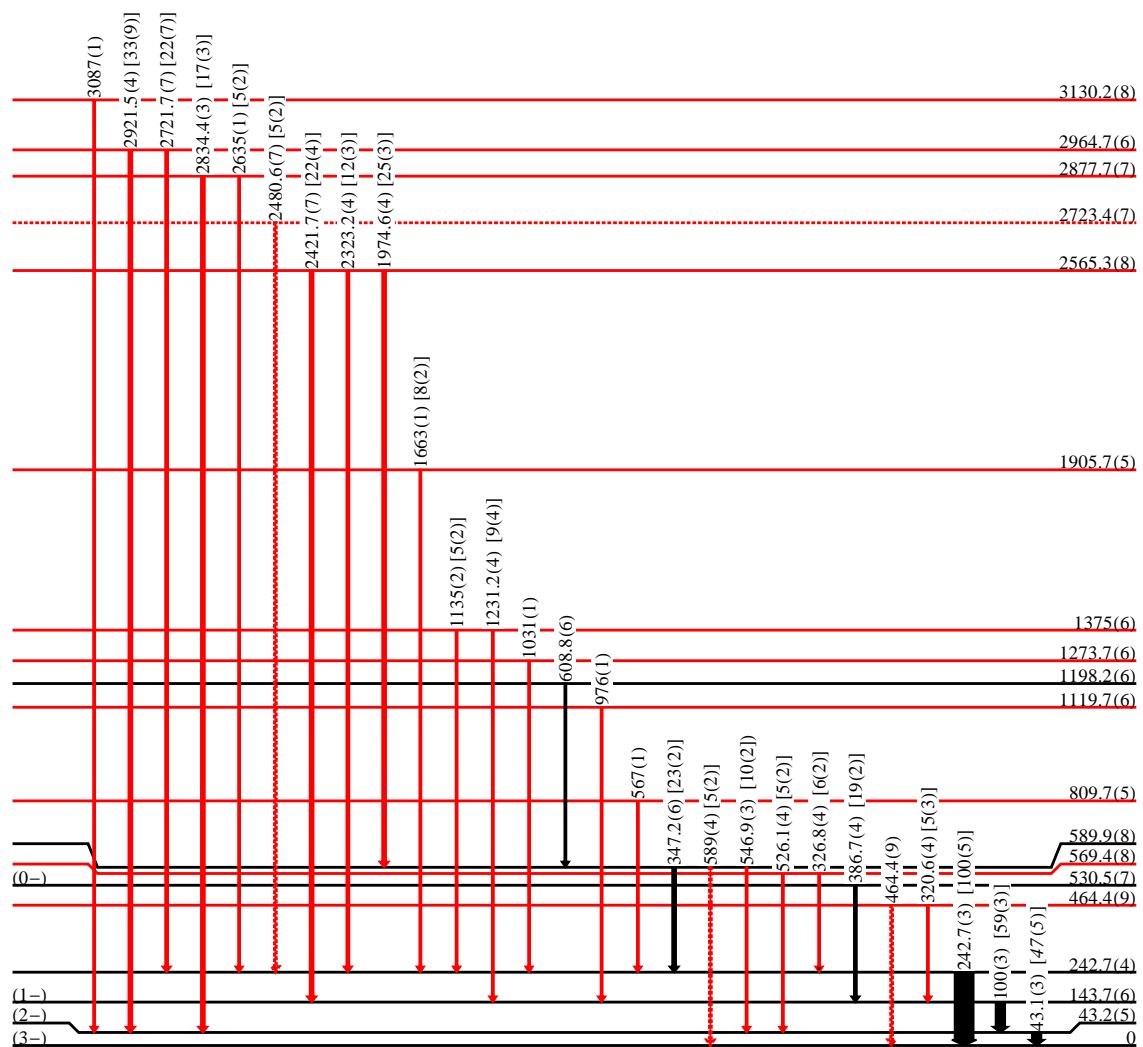
Figure 7.16: The resulting level scheme of ^{84}As. In black already known[35, 49, 51, 52], in red a newly discovered transitions. The two γ-lines to the ground state drawn with the dotted lines, to be confirmed. The assignement for the spin of the ground state from [50], and the low-lying state from [35].

Table 7.4: The final list of γ-lines observed in the β-decay of ^{84}Ga assigned to the de-excitation from the excited states of ^{84}As. The list contains the energy of the γ-ray, the intensity as relative to the most intense γ-ray, the energy of the excited level and the calculated half-life. The γ-rays with asterix: tentative assignment.

Energy [keV]	Relative intensity [%]	Level [keV]	Half-life [s]
43.1(3)	47(5)	43.2(5)	0.940(45)
100(3)	59(3)	143.7(6)	0.957(52)
242.7(3)	100(5)	242.7(4)	0.917(44)
320.6(4)	5(3)	464.4(9)	
326.8(4)	6(2)	569.4(8)	
347.2(6)	23(2)	589.9(8)	0.903(110)
386.7(4)	19(2)	530.5(7)	0.911(175)
*464.4(9)		464.4(9)	
526.1(4)	5(2)	569.4(8)	
546.9(3)	10(2)	589.9(8)	1.008(308)
567(1)		809.7(5)	
*589(4)	5(2)	589.9(8)	
608.8(6)		1198.2(6)	
976(1)		1119.7(6)	
1031(1)		1273.7(6)	
1135(2)	5(2)	1375(6)	
1231.2(4)	9(4)	1375(6)	
1663(1)	8(2)	1905.7(5)	
1974.6(4)	25(3)	2565.3(8)	1.120(345)
2323.2(4)	12(3)	2565.3(8)	0.917(266)
2421.7(7)	22(4)	2565.3(8)	1.044(285)
*2480.6(7)	5(2)	2723.4(7)	
2635(1)	5(2)	2877.7(7)	
2721.7(7)	22(7)	2964.7(6)	1.029(185)
2834.4(3)	17(3)	2877.7(7)	1.114(336)
2921.5(4)	33(9)	2964.7(6)	1.038(290)
3087(1)		3130.2(8)	

7.3 Spin assignment

Determination of the P_n ratio

It is important to assess the branching ratios and $\log ft$ values and assign the spins for the excited levels. The neutron emission probability P_n for ^{84}Ga was measured to be 70(15)% [113] and 74(14)% [37] and theoretically predicted as 60% [118]. We use the γ-ray intensities obtained in our experiment and known branching ratios to calculate the P_n value. Since the total production of gallium obtained in our experiment is not known, the neutron emission probability is estimated from the number of decaying daughter nuclei. The schematic decay scheme of ^{84}Ga is presented in Figure 7.18. The intensities of the γ-lines are relative to the one at 247.7keV ($1/2^+ \to 5/2^+$ transition in ^{83}Ge).

The measurement cycles were short (4 s collection + 1 s decay) and not all of the daughter nuclei, especially the longer lived ones, had time to decay and be detected. It is essential to know what was the loss in the spectra and take it into account for the calculation. The activity of the parent nuclei during the collection time and the decay time is governed by the equations:

$$\mathcal{A}(t) = \begin{cases} \Phi \left(1 - e^{-\lambda_1 t} \right) & \text{if } t \leq t_{coll}, \\ \Phi \left(1 - e^{-\lambda_1 t} \right) \left(1 - e^{-\lambda_1 (t - t_{coll})} \right) & \text{if } t > t_{coll}. \end{cases}$$

While for the daughter nuclei, the activity in time can be calculated from

$$\mathcal{A}(t) = \begin{cases} \Phi \left(1 - \frac{\lambda_2}{\lambda_2 - \lambda_1} e^{-\lambda_1 t} - \frac{\lambda_1}{\lambda_2 - \lambda_1} e^{-\lambda_2 t} \right) & \text{if } t \leq t_{coll}, \\ \Phi \left[\frac{\lambda_2}{\lambda_2 - \lambda_1} \left(1 - e^{-\lambda_1 t_{coll}} e^{-\lambda_1 (t - t_{coll})} \right) - \frac{\lambda_1}{\lambda_2 - \lambda_1} \left(1 - e^{-\lambda_2 t_{coll}} e^{-\lambda_2 (t - t_{coll})} \right) \right] & \text{if } t > t_{coll}. \end{cases}$$

One can estimate the missing γ-rays ratio, which is the ratio of the activities during the time of collection and decay and the total production (including the γ-rays which are emitted after the end of the cycle):

$$R = \frac{\int_{t_0}^{t_{coll}} A(t)\, dt + \int_{t_{coll}}^{t_{dec}} A(t)\, dt}{\int_{\infty} A(t)\, dt} \ . \tag{7.5}$$

Using Eq. 7.5 one obtains the ratio:

$$R(^{84}Ga)\Big|_{T_{1/2}=0.085(10)s} = 0.1111 \ ,$$

$$R(^{84}Ge)\Big|_{T_{1/2}=0.954(14)s} = 0.1727 \ , \tag{7.6}$$

$$R(^{83}Ge)\Big|_{T_{1/2}1.85(6)s} = 0.3743 \ .$$
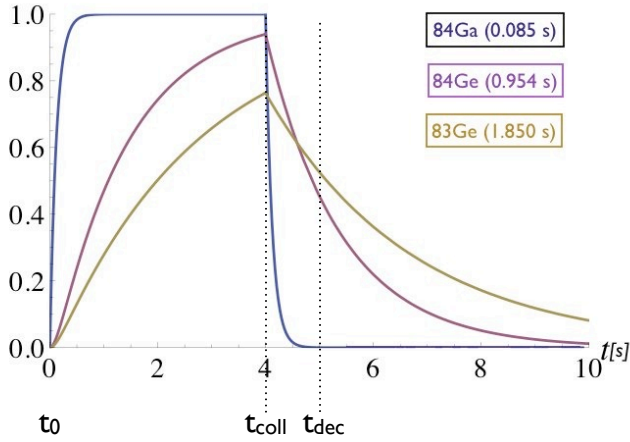
Figure 7.17: Intensity estimation as a function of time for mother nucleus (^{84}Ga) and the daughter nuclei ($^{83-84}$Ge). It is used to estimate the number of missing γ-rays.

the proportion of the γ-rays missing used to scale the intensities measured to obtain the total value of activity.

To calculate the number of the ^{83}Ge isotopes we use the most intensive line in the level scheme of ^{83}As with the energy of 306.5 keV for which the branching ratio was estimated by Winger [37] to be 15.3(11)%. The relative number of the ^{83}Ge is estimated as $109(4)/0.153(11) = 709(59)$. To know the total production of the ^{84}Ga isotopes the same calculation should be performed for ^{84}Ge. For this calculation four lines in ^{84}As are used. Their relative intensities, presented in Table 7.5, were found to be somehow different from the ones found in [86] and the choice of one γ-line which could serve best for this calculation is inconclusive. We use the weighted average of the relative intensities $I_{present}/I_{relative}$, the ratio of 0.8833(0.0377) which normalized with the factor for the intensity normalization 0.122(19) [86] which gives 724(117) decays of ^{84}Ge.

The resulting P_n ratio is 49(6)% which is a bit less that the values found in [113, 37] but still compatible within the lower (and its upper) error bar with 70(15)%[113]. From the investigation of the P_n ratio, the total production of ^{84}Ga was extracted to be $3.59(14)10^6$ ($P_n = 49(6)$%). Assuming $P_n = 74(14)$% the total production is $2.40(19)10^6$.

Determination of the $\log ft$ values

In order to assign the spins and parities to the excitation levels we calculate the $\log ft$ values which are qualitative indicators of the type of the β transition. It is, however, important to remember that since the information acquired on the levels schemes and γ-transitions in β-decay is not complete (only partial level schemes are presented), we

Table 7.5: The intensities of the most intense four γ-lines in ^{84}As relative to 247.7keV compared with the values from [86].

Energy$_\gamma$[keV]	Intensity$_{\text{present}}$	Intensity$_{\text{relative}}$	Intensity$_{\text{pt}}$/Intensity$_{\text{rel}}$
43.1(3)	71(5)	81(3)	0.873(65)
100(3)	89(3)	79(5)	1.130(78)
242.7(3)	151(4)	92(7)	1.638(131)
386.7(4)	29(2)	53(5)	0.547(64)
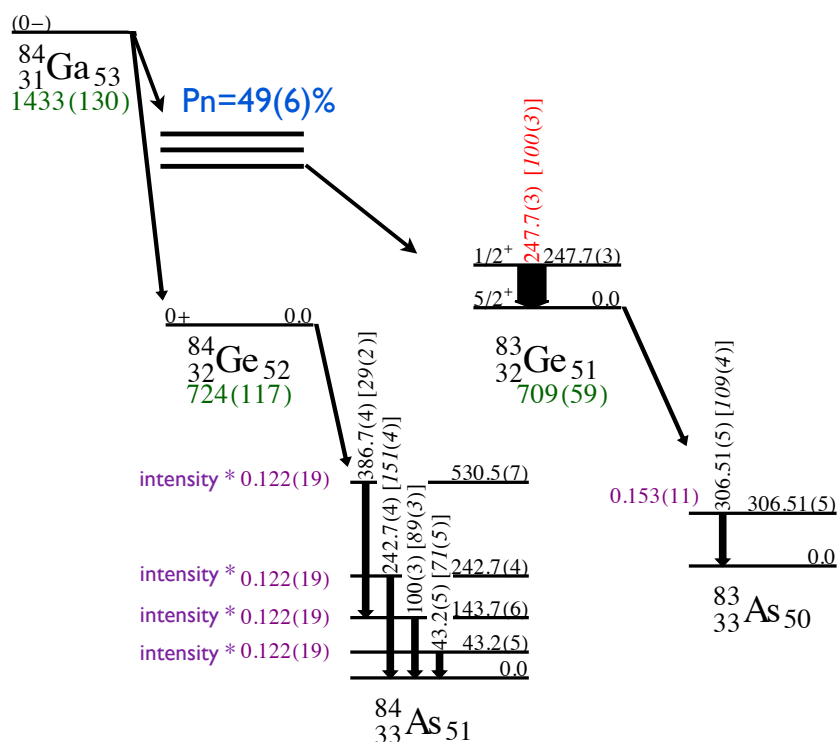
Figure 7.18: Schematic picture of the determination of the P_n ratio from the measured intensities of γ-lines in ^{83,84}As and known branching ratios [39, 37]. The estimated neutron emission probability: 49(6)%.

present here the relative populations of the levels.

The $\log ft$ values are calculated using two approaches:

- P_n ratio of 49(6)% with the assumptions presented in the previous subsection and the production calculated to be $3.59(14)10^6$,

- P_n ratio of 74(14)% [37], and the total production of $2.40(19)10^6$.

The $\log ft$ values were calculated using the available $\log ft$ calculator [116]. The population of the levels was calculated from the intensity of the γ-transitions. The relative population of the levels, $\log ft$ values and proposed spins are listed in Table 7.6 and Table 7.7. The results for the two different P_n ratios are very similar proving that the change (of 20%) in the probability of neutron emission does not change the type of the transition.

Table 7.6: The relative population, the $\log ft$ values and the spin assignements of the excitation levels in ^{84}Ge.

Energy [keV]	Spin and parity J^π	$P_n = 49(6)$ Population [%]	$\log ft$	$P_n = 74(14)$ Population [%]	$\log ft$
0.0	0^+	$< 43(9)$	$> 5.35(12)$	$< 24(8)$	$> 5.62(16)$
624.2(2)	2^+	2.1(5)	6.56(13)	4.3(4)	6.26(7)
1389.3(4)	$(1^+, 2^+)$	1.2(4)	6.7(2)	1.8(6)	6.52(16)
2228.1(3)	$(0^+, 1^+, 2^+)$	0.7(1)	6.78(13)	1.04(23)	6.62(11)
3502.3(6)	$(1^+, 2^+)$	3.0(5)	5.9(8)	5.05(61)	5.69(08)

Table 7.7: The relative population, the $\log ft$ values and the spin assignements of the excitation levels in ^{83}Ge.

Energy [keV]	Spin and parity J^π	$P_n = 49(6)$ Population [%]	$\log ft$	$P_n = 74(14)$ Population [%]	$\log ft$
0.0	$5/2^+$	$< 35(5)$	$> 4.47(7)$	$< 55(6)$	$> 4.26(12)$
247.7(3)	$1/2^+$	6.9(3)	5.1(1)	8.3(7)	5.03(12)
1045.9(4)	$(1/2^+, 3/2^+)$	3.7(2)	5.20(12)	5.2(5)	5.02(13)
1238.4(8)	$(3/2^+, 5/2^+)$	0.7(2)	5.85(15)	1.06(2)	5.6(4)
1452.7(4)	$(1/2^+, 3/2^+, 5/2^+)$	0.5(1)	5.90(16)	0.8(2)	5.72(17)
2026.4(5)	$(1/2^+, 3/2^+, 5/2^+)$	0.7(3)	5.6(2)	1.08(38)	5.4(2)
3238(1)	$(1/2^+, 3/2^+, 5/2^+)$	0.5(1)	5.4(2)	0.8(2)	5.16(21)

The proposed spins and parity for the excitation levels in ^{83,84}Ge are presented in Figure 7.19. The upper limits of the β-decay feedings for the ground state reflect (relative) potentially unobserved γ-ray transitions. The estimated $\log ft$ values for ^{84}Ge vary between $5.3 - 6.8$ indicating the first-forbidden character of the transitions where the spin changes $\Delta J = 0, \pm 1, \pm 2$ and the parity is not conserved. Thus, the excitation levels may have $J^\pi = 0^+, 1^+, 2^+$ except if there is transition to the level with the spin 0^+ like in case of the γ-line at 3502.3 keV. The spin and parity of the third excitation level (at 1389.3 keV) can be $1^+, 2^+$.
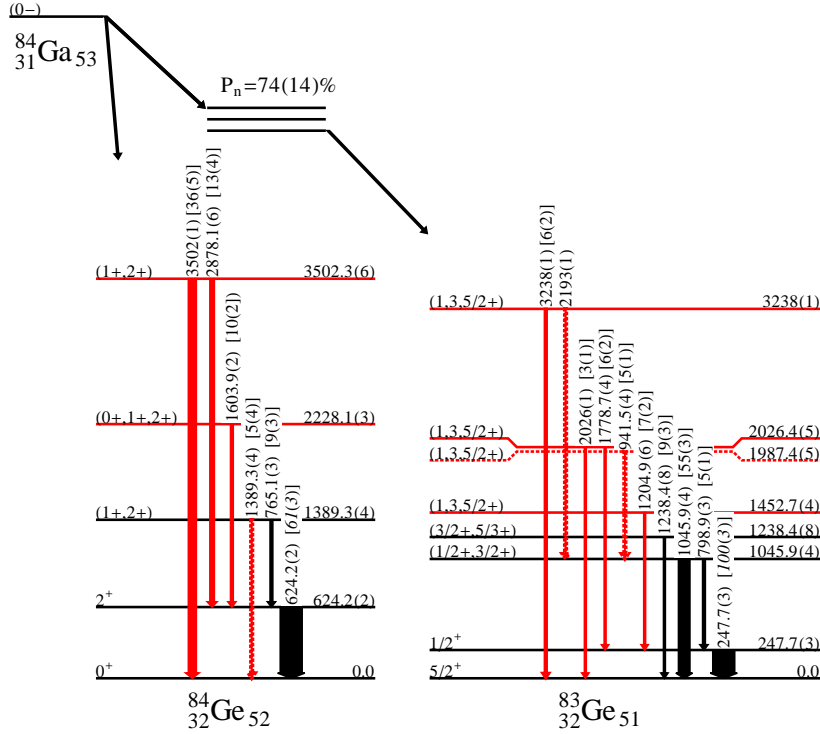
Figure 7.19: The final level scheme of the ^{83}Ge, ^{84}Ge isotopes with proposed spin assignement. The intensities of the γ-lines are relative to the line at 247.7keV.

As mentioned already earlier, the population numbers presented here are relative and include only the observed transitions while there is no information on the amount of the less intense transitions of higher energy. The estimated $\log ft$ values for ^{83}Ge are a bit smaller varying from value 5 to 6. This value of the $\log ft$ would be an indicator of the allowed transition ($\Delta J = 0, \pm 1$ and $J^\pi = -$), however, this is inconsistent with the spin of the first excited state in ^{83}Ge at 247.7 keV which is $1/2^+$. The spin and parity of the odd-odd mother nucleus is known to be 0^- [39]. Since there is a change of parity the allowed transition is not possible but the spin $1/2^+$ can be populated with the first-forbidden transition. The value of those $\log ft$ should have higher error bars as the estimation of the production was made taking into account the weighted average of the four γ-lines in ^{84}As. The missing γ-transitions and wrong branching ratios could lead to a wrong estimation of the population. Assuming the big error on the determination of the $\log ft$ values the transitions are assumed as first-forbidden and the populated levels have positive parities. The results of their assignment are presented in Table 7.7.

The spin and parity of level at 1045.9 keV is proposed to be $(1/2^+)$ or $(3/2^+)$. This level was strongly populated in β n-decay of ^{84}Ga and only weakly in β-decay of ^{83}Ga [37]. Since the spin and parity of ^{83}Ga is $5/2^-$ the most probable transition is to populate the ground state of ^{83}Ge with spin $5/2^+$. The transition from the ground state of ^{83}Ga to the $(1/2^+)$ state (e.g. the first excited state in ^{83}Ge at 247.7 keV) requires a change in spin $\Delta J = 2$ which is not favourable, while the transition to the state with spin $3/2^+$ is more favourable since is requires a change in spin $\Delta J = 1$. In the experiment with ^{83}Ga β-decay [37] the first excited state was populate very weakly (branching ratio of 0.42(10) %), the second at 1045 keV had a branching ratio of 0.65(13) and for the third at 1237.9 keV the branching ratio was estimated to be 1.91(12). This could give some indication for the assignement of the spins. In ^{84}Ga β n-decay the most intense γ-lines in the level scheme of ^{83}Ga are 247.7 keV and 1045.9 keV (and the populations of those two levels are the highest). While the first has a spin $1/2^+$ this could be an indication of the $(1/2^+)$ spin for the state at 1045.9 keV. But since the populations of those two states is not identical and the spin $(3/2^+)$ for this state cannot be excluded.

Contents

8.1   Nuclear structure of ^{84}Ge

The systematics of the excitation energies in isotonic or isotopic chains gives first clue which can help in assigning spins of the states and understanding their nature. Following the trends of $0^+, 2^+, 4^+$ states in even-even nuclei at $N = 48$ and $N = 52$ one can try to understand the general behavior and collectivity around $N = 50$. Studying the systematics of the $N = 48$ isotonic chain excited states (see Figure 8.1) one finds parabolic shape of the energies of first 2_1^+ and 4_1^+ excitation levels. The excited 2_1^+ state goes down from $Z = 38$, reaches minimum at the mid-shell (^{80}Ge and ^{82}Se) and then increases again at $Z = 28$. Very similar tendency appears for the 4_1^+ states. The 2_2^+ state, identified for $Z = 32 - 38$ isotopes, also goes down with decreasing proton number and becomes the second excited state known in ^{80}Ge. The systematics for the $N = 52$ chain is presented in Figure 8.2. The 2_1^+ state is identified in all itosopes with $Z = 32 - 38$. The energy of this state slightly decreases with decreasing proton number but is rather constant. The trend of the 4_1^+ states is very similar to the first 2^+ in $N = 52$. It is a slightly lower energy in ^{86}Se. The 2_2^+ state in ^{90}Sr is located just above 4^+ while in ^{88}Kr the 2_2^+ state is already below 4_1^+. This state, however, was not identified in ^{86}Se.

The systematics of the low-lying positive parity states in germanium isotopes ($N = 40 - 52$) is presented in Figure 1.5 (Chapter 1). The trend of the 2_1^+ state energy is almost constant from $N = 42$ to $N = 48$ (^{80}Ge) where the 2_1^+ state has energy 659.1 keV. This is very close to the energy of 2_1^+ state (624.2 keV) in ^{84}Ge. The second excited state in all germanium isotopes with $N = 42 - 48$ has a spin 2^+. The 2_2^+ state in ^{84}Ge has not yet been proposed.
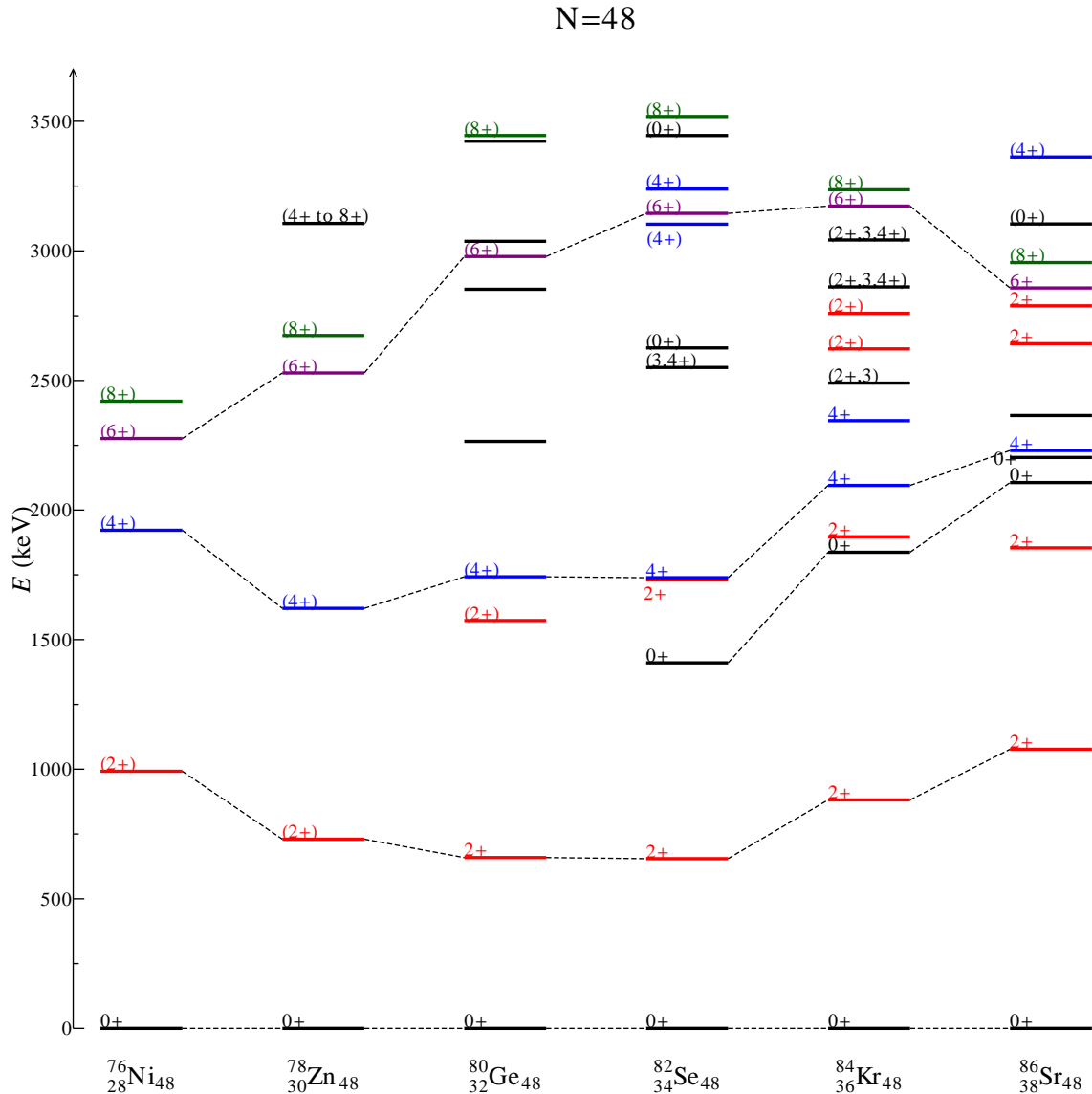
Figure 8.1: The systematics of the excitation energies in the $N = 48$ isotonic chain.

Shell model calculations for even-even nuclei at $N = 52$

As already explained in Chapter 3, in collaboration with the theory group from Strasbourg, I have created the effective interaction $ni78 - jj4b$. The goal was to perform the shell model calculations and obtain the spectroscopic description of our nuclei of our interest. The experimental energy spectra for three $N = 52$ isotones are compared to the shell model calculations in Figure 8.3. I traced the 2_2^+ states in calculated spectra of ^{88}Kr and ^{90}Sr using the known transitions from this state to the ground state 0^+ and the first excited state 2^+. Two transitions are possible from the state 2^+ to 2^+ ($M1$
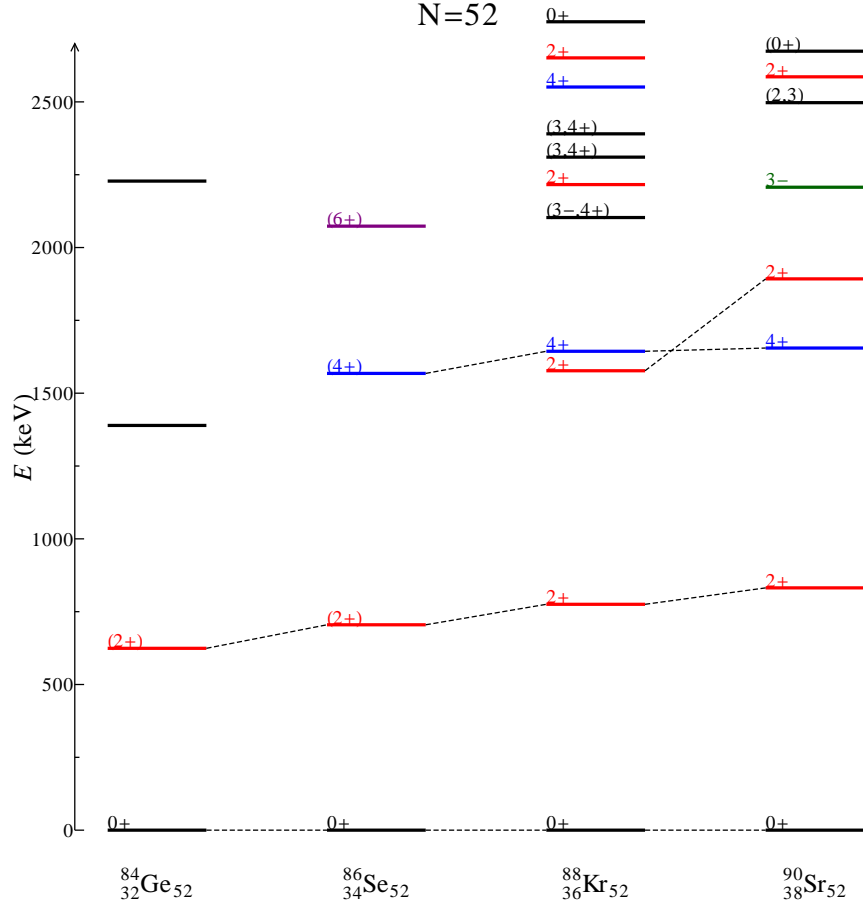
Figure 8.2: The systematics of the excitation energies in the $N = 52$ isotonic chain.

and $E2$). From the state with spin 2^+ to ground state 0^+ one transition can occure: the electric quadrupole $E2$ transition. The candidate for the 2_2^+ states were found from the calculated transition probabilities for γ-rays depopulating those states (details of the calculation of the probability are presented in next section). The identified states from the calculation are connected with the blue dashed lines with the correcponding experimental states in Figure 8.3.

The evolution of the $2_1^+, 2_2^+$ and 4_1^+ with the proton number is drawn in Figure 8.4. The experimental energies (symbols) are compared with our calculation (lines). The evolution of those states with different proton number is rather flat and the 2_2^+ state appear above 4_1^+ (in ^{86}Se and ^{90}Sr) and below 4_1^+ state (in ^{84}Ge and ^{88}Kr).
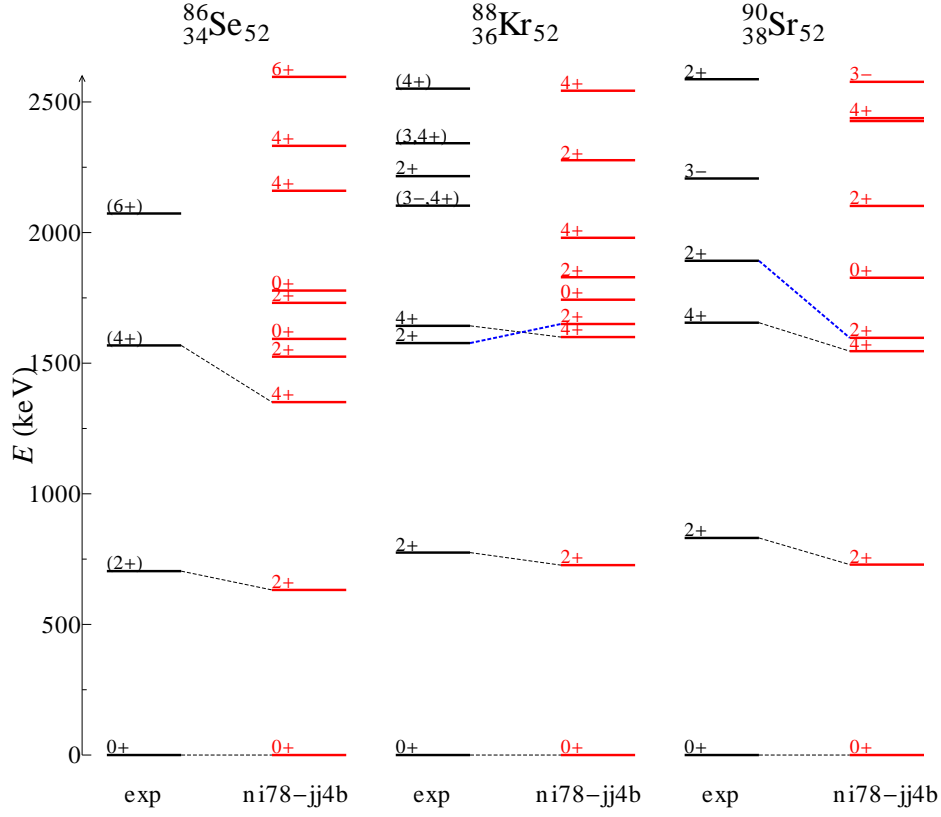
Figure 8.3: The experimental energy levels in $N = 52$ isotones compared with our shell model calculation.

Shell model calculations for ^{84}Ge

The results of the shell model calculations for ^{84}Ge compared with the experimental level schemes are presented in Figure 8.5. The ground state 0^+ is correctly reproduced with the wave function dominated by two components:

- $\pi p_{3/2}^2 \pi f_{5/2}^2 \otimes \nu d_{5/2}^2$

- $\pi f_{5/2}^4 \otimes \nu d_{5/2}^2$

The first 2^+ is predicted at close energy in comparison with the experimental value and its vawe finction is a composition of

- $\pi p_{3/2}^2 \pi f_{5/2}^2 \otimes \nu d_{5/2}^2$,

- $\pi p_{3/2}^2 \pi f_{5/2}^2 \otimes \nu d_{5/2}^1 \nu s_{1/2}^1$,

where the second component represents the one neutron excitation to the $\nu s_{1/2}$ orbit.
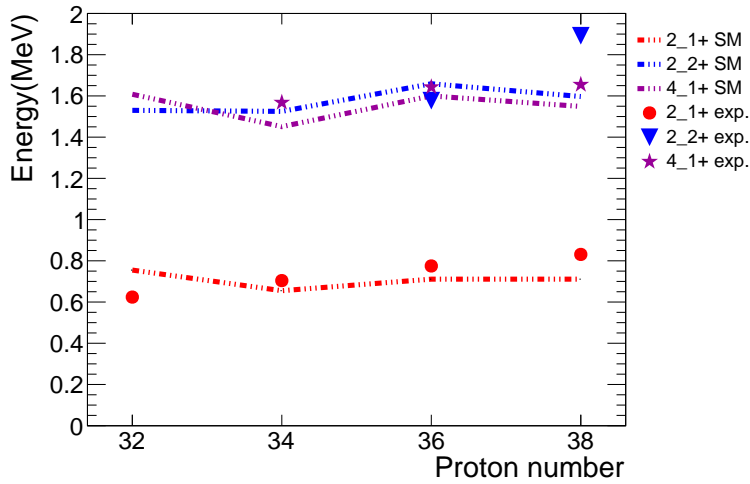
Figure 8.4: The experimental energies of $2_1^+, 2_2^+$ and 4_1^+ states for $Z = 32 - 38$ compared with theoretical calculation.
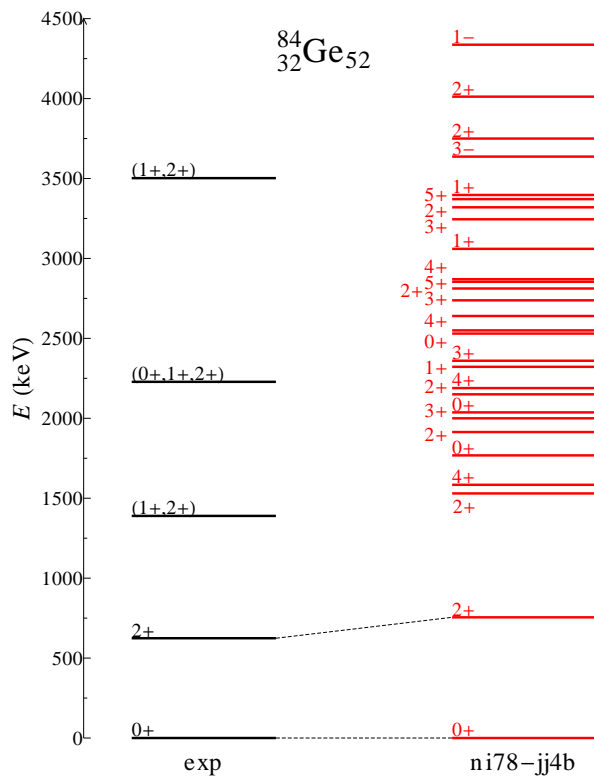
Figure 8.5: The resulting level scheme of ^{84}Ge in comparison with theoretical shell model calculation made with $ni78-jj4b$ interaction.

The level at 1389.1 keV

Starting from the assumption of (0^-) [39] spin of ^{84}Ga and using calculated $\log ft$ we assign two candidates for the second excited state spins 1^+ and 2^+. From the earlier comparison with the energy spectra of the $N = 52$ isotones and the $N = 40 - 52$ germanium isotopes there is no clear indication for this level to have a spin 1^+. The first 1^+ state predicted with the calculation is located at 2322 keV. This energy is quite high to be considered as a good fit for our experimental third excites state. We shall then consider two closest possible spin states: 2^+_2 at 1584 keV and 2^+_3 at 1873 keV. Their wave functions are presented in Table 8.1.

Table 8.1: The experimental energies of excitation levels in ^{84}Ge and proposed calculated ones with the spin assignements and wave functions.

Energy exp. [keV]	Energy calc. [keV]	J^π	Wave function
0.0	0.0	0^+	$34\% \; \pi p^2_{3/2} \pi f^2_{5/2} \otimes \nu d^2_{5/2}$
			$14\% \; \pi f^4_{5/2} \otimes \nu d^2_{5/2}$
624.2(2)	755	2^+	$25\% \; \pi p^2_{3/2} \pi f^2_{5/2} \otimes \nu d^2_{5/2}$
			$14\% \; \pi p^2_{3/2} \pi f^2_{5/2} \otimes \nu d^1_{5/2} \nu s^1_{1/2}$
1389.3(4)	1584	2^+	$23\% \; \pi p^2_{3/2} \pi f^2_{5/2} \otimes \nu d^2_{5/2}$
			$14\% \; \pi p^2_{3/2} \pi f^2_{5/2} \otimes \nu d^1_{5/2} \nu s^1_{1/2}$
			$14\% \; \pi p^1_{3/2} \pi f^3_{5/2} \otimes \nu d^2_{5/2}$
	1873	2^+	$22\% \; \pi p^2_{3/2} \pi f^2_{5/2} \otimes \nu d^2_{5/2}$
			$22\% \; \pi f^4_{5/2} \otimes \nu d^2_{5/2}$
unknown	1999	3^+	$20\% \; \pi p^1_{3/2} \pi f^3_{5/2} \otimes \nu d^2_{5/2}$
			$15\% \; \pi p^2_{3/2} \pi f^2_{5/2} \otimes \nu d^1_{5/2} \nu s^1_{1/2}$
			$11\% \; \pi p^2_{3/2} \pi f^2_{5/2} \otimes \nu d^2_{5/2}$

We consider two γ-ray transitions from this level, where one goes to the ground state 0^+ and the second to the first excited 2^+ state (Figure 8.6). In order to find a good candidate for the second 2^+ state in our theoretical spectrum we calculate the partial γ-ray transition probabilities for those γ-rays using Eq. 2.23. At first, to calculate the values for the mean-life we use the shell model calculation to obtain the reduced transition probabilities (B). The reduced transition probabilities for $E2$ transitions were calculated with two different sets of effective charges ($e_\pi = 1.5$, $e_\nu = 0.5$ and $e_\pi = 1.6$, $e_\nu = 0.6$). As shown in Chapter 3 Figure 3.5, to reproduce well the $B(E2; 2^+ \rightarrow 0^+)$ values for the $N = 50$ isotonic chain the effective charges were set to $e_\pi = 1.6$, $e_\nu = 0.6$. Thus, the values obtained with those charges are used in the preceding discussion. We present here the values calculated with standard charge $e_\pi = 1.5$, $e_\nu = 0.5$ only for comparison. As one can notice the small change
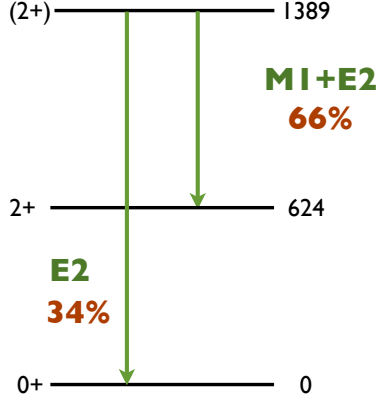
Figure 8.6: The schematic view of the possible electric and magnetic mode transitions assuming the 2^+ spin for the third excited state. The numbers in red represent the partial γ-ray transition probabilities.

in the effective charges does not influence a lot on the values of reduced transition probabilities. To calculate the magnetic transition the effective gyromagnetic factors were $g_\pi = 4.1895$, $g_\nu = -2.8695$ (from the multiplication of the bare values $g_\pi = 5.586$, $g_\nu = -3.826$ by the quenching factor 0.75 [119, 120, 121]).

Starting from the state with the spin and parity 2^+ the γ-ray depopulating to the state 2_1^+ (no parity change and no change in spin) may undergo $M1$ and $E2$ transitions. The calculated reduced transition probabilities are 0.015 μ_N for the magnetic and 227 $e^2\ fm^4$ for the electric. We calculate the meanlifes using Eq. 2.19 and Eq. 2.22:

$$\tau_{M1} = \frac{56.8}{(0.765)^3 \cdot 0.015}\mu_N^2\ \text{MeV}^3\ \text{fs} = 84.6 \cdot 10^{-12}s\ ,$$

$$\tau_{E2} = \frac{816}{(0.765)^5 \cdot 227}e^2\ \text{fm}^4\ \text{MeV}^5\ \text{ps} = 13.69 \cdot 10^{-12}s\ .$$

In the second step we consider the transition from the 2^+ to the ground state 0^+ with energy 1389 keV. In this case only $E2$ transition will be considered ($\Delta J = 2$). From Eq. 2.22 the meanlife for this γ-ray is $10.5 \cdot 10^{-12}$ [s].

Using Eq. 2.23 one calculates the partial transition probabilities for those γ-rays (results are presented in Table 8.2):

$$P_{2_2^+ \to 0^+} = \frac{\frac{1}{\tau_{E2_{2_2^+ \to 0^+}}}}{\frac{1}{\tau_{E2_{2_2^+ \to 0^+}}} + \frac{1}{\tau_{E2_{2_2^+ \to 2_1^+}}} + \frac{1}{\tau_{M1_{2_2^+ \to 2_1^+}}}} = \frac{10.14 \cdot 10^{10}}{29.27 \cdot 10^{10}} = 0.34\ .$$

One can see that the probability for the transition from the second 2_2^+ state to the first 2_1^+ is 66% while to the ground state 0_1^+ 34%. The same calculation when we consider

Table 8.2: The calculated reduced transition probabilities and the partial γ-ray transition probabilities for the assignement of the spin and parity of the experimental level at 1389 keV.

Transition Energy$_{\text{level}}$ [keV]	$e_\pi = 1.5,$ $e_\nu = 0.5$ $B(E2)$ e^2fm^4	$g_\pi = 4.1895,$ $g_\nu = -2.8695$ $B(M1)$ μ_{N}	$e_\pi = 1.6,$ $e_\nu = 0.6$ $B(E2)$ e^2fm^4	$P_{i \to f}$ $[\frac{1}{s}]$	ratio
$(2_1^+ \to 0_1^+)$	235	–	288		
755					
$(2_2^+ \to 0_1^+)$	15	–	16	$10.14 \cdot 10^{10}$	0.34
$(2_2^+ \to 2_1^+)$	190	0.015	227	$19.13 \cdot 10^{10}$	0.66
1584					
$(2_3^+ \to 0_1^+)$	45	–	50	$31.67 \cdot 10^{10}$	0.84
$(2_3^+ \to 2_1^+)$	43	0.53	62	$6.17 \cdot 10^{10}$	0.16
1873					
$(3_1^+ \to 2_2^+)$	430	126	505		
1999					

the third 2^+ state predicted at 1873 keV gives 84% to the ground state and 16% to the first 2^+ state (see Table 8.2).

From the experimental data we know that those two γ-ray transitions have relative intensities: 15(4)% to the first 2^+ state and 9(5)% to the ground state (relatively to each other 63% and 27%). The calculation with the third excited 2^+ gives result which is not compatible with the experiment (transition to the ground state 5 times stronger than to the first excited 2^+ state) and we reject this possibility. We assign for the third experimental excited level spin 2_2^+ which is consistent with the calculated spectrum where the second excited state is 2_2^+. The wave functions of the 2_1^+ and 2_2^+ excited states (see Table 8.1) are very similar with the biggest composition of the configuration with two neutrons in $\nu d_{5/2}^2$ and the second strongest with the excitation of one neutron to $\nu s_{1/2}$ obrital. The 2_2^+ state seems to be a more collective state with the third component created by the excitation of one proton from $\pi p_{3/2}$ to $\pi f_{5/2}$ orbital.

In Davydov and Filippov model [62], described in Chapter 2, the second 2^+ state can appear at a lower energy in case of axial asymmetry of the nucleus. The γ parameter (asymmetry parameter) can be extracted from the ratio of energies of those two 2^+ states, which in our case gives:

$$\frac{E_{2_2^+}}{E_{2_1^+}} = 1389.3/624.2 = 2.23$$

Spin and parity J^π	Q_{spec} $[e\ fm^2]$
2^+_1	-20.98
2^+_2	20.16
3^+_1	-1.8

Table 8.3: Calculated spectroscopic quadrupole moments for the first two 2^+ and one 3^+ states in ^{84}Ge.

This values, in Davydov's model, indicates $\gamma = 26°$ deformation. The amount of triaxiality can also be derived from the ratio of $B(E2)$ values, Eq. 2.12. With the values of the $B(E2)$'s from our shell model calculation we extract

$$\frac{B(E2;\ 2^+_\gamma \to 2^+_y)}{B(E2;\ 2^+_\gamma \to 0^+_y)} = \frac{227}{16} = 14.2\ .$$

which confirms γ asymmetry. This ratio of transition probabilities in the Davydov's model corresponds to $\gamma = 24°$.

As mentioned in Chapter 2, the spectroscopic quadrupole moments of the first two states with spins 2^+ for $K = 0$ and $K = 2$, $J = 2$ should have same value but the opposite sign. The Q_{spec} obtained for the first and the second 2^+ states predicted in our calculation are $-20.98\ [e\ fm^2]$ and $20.16\ [e\ fm^2]$, respectively (see Table 8.3). As can be noticed they have very close values and opposite signs which indicates that the 2^+_2 state is a member of a γ-band.

Going even further into the search of the states from the γ deformation band we consider the states of higher spin $3^+, 4^+, 5^+$. According to [62] the next members of the band have higher energies than the 2^+_2 state and high transition probabilities inside the band. We examine the structure of the 3^+_1 state calculated at 1999 keV. The specroscpic quadrupole moment for $K = 2$, $J = 3$ of this state is zero which corresponds to the requirement of the 3^+ state of the low-lying $K = 2$ γ-band. The composition of its wave function, presented in Table 8.1, is very similar to the one for 2^+_2 state and the reduced transition probabilities to the 2^+_2 (Table 8.2) are high. Thus, the 3^+_1 state is the second member of the γ-band predicted by our shell model calculation.

Similarities in the dynamic of ^{80}Ge and ^{84}Ge

We compare the low-lying energy spectrum of ^{80}Ge and ^{84}Ge. The former has 48 neutrons, two holes in the $\nu g_{9/2}$ orbital, while the later has two particles in $\nu d_{5/2}$ orbital. We use the relations of the energy and transition probabilities ratio given by the Davydov's model to show the similarities in the dynamic of those two isotopes.

The pictorial comparison of the spectra of ^{80}Ge and ^{84}Ge, and the tables with the energies of their excited states and $B(E2)$ values are presented in Figure 8.7.

E [keV]	^{80}Ge	^{84}Ge
2_1+	659	624
2_2+	1573	1389
$E(2_2^+)/E(2_1^+)$	2.39	2.23
4_1+	1743	
$E(4_1^+)/E(2_1^+)$	2.65	

B(E2) [e^2fm^4]	^{80}Ge	^{84}Ge
2_1-0_1	200(26)	288
2_2-0_1	23(7)	16
2_2-2_1		227
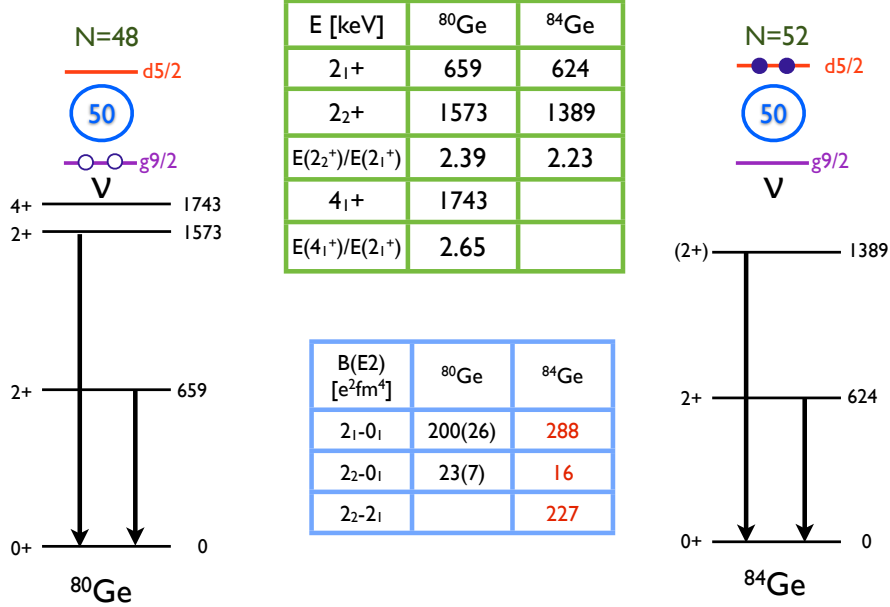
Figure 8.7: The pictorial comparison of the low lying energy states in ^{80}Ge and ^{84}Ge. The $B(E2)$ value for ^{80}Ge from [31]. The reduced transition probabilities for ^{84}Ge (in red) calculated with the shell model code.

The energies of the first and (in the hypothesis of the second 2^+ state in ^{84}Ge at 1389 keV) the second 2^+ excited states are close to each other. For both of those nuclei the ratio of the 2^+ energies ($E_{2_2^+}/E_{2_1^+}$) gives indication of γ deformation, according to Davydov's model. This deformation reaches $\gamma = 25°$ in case of ^{80}Ge and $\gamma = 26°$ for ^{84}Ge. The reduced transition probabilities calculated with the shell model interaction for ^{84}Ge, are presented in the blue table (in red) in Figure 8.7. These values indicating strong transition from the first excited to the ground state and weak transition from the second 2_2^+ state to the ground state. Another practically used value for the description of the nuclear structure in $4_1^+/2_1^+$ ratio (Chapter 2). The energy of the 4_1^+ state is known only for ^{80}Ge and the ratio with the 2_1^+ energy is 2.65 which suggests axial asymmetry in this nucleus.

From the comparison of the low-lying spectra of ^{80}Ge and ^{84}Ge we can conclude on similarities in the dynamics of those nuclei. With two holes in ^{80}Ge and two-particle in ^{84}Ge below and above $N = 50$, those two nuclei, using the Davydov's model, are

γ-deformed nuclei with the deformation parameter $\gamma \approx 25°$.

It should be stressed however, that the model chosen for the γ parameter calculation served us as a tool to get an approximate possible deformation parameter. This model assumes the rigidity of the nuclei which is not expected in case of our nuclei of interest. There exist other models that can be used to calculate the deformation parameters , e.g. the shape invariants in terms of the interacting boson model (IBM) [122, 123, 124]. With this algebraic model and using the $B(E2)$ values from the shell model calculation one can obtain γ and β deformation without assumption of the shape of the nucleus.

The level at 2228.1 keV

The candidates for the spin and parity of the level at 2228.1 keV are $0^+, 1^+, 2^+$. From the systematics of the germanium isotopes we know that in $^{74-76}$Ge the spins 1^+ states are located at 2402, 2600 keV and 2204 keV, respectively. Therefore, there is no clear reason to omit the possibility for the 1^+ as well as any other spin considered. The shell model calculation predict high density of low-spin levels with energies close to the corresponding level. Not much can be concluded from the wave functions neither the reduced transition probabilities as there is only one transition found from this state to the ground state. We shall, thus, conclude that there are three possibilities left for the spin assignement of this state.

The level at 3502.3 keV

The highest in energy observed in our experiment state in ^{84}Ge is located at 3502.3 keV. Two possibilities were discussed for the spin assignement of this level: $(1^+, 2^+)$. No clear restrictions can be made from the evolution of the levels in the systematics in the $N = 52$ chain, not in the systematics of germanium isotopes $N = 40 - 50$. From the spectrum of the shell model calculations one can be tempted to notice that there are 1^+ and 2^+ states predicted at this (or close) energy.

There are two transitions experimentally observed, one to the ground state and the second to the first excited state. It is usefull to calculate the partial γ-ray transition probabilities for this level, like in the discussion for the level at 1389 keV. For this calculations we consider the closest in energy to the experimental states with spins 1^+ and 2^+. We consider both magnetic $M1$ and electric $E2$ transitions. The $B(M1)$, $B(E2)$ values and the partial transition probabilities for all the states with calculated transition probabilities compatible with the experiment are listed in Table 8.4. Two states were found (Figure 8.8) with the partial transition probabilities in quite satisfac-

Figure 8.8: The schematic view of the possible electric and magnetic mode transitions assuming 1^+ (left) and 2^+ (right) spin for the highest energy observed excited state. In both cases the partial γ-ray transition probabilities are in quite good agreement with the experimental data.
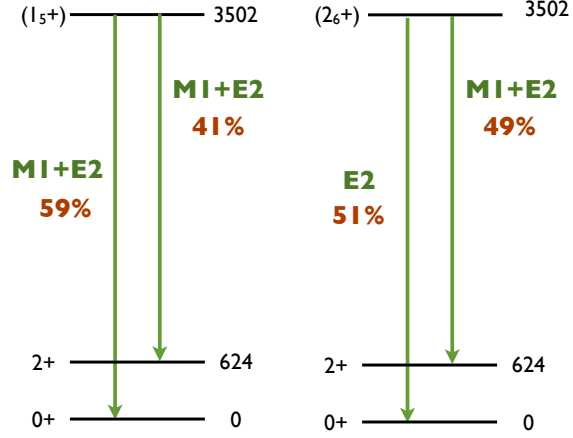
tory, however not excellent, agreement with experimental data (experimental relative intensities are: $77(9)\%$ and $23(8)\%$). The energies of both of those calculated states are $400 - 500$ keV lower than the experimental state, thus, they cannot be firmly assigned to correspond to this state, even with the transition probabilities and the possibilities of the spins remain open.

Table 8.4: The calculated reduced transition probabilities and the partial γ-ray transition probabilities for the assignement of the spin and parity of the experimental level at 3502 keV.

Transition Energy$_{\text{level}}$ [keV]	$B(M1)$ μ_{N}	$B(E2)$ e^2fm^4	$P_{i \to f}$ $[\frac{1}{s}]$	ratio
$(1_4^+ \to 0_1^+)$	0.21	0.0	$1.6 \cdot 10^{13}$	0.59
$(1_4^+ \to 2_1^+)$	0.026	0.0	$1.1 \cdot 10^{11}$	0.41
3060				
$(2_6^+ \to 0_1^+)$	$-$	3	$1.8 \cdot 10^{12}$	0.49
$(2_6^+ \to 2_1^+)$	0.026	0.02	$1.9 \cdot 10^{13}$	0.51
2640				

Summary

The signatures of collectivity were found in ^{84}Ge which has only 2 neutrons above magic $N = 50$ number. The final level scheme of ^{84}Ge compared with the theoretical calculation is presented in Figure 8.9. Two possible corresponding states were assigned for the 3rd and the 5th excited states. The possibility of the γ deformation in ^{84}Ge (with $\gamma \approx 25°$ according to [62]) was discussed. The two excitation levels predicted by the shell model calculation to belong to the γ-band are also drawn in Figure 8.9.
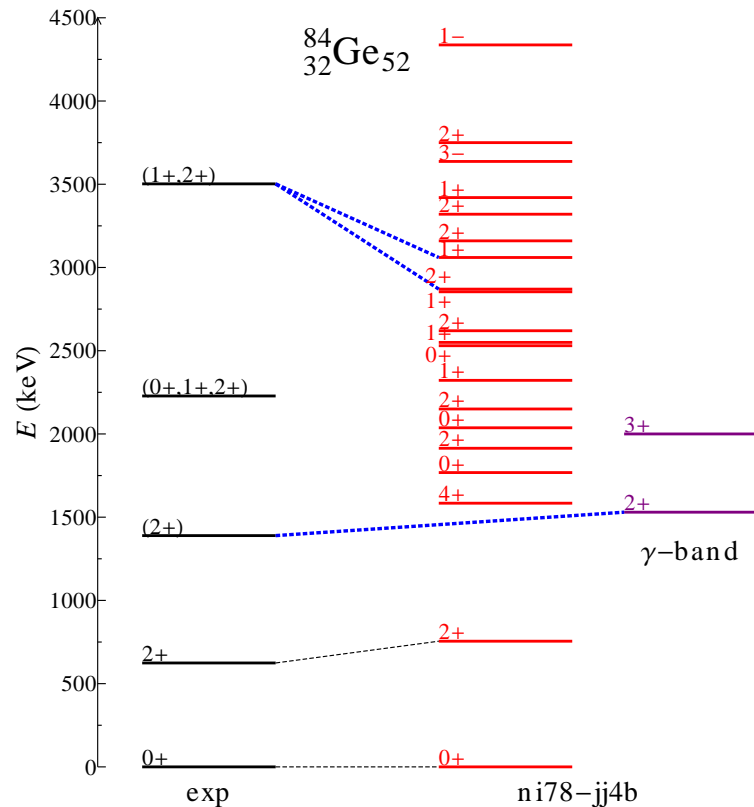
Figure 8.9: The experimental level scheme of ^{84}Ge in comparison with low-spin states obtained in theoretical calculation made with $ni78 - jj4b$ interaction.

Comparison with the Beyond Mean Field calculations

To get the idea on the quality of the shell model calculation we compare our results to the results of the Beyond Mean Field calculations [125, 126] with Hartree-Fock-Bogoliubov mean field potential and Gogny force. The experimental and theoretical energy spectra of ^{84}Ge are presented in Figure 8.10. As one can notice the calculated shell model spectrum agrees nicely with the beyond mean field calculation predicting

same parity states as similar energies for the first few states of our interest. The triaxial map of the potential (from the beyond mean field calculation) is presented on the right in Figure 8.10. The γ deformation is clearly visible indication prediction of completely γ soft nuclei. With the projection of the good quantum number one obtains the mean γ parameter which in this case is $30°$. This result is consistent with the discussion made on the base of the shell model calculations.
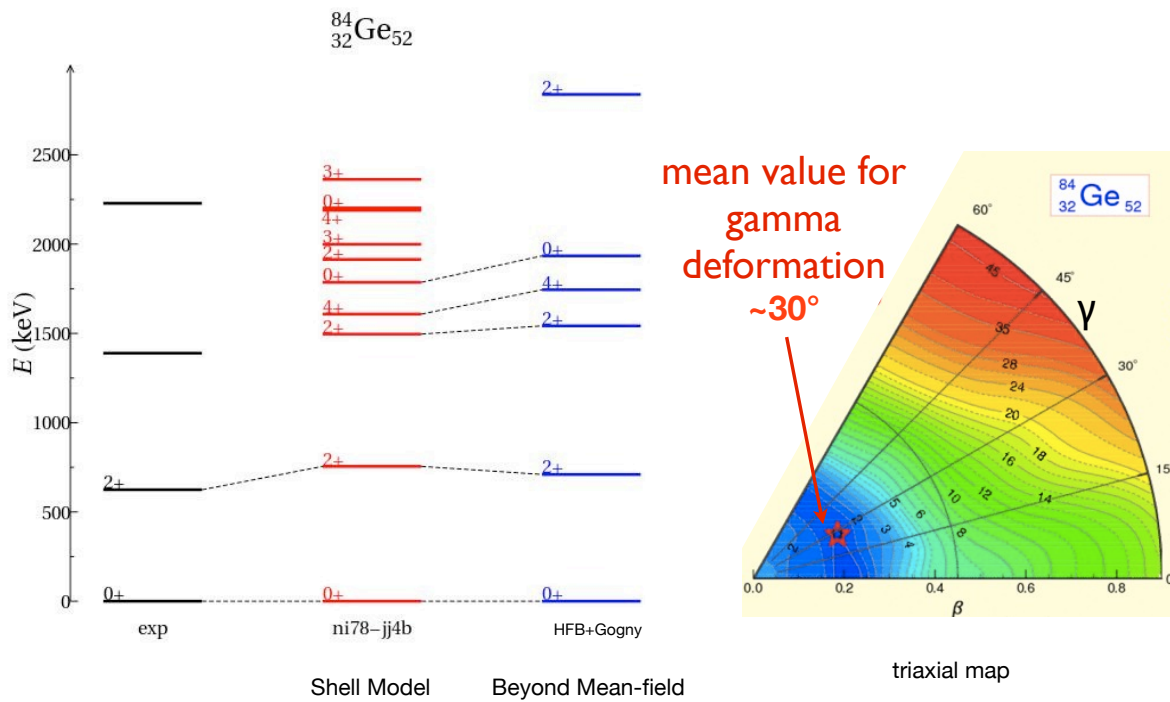
Figure 8.10: The experimental level scheme of ^{84}Ge in comparison with with the theoretical calculations : shell model calculations made with $ni78 - jj4b$ interaction and beyond mean field "HFB+Gogny" calculations. Data from [126].

8.2 Nuclear structure of ^{83}Ge

Shell model calculations for even-odd nuclei at $N = 51$

Before performing calculation for ^{83}Ge I tested the performance of our effective interaction calculating the energy spectra for even-odd nuclei at $N = 51$: ^{89}Sr, ^{87}Kr and ^{85}Se. The results are presented in Figure 8.11 where in the first column the first two states in the core even-even nuclei (core as considered by the core-coupling model) are presented, in the second column the experimental levels and in the third theoretical calculations.
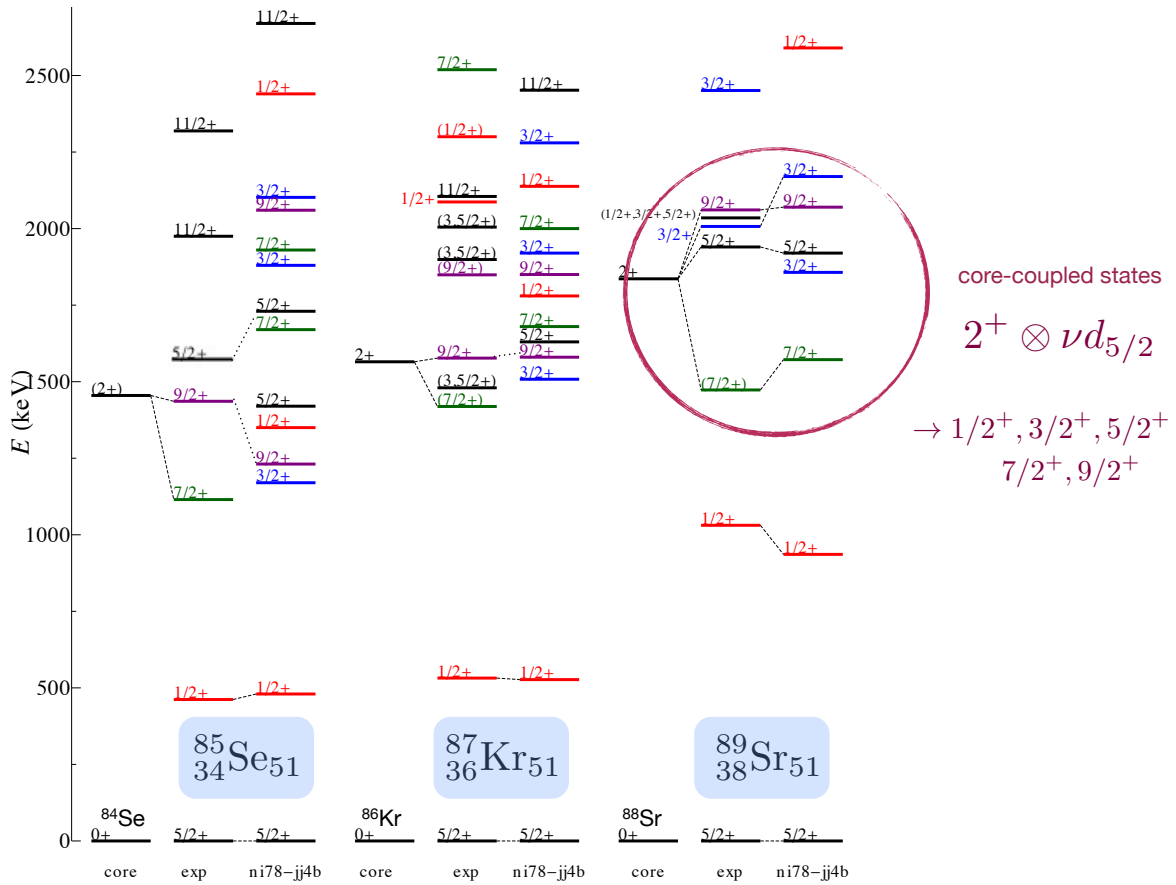
Figure 8.11: The systematics of the energy level of $N = 51$ even-odd nuclei compared with the shell model calculation.

The excitation levels in ^{89}Sr, both single-particle and core-coupled, are reproduced very well. When we compare the results for more exotic ^{87}Kr and ^{85}Se this agreement is not that obvious. Only higher spin $(7/2^+, 9/2^+)$ states were identified in ^{85}Se so

it is difficult to discuss the reliability of our calculation for its excitation states but obviously the $7/2^+$ is predicted to be too high while $9/2^+$ is reproduced quite well. The same happens for the $7/2^+$ state in ^{87}Kr, but the lower spin states and the state with spin $9/2^+$ are in relatively good agreement with experiment.

Shell model calculations for ^{83}Ge

The experimental energy spectrum for ^{83}Ge is compared with the shell model calculation in Figure 8.12. On the right side of the figure one can see the calculated ground state and the first excited 2^+ state in ^{82}Ge which has one neutron less than discussed ^{83}Ge (and in the weak-coupling model is considered as a core for ^{83}Ge). The wave functions of those two states are presented in Table 8.5. One can see that both states have contribution from two configurations of protons in the $\pi f_{5/2}^4$ orbit and $\pi p_{3/2}^2 \pi f_{5/2}^2$.

Table 8.5: Wave functions of the calculated ground state 0^+ and the first 2^+ excited state in ^{82}Ge.

Energy exp. [keV]	Energy calc. [keV]	J^π	Wave function
0.0	0.0	0^+	50% $\pi f_{5/2}^4$
			33% $\pi p_{3/2}^2 \pi f_{5/2}^2$
1347.51(7)	1328	2^+	53% $\pi f_{5/2}^4$
			18% $\pi p_{3/2}^2 \pi f_{5/2}^2$

Table 8.6: The experimental energies of excitation levels in ^{83}Ge and proposed calculated ones with the spin assignements and wave functions.

Energy exp. [keV]	Energy calc. [keV]	J^π	Wave function
0.0	0.0	$5/2^+$	40% $\pi p_{3/2}^2 \pi f_{5/2}^2 \otimes \nu d_{5/2}^1$
			33% $\pi f_{5/2}^4 \otimes \nu d_{5/2}^1$
247.7(3)	428	$1/2^+$	40% $\pi p_{3/2}^2 \pi f_{5/2}^2 \otimes \nu s_{1/2}^1$
			20% $\pi f_{5/2}^4 \otimes \nu s_{1/2}^1$
1045.9(4)	1180	$3/2^+$	35% $\pi f_{5/2}^4 \otimes \nu d_{5/2}^1$
			16% $\pi p_{3/2}^2 \pi f_{5/2}^2 \otimes \nu d_{5/2}^1$
	1450	$1/2^+$	33% $\pi f_{5/2}^4 \otimes \nu d_{5/2}^1$
			13% $\pi p_{3/2}^2 \pi f_{5/2}^2 \otimes \nu d_{5/2}^1$

With our interaction we reproduce well the ground state $5/2^+$ spin. The wave function of this state has two components:

- $\pi p_{3/2}^2 \pi f_{5/2}^2 \otimes \nu d_{5/2}^1$

- $\pi f_{5/2}^4 \otimes \nu d_{5/2}^1$

each with a single neutron in $\nu d_{5/2}$ orbital (see Table 8.6). When we compare the proton part of the wave function between ^{82}Ge and ^{83}Ge their compositions differ with the importance of the two components. In case of even-even ^{82}Ge the most favourable configuration was of four protons in $\pi f_{5/2}$, while when we add one neutron and form ^{83}Ge the configuration of two protons in $\pi p_{3/2}$ and two in $\pi f_{5/2}$ dominates. This proton configuration is favoured also in the first excited $1/2^+$ state, also well reproduced (in terms of spin and energy) by our interaction. This state is formed from the excitation of the neutron to the $\nu s_{1/2}$ orbital. In the following paragraphs we discuss the possible spins and parities of the higher excitation levels in ^{83}Ge using the shell model calculations.
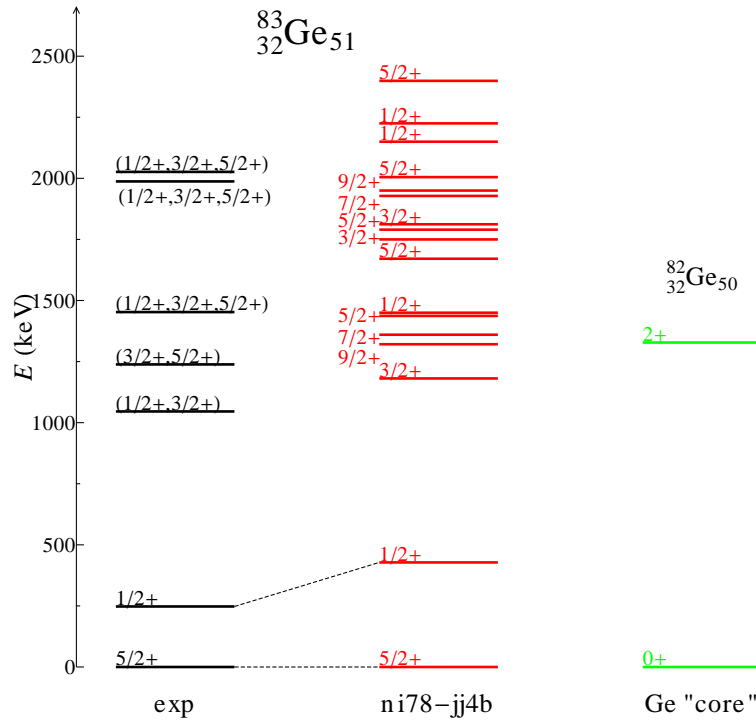
Figure 8.12: The resulting level scheme of ^{83}Ge in comparison with theoretical shell model calculation made with $ni78 - jj4b$ interaction.

Figure 8.13: The schematic view of the possible electric and magnetic mode transitions assuming the $1/2^+$ or $3/2^+$ spin for the third excited state in ^{83}Ge. The numbers in red represent the partial γ-ray transition probabilities.
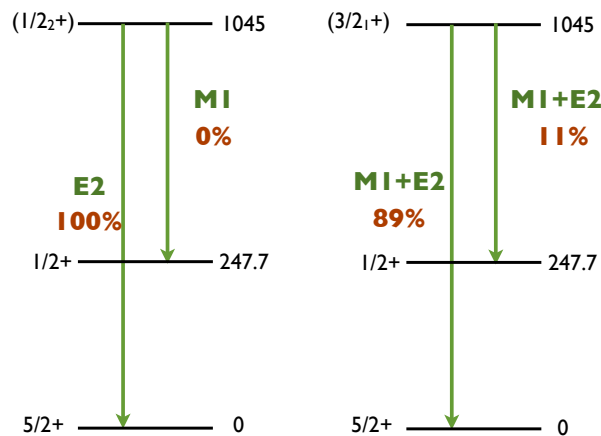
The level at 1045.9 keV

Two possibilities for the spins for this state are $(1/2^+)$ and $(3/2^+)$ (as discussed already in Chapter 7). We consider the first calculated $1/2^+$ state at 1450 keV and the first $3/2^+$ calculated state at 1180 keV as possible candidates for this state. Their wave functions are presented in Table 8.6. In both of them the single neutron is in the $\nu d_{5/2}$ orbital while protons form similar configurations to the ones seen in ^{82}Ge. There are two transitions from the state at 1045.9 keV, one to the ground state and the second to the first excited state. We proceed with the calculation of the partial γ-ray transition probabilities, which can be helpful for the spin assignment.

The two possible scenarios are presented in Figure 8.13 where the considered transitions are of the magnetic $M1$ and the electric $E2$ character. The results of the calculated reduced transition probabilities and the partial γ-ray transition probabilities are presented in Table 8.7. From the experimental data, the relative intensities of the transition from the state at 1045 keV to the ground state is $90(6)\%$ while the intensity to the first excited state is only $10(2)\%$. This result is compatible with the calculated value obtained for the $3/2^+$ spin state predicted at 1180 keV (89% and 11%). We use this argument for the assignment of the spin $3/2^+$ for the level at 1045 keV.

The level at 1238 keV

The spin and parity of this level was proposed by Perru [48] to be the $3/2^+$ or the $5/2^+$ member of the core-particle coupling multiplet since its energy is very close to the one of the 2_1^+ state of ^{82}Ge (1348 keV). The population of this state in β-decay of

Table 8.7: The calculated reduced transition probabilities and the partial γ-ray transition probabilities for the assignement of the spin and parity of the experimental level at 1045 keV.

Transition Energy$_{\text{level}}$ [keV]	$B(M1)$ μ_N	$B(E2)$ $e^2\text{fm}^4$	$P_{i \to f}$ $[\frac{1}{s}]$	ratio
$(3/2^+ \to 5/2^+)$	0.43	105	$8.66 \cdot 10^{12}$	0.89
$(3/2^+ \to 1/2^+)$	0.117	66	$1.06 \cdot 10^{12}$	0.11
1180				
$(1/2^+ \to 5/2^+)$	$-$	50		1.0
$(1/2^+ \to 1/2^+)$	0.0	$-$		0.0
1450				

^{83}Ga [37] was estimated to be twice higher than that of the $1/2^+$ first excited state or the state of 1045 keV, which as discussed earlier could be of spin $(3/2^+)$. This could give an indication that the state has a spin $5/2^+$ and is favoured over $1/2^+$, $3/2^+$ in β-decay from the ground state of ^{83}Ga (proposed spin $5/2^-$).

Following this hypothesis and the shell model calculation (Figure 8.12) the state at 1238 keV could be assigned (however very tentatively) to the second $5/2^+$ state calculated at 1437 keV. Its wave function consist of three components:

- $\pi p_{3/2}^2 \pi f_{5/2}^2 \otimes \nu d_{5/2}^1$

- $\pi f_{5/2}^4 \otimes \nu d_{5/2}^1$

- $\pi p_{3/2}^1 \pi f_{5/2}^3 \otimes \nu d_{5/2}^1$.

This wave function is similar to the one of the ground state and it includes also the third component with three protons in $\pi f_{5/2}$ orbital.

The level at 2026 keV

Two transitions were seen from the level at 2026 keV, one to the ground state, the second to the first excited state with relative intensities $3(1)\%$ and $6(2)\%$, respectively. Except for the assumption of rather low spin $1/2^+, 3/2^+, 5/2^+$, assuming that the state was populated from the β n-decay of ^{84}Ga with ground state spin (0^-), no restrictions were made for the spin assignment. As previously the partial γ-rays transition probabilities from this level were calculated. The closest in energy states with spin $1/2^+, 3/2^+, 5/2^+$ calculated with the shell model code were considered. The results are presented in Table 8.8. From this calculation the state which corresponds to the experimental one is of spin $1/2^+$ located at 2225 keV.

Table 8.8: The calculated reduced transition probabilities and the partial γ-ray transition probabilities for the assignement of the spin and parity of the experimental levels in ^{83}Ge at 2026 keV.

Transition Energy$_{\text{level}}$ [keV]	$B(M1)$ μ_{N}	$B(E2)$ $e^2\text{fm}^4$	$P_{i \to f}$ $[\frac{1}{s}]$	ratio
$(1/2_3^+ \to 5/2^+)$	–	3.38	$8.27 \cdot 10^{10}$	0.53
$(1/2_3^+ \to 1/2^+)$	0.0007	–	$7.42 \cdot 10^{10}$	0.47
1820				
$(1/2_4^+ \to 5/2^+)$	–	0.16	$1.07 \cdot 10^{10}$	0.04
$(1/2_4^+ \to 1/2^+)$	0.012	–	$2.33 \cdot 10^{12}$	0.96
2225				
$(3/2_3^+ \to 5/2^+)$	0.21	3	$31.07 \cdot 10^{12}$	0.99
$(3/2_3^+ \to 1/2^+)$	0.0001	0.4	$0.009 \cdot 10^{12}$	0.1
1812				
$(5/2_5^+ \to 5/2^+)$	0.002	0.006	$33.69 \cdot 10^{10}$	0.17
$(5/2_5^+ \to 1/2^+)$	–	56	$180.4 \cdot 10^{10}$	0.83
2000				
$(5/2_6^+ \to 5/2^+)$	0.02	2	$231.8 \cdot 10^{10}$	0.99
$(5/2_6^+ \to 1/2^+)$	–	0.32	$0.71 \cdot 10^{10}$	0.01
2400				

Summary

The final level scheme of ^{83}Ge compared with the theoretical calculation is presented in Figure 8.14. The possible states were assigned for the 3rd, 4th and 7th excited states.

Core-coupled states

As mentioned already earlier, in case of even-odd nuclei we consider single-particle and core-coupled states. Having assinged the spins and parities of the levels of interest one can try to make discussion of which of the states in ^{83}Ge is formed by the neutron weak coupling with the even-even core (see Figure 8.15).

We start from the identification of the $9/2^+$ core-coupled states in $N = 51$ isotones. We compare the wave functions of the first excited 2^+ state of even-even core and the core-coupled $9/2^+$ state in even-odd nuclei (see Figure 8.16). In case of ^{88,89}Sr and ^{86,87}Kr there are two same dominant proton configuration. For ^{84}Se there if one dominant
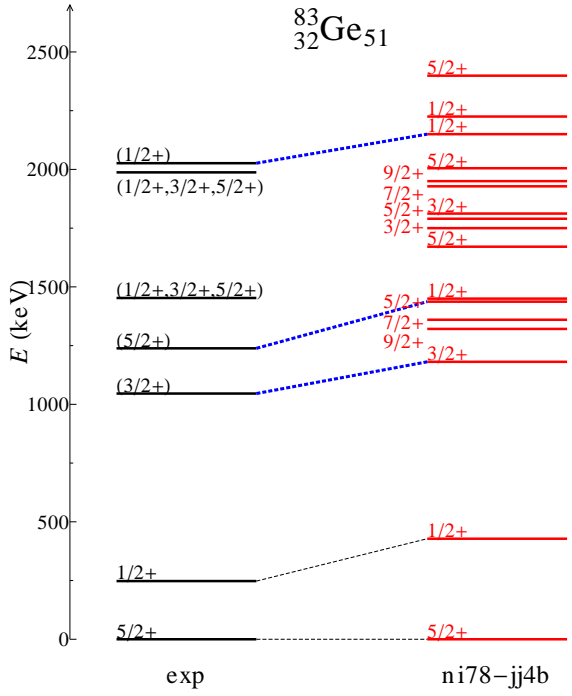
Figure 8.14: The experimental level scheme of ^{83}Ge in comparison with low-spin states obtained in theoretical calculation made with $ni78 - jj4b$ interaction.
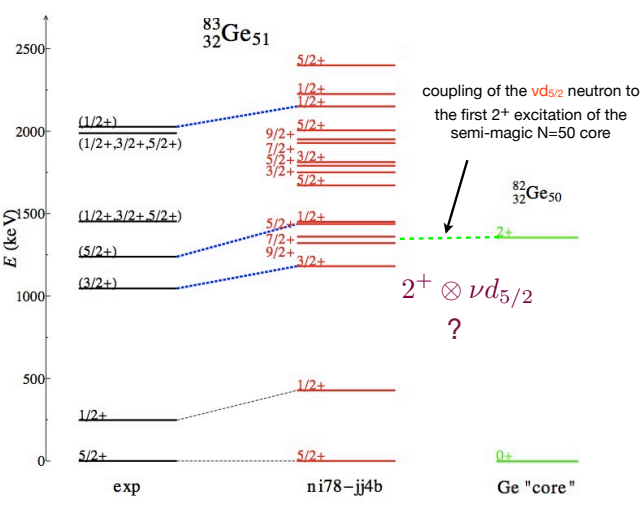
Figure 8.15: Search for the core-coupled states in the experimental and theoretical level scheme of ^{83}Ge.

proton configuration and the same in ^{85}Se with one neutron more. We can see that for those three nuclei the core-coupling model holds. The same cannot be concluded when investigating the wave functions of ^{83,83}Ge and ^{80,81}Zn. The wave function of 2^+ and $9/2^+$ states differ and new components appear when one adds neutron to the even-even core. This new component is dominant (in ^{83}Ge) indicating rahter strong than weak coupling in this nucleus. One added neutron destroys proton configuration and the connection to the weak core-coupling model is lost. The calculated with the shell model wave functions indicate changes at $Z = 32$ and $Z = 30$.
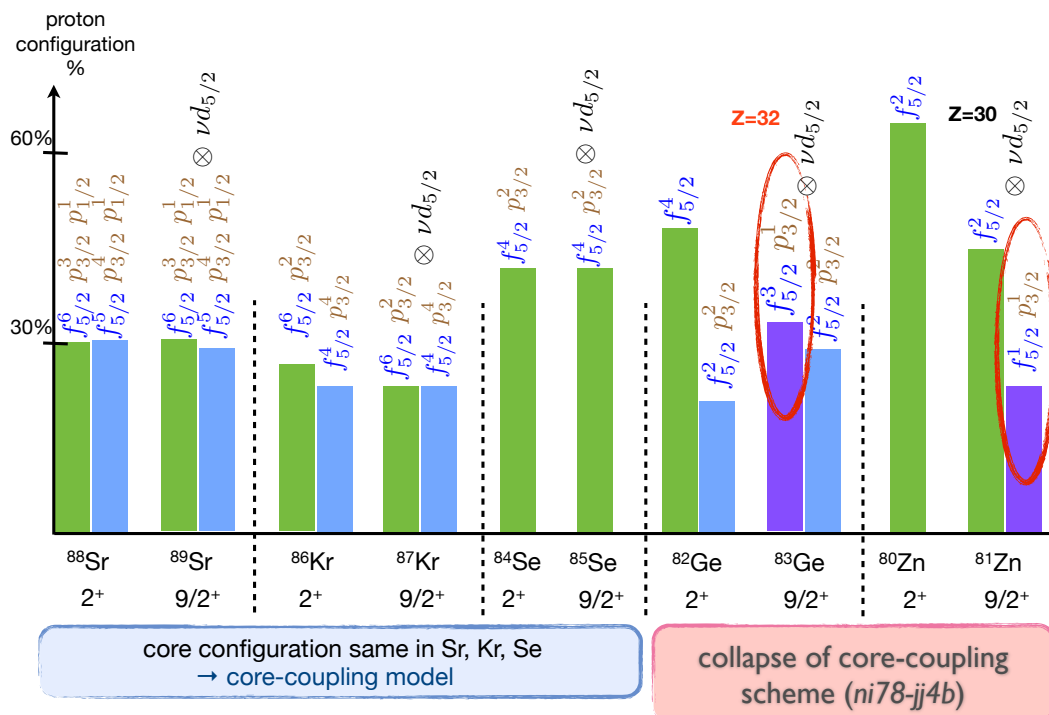
Figure 8.16: The composition of the wave functions to investigate the core-coupled states.

Conclusions and outlook

Contents

9.1   Conclusions

The optimization of various steps allowing production of the high-intensity radioactive beams is necessary and of particular interest for the future radioactive beam facilities like SPIRAL2 (GANIL) or EURISOL-DS. The production and separation process involves several important steps like powerful primary beam, feasible target material, good extraction and transport, rapidity and selectivity. In order to perform successfully the experiment of β-decay study we studied and optimized:

- primary beam: The primary beam of electrons used in our experiment to induce photo-fission in uranium carbide target intensity 10 μA. The experiment described in this thesis was the commissioning experiment for the ALTO facility and the first experiment where the electron beam intensity was maximal.

- target: Study of the release properties of different UC_x targets was discussed in Chapter 4. We studied different samples of uranium carbide targets in order to find the most optimal one that will be used, at first in our experiment, and later in SPIRAL2. The samples were first irradiated with deuteron beam of energy 26 MeV and intensity 20 nA and in the next step heated in the oven up to 1200 C. The activities from the pellets were measured after the heating with two germanium detectors. I performed simulations of the expected γ-ray spectrum to determine the feasibility of the experiment and the estimation of the expected counting rate.

- selectivity: For the ionization of gallium atoms we used newly developed laser ionization source. The gallium atoms were ionized in two steps: the first laser beam was used to excite the electron which was then ejected with the second laser beam. The efficiency of this source was estimated to be 10 times higher

than the surface ionization source (from the test of the stable ^{69}Ga beam). This laser ion souce was successfully used during our experiment. The comparison spectrum between the data acquired with and without the laser was presented in Figure .

Except for the optimization of the production, release and ionization of the fission products the detection system in the low-count rate β-decay study plays a very important role. Due to exoticity of the elements studied the statistics is low and it is desirable to have detection system with high enough efficiency and shielded from the background. I tested the performance of newly designed BGO shield (prototype for the ORGAM2 project at ALTO), and the Veto plastic detector. This study was performed in order to test the background subtraction in the configuration of germanium detector surrounded with BGO shield and the Veto plastic. This configuration with five germanium detectors surrounding the collection point is done in the new detection system BEDO (BEta Decay studies at Orsay). This detection system is currently commissioned at ALTO.

A priori to the experimental study of the β-decay of neutron rich gallium I built a shell model interaction in collaboration with K. Sieja and F. Nowacki from IPHC (Strasbourg). The new $ni78 - jj4b$ interaction has the following properties:

- ^{78}Ni core,

- valence space for protons is $2p_{3/2}, 1f_{5/2}, 2p1/2$ and $1g_{9/2}$,

- valence space for neutrons: $1g_{7/2}, 2d_{5/2}, 2d_{3/2}, 3s_{1/2}, 1h_{11/2}$.

I built the effective interaction which can reproduce well already known experimental data and which has predictive power for our nuclei of interest. I successfully used the $ni78 - jj4b$ interaction to perform theoretical calculation for excitation energies and reduced transition probabilities for $^{83-84}$Ge.

We performed experimental studies to probe the nuclear structure of the neutron-rich nuclei in the vicinity of ^{78}Ni via β-decay spectroscopy of ^{84}Ga. Using time spectra I discriminated half-lives of the mother nuclei. With $\gamma-\gamma$ coincidences new transitions were found which allowed us to improve levels schemes of:

- $N = 51$ even-odd ^{83}Ge: The constraints were put for the spin assignment of all the levels identified. Using shell model predictions I made tentative assignment of spins and parities to three of the states.

- $N = 52$ even-even ^{84}Ge: The third excitation state was assigned as 2_2^+ possibly belonging to the γ-band, as predicted by the shell model calculation. From the Davydov's model, ^{84}Ge is seen to have rigid asymmetry of $\gamma \approx 25°$. Similarities in the dynamics were found when comparing with ^{80}Ge.

- $N = 51$ odd-odd ^{84}As: Many new excited states and γ-transitions were found in this nucleus. This odd-odd nucleus is difficult to interpret with our shell model interaction and more theoretical work should be done in order to obtain reliable conclusions on the structure of ^{84}As.

9.2 Outlook

The experiment of β-decay described in this thesis was one of the few commissioning tests performed at the ALTO facility. After this successful run the safety authority has given in May 2012 the official authorization for the exploitation of ALTO. A broad physics program is planned for the up-coming years:

- work on the studies of differently manufactured UC_x targets continues, new prototypes are manufactured and tested,

- experiments are planned with thorium carbide target in order to reach elements with lower masses (close to $N = 50$) in fission reaction,

- the newly built detection system BEDO dedicated to study β-decay of radioactive species has been recently built and commissioned at ALTO. It has higher efficiency (absolute efficiency estimated to $5-6\%$ as compared with 2% efficiency of the system with two germanium detectors used in previous experiments). The future experiment planned is β-decay study of ^{81}Cu to populate excited states in ^{81}Zn,

- new neutron detector Tetra has been built at IPN Orsay in collaboration with Dubna (Russia). Next experiments are planned with full intensity $10\mu A$ electron beam and laser ion source to study the neutron emission probability of neutron rich gallium ($^{85-86}$Ga) using this neutron detector and germanium detector.

Bibliography

[1] C. Engelmann, Z. Phys. A **352**, 351 (1995). (Cited on page 1.)

[2] K. Sieja, F. Nowacki, K. Langanke and G. Martinez-Pinedoz, Physical Review **C 79**, 064310 (2009). (Cited on pages 1 and 28.)

[3] J. Duflo and A.P. Zuker, Phys. Rev. C **59**, R2347 (1999). (Cited on page 1.)

[4] T. Otsuka, T. Matsuo and D. Abe, Phys. Rev. Lett. **97**, 162501 (2006). (Cited on page 1.)

[5] T. Otsuka, T. Suzuki, M. Honma, Y. Utsuno, N. Tsun-oda, K. Tsukiyama and M. Hjorth-Jensen, Phys. Rev. Lett. **104**, 012501 (2010). (Cited on page 1.)

[6] K.T. Flanagan, P. Vingerhoets, M. Avgoulea, J. Billowes, M.L. Bissell, K. Blaum, B. Cheal, M. De Rydt, V.N. Fedosseev, D.H. Forest, C. Geppert, U. Köster, M. Kowalska, J. Krämer, K.L. Kratz, A. Krieger, E. Mané, B.A. Marsh, T. Materna, L. Mathieu, P.L. Molkanov, R. Neugart, G. Neyens, W. Nörtershäuser, M.D. Seliverstov, O. Serot, M. Schug, M.A. Sjoedin, J.R. Stone, N.J. Stone, H.H. Stroke, G. Tungate, D.T. Yordanov and Y.M. Volkov, Phys. Rev. Lett. **103**, 142501 (2009). (Cited on page 1.)

[7] T. Otsuka, T. Suzuki, R. Fujimoto, H. Grawe and Y. Akaishi, Phys. Rev. Lett. **95**, 232502 (2005). (Cited on page 1.)

[8] B. Fogelberg, Phys. Rev. Lett. **73**, 2413 (1994). (Cited on page 2.)

[9] K.L. Jones, A.S. Adekola, D.W. Bardayan, J.C. Blackmon, K.Y. Chae, K.A. Chipps, J.A. Cizewski, L. Erikson, C. Harlin, R. Hatarik, R. Kapler, R.L. Kozub, J.F. Liang, R. Livesay, Z. Ma, B.H. Moazen, C.D. Nesaraja, F.M. Nunes, S.D. Pain, N.P. Patterson, D. Shapira, J.F.S. Jr, M.S. Smith, T.P. Swan and J.S. Thomas, Nature **465**, 454 (2010). (Cited on page 2.)

[10] B. Bastin, S. Grévy, D. Sohler, O. Sorlin, Z. Dombrádi, N.L. Achouri, J.C. Angélique, F. Azaiez, D. Baiborodin, R. Borcea, C. Bourgeois, A. Buta, A. Bürger, R. Chapman, J.C. Dalouzy, Z. Dlouhy, A. Drouard, Z. Elekes, S. Franchoo, S. Iacob, B. Laurent, M. Lazar, X. Liang, E. Liénard, J. Mrazek, L. Nalpas, F. Negoita, N.A. Orr, Y. Penionzhkevich, Z. Podolyák, F. Pougheon, P. Roussel-Chomaz, M.G. Saint-Laurent, M. Stanoiu, I. Stefan, F. Nowacki and A. Poves, Phys. Rev. Lett. **99**, 022503 (2007). (Cited on page 2.)

[11] M. Stanoiu, D. Sohler, O. Sorlin, F. Azaiez, Z. Dombrádi, B.A. Brown, M. Bel-leguic, C. Borcea, C. Bourgeois, Z. Dlouhy, Z. Elekes, Z. Fülöp, S. Grévy, D. Guillemaud-Mueller, F. Ibrahim, A. Kerek, A. Krasznahorkay, M. Lewitow-icz, S.M. Lukyanov, S. Mandal, J. Mrázek, F. Negoita, Y.E. Penionzhkevich, Z. Podolyák, P. Roussel-Chomaz, M.G. Saint-Laurent, H. Savajols, G. Sletten, J. Timár, C. Timis and A. Yamamoto, Phys. Rev. C **78**, 034315 (2008). (Cited on page 2.)

[12] M.G. Porquet and O. Sorlin, Phys. Rev. C **85**, 014307 (2012). (Cited on pages 2 and 3.)

[13] O. Sorlin and M. Porquet, Progress in Particle and Nuclear Physics **61**, 602–673 (2008). (Cited on pages 2 and 7.)

[14] J. Hakala, S. Rahaman, V.V. Elomaa, T. Eronen, U. Hager, A. Jokinen, A. Kankainen, I.D. Moore, H. Penttilä, S. Rinta-Antila, J. Rissanen, A. Saas-tamoinen, T. Sonoda, C. Weber and J. Äystö, Phys. Rev. Lett. **101**, 052502 (2008). (Cited on page 3.)

[15] M. Bender, G.F. Bertsch and P.H. Heenen, Phys. Rev. C **78**, 054312 (2008). (Cited on page 3.)

[16] H. Fann, J. Schiffer and U. Stohbush, Phys. Lett. B **44**, 19 (1973). (Cited on pages 3 and 5.)

[17] P. Li, W. Daehnick, S.K. Saha, J. Brown and R. Kouzes, Nulc. Phys. A **469**, 393–406 (1987). (Cited on pages 3 and 5.)

[18] G. Winter, R. Schwengner, J. Reif, H. Prade, L. Funke, R. Wirowski, N. Nicolay, A. Dewald, P. v Brentano, H. Grawe and R. Schubart, Phys. Rev. C **48**, 1010–1019 (1993). (Cited on pages 3 and 5.)

[19] A. Prevost, M. Porquet, A. Astier, I. Deloncle, F. Azaiez, A. Buta, D. Curien, O. Dorvaux, G. Duchene, B. Gall, F. Khalfallah, I. Piqueras, M. Rousseau, M. Meyer, N. Redon, O. Stezowski, T. Venkova, R. Lucas and A. Bogachev, Eur. Phys. J. A **22**, 391–395 (2004). (Cited on pages 3 and 5.)

[20] T. Rząca-Urban, W. Urban, J.L. Durell, A.G. Smith and I. Ahmad, Phys. Rev. C **76**, 027302 (2007). (Cited on pages 3, 4, 5 and 6.)

[21] Y.H. Zhang, Z. Podolyàk, G.d. Angelis, A. Gadea, C. Ur, S. Lunardi, N. Marginean, C. Rusu, R. Schwengner, T. Kröll, D.R. Napoli, R. Menegazzo, D. Bazzacco, E. Farnea, S. Lenzi, T. Martinez, M. Axiotis, D. Tonev, W. Gel-letly, S. Langdown, P.H. Regan, J.J. Valiente Dobon, W. v Oertzen, B. Rubio,

B. Quintana, N. Medina, R. Broda, D. Bucurescu, M. Ionescu-Bujor and A. Iordachescu, Phys. Rev. C **70**, 024301 (2004). (Cited on page 4.)

[22] F.N. K. Sieja, arXiv:1201.0373 (2012). (Cited on pages 4 and 5.)

[23] S. Raman, C.W.Nestor and P.Tikkanen, At. Data Nucl. Data Tables **78**, 1 (2001). (Cited on pages 7 and 13.)

[24] E. Padilla-Rodal, A. Galindo-Uribarri, C. Baktash, J.C. Batchelder, J.R. Beene, R. Bijker, B.A. Brown, O. Castaños, B. Fuentes, J.G. d Campo, P.A. Hausladen, Y. Larochelle, A.F. Lisetskiy, P.E. Mueller, D.C. Radford, D.W. Stracener, J.P. Urrego, R.L. Varner and C.H. Yu, Phys. Rev. Lett. **94**, 122501 (2005). (Cited on pages 5, 6 and 7.)

[25] A. Gade, T. Baugher, D. Bazin, B.A. Brown, C.M. Campbell, T. Glasmacher, G.F. Grinyer, M. Honma, S. McDaniel, R. Meharchand, T. Otsuka, A. Ratkiewicz, J.A. Tostevin, K.A. Walsh and D. Weisshaar, Phys. Rev. C **81**, 064326 (2010). (Cited on page 7.)

[26] R. Lecomte, M. Irshad, S. Landsberger, G. Kajrys, P. Paradis and S. Monaro, Phys. Rev. C **22**, 2420–2423 (1980). (Cited on page 5.)

[27] W.T. Chou, D.S. Brenner, R.F. Casten and R.L. Gill, Phys. Rev. C **47**, 157–162 (1993). (Cited on pages 5 and 6.)

[28] A. Makishima, M. Asai, T. Ishii, I. Hossain, M. Ogawa, S. Ichikawa and M. Ishii, Phys. Rev. C **59**, R2331–R2333 (1999). (Cited on page 5.)

[29] Y. Toh, T. Czosnyka, M. Oshima, T. Hayakawa, H. Kusakari, M. Sugawara, Y. Hatsukawa, J. Katakura, N. Shinohara and M. Matsuda, The Eur. Phys. Journal A - Hadrons and Nuclei **9**, 353–356 (2000). (Cited on pages 5 and 6.)

[30] M. Sugawara, Y. Toh, T. Czosnyka, M. Oshima, T. Hayakawa, H. Kusakari, Y. Hatsukawa, J. Katakura, N. Shinohara, M. Matsuda, T. Morikawa, A. Seki and F. Sakata, The Eur. Phys. Journal A - Hadrons and Nuclei **16**, 409–414 (2003). (Cited on page 5.)

[31] H. Iwasaki, S. Michimasa, M. Niikura, M. Tamaki, N. Aoi, H. Sakurai, S. Shimoura, S. Takeuchi, S. Ota, M. Honma, T.K. Onishi, E. Takeshita, H.J. Ong, H. Baba, Z. Elekes, T. Fukuchi, Y. Ichikawa, M. Ishihara, N. Iwasa, S. Kanno, R. Kanungo, S. Kawai, T. Kubo, K. Kurita, T. Motobayashi, A. Saito, Y. Satou, H. Suzuki, M.K. Suzuki, Y. Togano and Y. Yanagisawa, Phys. Rev. C **78**, 021304 (2008). (Cited on pages 5, 6 and 120.)

[32] B. Kotliński, T. Czosnyka, D. Cline, J. Srebrny, C. Wu, A.B.L. Hasselgren, L. Westerberg, C. Baktash and S. Steadman, Nucl. Phys. A **519**, 646–658 (1990). (Cited on page 6.)

[33] R. Lecomte, G. Kajrys, S. Landsberger, P. Paradis and S. Monaro, Phys. Rev. C **25**, 2812–2814 (1982). (Cited on page 6.)

[34] P. Hoff and B. Fogelberg, Nucl. Phys. A **368**, 210 (1981). (Cited on page 6.)

[35] B. Tastet, Structure des noyaux de gallium, de germanium et d'arsenic riches en neutrons autour de n=50 et dèveloppement d'une source d'ionisation laser à alto, Université Paris-Sud 11, (2011). (Cited on pages 6, 9, 58, 60, 65, 98 and 102.)

[36] D. Verney, B. Tastet, K. Kolos, F.L. Blanc, F. Ibrahim, M.C. Mhamed, E. Cottereau, P.V.Cuong, F. Didierjean, G. Duchene, S. Essabaa, M. Ferraton, S. Franchoo, L. Khiem, C. Lau, J.F.L. Du, I. Matea, B. Mouginot, M. Niikura, B. Rousssiére, I. Stefan, D. Testov and J.C. Thomas. Study of the β-decay of ^{80}ga: additional elements on the proton structure on n=48,49 isotones toards z=28. to be published. (Cited on page 6.)

[37] J.A. Winger, K.P. Rykaczewski, C.J. Gross, R. Grzywacz, J.C. Batchelder, C. Goodin, J.H. Hamilton, S.V. Ilyushkin, A. Korgul, W. Królas, S.N. Liddick, C. Mazzocchi, S. Padgett, A. Piechaczek, M.M. Rajabali, D. Shapira, E.F. Zganjar and J. Dobaczewski, Phys. Rev. C **81**, 044303 (2010). (Cited on pages 6, 7, 9, 70, 90, 94, 95, 96, 98, 104, 105, 106, 109 and 129.)

[38] U. Koster. Workshop on neutron rich nuclei, 16-20 Mars 2008. (Cited on pages 7, 90 and 94.)

[39] M. Lebois, D. Verney, F. Ibrahim, S. Essabaa, F. Azaiez, M.C. Mhamed, E. Cottereau, P.V. Cuong, M. Ferraton, K. Flanagan, S. Franchoo, D. Guillemaud-Mueller, F. Hammache, C. Lau, F. Le Blanc, J.F. Le Du, J. Libert, B. Mouginot, C. Petrache, B. Roussière, L. Sagui, N. d Séréville, I. Stefan and B. Tastet, Phys. Rev. C **80**, 044308 (2009). (Cited on pages 7, 67, 90, 94, 96, 106, 108 and 116.)

[40] S. Padgett, M. Madurga, R. Grzywacz, I.G. Darby, S.N. Liddick, S.V. Paulauskas, L. Cartegni, C.R. Bingham, C.J. Gross, K. Rykaczewski, D. Shapira, D.W. Stracener, A.J. Mendez, J.A. Winger, S.V. Ilyushkin, A. Korgul, W. Królas, E. Zganjar, C. Mazzocchi, S. Liu, J.H. Hamilton, J.C. Batchelder and M.M. Rajabali, Phys. Rev. C **82**, 064314 (2010). (Cited on page 7.)

[41] T.A. Hughes, Phys. Rev. **181**, 1586–1596 (1969). (Cited on page 8.)

[42] E.A. Henry, W.L. Talbert and J.R. McConnell, Phys. Rev. C **7**, 222–238 (1973). (Cited on page 8.)

[43] S.M. Abecasis, J. Davidson and M. Davidson, Phys. Rev. C **22**, 2237–2242 (1980). (Cited on page 8.)

[44] J.S. Thomas, G. Arbanas, D.W. Bardayan, J.C. Blackmon, J.A. Cizewski, D.J. Dean, R.P. Fitzgerald, U. Greife, C.J. Gross, M.S. Johnson, K.L. Jones, R.L. Kozub, J.F. Liang, R.J. Livesay, Z. Ma, B.H. Moazen, C.D. Nesaraja, D. Shapira, M.S. Smith and D.W. Visser, Phys. Rev. C **76**, 044302 (2007). (Cited on pages 8, 9, 95 and 98.)

[45] N.A. Detorie, P.L. Jolivette, C.P. Browne and A.A. Rollefson, Phys. Rev. C **18**, 991–1002 (1978). (Cited on page 8.)

[46] A. Saganek, V. Meyer, S. Mirowski, M. Oteski, M. Sieminski, E. Wesolowski and Z. Wilhelmi, J. Phys. **10**, 549 (1984). (Cited on page 8.)

[47] J.S. Thomas, D.W. Bardayan, J.C. Blackmon, J.A. Cizewski, U. Greife, C.J. Gross, M.S. Johnson, K.L. Jones, R.L. Kozub, J.F. Liang, R.J. Livesay, Z. Ma, B.H. Moazen, C.D. Nesaraja, D. Shapira and M.S. Smith, Phys. Rev. C **71**, 021302 (2005). (Cited on pages 9, 95 and 98.)

[48] O. Perru, Eur. Phys. J. **A 28**, 307 – 312 (2006). (Cited on pages 9, 53, 95, 96, 98 and 128.)

[49] M. Lebois, Structure des noyaux de germanium et de gallium riches en neutrons au-delà de N = 50 à alto, Université Paris-Sud 11, (2008). (Cited on pages 9, 67, 83, 95, 98 and 102.)

[50] J.V. Kratz, Nucl. Phys. A **250**, 13 (1975). (Cited on pages 9 and 102.)

[51] J. Omtvedt, B. Fogelberg and P. Hoff, Z. Phys. A **339**, 349 (1991). (Cited on pages 9, 98 and 102.)

[52] J.A. Winger. Failure of the ^{78}Ni core for Z > 28, N > 50, 2007. (Cited on pages 9, 98 and 102.)

[53] R. Casten, *Nuclear Structures from a Simple Perspective*, Oxford University Press, (1990). (Cited on pages 11, 13, 17, 18 and 20.)

[54] G. Gamow, Proc. Roy. Soc. **[A] 136**, 386–387 (1929). (Cited on page 12.)

[55] G. Gamow, Proc. Roy. Soc. **[A] 126**, 632–644 (1930). (Cited on page 12.)

[56] N. Bohr, Nature **137**, 344–348 (1936). (Cited on page 12.)

[57] N. Bohr and J.A. Wheeler, Phys.Rev. **56**, 426–450 (1939). (Cited on page 12.)

[58] C. Weizsacker, Z.Phys. **96**, 431–458 (1935). (Cited on page 12.)

[59] F. Nowacki. Structure en couche des noyaux: de la stabilité à la limite d'existance, jolie-curies school, 2002. (Cited on page 15.)

[60] M. Goeppert-Mayer, Phys. Rev. **75**, 1969 (1949). (Cited on page 15.)

[61] O. Haxel, J. Hans, D. Jensen and H.E. Suess, Phys. Rev. **75**, 1766 (1949). (Cited on page 15.)

[62] A. Davydov and G. Filippov, Nucl .Phys. **8**, 237–249 (1958). (Cited on pages 17, 18, 19, 118, 119 and 123.)

[63] B.A. Brown, *Lecture Notes in Nuclear Structure Physics*, National Superconducting Cyclotron Laboratory and Department of Physics and Astronomy, Michigan State University, (2005). (Cited on page 21.)

[64] B.J. Brussaard and P.W.M. Glaudemans, *Shell Model applications in nuclear spectroscopy*, North Holland Publishing Company, (1977). (Cited on page 22.)

[65] N. Smirnova. Shell structure evolution and effective in-medium nn interaction, ecole jolie curie, 2009. (Cited on pages 23 and 24.)

[66] S. Bogner, R. Furnstahl and A. Schwenk, Progress in Particle and Nuclear Physics **65**, 94–147 (2010). (Cited on page 25.)

[67] S. Bogner, T. Kuo and L. Coraggio, Nuclear Phys. A **684**, 432 (2001). (Cited on page 25.)

[68] S. Bogner, Phys. Rev. C **2002**, 051301 (65). (Cited on page 25.)

[69] A. Poves and A. Zuker, Phys. Rep. **70**, 235 (1981). (Cited on page 25.)

[70] G. Martinez-Pinedo, A. Zuker, A. Poves and E. Caurier, Phys. Rev. **C 55**, 187 (1997). (Cited on page 25.)

[71] F. Nowacki, Description microscopique des processus faibles dans les noyaux spheriques, IReS Strasbourg school, (1996). (Cited on page 25.)

[72] M. Homna, T. Otsuka, B.A. Brown and T. Mizusaki, Phys. Rev. **C 65**, 061301(R) (2002). (Cited on page 25.)

[73] T. Otsuka, M. Homna and T. e al., Prog. Part. Nucl. Phys. **47**, 319 (2001). (Cited on page 25.)

[74] M. Dufour and A. Zuker, Phys. Rev. C **54**, 1641 (1996). (Cited on pages 25 and 26.)

[75] E. Caurier and F. Nowacki, Acta Physica Polonica **B 30**, 705 (1999). (Cited on page 27.)

[76] A. Poves and F. Nowacki, Lecture Notes in Physics **581**, 70 (2001). (Cited on page 27.)

[77] J.A. Winger, J.C. Hill, F.K. Wohn, R.L. Gill, X. Ji and B.H. Wildenthal, Phys. Rev. C **38**, 285–294 (1988). (Cited on page 28.)

[78] D. Verney, F. Ibrahim, C. Bourgeois, S. Essabaa, S. Galès, L. Gaudefroy, D. Guillemaud-Mueller, F. Hammache, C. Lau, F.L. Blanc, A.C. Mueller, O. Perru, F. Pougheon, B. Roussière, J. Sauvage and O. Sorlin, Phys. Rev. C **76**, 054312 (2007). (Cited on pages 28 and 53.)

[79] F. Clapier, A.C. Mueller, J. Obert, O. Bajeat, M. Ducourtieux, A. Ferro, A. Horbowa, L. Kotfila, C. Lau, H. Lefort, S. Kandri-Rody, N. Pauwels, J.C. Potier, J. Proust, J.C. Putaux, C.F. Liang, P. Paris, A.C.C. Villari, R. Lichtenthäler, L. Maunoury and J. Lettry, Phys. Rev. ST Accel. Beams **1**, 013501 (1998). (Cited on pages 36 and 53.)

[80] H. Ravn and B. Allardyce, Treatise on Heavy-Ion Science; Plenum Press, New York **8** (1989). (Cited on page 36.)

[81] K. Peräjärvi, U.C. Bergmann, V.N. Fedoseyev, A. Joinet, U. Köster, C. Lau, J. Lettry, H. Ravn and M. Santana-Leitner, Nucl. Inst.and Meth. in Physics Research Section B: Beam Interactions with Materials and Atoms **204**, 272 – 277 (2003). (Cited on page 36.)

[82] B. Roussière, F. Ibrahim, J. Sauvage, O. Bajeat, N. Barré, F. Clapier, E. Cottereau, C. Donzaud, M. Ducourtieux, S. Essabaa, D. Guillemaud-Mueller, C. Lau, H. Lefort, C.F. Liang, F.L. Blanc, A.C. Mueller, J. Obert, N. Pauwels, J.C. Potier, F. Pougheon, J. Proust, O. Sorlin, D. Verney and A. Wojtasiewicz, Nucl. Inst. and Meth. in Physics Research Section B: Beam Interactions with Materials and Atoms **194**, 151 – 163 (2002). (Cited on page 36.)

[83] B. Roussière, O. Bajeat, N. Barré, C. Bourgeois, F. Clapier, E. Cottereau, C. Donzaud, M. Ducourtieux, S. Essabaa, D. Guillemaud-Mueller, F. Ibrahim, C. Lau, F.L. Blanc, H. Lefort, C. Liang, A. Mueller, J. Obert, N. Pauwels, J. Potier, F. Pougheon, J. Proust, J. Sauvage, O. Sorlin, D. Verney and A. Wojtasiewicz, Nucl. Instr. and Meth. in Physics Research Section B: Beam Interactions with Materials and Atoms **246**, 288 – 296 (2006). (Cited on page 36.)

[84] CEA/CNRS. Technical report of the radioactive beam section, 2007. (Cited on page 36.)

[85] H. Bateman, Proc. Cambridge Phil. Soc. **16**, 423 (1910). (Cited on page 40.)

[86] Nuclear data sheets. http://www.nndc.bnl.gov/nds/. (Cited on pages 42, 43, 105 and 106.)

[87] T. England and B. Rider. Fission product yields per 100 fissions for 238u high-energy neutron fission decay. LA-UR-94-3106, ENDF-349. (Cited on page 42.)

[88] B. Hy, N. Barre-Boscher, A. Ozgumus, B. Roussiere, S. Tusseau-Nenez, C. Lau, M.C. Mhamed, M. Raynaud, A. Said, K. Kolos, E. Cottereau, S. Essabaa, O. Tougait and M. Pasturel, Nuclear Instruments and Methods in Physics Research Section B: Beam Interactions with Materials and Atoms **288**, 34 – 41 (2012). (Cited on page 49.)

[89] C. Lau, Etude de la production de faisceaux riches en neutrons par fission induite par neutrons rapides, ph. d. thesis, Université Denis Diderot - Paris VII, (2000). (Cited on pages 53 and 68.)

[90] C. Lau, B. Roussière, D. Verney, O. Bajeat, F. Ibrahim, F. Clapier, E. Cottereau, C. Donzaud, M. Ducourtieux, S. Essabaa, D. Guillemaud-Mueller, F. Hosni, H. Lefort, F.L. Blanc, A. Mueller, J. Obert, N. Pauwels, J. Potier, F. Pougheon, J. Proust, J. Sauvage and A. Wojtasiewicz, Nucl. Instr. and Meth. in Physics Research **B 204**, 246–250 (2003). (Cited on page 53.)

[91] F. Ibrahim, Eur. Phys. J. **A 15**, 357 (2002). (Cited on page 53.)

[92] F. Ibrahim, D. Verney, M. Lebois, B. Roussiére, S. Essabaa, S. Franchoo, S. Gales, D.G. Mueller, C. Lau, F.L. Blanc, J.L. Du, M. Mhamed, A. Mueller and J. Sauvage, Nuclear Physics **A 787**, 110 – 117 (2007). (Cited on page 53.)

[93] T. v Egidy, F.J. Hartmann, D. Habs, K. Lobner and H. Niefneker, World Scientific, Singapore, 54 (1997). (Cited on page 53.)

[94] P. Lestone and A. Gavron, Phys. Rev. **C 49**, 372 (1994). (Cited on pages 53 and 54.)

[95] N. Pauwels, University Paris Sud 11, (1998). (Cited on page 54.)

[96] M. Mirea, R. V. A. al. Il Nuovo Cimento **A 111**, 267 (1998). (Cited on page 54.)

[97] C.M. Zoller, Fachbereich Physik der Technischen Hochschule Darmstadt, (1995). (Cited on page 55.)

[98] W. Diamond, Nucl. Inst. and Meth. **A 432**, 471 (1999). (Cited on page 54.)

[99] Y. Oganessian, Nuclear Physics **A 701**, 87 – 95 (2002). (Cited on pages 54 and 56.)

[100] U. Köster, Ausbeuten und spektroskopie radioaktiver isotope bei lohengrin und isolde, Physik-Department der Technischen Universität München, (1999). (Cited on pages 57, 64 and 65.)

[101] R. Kirchner, Nucl. Instr. and Meth. in Physics Research Section A: Accelerators, Spectrometers, Detectors and Associated Equipment **292**, 203 – 208 (1990). (Cited on page 57.)

[102] S. Sundell, Nucl. Instr. and Meth. **B 70**, 160 (1992). (Cited on pages 58 and 59.)

[103] R. Kirchner and E. Roecki, Nucl. Inst. Meth. **A 133**, 187 – 204 (1976). (Cited on page 58.)

[104] W. Jesse and J. Sadauskis, Phys. Rev. **100**, 1755 (1955). (Cited on page 59.)

[105] G. Hurst, Rev. Mod. Phys. **51** (1979). (Cited on page 59.)

[106] H. Friedrich, *Theoretical Atomic Physics*, Springer, Berlin, Heidelberg, (1998). (Cited on page 61.)

[107] L.J. Radziemski, *Reference data on atoms, molecules end ions*, Springer, (1985). (Cited on page 61.)

[108] R.V. Ambartsumyan, JETP Lett. **21**, 276 (1975). (Cited on page 61.)

[109] E.F. Worden, R.W. Solarz, J.A. Paisner and J.G. Conway, J. Opt. Soc. Am. **68**, 52 –61 (1978). (Cited on page 61.)

[110] M.C. Mhamed, Production des noyaux exotiques par photofission. le project alto : Premieres resultats, Universite d'Evry Val d'Essone, (2006). (Cited on page 62.)

[111] P. Paris, C. Liang, D. Lecouturier, M. Arianer, J. Obert, A. Caruette, A. Ferro, J. Fournet, J. Putaux and J. Sarrouy, Nucl. Inst. and Meth. in Physics Research **186**, 91 – 98 (1981). (Cited on page 68.)

[112] J.C. Putaux, Nucl. Instr. and Meth., 321 (1981). (Cited on page 68.)

[113] K.-L.Kratz, H.Gabelmann, P.Mollear, B.Pfeiffer, H.L.Ravn, A.Wohr and t ISOLDE Collaboration, Z.Phys. A **340**, 419 (1991). (Cited on pages 71, 86, 90, 104 and 105.)

[114] D. Abriola, M. Bostan, S. Erturk, M. Fadil, M. Galan, S. Juutinen, T. Kibédi and F. Kondev, Nuclear Data Sheets **110**, 2815–2944 (2009). (Cited on page 76.)

[115] G.F. Knoll, *Radiation detection and measurement*, John Wiley & Sons, (1979). (Cited on pages 78 and 81.)

[116] National nuclear data center, logft calculator. `http://www.nndc.bnl.gov/logft/`. (Cited on pages 81, 93, 94 and 107.)

[117] J. Bris, R. Sellem, J. Artiges, J.F. Clavelin, S. Du, X. Grave, O. Hubert, J. Sauvage and B. Roussiòre. Notice de l'acquisition comet-narval. institut de physique nucléaire, 2005. (Cited on page 83.)

[118] I.N. Borzov, Phys. Rev. C **71**, 065801 (2005). (Cited on page 104.)

[119] E. Caurier, A. Poves and A.P. Zuker, Phys. Rev. Lett. **74**, 1517–1520 (1995). (Cited on page 117.)

[120] P. v Neumann-Cosel, Phys. Lett. **B443**, 1 (1996). (Cited on page 117.)

[121] E. Caurier, G. Martinez-Pinedo, F. Nowacki, A. Poves and A. Zuker, Reviews of Modern Physics **77**, 427–488 (2005). (Cited on page 117.)

[122] V. Werner, N. Pietralla, P. v Brentano, R.F. Casten and R.V. Jolos, Phys. Rev. C **61**, 021301 (2000). (Cited on page 121.)

[123] V. Werner, P. v Brentano and R. Jolos, Physics Letters B **521**, 146 – 152 (2001). (Cited on page 121.)

[124] V. Werner, C. Scholl and P.v. Brentano, Phys. Rev. C **71**, 054314 (2005). (Cited on page 121.)

[125] J.P. Delaroche, M. Girod, J. Libert, H. Goutte, S. Hilaire, S. Peru, N. Pillet and G.F. Bertsch, Phys. Rev. C **81**, 014303 (2010). (Cited on page 123.)

[126] CEA. Beyond mean field calculations www.phynu.cea.fr. (Cited on pages 123 and 124.)